
Molecular characterization of Ariadne RBR E3 ubiquitin ligases in *Arabidopsis*.

Dissecting the mode of action of Spyros in *Arabidopsis*.

Dissertation
zur Erlangung
des Doktorgrades der Naturwissenschaften (Dr. rer. nat.)

vorgelegt der
Naturwissenschaftlichen Fakultät I – Biowissenschaften
Martin-Luther-Universität Halle-Wittenberg

von Frau Elena Moreno Castillo

1. Gutachter: Prof. Dr. Steffen Abel
2. Gutachter: Prof. Dr. Tina Romeis
3. Gutachter: Prof. Dr. Marco Trujillo

Datum der Verteidigung: 02.09.2024

Summary

In this thesis I will show the culmination of 4.5 years of research encompassing two ambitious projects covered in **Section I (2021-2023)** and **Section II (2019-2021)**. My host lab sought to understand how protein ubiquitylation impacts cell signaling. Within this frame, I became interested in characterizing the ARIADNE (ARI) family of E3 ubiquitin ligases during the second period of my PhD, the results obtained are covered in **Section I**.

Protein ubiquitylation plays a crucial role in almost all cellular processes in eukaryotes. This is achieved by the concerted action of E1—E2—E3 enzymes, where the E3 often defines the protein substrate to be ubiquitylated. A particular family of E3 ubiquitin ligases, called Ariadne RBRs (ARIs), catalyze ubiquitin transfer through a 2-step enzymatic reaction upon activation. These proteins are essential in *Drosophila* and *Caenorhabditis* and their mechanism was recently described in humans (HsARIs). However, the functions and mechanism of ARI proteins are largely unknown in plants. Here, we aimed to biochemically characterize AtARIs and uncover their biological function in *Arabidopsis thaliana* (*Arabidopsis*). First, we identified relevant AtARIs by comparing them to HsARIs in terms of sequence and structure. A group of E2s, called group VI, seem to constitute the physiological E2s that mediate AtARI auto-ubiquitylation, based on results from protein—protein interaction assays and *in vitro* ubiquitylation assays. Two potential activation mechanisms appear feasible for AtARIs: E3—E3 binding and phosphorylation, where the other E3 corresponds to AtCUL3A and/or AtPUB26. Finally, a putative substrate of AtARIs was identified as SUMOylated-eIF4E1 based on results from protein—protein interaction assays and *in vitro* ubiquitylation assays. This protein accumulated in *ari1ari2* knock-out mutants. Triple knock-out mutants do not show a visible phenotype which hints towards redundancy of AtARIs and/or requirement of these proteins in untested specific conditions. The results in this thesis set the foundation for studying ARIs *in planta*.

The other project, developed during the first period of my PhD, is covered in **Section II**. It involves the elucidation of the molecular mechanism of Spyro molecules, which were hypothesized to act as Brassinosteroids in plants.

Brassinosteroids (BRs) comprise a family of plant steroids involved in acclimation to environmental stresses, cell elongation, and resistance to pathogens. Due to their effect in plants, BRs have been broadly used as growth regulators for agricultural production. However, content in natural sources is low, and both isolation from plant material and organic synthesis are expensive. Putative analogues of BRs, called Spyros, were developed by our collaborators in Cuba in order to lower the production cost and increase BR-activity. While the growth promoting effects of one of these Spyros, namely DI-31, have been extensively

assessed in agricultural fields, seldom do we know how they truly work. Understanding the mechanisms by which compounds regulate plant responses represents an important direction for boosting crop yield by further derivatization. In order to establish the mode of action of three Spyros (DI-31, MH-5 and DG-15), it was evaluated whether they activate the BR-signaling pathway *in planta* by I) binding to the BR-receptor, II) promoting BR-controlled transcription factor translocation, and III) mediating BR-marker genes' expression. Experiments in *Arabidopsis thaliana* and *Nicotiana benthamiana* showed that all Spyros have little effect on hypocotyl and root length at the seedling stage, while promoting growth of adult plants. Both DI-31 and MH-5 were unable to rescue BR-deficient mutant plants and did not upregulate BR-marker genes such as *BAS1*. Based on molecular dynamic simulations, none of the Spyros mimic the dynamic behavior of natural BRs when bound to BRI1. Thus, Spyros do not seem to act as typical BR compounds. Based on RNAseq and proteomic data, it is possible that either these compounds elicit a non-canonical BR response (non BRI1 signaling), or they constitute a new class of growth promoting steroids by binding to MSBP2 or another unknown receptor. Collectively, my results provide a new perspective for studying growth-promoting steroids in plants with a high potential to impact the research direction of crop improvement over the next decades.

After two years of research, the initial hypothesis that Spyros were classical/canonical BRs was discarded. Even though this opened a new and exciting line of research, there was simply not enough time to perform a deep study to elucidate the molecular mechanism of Spyros. This would include identifying the unknown receptor of Spyros and validating this receptor through *in vitro* and *in vivo* binding assays. Thus, I shifted my focus into the project, covered in Section I, with a higher chance of success and to be completed in less than 2 years. This decision was encouraged by the PhD committee and accepted by the DAAD evaluation committee.

Zusammenfassung

In dieser Arbeit werde ich den Höhepunkt von 4,5 Jahren Forschung darstellen, die zwei ehrgeizige Projekte umfasst, die in Abschnitt I (2021-2023) und Abschnitt II (2019-2021) behandelt werden. Mein Gastlabor versuchte zu verstehen, wie sich die Ubiquitylierung von Proteinen auf die Zellsignalgebung auswirkt. In diesem Rahmen interessierte ich mich für die Charakterisierung der ARIADNE (ARI)-Familie von E3-Ubiquitin-Ligasen während des zweiten Abschnitts meiner Promotion; die erzielten Ergebnisse werden in Abschnitt I behandelt.

Die Ubiquitylierung von Proteinen spielt bei fast allen zellulären Prozessen in Eukaryonten eine entscheidende Rolle. Dies geschieht durch die konzertierte Aktion von E1-E2-E3-Enzymen, wobei das E3-Enzym häufig das zu ubiquitinierende Proteinsubstrat bestimmt. Eine bestimmte Familie von E3-Ubiquitin-Ligasen, die so genannten Ariadne-RBRs (ARIs), katalysieren den Ubiquitin-Transfer durch eine zweistufige enzymatische Reaktion bei der Aktivierung. Diese Proteine sind in *Drosophila* und *Caenorhabditis* essentiell, und ihr Mechanismus wurde kürzlich beim Menschen beschrieben (HsARIs). Die Funktionen und der Mechanismus der ARI-Proteine sind jedoch in Pflanzen weitgehend unbekannt. Wir haben uns zum Ziel gesetzt, AtARIs biochemisch zu charakterisieren und ihre biologische Funktion in *Arabidopsis thaliana* (Ackerschmalwand) aufzudecken. Zunächst identifizierten wir relevante AtARIs, indem wir sie in Bezug auf Sequenz und Struktur mit HsARIs verglichen. Eine Gruppe von E2s, genannt Gruppe VI, scheint die physiologischen E2s zu bilden, die die Auto-Ubiquitylierung von AtARI vermitteln, basierend auf den Ergebnissen von Protein-Protein-Interaktions-Assays und *in vitro* Ubiquitylierungs-Assays. Zwei potenzielle Aktivierungsmechanismen scheinen für AtARI in Frage zu kommen: E3-E3-Bindung und Phosphorylierung, wobei das andere E3 mit AtCUL3A und/oder AtPUB26 übereinstimmt. Schließlich wurde ein mutmaßliches Substrat von AtARIs als SUMOyliertes-eIF4E1 auf der Grundlage von Ergebnissen aus Protein-Protein-Interaktions-Assays und *In-vitro*-Ubiquitylierungs-Assays identifiziert. Dieses Protein reicherte sich in *ari1ari2*-Knock-out-Mutanten an. Dreifach-Knock-out-Mutanten zeigen keinen sichtbaren Phänotyp, was auf eine Redundanz der AtARIs und/oder die Notwendigkeit dieser Proteine unter noch nicht getesteten spezifischen Bedingungen hindeutet. Die Ergebnisse dieser Arbeit bilden die Grundlage für die Untersuchung von ARIs *in planta*.

Das andere Projekt, das in der ersten Phase meiner Doktorarbeit entwickelt wurde, wird in Abschnitt II behandelt. Es beinhaltet die Aufklärung des molekularen Mechanismus von Spyro-Molekülen, von denen angenommen wurde, dass sie als Brassinosteroide in Pflanzen wirken.

Brassinosteroide (BRs) sind eine Familie von Pflanzensteroiden, die an der Anpassung an Umweltstress, der Zelldehnung und der Resistenz gegen Krankheitserreger beteiligt sind. Aufgrund ihrer Wirkung in Pflanzen werden BRs in großem Umfang als Wachstumsregulatoren in der landwirtschaftlichen Produktion eingesetzt. Der Gehalt in natürlichen Quellen ist jedoch gering, und sowohl die Isolierung aus Pflanzenmaterial als auch die organische Synthese sind teuer. Mutmaßliche Analoga von BRs, genannt Spyros, wurden von unseren Mitarbeitern in Kuba entwickelt, um die Produktionskosten zu senken und die BR-Aktivität zu erhöhen. Während die wachstumsfördernden Wirkungen eines dieser Spyros, nämlich DI-31, in landwirtschaftlichen Bereichen ausgiebig bewertet wurden, wissen wir nur selten, wie sie wirklich funktionieren. Das Verständnis der Mechanismen, durch die die Verbindungen die Reaktionen der Pflanzen regulieren, ist ein wichtiger Weg, um die Ernteerträge durch weitere Derivatisierung zu steigern. Um die Wirkungsweise von drei Spyros (DI-31, MH-5 und DG-15) zu ermitteln, wurde untersucht, ob sie den BR-Signalweg in Pflanzen aktivieren, indem sie I) an den BR-Rezeptor binden, II) die BR-gesteuerte Translokation von Transkriptionsfaktoren fördern und III) die Expression von BR-Markergenen vermitteln. Experimente mit *Arabidopsis thaliana* und *Nicotiana benthamiana* zeigten, dass alle Spyros nur geringe Auswirkungen auf die Hypokotyl- und Wurzellänge im Keimlingsstadium haben, während sie das Wachstum erwachsener Pflanzen fördern. Sowohl DI-31 als auch MH-5 waren nicht in der Lage, BR-defiziente Mutanten zu retten, und haben BR-Markergene wie *BAS1* nicht hochreguliert. Basierend auf molekulardynamischen Simulationen ahmt keines der Spyros das dynamische Verhalten natürlicher BRs nach, wenn sie an *BRI1* gebunden sind. Somit scheinen die Spyros nicht wie typische BR-Verbindungen zu wirken. Auf der Grundlage von RNAseq- und Proteomdaten ist es möglich, dass diese Verbindungen entweder eine nicht-kanonische BR-Reaktion (ohne *BRI1*-Signalisierung) auslösen oder eine neue Klasse von wachstumsfördernden Steroiden darstellen, die an *MSBP2* oder einen anderen unbekannten Rezeptor binden. Insgesamt bieten meine Ergebnisse eine neue Perspektive für die Untersuchung von wachstumsfördernden Steroiden in Pflanzen mit einem hohen Potenzial, die Forschungsrichtung der Pflanzenverbesserung in den nächsten Jahrzehnten zu beeinflussen.

Nach zwei Jahren Forschung wurde die ursprüngliche Hypothese, dass es sich bei Spyros um klassische/kanonische BRs handelt, verworfen. Obwohl dies einen neuen und spannenden Forschungszweig eröffnete, reichte die Zeit einfach nicht aus, um den molekularen Mechanismus von Spyros eingehend zu untersuchen. Dies würde die Identifizierung des unbekannten Rezeptors von Spyros und die Validierung dieses Rezeptors durch In-vitro- und In-vivo-Bindungstests beinhalten. Daher konzentrierte ich mich auf das in Abschnitt I beschriebene Projekt, das größere Erfolgsaussichten hatte

und in weniger als zwei Jahren abgeschlossen werden sollte. Diese Entscheidung wurde vom Promotionsausschuss befürwortet und vom Bewertungsausschuss des DAAD akzeptiert.

Table of Contents

Summary	1
Zusammenfassung.....	3
List of abbreviations	8
SECTION I.....	11
I. INTRODUCTION	11
I.1. Ubiquitylation and the ubiquitin code.	11
I.2. Ubiquitylation requires E1, E2 and E3 enzymes.....	14
I.3. The UBC family, structure and function.	14
I.4. The E3 ubiquitin ligases.	19
I.5. The Ariadne RBR E3 ubiquitin ligases.	21
I.6. Aims and objectives.....	27
II. RESULTS.....	29
II.1. Six putative orthologue and parologue AtARIs were selected for studying RBR E3 Ariadne ligases.	29
II.2. All AtARIs interact with Group VI E2s through the RING1 domain.	31
II.3. UbiGate may not be well suited for analyzing E2 reactivity towards AtARIs.	35
II.4. Group VI E2s AtUBC8 and AtUBC28 mediate the autoubiquitylation of ortho-group AtARIs.	36
II.5. Other E3s interact with AtARIs.	38
II.6. eIF4E1, a putative substrate of AtARIs.	39
II.7. eIF4E1 and eIF(iso)4E accumulate in <i>ari1ari2</i> knock-out mutants.....	44
III. DISCUSSION AND FUTURE PERSPECTIVES	45
III.1. Group VI E2s mediate the ubiquitylation of AtARIs.	46
III.2. E3—E3 binding and AtARI phosphorylation constitute potential activation mechanisms.	49
III.3. SUMOylated eIF4E1 constitutes a putative substrate of AtARIs.	50
III.4. ARIs may have redundant functions in <i>Arabidopsis</i> and/or may be related to coping with stress.	52
SECTION II.....	54
I. INTRODUCTION	54
I.1. Brassinosteroids, an essential steroidal phytohormone family.....	54
I.2. Molecular mechanism of BRs in plants.	55
I.3. Using of BR in crops.....	59
I.4. Preliminary data.	62
I.5. Aims and objectives.....	63

II. RESULTS	64
II.1. Phenotypic effect of Spyros in Plants	64
II.2. Mode of action of Spyros	67
II.3. Do Spyros constitute a new class of growth regulators?	72
III. DISCUSSION AND FUTURE PERSPECTIVES	74
III.1. Spyros, a non-classical BR or a new growth-promoting steroid?	74
MATERIALS AND METHODS	78
REFERENCES	94
SUPPLEMENTARY INFORMATION	105
SUPPLEMENTARY MATERIALS AND METHODS	138
Acknowledgements	173
Curriculum vitae	175
List of publications	177
Eidesstattliche Erklärung (Statutory declaration)	178

List of abbreviations

Throughout this thesis the amino acid three-letter or one-letter code is used according to IUPAC-IUB (recommendations 1983).

ABA	Abscisic acid
AD	Activation domain
ARI	Ariadne RBR ligases
ATP	Adenosine-triphosphate
BEH1	BES1 HOMOLOGUE 1
BES1	BRI1-EMS SUPPRESSOR 1
bHLH	Basic helix-loop-helix
BIN2	GLYCOGEN SYNTHASE KINASE3-LIKE KINASE BRASSINOSTEROID INSENSITIVE 2
BL	Brassinolide
BPCS	Biotin-tagged Photoaffinity Castasterone
BR	Brassinosteroid
BRI1	BRASSINOSTEROID INSENSITIVE 1
BRLs	BRI1-Like proteins
BRRE	BR Response Element
BSKs	BR SIGNALING KINASES
BSU1	BRI1-SUPPRESSOR1
BZR1	BRASSINAZOLE-RESISTANT 1
CDG1	CONSTITUTIVE DIFFERENTIAL GROWTH 1
COP1	Constitutively Photomorphogenic 1
CRLs	Cullin RING ligases
DBD	DNA-binding domain
DNA	Deoxyribonucleic acid
DUB	De-ubiquitinating enzyme
eBL	Epibrassinolide
ECD	Ecdysteroid
elf	Eukaryotic Initiation translation Factor
ER	Endoplasmic reticulum

ERAD	Endoplasmic reticulum-associated degradation
Fig.	Figure
GO	Gene ontology
HECT	Homologous to E6AP C-Terminus
IBR	In-between RING domain
KIB1	KINK SUPPRESSED IN BZR1-1D
LIE	Linear Interaction Energy
LRR	Leucine Rich Repeat
MAMP	Microbe-associated molecular pattern
MC	Montecarlo
MD	Molecular Dynamics
MS/MS	Tandem Mass Spectrometry
NEDD8	Neural precursor cell-expressed developmentally downregulated protein 8
NLS	Nuclear localization signal
PP2A	PROTEIN PHOSPHATASE 2A
PROTACs	Proteolysis targeting chimeras
PSM	Peptide spectral mass
PTM	Post-translational modification
qRT-PCR	Real-time quantitative reverse transcription PCR
RBR	RING in-between-RING Rcat
Rcat	Required for catalysis domain
RCR	RING-Cys-relay
REP	Repressor element of Parkin
RING	Really Interesting Gene
RLIT	Rice Lamina Inclination Test
RMSF	Root Mean Square Fluctuation
RNA	Ribonucleic acid
SCF	SKP, Cullin, F-box containing E3 ubiquitin ligase
SERKS	SOMATIC EMBRYOGENESIS KINASES
SUMO	Small ubiquitin-like modifier
Supp.	Supplementary

TF	Transcription factor
Ub	Ubiquitin
Ub	Ubiquitin
UBA	Ubiquitin Associated domain
UBA1	Ubiquitin-activating enzyme 1
UBA-L	UBiquitin Associated-like domain
UBC8	Ubiquitin-conjugating enzyme 8
UBL	Ubiquitin-like proteins
UIM	Ubiquitin interacting motifs
WT	Wild-type
Y2H	Yeast-two-hybrid
YFP	Yellow Fluorescent Protein

SECTION I

I. INTRODUCTION

I.1. Ubiquitylation and the ubiquitin code.

Protein ubiquitylation is a **post-translational modification** (PTM) conserved in all eukaryotes which plays a crucial role in almost all cellular processes ^{1,2}. It is defined as the covalent attachment of ubiquitin (Ub) to specific residues in a substrate protein. The most studied ubiquitylation, often referred to as canonical ubiquitylation, is the attachment of the Ub carboxyl terminus to lysine residues within substrate proteins through an isopeptide bond (**Fig. 1A**) ¹. Ubiquitylation of serine/threonine and cysteine residues generates oxyester and thioester bonds, respectively, which compared to the canonical lysine isopeptide, differ in intrinsic stability, proximity to substrate backbone and rotational freedom (**Fig. 1A**). Other non-canonical ubiquitylation mechanisms have been recently described. These encompass ubiquitylation of non-proteinaceous substrates including nucleotides, lipids and sugars. However, they are not within the scope of this thesis and will not be further discussed (for reviews, see refs. ^{1,3}).

When Ub is bound to only one residue in the substrate this is defined as mono-ubiquitylation (monoUb), while the attachment to multiple residues in the substrate is referred as multimono-ubiquitylation (multiUb) (**Fig. 1B**). Additionally, primary amine groups within the ubiquitin can act as anchor points for further attachment to the carboxyl terminus of a second ubiquitin molecule. Eight residues containing primary amines have been identified in ubiquitin that can form these linkages. These constitute the N-terminus (M1), K6, K11, K27, K29, K33, K48 and K63. In general, these linkages can generate either homotypic or heterotypic poly-ubiquitylation chains (polyUb). In homotypic polyUb, the same type of lysine (e.g., K48) is used for the linkage between all ubiquitin molecules (**Fig. 1B**). In heterotypic polyUb however, different lysine residues could be used, or even a combination of ubiquitin and ubiquitin-like proteins (**Fig. 1B**). The most known ubiquitin-like proteins include SUMO (**S**mall **u**biquitin-like **m**odifier) and NEDD8 (**N**eural precursor cell-expressed **d**evelopmentally **d**ownregulated **p**rotein **8**) ³. The attachment points govern the relative orientation of the ubiquitins in a chain and therefore, each generated polyUb chain will possess a specific topology (**Fig. 1-2**).

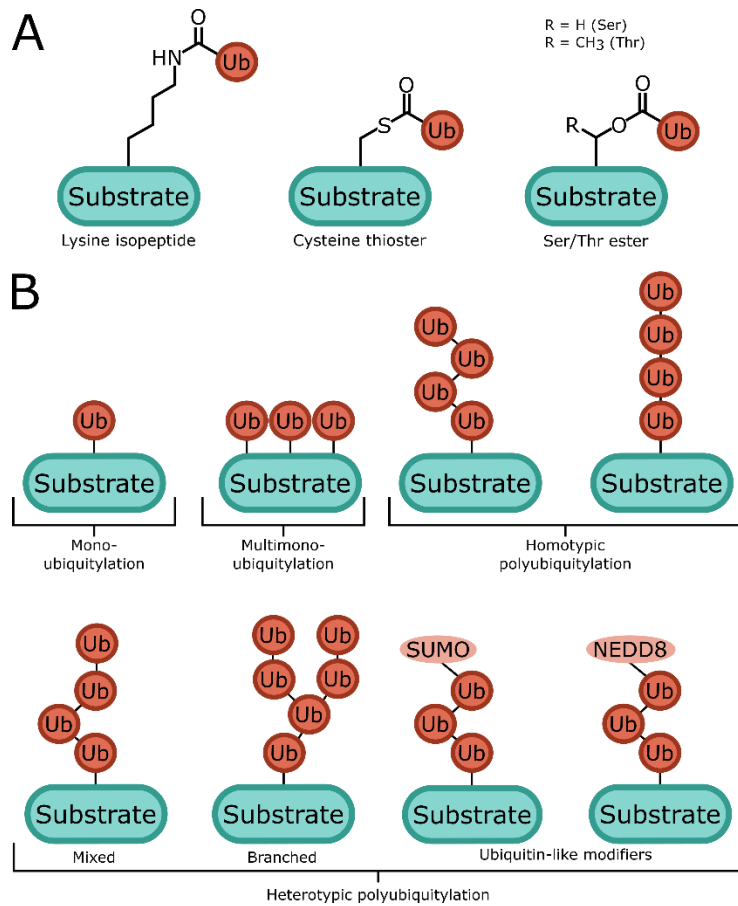


Figure 1. A simplified overview of the Ubiquitin code. A) Ubiquitin can be attached to lysine, cysteine and serine/threonine in a protein substrate through isopeptide, thioester and ester bonds, respectively. **B)** A second layer of diversification of ubiquitin attachment. A single ubiquitin can be attached to a substrate (mono-ubiquitylation), while the attachment to multiple residues is defined as multimono-ubiquitylation. When ubiquitin or a ubiquitin-like protein (light red) is attached to another ubiquitin molecule, it can generate different types of ubiquitin chains (homotypic and heterotypic poly-ubiquitylation). Figures adapted from ^{1,3}.

Different homotypic chain topologies (Fig. 2) vary from highly compact forms (K48-, or K11-linked) to extended chains (K63-linked and M1-linear) ^{4,5}. Additionally, the linkage type defines the accessibility of interaction surfaces on the involved ubiquitins. The K48- and K63-linked ubiquitylation are two of the most well studied linkage type. The main function of K48-linkages is to target substrates for proteasome-mediated degradation ⁶. K63-linkages play a predominant role during endocytosis of numerous membrane-bound receptors and transporters, such as the auxin efflux carrier PIN2 or the iron transporter IRT1 in *Arabidopsis* ⁷⁻¹¹. A summary of the role of each linkage in mammals is depicted in Fig. 2 ⁶.

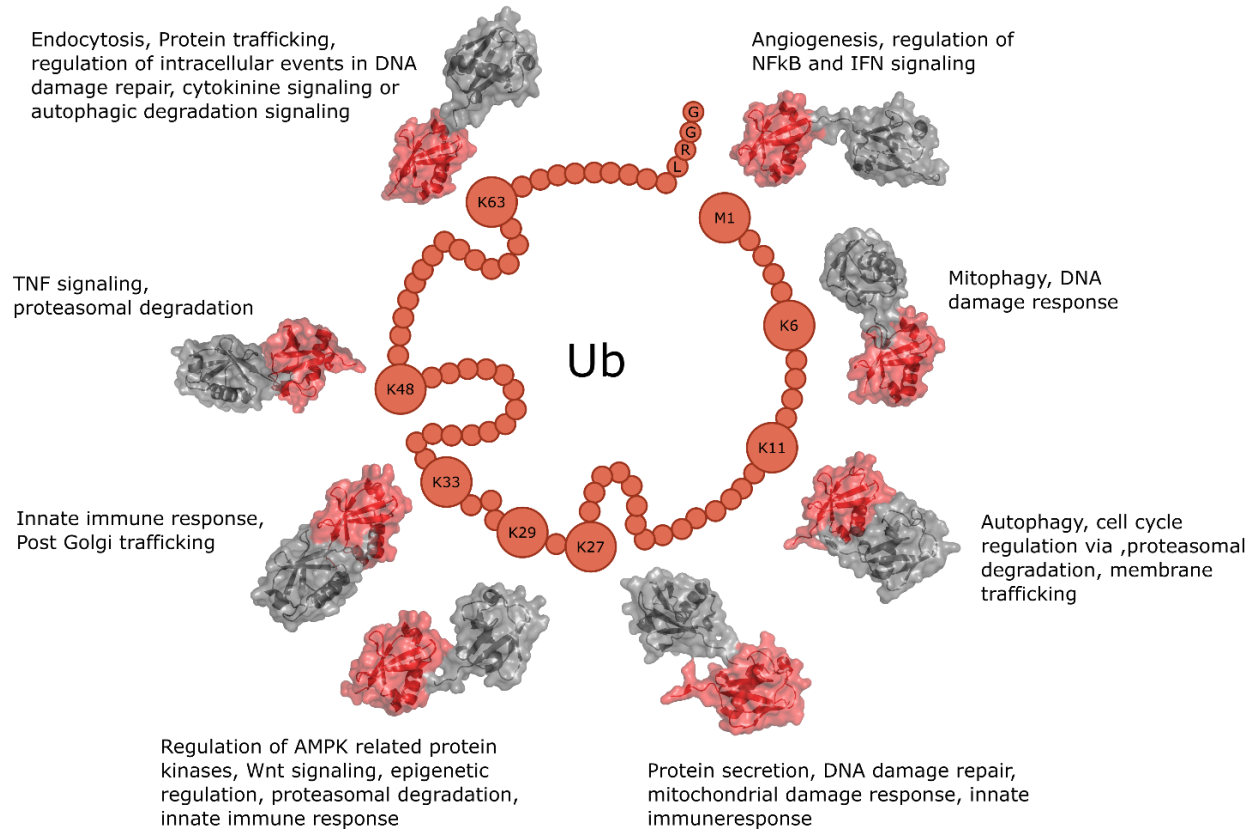


Figure 2. Ubiquitin-ubiquitin linkage defines chain topology and determines protein fate. An acceptor ubiquitin (red) undergoes ubiquitylation through one of eight residues (seven lysine and the N-terminal methionine). The resulting Ub chains show different topologies: from globular (e.g., K48- or K11-linked) to elongated (K63- or M1-linked). The recognition of Ub chains results in different processing of target proteins, enabling numerous cellular functions, for instance in mammals, as indicated for each linkage-type ⁶. PDBs used: 2JF5 (K63), 2XEW (K11), 4S22 (K29), 5AF4 (K33), 6NJD (M1), 6QML (K27), 5MN9 (K48), 7E62 (K6).

The different topologies of the polyUb chain can be recognized and read specifically, like a code. Taken altogether, the many different layers involved in ubiquitylation constitute the ubiquitin code (**Fig. 1-2**): I) modified residue in the substrate, II) type of ubiquitylation (mono, multi, poly, etc.), III) ubiquitin-ubiquitin linkage, IV) additional ubiquitin modifications. The readers of this code recognize the overall shape of the ubiquitin chains, thus linking the modified substrate to downstream events, such as degradation, relocation, formation of multiprotein complexes and activation of enzymatic pathways. Therefore, ubiquitylation governs the fate of the substrate proteins and thus dictates the cellular process where it is involved ³.

The diversity of the ubiquitin code is enabled by the E1(s), E2s and E3s enzymes, which serve as the code's writers, and the DUBs, which function as the erasers ³. The DUBs (De-ubiquitylating enzymes) constitute a family of proteases (over 100 in *Arabidopsis*) specialized in cleaving ubiquitins from Ub chains and substrates ^{12,13}. Upon DUB action, a further modification of a Ub chain is possible, which might shift the

fate of a substrate or counteract unwanted side reactivities^{14,15}. The DUBs will not be further discussed since they are outside the scope of the thesis.

I.2. Ubiquitylation requires E1, E2 and E3 enzymes.

Substrate ubiquitylation requires the concerted action of at least three proteins classes, the E1 **ubiquitin-activating enzyme** (UBA), E2 **ubiquitin-conjugating enzyme** (UBC) and an E3 ubiquitin ligase. In the first step, the E1 uses ATP to generate a thioester bond between its active site cysteine and the glycine carboxyl-terminus of ubiquitin (G76). The E2 interacts with the ubiquitin-loaded-E1 (E1~Ub, where ~ denotes a covalent bond), and consequently, Ub is transferred to the E2. In this reaction a second thioester bond is formed between the cysteine in the E2's active site and the G76 of ubiquitin (E2~Ub) (Fig. 3). The E3 associates with the E2~Ub and the substrate, thus guiding the Ub into proximity to the substrate (Fig. 3). The E3s function as scaffolds, facilitating ubiquitin transfer from the E2 onto, for example, an exposed lysine on the substrate. However, many E3s can possess further enzymatic function by forming an intermediate E3~Ub conjugate and subsequently transferring the Ub to the substrate¹⁶. The cycle can be repeated several times resulting in the generation of a multimonoo- and/or poly-ubiquitylated substrate¹⁷.

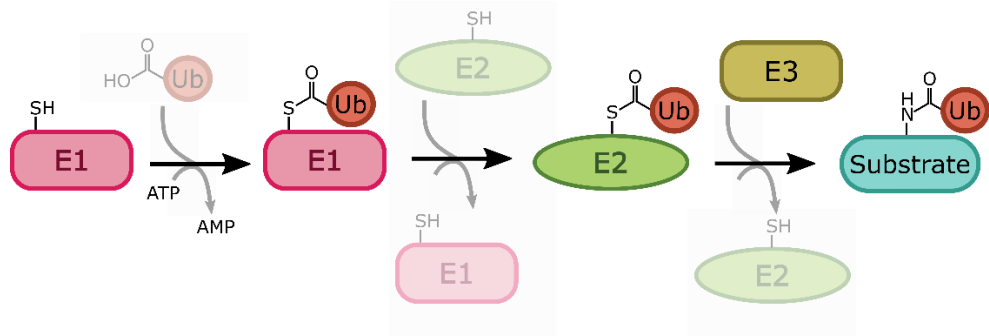


Figure 3. Ubiquitin transfer is an ATP-initiated process carried out by E1, E2 and E3 enzymes. E1 utilizes ATP to generate an activated form of ubiquitin (E1~Ub). The obtained intermediate interacts with an E2 enzyme and passes the Ub onto the E2. The E2~Ub associates with an E3, and both mediate the transfer of Ub onto the substrate. The cycle can be repeated and several ubiquitylated substrate derivatives can be obtained. Figure adapted from¹⁷.

E1s function as gatekeepers of Ub signaling¹⁸ with few representatives per species, e.g. two members in both human and *Arabidopsis*^{19,20}. Due to the small number of E1 enzymes, they cannot allow for great specificity and diversity that is seen in the ubiquitin code. Therefore, the selection of the target protein, as well as the different ubiquitin modifications, has to come from the other enzymes²¹.

I.3. The UBC family, structure and function.

The E2 ubiquitin conjugating enzymes (E2s) greatly influence the fate of targeted substrates by their capability to drive the formation of specific chain types²². E2 numbers in higher eukaryotes remained

similar, with 42 members in *Arabidopsis* and 37 in humans (numbers including E2s for ubiquitin-like proteins: SUMO, NEDD8, URM1, ATG8 and ATG10, but excluding inactive variants)¹⁶. All E2s interact with an E1 enzyme and one or more E3s. In addition, E2s may directly engage a target protein and thus play a role in the determination of where and how a target is modified by Ub. Some E2s also function outside the traditional Ub transfer pathways to regulate the activity of other enzymes²³.

Canonical E2s share a highly conserved common structure called the UBC domain, comprising approximately 150 amino acids with typically four α -helices and a β -sheet composed of four anti-parallel strands (**Fig. 4**). The majority of E2s consist almost exclusively of the UBC domain (e.g., AtUBC8, **Fig. 4**). However, some display N- or C-terminal extensions, which in most cases are predicted to be mostly unstructured with basic or acidic character (**Fig. 5B**). Specifically, the C-terminal extension of Cdc34 (a human E2) interacts and stabilizes Ub, which is critical for Ub discharge²⁴. Most surfaces of the UBC domain play a role during ubiquitin attachment by coordinating interactions with the components of the ubiquitylation cascade.

The Ub-carrying-E1 binds the E2 mainly through its α -helix 1 (H1) and loop 4 (L4) (**Fig. 4**). Consequently, the active sites of both E1 and E2 come into proximity, generating a second E1—E2 interface that allows the transfer of Ub from the E1 to the E2 through the transthiolation reaction (transfer from a thioester to a thiol group). Conservation of residues in this second interface varies among *Arabidopsis* E2s¹⁶. Nevertheless, *in vitro* activity assays confirm that the majority of *Arabidopsis* E2s are active in the presence of AtUBA1^{12,22,25}.

A well-conserved triad of residues, termed the HPN-motif, is located approximately ten amino acids to the N-terminus of the active-site cysteine (**Fig. 4**). This triad is involved in the aminolysis reaction (transfer from a thioester to an amino group) to create a peptide bond between the C-terminus of ubiquitin (G76) and a lysine on the target protein (isopeptide bond). For example, the side chain of N77 in HsUBCH5A (a human E2) forms a hydrogen bond with the carbonyl of the isopeptide bond²⁶. Less conserved residues may provide a microenvironment for catalysis, suggesting a diversity in E2 reactivity¹⁶.

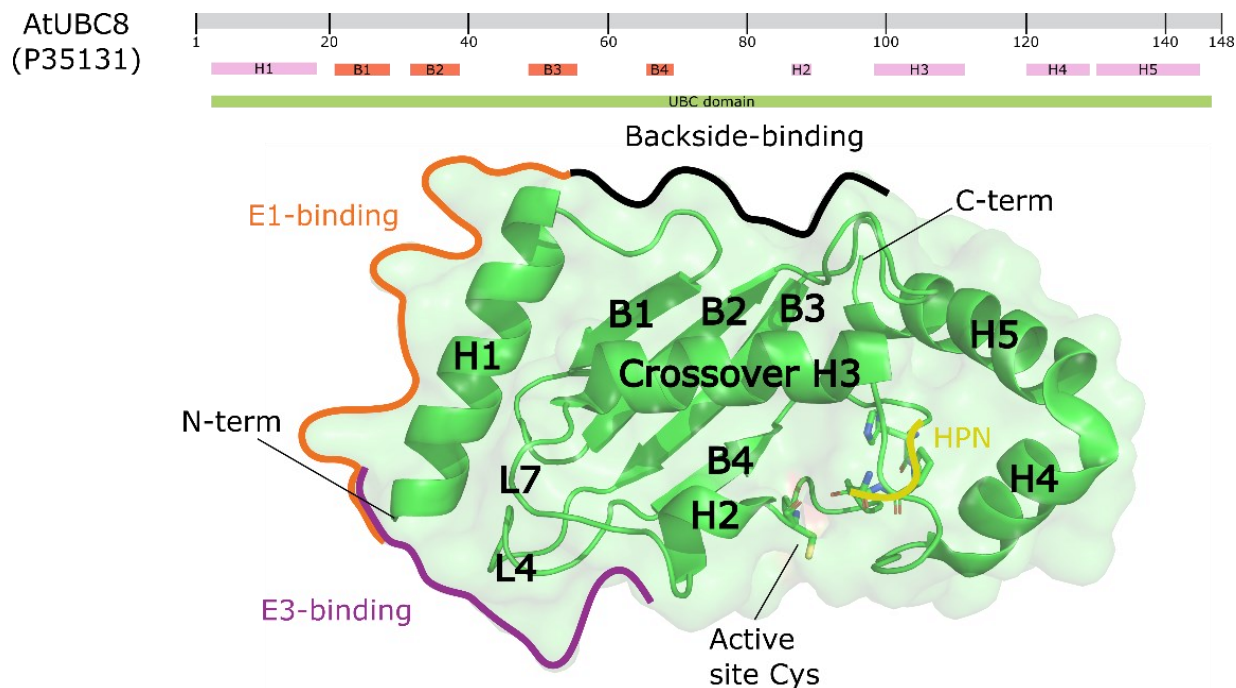
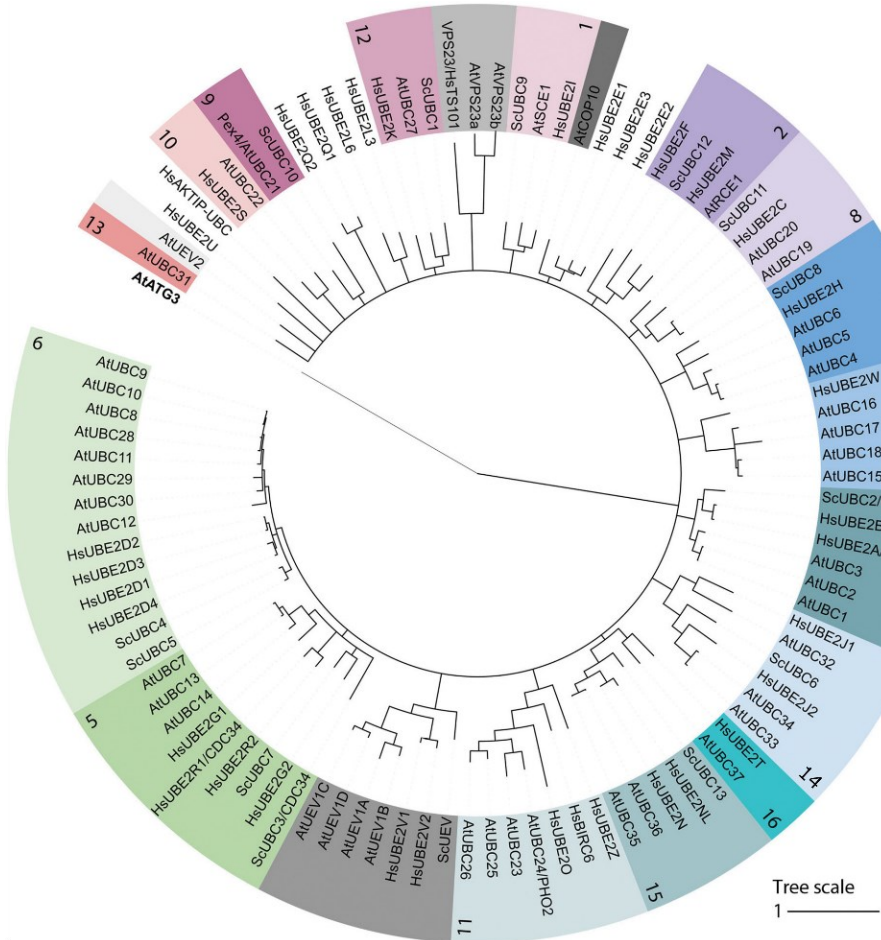


Figure 4. Overview of E2 structure. Primary structure (up) and 3D structure (down) of AtUBC8 (P35131). Essential structural features and common binding surfaces described in the text are labeled on a representative UBC domain (AtUBC8; PDB ID: 4X57) shown in green (adapted from ²³). Numbering of α -helices and β -strands were based on 3D structure. Numbering may vary between E2s, especially since H2 may not exist in other E2s.

The backside surface of the UBC domain, located opposite to the catalytic pocket, has been shown to bind ubiquitin non-covalently (**Fig. 4**). It is composed of the C-terminal end of H1, the β -sheet, the loop connecting H1 and the first strand of the β -sheet (B1), as well as potentially the C-terminus ^{23,27}. This region allows the positioning of ubiquitin for aminolysis. Additional interfaces provided by the E3 ligase can also increase reactivity and chain building processivity ^{16,26,28,29}.

Both the E1 and E3 interact with the UBC domain using partly overlapping surfaces (**Fig. 4**). The shared interface implies that the E2 needs to uncouple from the E3 before it can be reloaded by a new E1 ³⁰. Comparison of the E2–E3 interfaces, even between structurally and functionally distinct E3 ligases, reveals striking similarities. Loops 4 and 7 (L4 & L7) of E2s are engaged by both U-box/RING and HECT ligases (**Fig. 4**); E3s will be described in the next epigraph. Finally, the H1 also engages in various interactions including hydrophobic and hydrogen bonds. The E2–E3 pairing resulting from hydrophobic interaction are normally weak, with a K_D in the micromolar range, which are proposed to allow a quick exchange of E2s after the Ub binding reaction. Identification of physiological E2–E3 pairs has remained one of the key challenges to elucidate ubiquitylation mechanisms ¹⁶.

A



B

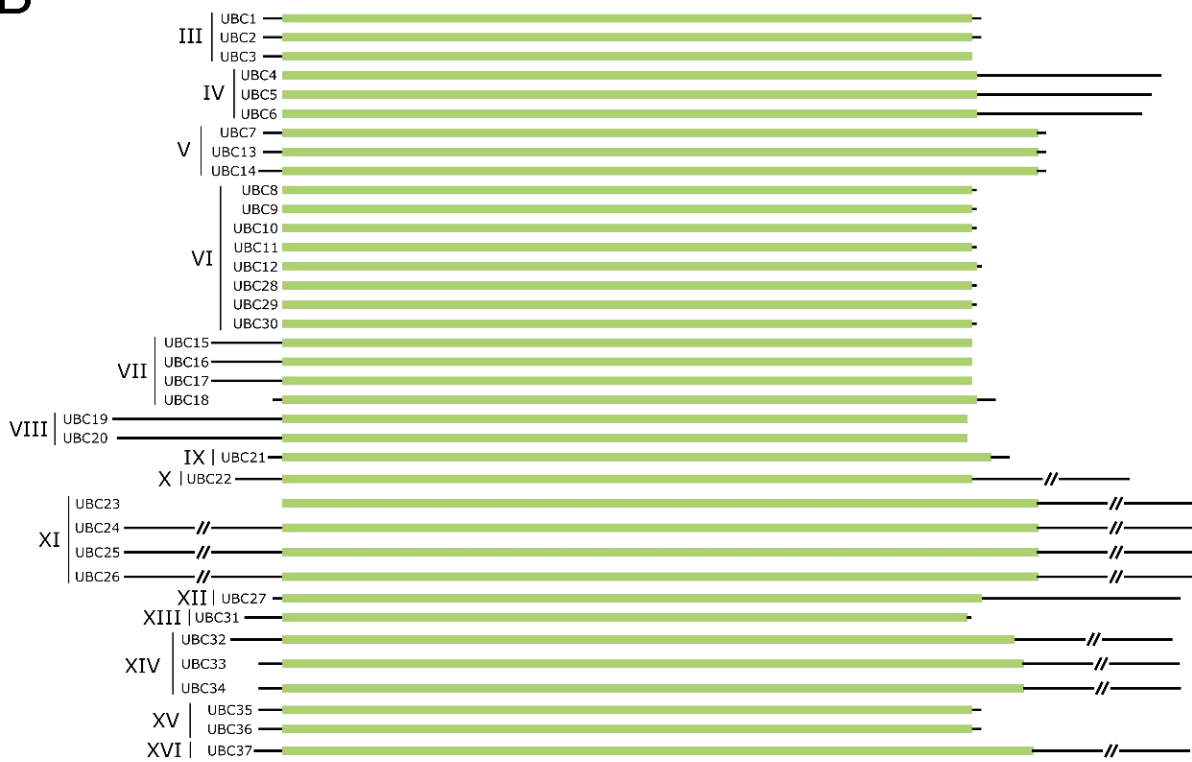


Figure 5. Phylogenetics analysis of *Arabidopsis* E2s. A) Phylogenetic tree of the protein sequences of UBC domains from *Arabidopsis thaliana* (At), human (*Homo sapiens*, Hs) and yeast (*Saccharomyces cerevisiae*, Sc) were used. *Arabidopsis* ATG3, which is distantly related to E2s, was included as an outgroup (extracted from ¹⁶, License number: 1437218-1). Numbers denote the *Arabidopsis* E2 groups as previously annotated ³¹. **B)** Depiction of UBC domains (green) and N-terminal/C-terminal regions. Regions longer than 50 residues were simplified for better depiction.

Based on phylogenetic analysis, the large majority of *Arabidopsis* E2s group well with human and yeast homologues and display conserved functions (Fig. 5A). Group III of E2s, belonging to Rad6 homologues, were shown to mediate monoubiquitylation of histone 2B affecting flowering transition ³². AtUBC5 from Group IV interacts *in vitro* with AtPUB13 (a Plant U-Box E3) and although the function of UBC5 in plants is unknown, its closest homologue in humans, UBE2H, is active with HsMARCH E3s, which in analogy to AtPUB13, are involved in the regulation of plasma membrane proteins ²². Group VI is the most used E2s for *in vitro* ubiquitylation assays. This include AtUBC8, which is closely related to the human UBE2Ds that show proclivity to attach Ub to any lysine coming close to their active site, and thus, adding the first ubiquitin ³³. However, they display a tendency to generate K11-linked Ub chains ³⁴. Silencing of this group, which are likely required for ubiquitin-priming, impairs early signaling triggered by the immune receptor FLS2 in *N. benthamiana* plants ³⁵. Interestingly, they also contributed to the degradation of the host kinase Pto by the *Pseudomonas syringae* effector AvrPtoB, which is an E3 ligase ³⁵. The group VII clade, which lacks a yeast homologue, harbors the *Arabidopsis* AtUBC15-AtUBC18 and the human UBE2W, which displays reactivity to the N-terminal α -amino group of substrates ³⁶. The sole member of Group X, AtUBC22, is likely to be the orthologue of human UBE2S and potentially generate K11-linked Ub chains ³⁷. Accordingly, *ubc22* mutants show defects in chromosome segregation in female meiosis ³⁸. Group XI includes E2s with large N- and C-terminal extension such as the AtUBC24/AtPHO2 or the human HsUBE2O or HsBIRC6. AtUBC24 is localized to the ER (Endoplasmic reticulum) and was shown to mediate the degradation of AtPHO1, which is important for the regulation of phosphate levels ³⁹. AtUBC26 pairs with a putative RBR-type E3 AtRSL1 to regulate ABA receptor levels ⁴⁰. Group XIV of E2s act in the ERAD (Endoplasmic reticulum-associated degradation) and have been shown to mediate degradation of integral membrane proteins ⁴¹⁻⁴⁴. Group XV of E2s (AtUBC35 and AtUBC36) cooperates with the UEV cofactors (AtUEV1A-D) generating K63-linked chains ^{10,12}. Accordingly, these E2s are together essential, as K63 chains are involved in a wide range of processes including iron homeostasis ⁴⁵, immunity ²², and prominently vesicle trafficking ⁴⁶. UEVs lack a catalytic cysteine but have been shown to contribute to chain building by binding Ub through their own backside ¹⁶.

An interesting E2 that is not found in *Arabidopsis* or yeast but is present in humans, and *Caenorhabditis elegans*, is HsUBE2L3 (also called UBCH7 in humans or UBC-18 in *C. elegans*). This E2 is not reactive towards

lysine and only exhibits reactivity towards cysteine. The implication is that HsUBE2L3, although it binds to many RING domains, is only functional as an E2 with HECT- and RBR-type E3s (Fig. 5)^{16,23,47-53}.

I.4. The E3 ubiquitin ligases.

Since 1990, three major classes of E3 ubiquitin ligases with hallmark catalytic domains have been identified. These are called “RING/U-box” (Really Interesting New Gene/U-box), “HECT” (Homologous to E6AP C-Terminus) and “RBR” (RING in-between-RING Rcat)⁵⁴. Other E3s have been recently discovered, such as the sole member of the RCR class (RING-cysteine-relay), human MYCBP2, which possess two catalytic cysteines that facilitates an internal Ub relay mechanism; and the human RNF213, which contains a newly identified domain, called “RZ finger”, harboring its active site cysteine^{1,54}.

RING/U-box E3s are the most abundant type of ubiquitin ligases, with ~540 members in *Arabidopsis* and ~600 in humans^{16,17}. They are characterized by the presence of a zinc-binding domain called RING or by a U-box domain, which adopts the same RING fold but does not contain zinc. The RING and U-box domains are responsible for recruiting the E2~Ub and for guiding Ub transfer. RING E3s mediate the direct transfer of Ub from the E2~Ub to the substrate, functioning as a scaffold to orient the E2~Ub towards the substrate. RING E3s can function as monomers, homodimers, or heterodimers. Similarly, U-box domains can work as monomers or homodimers. RING E3s can be regulated in different ways, including neddylation (NEDD8 binding), phosphorylation, and interaction with small molecules. Some RING E3s are composed by multiple subunits, such as the Cullin-RING ligases (CRLs). CRLs are a highly diverse class of ubiquitin ligases characterized by several common features. They are assembled on a Cullin scaffold, where RBX1 (RING-box protein 1) binds at its N-terminus providing the RING domain and therefore the capability to recruit E2~Ub. At the C-terminus, the receptor module is bound, which is composed by an adapter protein that serves as a platform for a substrate receptor (responsible for substrate specificity). Around 870 receptor modules for CRLs have been identified in *Arabidopsis*⁵⁵, this technically boosts the numbers of RING E3s in *Arabidopsis* tremendously due to the combining potential of receptor modules and CRLs. Specifically, complexes involving *Arabidopsis* Cullin 1 (AtCUL1) possess a prominent role in phytohormone signaling, including auxin, jasmonate, gibberellic acid, ethylene, and strigolactones⁵⁶. The receptor module of CUL1 is formed by an F-box protein (substrate receptor) and SKP1 (adapter protein), resulting in an SCF complex (SKP1—CUL1—F-box). F-box proteins have an F-box motif, which binds to SKP1, which in turn binds to CUL1’s N-terminal domain. Most F-box proteins also have distinct protein–protein interaction domains that recruit substrates to the CUL1—RBX1 core⁵⁰.

In contrast to RING E3s, the HECT E3 ligases receive ubiquitin from E2s and form an E3~ubiquitin intermediate (E3~Ub), chemically participating in Ub attachment¹⁶. Only 7 and ~30 members have been identified in *Arabidopsis* and humans, respectively^{17,57}. These E3s catalyze Ub transfer to the substrate protein through a two-step reaction. First, Ub is transferred to a catalytic cysteine on the E3 and then from the E3 to the substrate. The conserved HECT domain is located at the C-terminus of the E3 and is characterized by a bi-lobar architecture. The N-terminal lobe interacts with the E2~Ub, whereas the C-terminal lobe contains the catalytic cysteine. The two lobes are connected by a flexible hinge that allows changes in their relative orientations during Ub transfer. In these E3s, substrate specificity is determined by sequences upstream of the catalytic HECT domain⁵⁸. The catalytic activity of HECT E3s is often regulated by intramolecular interactions that keep the protein in an autoinhibited state, which is released in response to various signals⁵⁸.

The remaining class of E3 constitute the RBR family and so far, ~42 and ~14 members have been identified in *Arabidopsis* and humans, respectively^{16,59}. This type of E3 constitute a hybrid between RING and HECT ligases. Analogous to HECT, they perform Ub transfer to the substrate through a two-step reaction, where ubiquitin is first transferred to a catalytic cysteine on the E3 and then to the substrate. The RBR name derives from the presence of two predicted RING domains (RING1 and RING2) separated by an IBR (In-between-RING) domain. Similar to RING ligases, the RING1 domain recruits the E2~Ub, while the RING2 domain possesses the catalytic cysteine. However, the RING2 does not resemble the canonical RING E3 structure and has been re-branded as Rcat (Required-for-catalysis) domain. The IBR domain adopts the same fold as the Rcat domain while lacking the catalytic cysteine residue. All three RING1, IBR and Rcat are zinc binding domains. RBR E3 ligases contain additional domains that are specific to each member. Several domains are involved in intramolecular interactions that keep the protein in an autoinhibited state. Autoinhibition is released through various mechanisms, such as phosphorylation or protein–protein interactions^{17,60}. These modes of inhibition differ between members of the family. For example, in human Parkin, the proposed E2-binding site is blocked by the small helix called REP (Repressor element of Parkin), disruption of which promotes enhanced E2 binding. However, blocking the E2-binding site is not a universal mechanism for regulating RBR activity, another human RBR called HHARI is able to recruit HsUBE2L3 (also called HsUBCH7) with sub-micromolar affinity, even in its inhibited conformation⁵⁹. Besides autoinhibition, allosteric activation by Ub or UBLs is emerging as a common regulatory feature of human RBR E3 ligases. Phosphorylated Ub (in S65) binds to Parkin, to an interface between the RING1 and IBR domains, which is critical for activation. Similarly, HHARI is activated upon interaction with neddylated CUL1–RBX1 complex. Human HOIP is activated by M1-linked di-ubiquitin (di-Ub) and this binding site is

required for HOIP-mediated NF- κ B activation in cells. Similarly, human RNF216 is allosterically activated by K63 di-Ub, but not other di-Ub linkages⁶¹.

I.5. The Ariadne RBR E3 ubiquitin ligases.

As previously mentioned, RBR E3 ligases can contain additional domains outside the RBR core. Ariadne RBRs forms the largest and most diverse of this E3 class. Ariadne RBRs (ARIs) have in common an additional C-terminal “Ariadne” domain⁶². ARI proteins are present in all eukaryotes and some of their viruses^{63,64}. The Ariadne RBRs (DmARI-1 and DmARI-2) were originally identified in *Drosophila melanogaster* where they were shown to be important for development⁶⁵. The human homologue of DmARI-1, HHARI, is highly expressed in nuclei, where it co-localizes with nuclear bodies including Cajal, promyelocytic leukemia, and Lewy bodies, suggesting a nuclear function of HHARI. It was shown that this ARI is an essential RBR with roles in genotoxic stress signaling and organogenesis^{47,66–69}. The mammalian homologue of DmARI-2, TRIAD1, has been implicated in haematopoiesis, specifically in myelopoiesis. Moreover, TRIAD1 is essential for embryogenesis, and TRIAD1-deficient mice die due to a severe and lethal multiorgan immune response⁷⁰.

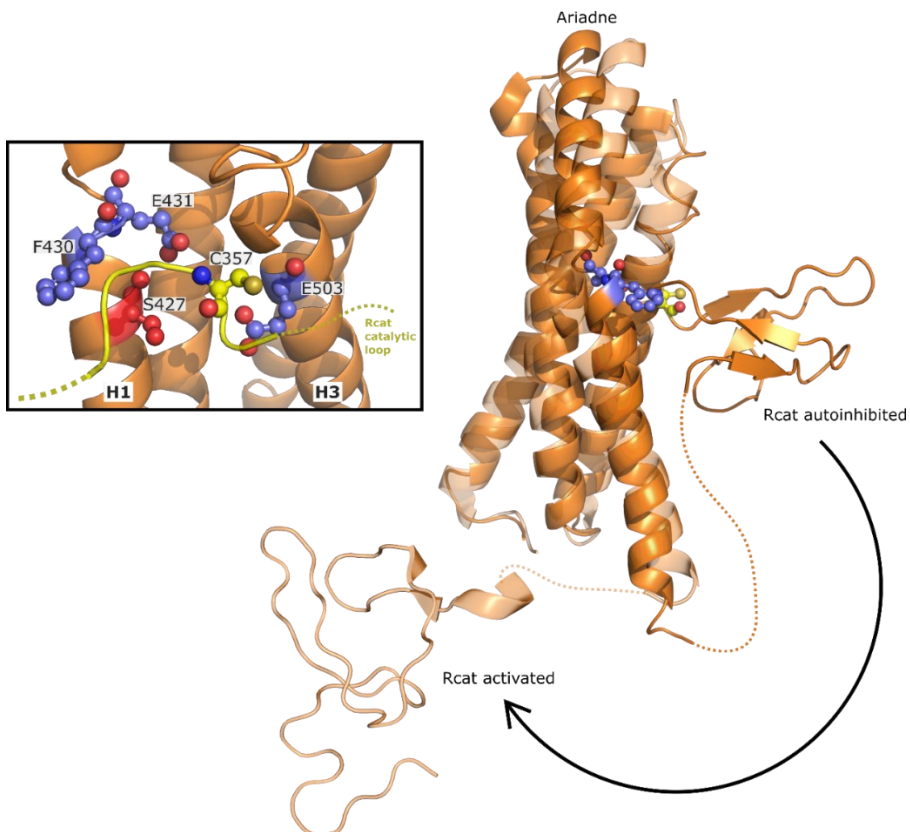


Figure 6. Upon activation of human ARIs, Rcat domain re-arranges. Overview of HHARI 3D structure in the autoinhibitory and active (with transparency) conformations. The Ariadne and Rcat domains’ overall structure (right)

and zoom-in of the Ariadne—Rcat interface (left). Important residues are represented in ball and stick. The structural activation residues from helices 1 (H1) and 3 (H3) are depicted in blue, while the phosphosite is depicted in red. Only the catalytic loop from the Rcat domain (yellow loop) is represented in the zoom-in for better depiction. Active site cysteine is also represented in yellow (PDB code: 4KC9, for autoinhibited and 7B5N, for activated).

The Ariadne domain is an elongated four-helix bundle. A groove between the first and third helices (H1 and H3) of the Ariadne domain secures the catalytic cysteine loop from the Rcat domain, keeping the protein in an autoinhibited state (Fig. 6). Activation and ubiquitylation mechanisms of human ARIs (HHARI and TRIAD1) have been recently described through CRL-binding and phosphorylation, both processes involving the Ariadne domain and resulting in the re-arrangement of the catalytic domain, or Rcat (Fig. 6)^{49,50,52}. HsUBE2L3 (also known as HsUBCH7) and HsUBE2D3 (also known as HsUBCH5C) are the E2s typically used in ubiquitylation/structural assays involving HsARIs. HsUBE2L3 discharges Ub only to a cysteine, while HsUBE2D3 discharges Ub to either lysine or cysteine^{49,50,52,53,71}. HsUBCH7 (HsUBE2L3) was identified as an HsARI specific E2 (as well as RBR- and HECT-type E3s), since the mutations H205A and H158A in RING1 domain of HHARI and TRIAD1, respectively; abolishes the specific interaction between these HsARIs and the E2 (Fig. 7A)⁷⁰.

I.5.1. Molecular mechanism of human ARIs: HHARI and TRIAD1.

I.5.1.1. HHARI-mediated ubiquitylation requires binding to neddylated CRL.

HHARI (also called ARIH1) can be activated upon binding a neddylated CRL (NEDD8-modified CRL) and thus ubiquitylate substrates bound to CRLs (CRL-dependent ubiquitylation). First, HsCUL1—HsRBX1 binds the receptor module (adapter protein plus substrate receptor) containing the substrate: SCF^{substrate}. After neddylation of the SCF^{substrate}, both HsRBX1 and HsNEDD8 contact an autoinhibited HHARI—E2~Ub complex (E2 = HsUBCH7). As a result, several conformational changes occur within the RBR core and the Ariadne domain that leads to its activation (Rcat release) and autoubiquitylation in the active site Cys (Rcat~Ub). These include: straightening of RTI helix, kinking of H1 within the Ariadne domain through residues F430-E431 (termed *switch helix*) and remodeling of the IBR-Rcat linker into a helix (termed *Ub-guided helix*) (Fig. 7-8). The Rcat~Ub is then relocated closer to the CRL-substrate and thus driving its ubiquitylation. Ubiquitin transfer to the substrate would enable the previously mentioned conformational changes to go back to their initial position, HHARI will dislodge itself from the SCF^{substrate~Ub} and becomes once again autoinhibited. At this point the SCF is bound to a monoubiquitylated substrate and can therefore, continue the ubiquitylation cascade (poly-ubiquitylation). Since HsRBX1 is now free from the HHARI, other E2s can enter the cascade through HsRBX1-binding. These E2s could be different from HsUBCH7, and will define the growing chain linkage specificity (Fig. 7)⁴⁹. Additionally, HHARI can be

activated through interaction with neddylated HsCUL2, HsCUL3 and HsCUL4A^{70,72}. However, only the mechanism, based on structural data (cryoEM, X-ray), was described for the HHARI—HsCUL1 combination (Fig. 8).

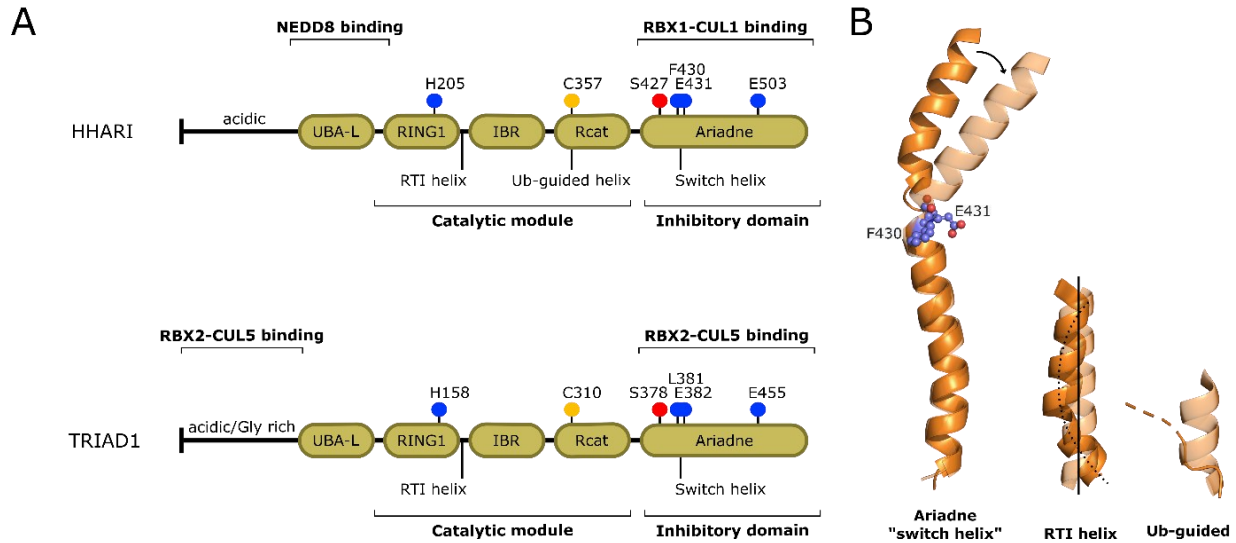


Figure 7. Domain organization in human ARIs and conformational changes required for activation. A) Both HHARI and TRIAD1 possess UBA-L, RBR core (catalytic module) and the Ariadne (inhibitory) domain. Both HHARI and TRIAD1 possess conserved residues: a His required for RING1 domain folding (blue in RING1), active site Cysteine (yellow in Rcat), putative phosphorylation site (Serine, red in Ariadne domain) and autoinhibiting residues (blue in Ariadne domain). Main difference of CRL-dependent activation between HHARI and TRIAD1 lie in the binding to neddylated Cullins. **B)** Conformational changes in defined stretches of HHARI (switch helix, RTI helix and Ub-guided helix) as a result of CRL-dependent activation. Active HHARI is represented with transparency. (PDB code: 4KC9, for autoinhibited and 7B5N, for activated).

I.5.1.2. TRIAD1-mediated ubiquitylation requires binding to neddylated CRL.

While HHARI partners with neddylated HsCUL1—HsRBX1, TRIAD1 (also called ARIH2) partners with neddylated HsCUL5—HsRBX2 and also ubiquitylates substrates previously bound to CRLs (CRL-dependent ubiquitylation). This latter E3-E3 platform requires the adapter protein ELOB (Elongin B—Elongin C) and the substrate receptor BC-box. The overall ubiquitylation mechanism of TRIAD1 is similar to HHARI. For instance, the Ariadne domains, in both HHARI and TRIAD1, mediate homologous autoinhibitory interactions with the Rcat domains, and homologous interactions with their cognate HsCUL—HsRBX partners. Furthermore, many structural features involved in the mechanism are conserved between HHARI and TRIAD1. Such is the case of the switch helix (the kink located in residues L381 and E382), the RTI helix and the residues contacting the catalytic cysteine loop (HHARI^{F430/E431/E503} and TRIAD1^{L381/E382/E455}) (Fig. 7). When these residues (referred in this thesis as *structural activation residues*: Fig. 9) are simultaneously mutated to alanine in HHARI and TRIAD1, it generates a hyperactive version of the protein increasing its activity and binding to HsCULs^{49,50,52}. However, the main difference between the ubiquitylation

mechanisms of HHARI—HsCUL1 and TRIAD1—HsCUL5 lies in the role of HsNEDD8. As previously mentioned, HsNEDD8 (linked to HsCUL1) binds directly to the UBA-L domain of HHARI. Conversely, TRIAD1 recognizes HsCUL5 directly, the latter being re-structured by neddylation. HsNEDD8 allosterically generates TRIAD1-binding surfaces that are not present in an un-neddylated HsCUL5. Furthermore, additional contacts between HsCUL5 and the N-terminal region of TRIAD1 are also established. The Ub-guided helix formation that was observed for HHARI, is not present in TRIAD1 (Fig. 6-7)⁵⁰.

The E3—E3 complex provides an advantage over single E3s regarding accessibility to substrates and E2 usage. Several substrates possess folded structures or limited length and therefore, cannot be reached by a typical E3—E2~Ub (RING E3 mechanism). By using an E3—E3 platform and taking the advantage of the large and flexible structure of ARIs, the substrate can now be reached and thus, ubiquitylated. Once the substrate is primed with ubiquitin the single-E3 ubiquitylation mechanism can follow. As a consequence, the rate of the reaction will increase and more target substrates (than it was originally thought) can be modified. Furthermore, there will be more possible types of ubiquitin chains generated by the combinatorial potential of E3—E3—E2 and E3—E2^{49,50}.

I.5.1.3. Phosphorylation of HHARI and TRIAD1.

So far, both human ARIs have been described to ubiquitylate CRL-dependent substrates. However, most recently it was shown that human ARIs can ubiquitylate substrates independent of CRLs. Therefore, there is an alternative mechanism for releasing the autoinhibition of ARIs. In 2022, it was demonstrated that mimicry of a phosphorylation event observed in cells activates HHARI robustly independent of CRL binding⁵². Two sites of phosphorylation in HHARI, S427 and S517, were previously identified in a high throughput phosphoproteomic analysis of human ovarian and xenograft breast tumors⁷³. Both serine residues are located in the auto-inhibitory Ariadne domain, with S427 located on a helix implicated in activation by CRLs, and that forms the interface with Rcat (H1 in Fig. 6)⁵². Wild-type HHARI has almost undetectable auto-ubiquitylation activity in *in vitro* ubiquitylation assays, while a triple-point mutant (HHARI^{F430A/E431A/E503A} and TRIAD1^{L381A/E382A/E455A}) in the Ariadne domain overcomes auto-inhibition and exhibits robust autoubiquitylation activity mediated by HsUBCH7^{48–50,52,70}. HHARI auto-ubiquitylation was similarly enhanced with HHARI^{S427D}, while HHARI^{S517D} showed minimal to no change in auto-ubiquitylation levels in *in vitro* ubiquitylation assays. HHARI^{S427} is adjacent to residues HHARI^{F430} and HHARI^{E431}, suggesting that changes at the Ariadne—Rcat interface can lead to activation. A phosphomimic mutation in TRIAD1^{S378} (equivalent to HHARI^{S427}) also activated it for auto-ubiquitylation. Quantitative XL-MS data from the Klevit laboratory⁵² indicated that Rcat is released even in auto-inhibited HHARI, albeit at low frequency. It is

possible that a kinase can access and modify S427 during such an event and, once modified, the Ariadne domain will remain disengaged from Rcat. An alternative possibility is that S427 may be phosphorylated while HHARI is bound to a CRL, as the serine is accessible in this conformation. Importantly, the phosphomimic model and the CRL-activated mechanism both involve allosteric changes in the switch helix (Fig. 7-8)⁵².

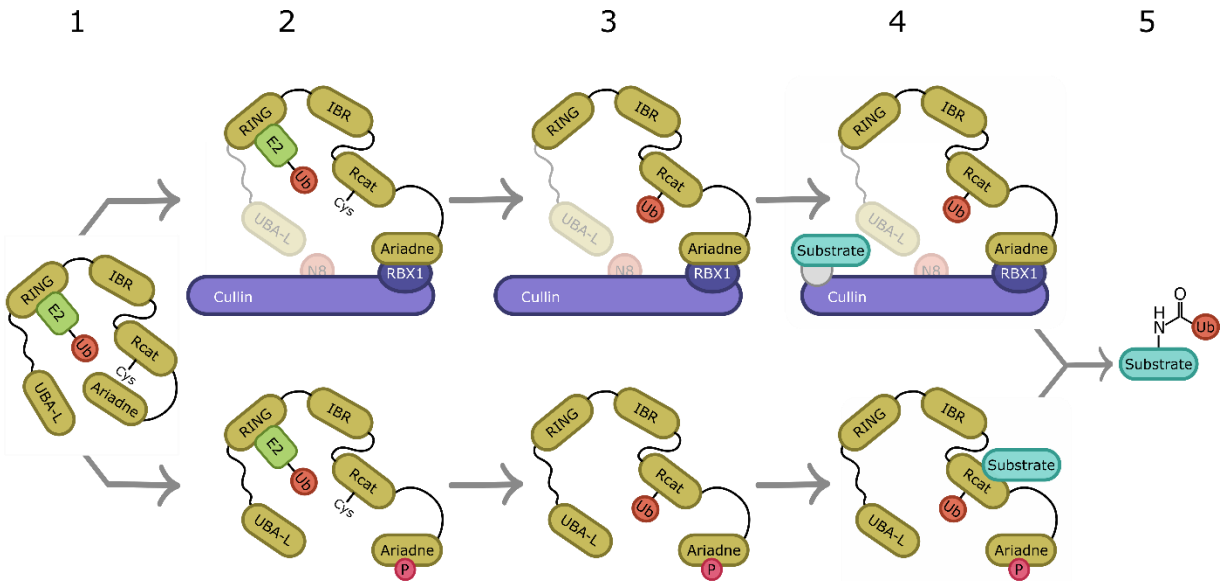


Figure 8. General overview of HsARI-mediated ubiquitylation. First, release of autoinhibition is promoted by disrupting the Rcat—Ariadne interface. This can happen either allosterically through a direct protein—protein interaction with neddylated CRLs or by direct phosphorylation of the Ariadne domain. Consequently, the active site cysteine is exposed (1 → 2). The E2~Ub that was bound to the RING1 domain can then transfer the Ub to the exposed cysteine (2 → 3). The substrate is presented either by the SCF complex or the Rcat domain of HsARIs (3 → 4) and thus driving its ubiquitylation (4 → 5). The Rcat can then recapture the Ariadne domain resuming its autoinhibited conformation (1)^{49,50,52}.

Following genotoxic stress, 4EHP (mammalian translational repressor) is mono-ubiquitylated at detectable levels and its association with the mRNA 5' cap is dependent on HHARI⁶⁸. Importantly, *in vitro* modification of 4EHP by HHARI or TRIAD1 was just recently shown. 4EHP is ubiquitylated primarily with a single ubiquitin in the presence of either active HHARI species (HHARI^{S427D} and HHARI^{F430A/E431A/E503A}) and TRIAD1^{S378D} in the presence of HsUBCH7. Moreover, the substrate binding site was narrowed down to the C-terminal residues of the Rcat domain⁵². Sixteen additional putative substrates were recently identified for DmARI-1 in *D. melanogaster*, one of them involved in neurotransmitter release⁷⁴.

Even though there are distinct features between HHARI- and TRIAD1-mediated ubiquitylation, there is a common mechanism that can be visualized in Figure 8.

1.5.2. ARIs in *Arabidopsis thaliana*.

In non-plant organisms such as fungi, invertebrates and vertebrates, the ARI class consists only of one to four genes. In the plant kingdom, however, the ARI class is strikingly enlarged^{63,75}. Compared to the two human ARIs, fourteen ARI genes and two pseudogenes from *Arabidopsis thaliana* have been identified and characterized since 2003 (**Supp. Fig. S1**)⁷⁶.

Sequence comparison and phylogenetic analyses, performed by the Marie-Theres Hauser Group in 2003, divided the AtARI proteins into three subgroups. Two groups are absent in yeast, invertebrates, and vertebrates including mammals, and may therefore represent new subgroups specific to plants (Subgroups B and C in **Supp. Fig. S1**)⁷⁶. It seems that ARIs highly diversified in the plant kingdom and may present undiscovered new functions *in planta*. It is possible that due to duplication events they could also present redundant functions between the members of the same clade. Part of the expansion in *Arabidopsis* is a consequence of genome duplications, while the tandem duplications point to unequal crossover events or even retro-position in the case of one member^{76–78}.

However, since 2003 plant ARIs have been understudied and only a few research papers have been published so far^{31,75,77,79–82}. Furthermore, the unifying mechanism of RBR type of E3 ligase was just recently described⁶¹ and many of the ARIs (and other RBRs) were misclassified as RING ligases. Even now, some labs keep omitting RBRs as a standalone type of E3 ligases *in planta*⁸³.

Like their human counterpart, all AtARIs possess the RBR core and the Ariadne domain. However, some of them lack specific domains or present additional ones⁷⁶ (**Supp. Data 1**). Only AtARI15 lacks the UBA-L domain⁷⁶, while AtARI8, AtARI13/14/15/16 present an RanBP2 domain downstream the Ariadne domain at the extreme C-terminal end⁸⁴. The RanBP2 is a member of the zinc finger family with unique functions and an unusually diverse distribution in plants and can mediate interactions with proteins or RNA. The presence of the C-terminal RanBP2 was not noted in the original description of the family, and no subsequent study has explored its function⁸⁴. Another feature that varies within the AtARI family is the presence of the catalytic cysteine, AtARI1/2/3/5/7/8/9/10/11 possess this residue in the Rcat domain. However, the rest of the AtARIs lack this cysteine and may therefore, possess a different residue reactivity or even act as a regulatory protein^{76,85} (**Supp. Data 1**).

Bioinformatic analyses suggested that most AtARIs might be localized in the nucleus or shuttle between nucleus and cytoplasm, except for AtARI10 and AtARI15 with a ~20% nuclear localization prediction⁷⁶. Such a dual localization has been found for the human homologue HHARI^{86–88} and for ARI12 homologues in soybean⁷⁹. cDNA samples from root, leaf, stem, flower and green siliques from *Arabidopsis* were

analyzed in 2003 to check for ARI's expression pattern. In this experiment they saw that AtARI1/2/3/5/7/8/15 are expressed to a similar level in all organs, with the highest expression belonging to AtARI1, whereas no transcripts could be detected for AtARI11/13/14. The expression of the AtARI9/10 was below the limit for a reliable quantification with real-time PCR. AtARI12 and AtARI16 are expressed in an organ-specific manner in the roots and siliques, respectively⁷⁶.

There is currently little knowledge regarding the function and activity of plant ARIs, even less so their molecular mechanism, in contrast to their human counterparts. In fact, autoubiquitylation activity has only been proven for AtARI8 and AtARI12^{31,80,81}. AtARI12 seems to be involved in the UV-B pathway through interaction with COP1 (Constitutively Photomorphogenic 1), which is a key component of the light signaling pathway^{77,81}. The overexpression of a soybean Ariadne-like gene causes aluminum tolerance in *Arabidopsis*⁸². The orthologous gene of AtARI7 in *Hypericum perforatum* was associated with apospory⁸⁹. More recently, 39 ARI genes were identified in *Brassica napus*, where some of them were significantly responsive towards abiotic stresses such as dehydration, cold, ABA and salinity treatments⁹⁰.

I.6. Aims and objectives.

Presently, the functions of ARI proteins are largely unknown in plants⁷⁶. While knockout mutants of ARI genes are lethal in *Drosophila*⁶⁵ and *Caenorhabditis*⁵¹, no knockout phenotypes have been described in *Arabidopsis* that would allow a conclusion on their function^{77,90}. Since there is higher variability in *Arabidopsis* ARIs compared to non-plant organisms', these proteins may have evolved to fulfill specialized roles in planta. Although there is some biochemical evidence for the mechanism of action of human ARIs^{49,50,52} (Fig. 6-8), there is little to no knowledge on the role of AtARIs in the context of plant ubiquitylation. Therefore, the aim of this thesis is to investigate the molecular and biological functions of AtARIs. In order to fulfill the aim of the thesis, I designed the following objectives:

Objective I. Out of 16 AtARIs, which should be studied to assess their function?

Compared to the two human ARIs, fourteen ARI genes and two pseudogenes from *Arabidopsis thaliana* have been identified and characterized since 2003⁷⁶. Furthermore, it is possible that AtARI genes may have redundant functions. Therefore, I aim to analyze AtARIs by sequence and structural analysis in comparison with mammalian ARIs to identify most relevant AtARIs to prioritize the research. The comparison will be based on the available structural information of the human ARIs (HHARI/TRIAD1) obtained by the Klevit's and Schulman's Labs^{49,50,52} that was described in the previous sections.

Objective II. What is the pairing selectivity of E2s—AtARIs?

The ubiquitylation cascade involves E1—E2—E3 enzymes. Specifically, E2 and E3 enzymes ensure Ub chain type, and substrate specificity across tissues and developmental stages ^{91,92}. In order to fully understand the biological role played by any E3, it is of utmost importance to identify its physiological E2 counterparts, as they define to a large extent its biochemical properties ²². Therefore, I aim to identify the E2—AtARI pairing employing *in vitro* and *in vivo* protein—protein interaction assays. The next step after E2~Ub binding to an RBR E3, is the transfer of ubiquitin to the active site cysteine. Therefore, I will also assess the Ub transfer between different E2s and AtARIs through *in vitro* ubiquitylation assays.

Objective III. Could AtARI's activation be mediated by E3s such as CRLs and/or phosphorylation?

Another aspect of the ubiquitylation cascade in frame of the ARIs, is their specific activation. ARIs possess the Ariadne domain involved in intramolecular interactions that keep the protein in an autoinhibited state. Autoinhibition in human ARIs can be released through two mechanisms, phosphorylation or protein—protein interactions with CRLs ^{49,50,52}. In order to establish the activation mechanism of AtARIs, I will perform *in vitro* and semi-*in vivo* protein—protein interaction assays. This would allow me to identify which E3s could activate AtARIs, including CRLs. Phosphomimic protein mutants of AtARIs will be generated and their interaction/activity will also be assessed.

Objective IV. What could be the putative substrates of AtARIs?

The last step of the ubiquitylation cascade is the transfer of Ub to the substrate. Human ARIs recognize CRL-dependent and CRL-independent substrates ^{49,50,52}. It was recently shown that human ARIs can ubiquitylate 4EHP, an mRNA 5' cap binding protein that negatively regulates the initiation of translation. *Arabidopsis thaliana* uses two canonical eIF4E isoforms (eukaryotic Initiation of translation Factors), named eIF4E1 and eIF(iso)4E, and three non-canonical ones, named nCBP (homologue of mammalian 4EHP), eIF4EB and eIF4EC ^{93,94}. Preliminary experiments performed in the Hauser group, established that AtARI1/2/5/7/12 interact with eIF4E1 through GAL4 Yeast-two-hybrid assays (Y2H) ⁹⁵. Therefore, these translation factors constitute a potential venue for substrate identification assays. I will perform *in vitro* and *in vivo* protein—protein interaction assays, as well as *in vitro* ubiquitylation assays, to confirm the identification of AtARIs' substrates.

Objective V. What is the biological function of AtARIs in planta?

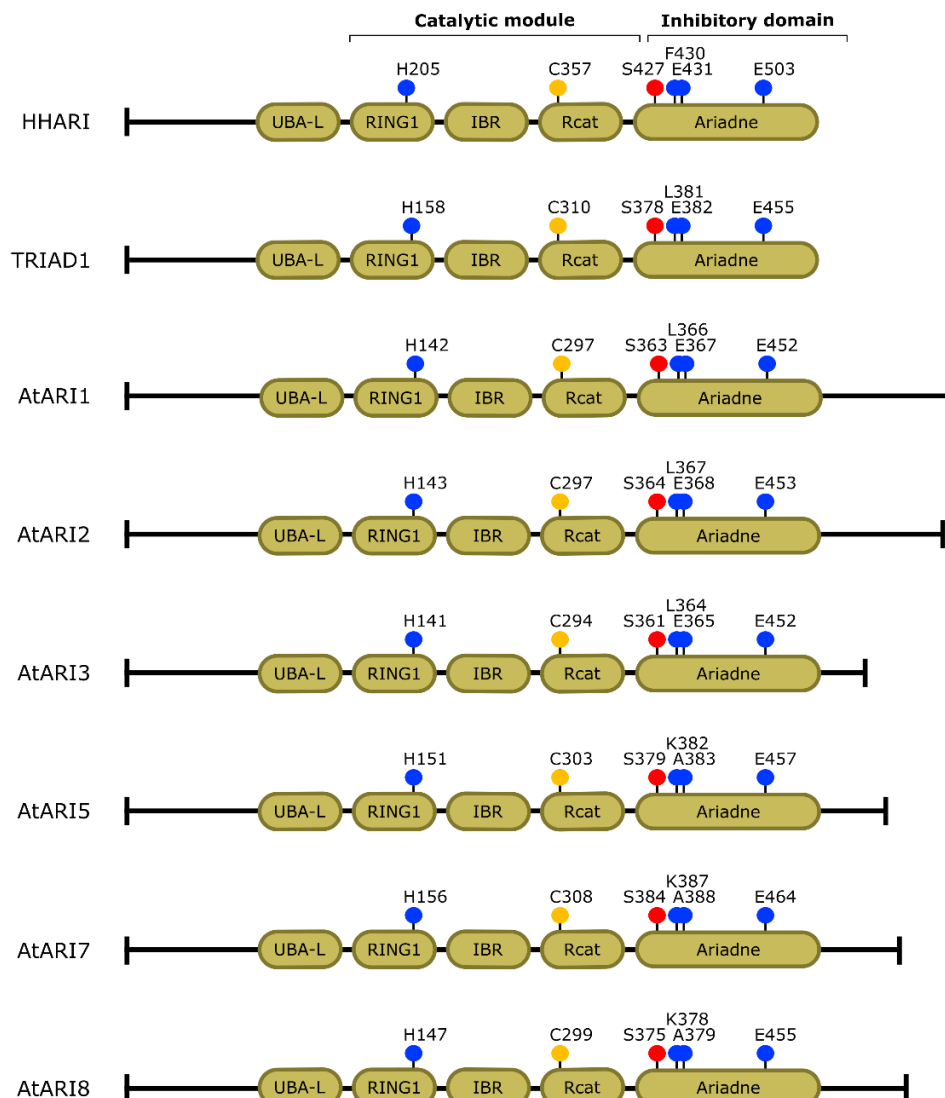
It is important to note that in *Arabidopsis* and rice the expression of the *ARI* genes is highly variable and some of the members are induced by diverse stresses ^{75,76}. These findings are consistent with the hypothesis that tandemly duplicated genes are more frequently involved in stress responses ^{96,97}. Thus, it is likely that *AtARI* genes either have redundant functions and/or are important for specific environmental

conditions⁷⁷. Therefore, I aim to generate and phenotypically characterize CRISPR/Cas9 lines for assessing the biological role of *AtARIs* in *planta*. For this, I will generate single, double and triple mutants of *AtARI1/2/3* and *AtARI5/7/8* and identify phenotypic changes upon diverse abiotic and biotic stresses.

II. RESULTS

II.1. Six putative orthologue and parologue AtARIs were selected for studying RBR E3 Ariadne ligases.

Recently, the mechanism of ARIs in humans was uncovered through structural studies^{49,50,52}. Many structural features, involved in the ubiquitylation mechanism, were identified (**Fig. 6-9, Supp. Data 1**). Furthermore, with the availability of alpha-fold structures of the AtARIs it made the study of these proteins easier. Taking the data generated by the Hauser group⁷⁶ as a foundation, I used the newly identified protein features from human ARIs^{49,50,52} to further characterize the AtARIs based on structural alignment. I used alpha-fold structures available at UniprotKB (**Fig. 9, Supp. Data 1, Supp. Fig. S1-S2**) and aligned them with either active or inhibited HHARI (HsARI1: 4KC9 & 7B5L) and TRIAD1 (HsARI2: 7ONI). I identified key sequences and residues that were conserved between all the ARIs and check for the existence of certain domains (**Fig. 9, Supp. Data 1**).



Name	His in RING1	Catalytic Cys	RTI-helix*	Ub-guided-helix*	Ariadne inhibitory residues*	Structural activation residues			P-Ser*
						Start	Middle	End	
ARI1	H142	C297	KKRPDLAKFDRYLLESYEDN	ETINWITVHT	EKLSQLFLEE	L366	E367	E452	S363
ARI2	H143	C297	KSQPDLAEKFDRFLLESYEDN	ETVNWITVHT	EKLSKFLEE	L367	E368	E453	S364
ARI3	H141	C294	VSPELADRYDRFLIESYVEDN	ETVNWITVNT	EKLSKILEE	L364	E365	E452	S361
ARI5	H151	C303	KEDKEKYYRYFLRSYEVN	ENMMWILANS	ERLHKCVEK	K382	A383	E457	S379
ARI7	H156	C308	EDEKEKYNRFLRSYEDN	ENMMWILANS	ERLHQCVKEK	K387	A388	E464	S384
ARI8	H147	C299	DKDKQKYTSYFVRSYVEDN	ENMMWILANS	ERLHQCAEK	K378	A379	E455	S375
HHARI	H205	C357	DSVKVLYQHLLTNSFVECN	ETSNWIAANT	EVLSGYLER	F430	E431	E503	S427
TRIAD1	H158	C310	NEELREKYRRLFRDYVESH	NO	ANLSWKVER	L381	E382	E455	S378

Figure 9. Structural features from HHARI/TRIAD1 are conserved in AtARIs. Domains and residues were identified from aligning alpha fold structures with 4KC9 (autoinhibited HHARI) or 7B5L (active HHARI) or 7ONI (active TRIAD1). *Features first identified for HHARI and TRIAD1 from ^{49,50,52}.

Most of the AtARIs present an UBA-L domain, except AtARI15. AtARI1 to AtARI11 possess the active site cysteine and a conserved serine that is phosphorylated in humans which consequently releases the auto-inhibition (Fig. 9, Supp. Data 1). The Ub-guided helix, which is present only in HHARI, is conserved within

AtARI1/2/3; AtARI5/7/8 and ARI9/10/11 (**Fig. 9, Supp. Data 1**). A similar behavior occurs for the RTI-helix, the Ariadne inhibitory residues and the structural activation residues (SAR) (**Fig. 9, Supp. Data 1**).

According to Mladek and collaborators ⁷⁶, AtARIs fall into three groups: A with AtARI1/2/3/4, B with AtARI5/6/7/8/9/10/11/12, and C with AtARI13/14/15/16 (**Supp. Fig. S1**). Group A radiates closer to ARI proteins of yeast, invertebrates, and vertebrates ⁷⁶ and possess more conserved features compared to HHARI/TRIAD1 (**Fig. 9, Supp. Data 1**). Furthermore, AtARI1/2/3 are expressed to a similar level in all organs, where the highest expression level was detected for AtARI1 ⁷⁶. Hence, this group was defined as the *ortho-group* (AtARI1/2/3) and was further used for the current study as the AtARIs with the highest probability of behaving like HHARI/TRIAD1. Group C from Mladek was reclassified here as AtARI12/13/14/15/16, since none of them presented an active site cysteine, which would suggest an alternative ubiquitylation mechanism. In addition, this group presented the most variation of key features (**Supp. Data 1**) and their expression varies between organs, e.g., AtARI12 is expressed preferentially in roots, while AtARI14 is mostly expressed in closed flowers and AtARI16 is preferentially expressed in green siliques ^{76,85}. Group B includes then AtARI5/6/7/8/9/10/11, of which AtARI5/7/8 are expressed ubiquitous regarding tissue specificity ⁷⁶. This latter group was further used for the current study as a representation of plant specific ARIs, which could possess a different mechanism than HHARI/TRIAD1 and thus renamed *para-group*. Both ortho- and para-groups have a conserved His in the RING1 domain, that aligns with the His residues from HHARI and TRIAD1 that are necessary for RING folding and thus E2 interaction. AtARI4 and AtARI6 were excluded from the analysis since they constitute pseudogenes. It is of note that all AtARIs possess a C-terminal unstructured stretch downstream the Ariadne domain that is not present in neither HHARI nor TRIAD1.

II.2. All AtARIs interact with Group VI E2s through the RING1 domain.

In order to elucidate the mechanism of ARIs in *Arabidopsis*, we evaluated the pairing selectivity between 34 E2s in *Arabidopsis* with the selected six AtARIs. For this, we used first an *in vitro* approach for evaluating protein—protein interaction (**Fig. 10A, Supp. Fig. S3-S4**). The LexA yeast two-hybrid (Y2H) assay was used, where E2s and AtARIs were expressed as recombinant proteins, N-terminally fused to either DNA-binding domain (DBD, bait) or an activation domain (AD, target). If both proteins interact, DBD—AD proximity will induce the expression of a β -galactosidase (LacZ gene) that will catalyze the hydrolysis of X-Gal, resulting in the generation of a blue colored yeast colony ⁹⁸.

The overall interaction pattern occurs similarly regardless of which protein was fused to AD or DBD (**Supp. Fig. S3-S4**). However, the best results were obtained when DBD was fused to the AtARIs and the AD to the

E2s (**Supp. Fig. S4**), since no signal (or very faint) was spotted for AD-AtARI2 or AD-AtARI7 combinations (**Supp. Fig. S3**). Furthermore, DBD-AtUBC35, DBD-AtUBC36 and DBD-AtUBC37 did not show any interaction with AD-AtARI1 as in their counterparts (**Supp. Fig. S3**). All native AtARIs interacted with most members of Group VI of E2s, except for AtUBC9 and AtUBC12 (**Fig. 10A left**). This phylogenetic group is composed by AtUBC8, AtUBC9, AtUBC10, AtUBC11, AtUBC12, AtUBC28, AtUBC29 and AtUBC30¹⁶. Additionally, DBD-AtARI1 showed the highest versatility regarding E2 interaction. Besides Group VI, AtARI1 interacted with AtUBC15, AtUBC16, AtUBC17, AtUBC18, AtUBC35, AtUBC36 and AtUBC37 (**Fig. 10A, Supp. Fig. S3-S4**). While AtARI5, AtARI7 and AtARI8 (para-group) interacted additionally with AtUBC31, showing a clear difference with the ortho-group: AtARI1, AtARI2 and AtARI3 (**Fig. 10A, Supp. Fig. S3-S4**).

The E2—AtARI interaction is predicted to occur through the RING domain of ARIs. The RING domains of all AtARIs were previously predicted from UniprotKB (sequence) and confirmed from alpha fold structures (**Supp. Data 2**). Once the RING domains were identified for each ARI, they were aligned with human ARIs (HHARI and TRIAD1) to identify conserved residues within the domain (**Fig. 9**). A conserved histidine was found that aligned with H205 and H158 from HHARI and TRIAD1, respectively (**Fig. 9**). These histidine residues were mutated to alanine and the Y2H was repeated for these versions. These mutations are predicted to de-stabilize and unfold the RING1 domain, thus abolishing the E2—AtARI interaction. In all cases the once positive interactions were completely abolished (**Fig. 10A right, Supp. Fig. S5-S6**), except for DBD-AtARI8^{H147A} where there was autoactivating signal. Yeast colonies that would express DBD-AtARI2^{H143A} did not grow and were not included in further Y2H analysis. Taken altogether, these results hint towards the specific pairing of E2s with ARIs through the RING1 domain. Of all evaluated ARIs, the ortho-group seems the most promising regarding E2 binding and conserved structural features. Therefore, most of the following experiments were restricted to the ortho-group.

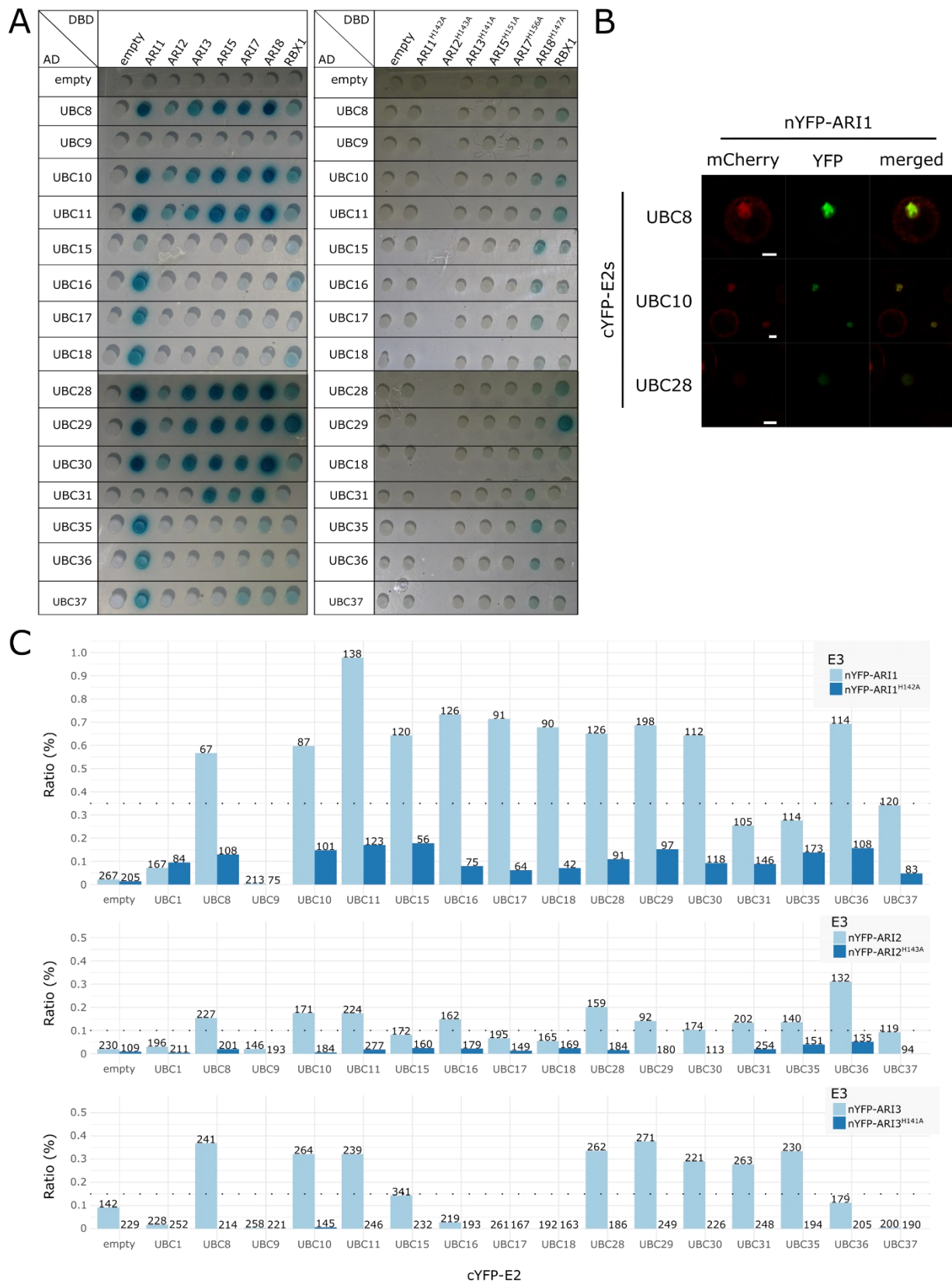


Figure 10. Group VI of E2s interact with AtARIs. A) LexA Y2H assays between eight DBD-AtARIs (native: left and mutant: right) and AD-E2s. Presence of interaction is depicted in blue **B-C)** BiFC assays between three nYFP-AtARIs

and a subset of cYFP-E2s in *Nicotiana benthamiana* protoplasts. **B)** Microscopy image of protoplasts where nYFP-AtARI1 and a subset of cYFP-E2s are expressed and interacting. Scale bar corresponds to 10 μ m. **C)** Ratio in percentage between the total amount of protoplasts where YFP signal (interaction) was observed and the total amount of protoplasts where mCherry signal was observed. Total amount of evaluated protoplasts is depicted on top of each column. Light blue columns correspond to native nYFP-AtARIs, and dark blue columns correspond to mutated versions of nYFP-AtARIs. Cut-off for interaction was set to 0.35 for AtARI1, 0.10 for AtARI2 and 0.18 for AtARI3.

Interactions between E2s and E3s are usually weak, impairing their characterization through classical techniques such as immunoprecipitation or pull down ⁹⁹. Therefore, our *in vitro* results were confirmed using the *in vivo* approach BiFC (Bimolecular Fluorescence Complementation) in *Nicotiana benthamiana* protoplasts. In BiFC, two non-fluorescent fragments irreversibly reconstitute to form a visible fluorescence reporter that allows the visualization of protein—protein interactions in living cells ¹⁰⁰. This assay is particularly useful for monitoring transient interactions ¹⁰⁰, such as the E2—E3 interaction; and enables visualization of the subcellular locations of specific protein complexes in the normal cellular environment ¹⁰¹.

The proteins of interest were fused to non-fluorescent fragments of YFP: N-terminal (nYFP) and C-terminal YFP (cYFP) ¹⁰¹. In this case, I fused ortho-group AtARIs to nYFP and a subset of E2s to cYFP. These were transiently co-expressed in protoplasts extracted from *N. benthamiana* leaves. The interaction between E2s and AtARIs would reconstitute the YFP, and the signal can be visualized using a fluorescence microscope. Additionally, NLS-mCherry (NLS: nuclear localization signal) was co-expressed with all combinations of E2s and AtARIs as an expression control. The major drawback of BiFC is that the fluorescent protein halves are prone to self-assembly independent of a protein—protein interaction event. Therefore, it is imperative to use proper negative controls, such as mutant versions of the proteins to assess the absence of interaction or known non-interacting proteins, rather than using a YFP fragment alone ¹⁰². Hence, as negative controls I used the mutant versions of AtARIs in the RING1 domain (from the nYFP side) and non-interacting proteins AtUBC1/AtUBC9 (from the cYFP side). Moreover, cYFP alone was included in the study as an additional negative control. A ratio was then calculated from the number of protoplasts that show a YFP signal (BiFC positive) and the total amount of transformed protoplasts (presented mCherry signal) (**Fig. 10B-C, Supp. Fig. S7-S10**). I defined interaction as a number higher or equal than two times the highest ratio of any of the negative controls (nYFP-AtARI mutant versions, cYFP, cYFP-AtUBC1 or cYFP-AtUBC9). This cut-off is represented as a dotted line in **Fig. 10C**.

Interaction between all AtARIs and Group VI of E2s was confirmed with BiFC (AtUBC8, AtUBC10, AtUBC11, AtUBC28, AtUBC29 and AtUBC30) (**Fig. 10C**). Additionally, AtARI1 interacted with AtUBC15, AtUBC16, AtUBC17, AtUBC18 and AtUBC36 as in the Y2H, confirming again this interaction (**Fig. 10C**). In the case of

AtARI2, additional interactions were observed that were not spotted in the Y2H. This would be the case of AtUBC16, AtUBC31, AtUBC35 and AtUBC36. AtARI2 signal was always absent or faint in Y2H and therefore, it is possible that there were false negatives in this assay. Regarding AtARI3, it additionally interacted with AtUBC31 and AtUBC35, which were not observed in Y2H.

Based on the microscopy images, all these complexes seem to be localized to the nucleus (**Supp. Fig. S7-S10**). In many cases, specks were observed in the interaction zone for the AtARI1—E2s combinations (**Supp. Fig. S7-S8 white arrows**).

II.3. UbiGate may not be well suited for analyzing E2 reactivity towards AtARIs.

In order to correctly assess the pairing selectivity of E2s and AtARIs, further aspects must be taken into consideration. Interaction does not imply activity, therefore, autoubiquitylation activity of the ortho-group AtARIs was evaluated (**Supp. Fig. S11-S12**). Here, I used a synthetic biology approach called UbiGate in which autoubiquitylation is reconstituted in bacteria by co-expressing the E3 of interest with an operon containing Ub, AtUBA1 (E1), and one of the E2s. E3 autoubiquitylation is detected by Western blot, as a read-out for activity^{12,99}. In a first round, *Escherichia coli* strains were co-transformed with GST-AtARIs and a construct containing the E1, an HA-E2 (Hemagglutinin-E2) and His-Ub. After assessing the right conditions for expression (strain, expression time and temperature), GST-AtARI1 was successfully modified with ubiquitin in the presence of several E2s (**Supp. Fig. S11**). These E2s were identified as Group VI (AtUBC8, AtUBC10, AtUBC11, AtUBC28, AtUBC29 and AtUBC30), Group VII (AtUBC15, AtUBC16, AtUBC17, AtUBC18) and AtUBC31. However, I was unable to obtain reproducible results for GST-AtARI1 and no reaction was obtained for GST-AtARI2 and GST-AtARI3. It is possible that the GST moiety interferes with the autoubiquitylation of the AtARIs, since the latter has a very flexible structure (**Supp. Fig. S2**), or AtARIs are not active, or they are unstable prior to modification. In order to overcome these limitations, native and hyperactive AtARIs were expressed and purified. Hyperactive versions of AtARIs were created by mutating a conserved serine to aspartate in the Ariadne domain, mimicking a phosphorylation event. Purified tag-less AtARI1 (hyperactive: AtARI1^{S363D}) and two-step-purified tag-less AtARI2 (native and hyperactive: AtARI2^{S364D}) and AtARI3 (native and hyperactive: AtARI3^{S361D}) were mixed with bacterial lysate from the UbiGate system (Ub + E1 + HA-E2), avoiding co-transformation, and incubated at 37°C for 30 min (**Supp. Fig. S12**). Two-step-purification (~1 day) was performed for AtARI2 and AtARI3 variants since both proteins lost their activity during a 3-day purification procedure at 4°C (**Supp. Fig. S14**). In order to see the autoubiquitylation, fluorescein modified Ub was also added to the mix. In all cases, absence of the UbiGate- and AtUBC1- bacterial lysate were included as negative controls. Hyperactive variants AtARI2^{S364D}

and AtARI3^{S361D} were not properly expressed and therefore, it was difficult to see any modifications (Supp. Fig. S12). Even though there were inconsistencies in this assay, Group VI E2s mediated the autoubiquitylation of AtARI1^{S363D}, AtARI2 and AtARI3 (Supp. Fig. S12). Active E2s were consequently defined as interacting in both Y2H and BiFC and UbiGate-reactive. Therefore, Group VI E2s seems to be the physiological relevant E2s that mediate ubiquitylation with the AtARIs.

II.4. Group VI E2s AtUBC8 and AtUBC28 mediate the autoubiquitylation of ortho-group AtARIs.

After identifying which type of E2 mediates the autoubiquitylation of AtARIs, I aimed to confirm this via *in vitro* ubiquitylation (IVU) assays. All the components of the ubiquitylation cascade (E1, E2 and E3) were expressed in *E. coli* and purified, as stated in the methods section, and fluorescein modified Ub was purchased. AtUBC8 and AtUBC28 were used as representative E2s. The reactions were first performed under non-reducing conditions (Fig. 11A-B), and it was stopped by adding reducing or non-reducing SDS buffer (+ or - β -mercaptoethanol, respectively). Under non-reducing conditions, we can assess the ubiquitylation in both cysteine (including active site) and lysine residues of AtARIs, while under reducing conditions mainly lysine residues can be assessed. Thioester bonds are more labile than iso-peptide (amide) bonds, and therefore affected by reducing agents such as β -mercaptoethanol or DTT.

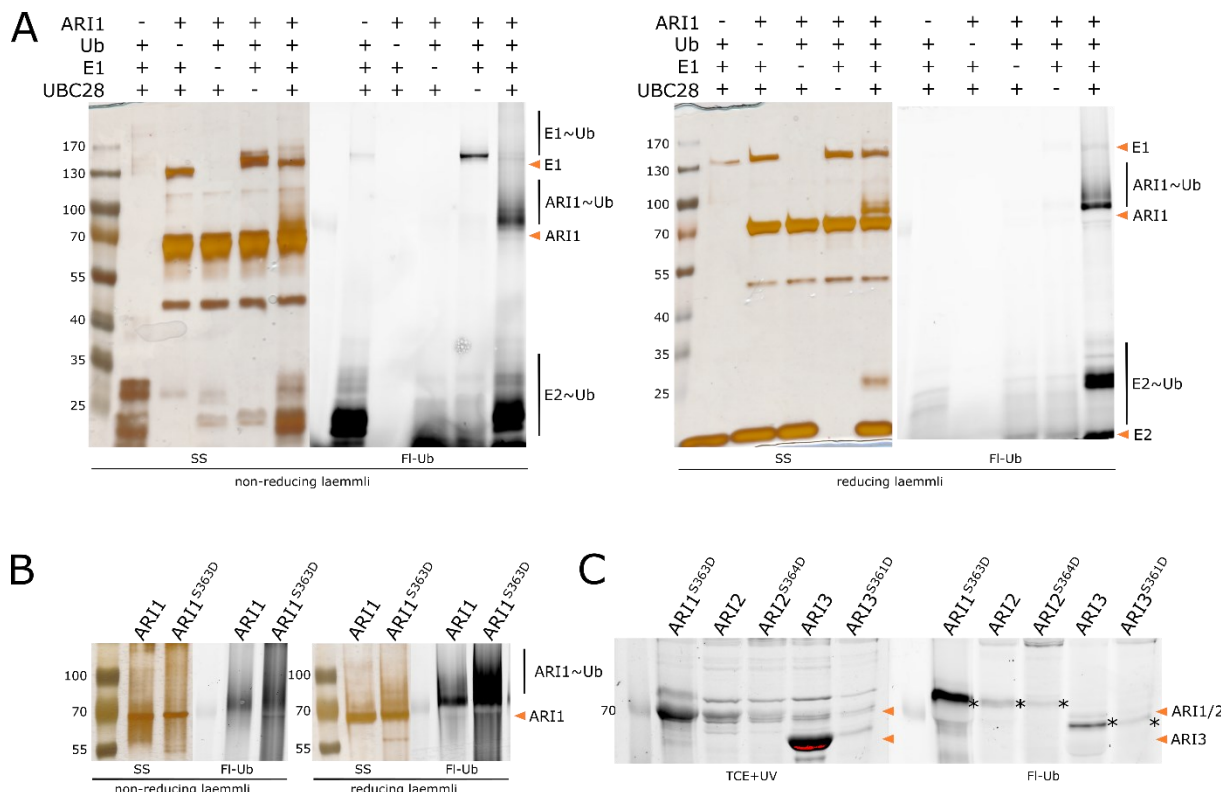


Figure 11. Group VI E2s AtUBC8 and AtUBC28 mediate the autoubiquitylation of ortho-group AtARIs. A) Autoubiquitylation assay of AtARI1 mediated by AtUBC28 in non-reducing conditions. Silver stained (SS) and 488nm

fluorescence scan (Fl-Ub) of autoubiquitylation reactions using non-reducing (left) and reducing SDS-Buffer (right). **B**) Autoubiquitylation reactions of AtARI1 and AtARI1^{S363D} mediated by AtUBC8 in non-reducing conditions, all components are present. Silver stained (SS) and 488nm fluorescence scan (Fl-Ub) of autoubiquitylation reactions using non-reducing (left) and reducing SDS Buffer (right). **C**) Autoubiquitylation reaction in reducing conditions of AtARI1^{S363D}, AtARI2, AtARI2^{S364D}, AtARI3 and AtARI3^{S361D} mediated by AtUBC8, all components are present. Protein visualization was performed with Trichloroethanol (TCE) in-gel and irradiating with UV for 1-2 min in BioRad transilluminator. Asterisks represent Ub~AtARIs and orange triangles depict non-ubiquitylated proteins.

AtUBC8 and AtUBC28 mediated the autoubiquitylation of AtARI1 (**Fig. 11A-B, Supp. Fig. S13A, Supp. Fig. S14A, Supp. Fig. S15A**), which can be denoted by the smear above 70 kDa corresponding to AtARI1~Ub in both silver stain and fluorescence scan. This high molecular smear is only visible when all components are present, and it is shortened when reducing SDS buffer is used to stop the reactions. Considering that there are 42 lysine and 33 cysteine residues in AtARI1, it is evident that the number of possible ubiquitylated AtARI1 species is greatly diminished under reducing conditions. However, when using AtARI1^{S363D} the smear seems more intense and with higher amount of AtARI1~nUb species, even under reducing conditions (**Fig. 11B**). This hints towards the increase in activity of AtARI1^{S363D}.

Purified AtARI2 and AtARI3 were not able to autoubiquitylate at first (**Supp. Fig. S14, Supp. Fig. S15A**). The purification process lasted 3-4 days and it is possible that these enzymes lost their activity during the purification procedure. Furthermore, AtARI1 and AtARI2 seem to homodimerize (bands above 130 kDa) under non-reducing conditions (likely non-native disulfide bridges) and it seems to be enhanced with their hyperactive versions (**Supp. Fig. S14, Supp. Fig. S15A**). According to Y2H data, AtARI1 establishes homo- and hetero-dimers of so far unknown functionality (**Supp. Fig. S16**); this could also explain the specks observed on BiFC (**Supp. Fig. S7**). Furthermore, homodimerization could affect the autoubiquitylation activity of these enzymes. Therefore, fast-purified AtARI2 and AtARI3 were further used in IVU assays, where the purification process lasted less than a day. Additionally, IVUs were performed under slightly reducing conditions to avoid homodimerization of AtARIs.

Next, I assessed the activity of AtARI2 and AtARI3, compared to AtARI1^{S363D}, under slight reducing conditions, with the addition of 0.5 mM DTT to the IVU reaction (**Fig. 11C, Supp. Fig. S13B-D, Supp. Fig. S15B**). In this case, AtUBC8 mediated the autoubiquitylation of AtARI1^{S363D} under reducing conditions, which can be observed as a single dark band above the 70 kDa (**Fig. 11C asterisk**). Both AtARI2 and AtARI3 had a similar behavior to AtARI1^{S363D}, although not as strong. Again, AtARI2^{S364D} and AtARI3^{S361D} had a lower expression than their native versions, and therefore the reaction products were difficult to observe. Overall, AtUBC8 was able to mediate the autoubiquitylation of all the AtARIs.

II.5. Other E3s interact with AtARIs.

So far, I had shown data characterizing the first steps of the AtARIs' mechanism: E2—ARI interaction and the consequent transfer of ubiquitin from the E2 to the ARIs. Another aspect of the ARIs' mechanism is related to its activation. It has been shown for HHARI and TRIAD1, that HsCUL—HsRBX interaction and HsARIs phosphorylation may constitute signals for their activation^{49,50,52}. Therefore, I performed LexA Y2H between all the *Arabidopsis* Cullins (except AtCUL4) and AtRBX1A against all the AtARIs and several mutant or domain versions (Fig. 12, Supp. Fig. S17-S19). AtCUL4 was not available for this assay.

Several hyperactive or semi-hyperactive versions were created for the AtARIs. One leucine and two glutamates (when possible) were mutated to alanine in ortho-group AtARIs. These residues are part of the SAR group and are in direct contact with the catalytic cysteine loop. When all of them are mutated to alanine in HHARI and TRIAD1, it enhances the interaction with HsCullins (even unmodified) and improves the ubiquitylation^{49,50}. However, in the para-group of AtARIs these residues are not conserved between human and *Arabidopsis* (Fig. 9, Supp. Data 1). The start residue was a lysine instead of a hydrophobic residue and the middle residue was an Ala instead of an acidic residue. I was not able to obtain all the triple mutants for the AtARIs, and therefore, only a few were evaluated in this assay. Another way of generating hyperactive versions is to mutate a conserved serine across all AtARIs, also present in HHARI and TRIAD1⁵², to aspartate in order to obtain a phosphomimic version. This phosphomimic mutation has the same structural effect as the triple mutant⁵².

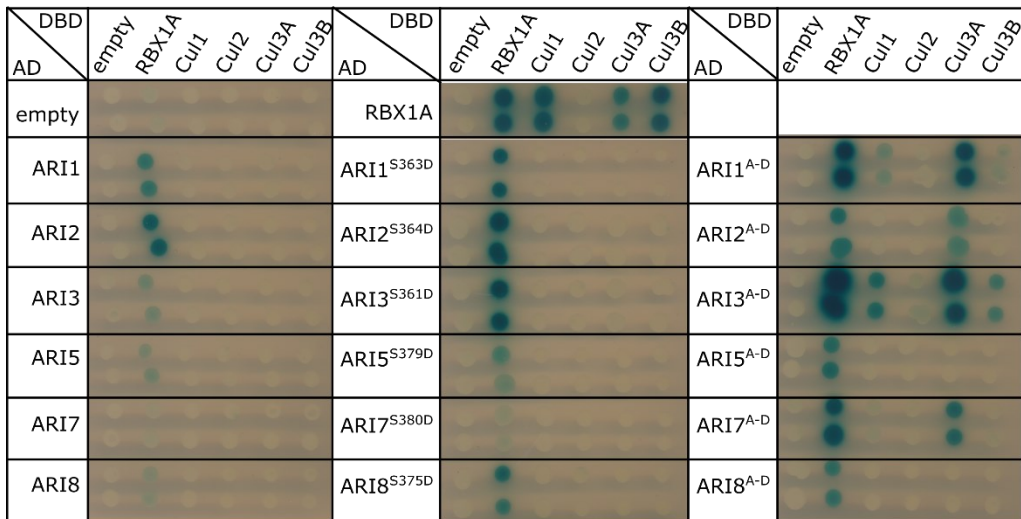


Figure 12. AtARIs interact with AtRBX1A and AtCul3A. LexA Y2H assays between DBD-AtCullins/AtRBX1A and AD-AtARIs (native, hyperactive and A-D: Ariadne domains). Presence of interaction is depicted in blue. AD-AtRBX1A was used as a control for AtCullin interaction.

All native AtARIs, except AtARI7, seem to interact with AtRBX1A and the signal was enhanced in most cases when using hyperactive mutant versions (Fig. 12, Supp. Fig. S17-S19). However, no signal was obtained between the AtARIs (native and mutants) and the AtCullins. Therefore, I continued by evaluating the specific domain that is predicted to interact with AtRBX1A—AtCullins. In this case, the Ariadne domain of all AtARIs interacted with AtRBX1A, while most interacted with AtCUL3A and to a lower extent with AtCUL1 and AtCUL3B. Hence, AtCUL3A would be a good candidate for evaluating the Cullin-dependent activation of AtARIs (Supp. Fig. S17-S19). It is possible that regions outside the Ariadne domain, such as the downstream C-terminal region, could further regulate the activity of AtARIs, and therefore prevent the Cullin interaction even in a hyperactive state.

It is also possible that other E3s could regulate the activity of AtARIs. Therefore, I also pursued a proteomics approach, where I used immobilized GST or GST-AtARIs from the para- and ortho-groups as bait and incubated them with plant lysate. The obtained protein eluates were identified via tandem Mass spectrometry (MS/MS) (Supp. Data 3). Only GST-AtARI7 from the para-group was not included, due to difficulties during the cloning process. Interacting proteins were defined as such when: less than two peptides were recovered from at least two biological replicates from the GST control and more/equal than two peptides were recovered from at least two biological replicates from the GST-AtARI baits. One E3 was identified from this experiment that interacted with all AtARIs (AtARI1 to AtARI8). This E3 is a U-Box E3 ligase called AtPUB26. While all those potential interaction partners might be regulated by AtARIs, in one way or another, I will focus on the putative AtARIs' substrates because of their general relevance and available proteomic data.

II.6. eIF4E1, a putative substrate of AtARIs.

Using the data from the previously mentioned proteomics approach, I identified members of the eukaryotic initiation of translation machinery that interacted, either directly or indirectly, with AtARIs (Table 1, Supp. Data 3). This protein complex, named eIF4, is formed by an mRNA-poly(A) binding protein (PABP), a helicase (eIF4A), an mRNA-cap binding protein (eIF4E) and a scaffold protein (eIF4G) bringing together eIF4E and eIF4A¹⁰³. All AtARIs interacted with mRNA-poly(A) binding proteins (PABP2, PABP4 and PABP8) as well as one of the scaffold proteins eIFiso4G1. All AtARIs, except AtARI3, interacted with the helicase (eIF4A1), while only AtARI3 interacted with a different scaffold protein (eIFiso4G2). Interestingly, AtARI1, AtARI2 and AtARI5 interacted additionally with another helicase (eIF4A-III). It is also noticeable that AtARI1 and AtARI2 pull-downed the same proteins of this complex, suggesting a similar activity.

A member of this complex in humans, called 4EHP, was previously identified as a substrate of both HHARI and TRIAD1⁵². In humans, 4EHP (or HsEIF4E2) is an mRNA-cap binding protein that represses translation. *Arabidopsis thaliana* possess five similar mRNA cap binding proteins: eIF4E1, eIF(iso)4E, nCBP, eIF4EB and eIF4EC, the first two constitute the canonical proteins and the latter three, the non-canonical^{93,94}. It is possible that *Arabidopsis* ARIs may have a similar substrate than human ARIs. Even though that the cap binding proteins were not identified in the proteomics assay, it is still possible that they constitute substrates of AtARIs, especially since most members of the complex was pull-downed using GST-AtARIs as bait. Therefore, further experiments were performed to assess whether this protein could constitute an AtARI substrate.

Table 1. Identified interacting proteins from the eukaryotic initiation of translation machinery. Numbers depict PSM values (~amount of identified peptides) for each biological replicate (1 to 3) in each sample.

Accession	Description	GST			GST-AtARI1			GST-AtARI2			GST-AtARI3			GST-AtARI5			GST-AtARI8		
		1	2	3	1	2	3	1	2	3	1	2	3	1	2	3	1	2	3
AT4G34110	PABP2	0	0	0	6	2	5	3	5	6	4	2	0	3	8	5	0	2	7
AT5G57870	eIFiso4G1	0	0	1	6	4	9	2	3	10	5	2	0	1	6	19	1	5	12
AT2G24050	eIFiso4G2	0	0	0	0	0	1	0	0	2	0	0	0	0	2	5	0	0	3
AT3G19760	EIF4A-III	0	0	0	2	3	2	0	2	2	0	0	0	2	4	2	0	0	2
AT1G49760	PABP8	0	0	0	6	5	6	0	6	6	8	5	0	3	11	5	1	3	5
AT2G23350	PABP4	0	0	0	7	2	8	0	3	4	6	3	0	5	6	11	0	5	4
AT3G13920	EIF4A1	0	0	0	21	12	13	0	10	14	22	0	0	11	15	17	0	19	16

Next, I assessed whether the canonical eIF4E1 and eIF(iso)4E protein could constitute substrates of the AtARIs. This was based on the information found in the literature^{52,95} and that GST-AtARIs interact with members of the initiation of translation complex. First, I evaluated whether these proteins interacted with AtARIs *in vivo*. I performed a BiFC assay, where eIF4E1 and eIF(iso)4E were fused to cYFP and the AtARIs to nYFP and expressed in protoplasts extracted from *N. benthamiana* leaves. Both proteins seem to interact with all the AtARIs (Fig. 13A).

Other assays were performed to verify the interaction. However, in LexA Y2H the DBD-eIF4E1 is autoactivating and DBD-eIF(iso)4E requires a longer time for developing a signal (Supp. Fig. S20). Both problems result in a higher background noise signal and should not be considered for analysis. When using GST or GST-AtARIs as bait in a pull-down assay, I was not able to recover 6xHis-SUMO-eIF4E1 or 6xHis-SUMO-eIF(iso)4E (Supp. Fig. S21A). However, when 6xHis-ARIs were used as bait in a similar set up, it was only possible to recover partially GST-eIF4E1, since GST-eIF4E1 was found in both flow through and elution

fractions; but not GST-eIF(iso)4E (**Supp. Fig. S21B**). Additionally, GST-eIF4E1 seems to interact with 6xHis-SUMO-GFP (**Supp. Fig. S21B**). If these proteins constitute a substrate of AtARIs, they could interact transiently and would not be easily recovered from a pull-down. However, they did interact in the BiFC with AtARIs, where additional factors could mediate or improve the interaction. Therefore, I continued to assess their modification mediated by AtARIs employing IVU assays.

I used several versions of both proteins for the IVU assays: tag-less, GST-tagged and 6xHis-SUMO-tagged. Only when eIF4E1 was tagged with SUMO, a ubiquitin-like protein, the AtARIs were able to modify it with Ub (**Fig. 13B-C, Supp. Fig. S22A-B**). In all cases, product formation (eIF4E1~nUb) was difficult to follow via fluorescence gel. However, when I performed a western blot, a reduction of the unmodified substrate was visible after 30 min of reaction. The lowest substrate signal (highest activity of AtARIs) was visualized for all AtARIs down to a 0.01-0.03 reduction from the initial quantity (1), except for AtARI1 with 0.78-0.93 of unmodified substrate (**Fig. 13B-C, Supp. Fig. S22A-B**). All measurements were performed using the anti-SUMO blot for homogeneous quantification between the control (6xHis-SUMO-GFP) and the putative substrates. On the other hand, eIF(iso)4E was either slightly modified by AtARI1^{S363D} (**Fig. 13C**) or not at all (**Supp. Fig. S22A-B**). Tag-less, as well as GST-tagged, eIF4E1 and eIF(iso)4E were not modified by AtARI1 or AtARI1^{S363D} (**Supp. Fig. S22C-D**).

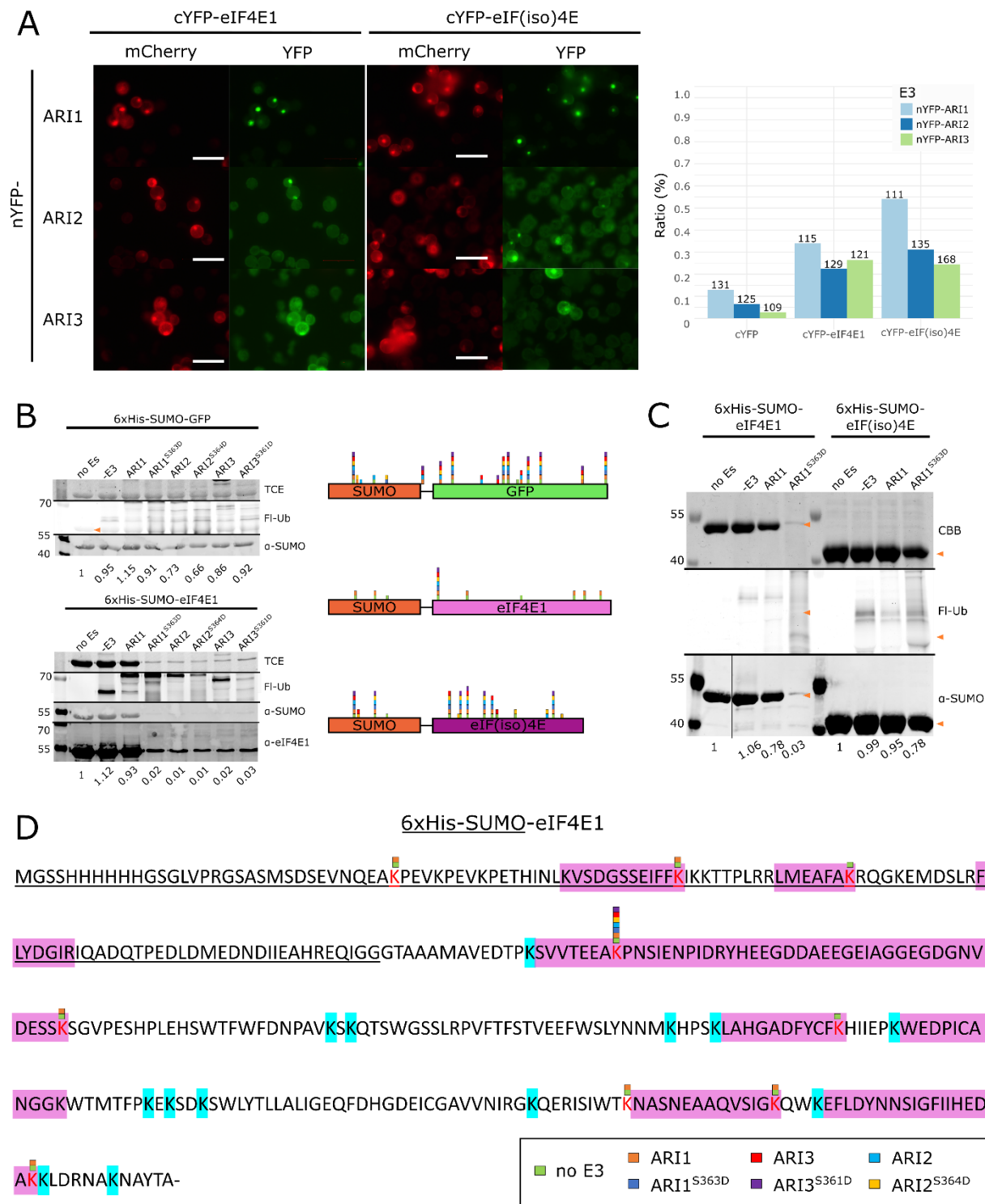


Figure 13. eIF4E1, a putative substrate of AtARIs. A) BiFC assay between three nYFP-AtARIs and cYFP-eIF4E1/eIF(iso)4E in *Nicotiana benthamiana* protoplasts. Microscopy image of protoplasts where nYFP-AtARI1 and cYFP- eIF4E1/eIF(iso)4E are expressed and interacting (left). Scale bar corresponds to 100 μ m. Ratio in percentage between the total amount of protoplasts where YFP signal (interaction) was observed and the total amount of protoplasts where mCherry signal was observed. Total amount of evaluated protoplasts is depicted on top of each column. Each color corresponds to an nYFP-AtARI. **B)** *In vitro* ubiquitylation assay of 6xHis-SUMO-GFP, 6xHis-eIF4E1 and 6xHis-SUMO-eIF(iso)4E using all ortho-group AtARIs. Protein visualization was performed with Trichloroethanol

(TCE) in-gel and irradiating with UV for 1-2 min in BioRad transilluminator, while Ub~proteins were visualized with a 488nm fluorescence scan (Fl-Ub), and the sites identified with MS/MS (right). **C**) *In vitro* ubiquitylation assay of 6xHis-eIF4E1 and 6xHis-SUMO-eIF(iso)4E using AtARI1 and AtARI1^{S363D}. Protein visualization was performed with Coomassie Brilliant Blue (CBB), while Ub~proteins were visualized with a 488nm fluorescence scan (Fl-Ub) **B-C**) Further visualization was performed with immunoblots (α -SUMO and α -eIF4E1). Quantification of substrate disappearance was performed using the α -SUMO immunoblot and are located at the bottom of each blot. **D**) MS coverage of 6xHis-SUMO-eIF4E1 in the presence of AtARI1^{S363D} (magenta highlighting). Underlined sequence corresponds to 6xHis-SUMO. Lysine residues highlighted in cyan were not covered in any conditions. Colored squares on top of red Lysine correspond to ubiquitylation in the absence or presence of an AtARI.

In order to identify the ubiquitylation sites of eIF4E1, MS/MS analysis of the IVU reactions from **Figure 13B** were performed (**Table 2**, **Fig. 13B right**, **Fig. 13D**, **Supp. Data 5**). Both SUMO-GFP and SUMO-eIF(iso)4E, had a low percentage of Ub-modified peptides (measured as PSM) with approximately 10% (**Table 2**, **Supp. Data 5**). The total amount of identified peptides (a measure for amount of proteins) was suitable for this assay (~250 PSM for SUMO-eIF(iso)4E and ~600 for SUMO-GFP in **Table 2**) and corresponds well with what is seen in the blots (**Fig. 13B left**). Regrettably, this was not the case for eIF4E1. Even though all reactions started with the same amount of eIF4E1 proteins, there was a striking difference in the amount of identified peptides of eIF4E1. In the reactions where no E3 or AtARI1 was added, the total PSM was in the range of 300-400 (suitable), which mostly corresponds to the unmodified substrate (PSM: 277-352) (**Table 2**). This aligns well with the results from the blots. However, the total PSM of eIF4E1 was extremely low in the reactions where any of the rest of AtARIs were used, ranging from 19 to 57, of which most corresponds to the unmodified substrate. Furthermore, the sequence coverage was lower as well, decreasing from ~55% (no E3/AtARI1) to 30% (rest of AtARIs). Therefore, some Ub~eIF4E1 (most likely) were not identified through MS analysis (**Supp. Data 5**), or by antibodies (**Fig. 13B**). Based on this result it is unlikely that the true ubiquitylation sites correspond to the ones identified in this assay, e.g. K16 in eIF4E1 (false positive). The peptide where this lysine is positioned was the only one identified that was modified with Ub in all samples (**Fig. 13D**, **Supp. Data 5**). There are 20 solvent-exposed lysine residues in eIF4E1 that could potentially be modified by Ub, however, only 7 were covered by MS (**Fig. 13D**).

Table 2. Summary of MS/MS analysis of IVU reactions. PSM and Coverage of substrates in the different reactions (no E3 or AtARIs).

Substrate	E3	PSM of modified peptides	PSM of unmodified peptides	Total PSM	Percentage of ubiquitylation	Substrate Coverage
SUMO-GFP	No	47	576	623	8%	81
SUMO-GFP	AtARI1	46	613	659	7%	83
SUMO-GFP	AtARI1 ^{S363D}	33	447	480	7%	83
SUMO-GFP	AtARI2	73	507	580	13%	81

SUMO-GFP	AtARI2 ^{S364D}	46	480	526	9%	83
SUMO-GFP	AtARI3	59	514	573	10%	83
SUMO-GFP	AtARI3 ^{S361D}	38	500	538	7%	83
SUMO-eIF4E1	No	54	352	406	13%	61
SUMO-eIF4E1	AtARI1	30	277	307	10%	53
SUMO-eIF4E1	AtARI1 ^{S363D}	4	53	57	7%	35
SUMO-eIF4E1	AtARI2	2	27	29	7%	26
SUMO-eIF4E1	AtARI2 ^{S364D}	1	19	20	5%	23
SUMO-eIF4E1	AtARI3	2	35	37	5%	28
SUMO-eIF4E1	AtARI3 ^{S361D}	1	42	43	2%	33
SUMO-eIFiso4E	No	39	340	379	10%	52
SUMO-eIFiso4E	AtARI1	40	294	334	12%	50
SUMO-eIFiso4E	AtARI1 ^{S363D}	21	211	232	9%	50
SUMO-eIFiso4E	AtARI2	35	261	296	12%	53
SUMO-eIFiso4E	AtARI2 ^{S364D}	23	229	252	9%	50
SUMO-eIFiso4E	AtARI3	20	228	248	8%	49
SUMO-eIFiso4E	AtARI3 ^{S361D}	13	206	219	6%	46

All values were obtained from **Supp. Data 5**. Total PSM are colored from lowest possible value (0: red) to good coverage (>300: green). Percentage and coverage are colored from lowest possible value (0: red) to highest possible value (100: green). Percentage of ubiquitylation was calculated as: *PSM of modified peptides/Total PSM*100%*



Additionally, auto-ubiquitylation sites of AtARIs mediated by AtUBC8 were identified: 13 for AtARI1, 15 for AtARI2 and 18 for AtARI3 (**Supp. Data 5, Supp. Fig. S25**). This further confirms the pairing activity of AtARIs and AtUBC8.

II.7. eIF4E1 and eIF(iso)4E accumulate in *ari1ari2* knock-out mutants.

In order to analyze the biological effect of ARIs *in planta* I generated CRISPR-Cas9 mutants of *AtARI1*, *AtARI2* and *AtARI3* (**Supp. Fig. S23-S24, Supp. Data 4**). At a first glance, all the possible mutant combinations of the ortho-group AtARIs do not show any visible phenotype at any stage of development (data not shown). At the seedling stage (5-6 days old) the triple mutant grew up to a similar root length compared to Col-0 (**Supp. Fig. S23B**). Furthermore, this triple mutant responds like wild-type to various stresses: 100-400 mM Mannitol and 150 mM NaCl after 4 days of treatment (**Supp. Fig. S23B**). These abiotic stresses were tested since *AtARI1* is upregulated upon drought, salt and heat stress based on differential expression experiments curated in Expression Atlas (<https://www.ebi.ac.uk/gxa/home>).

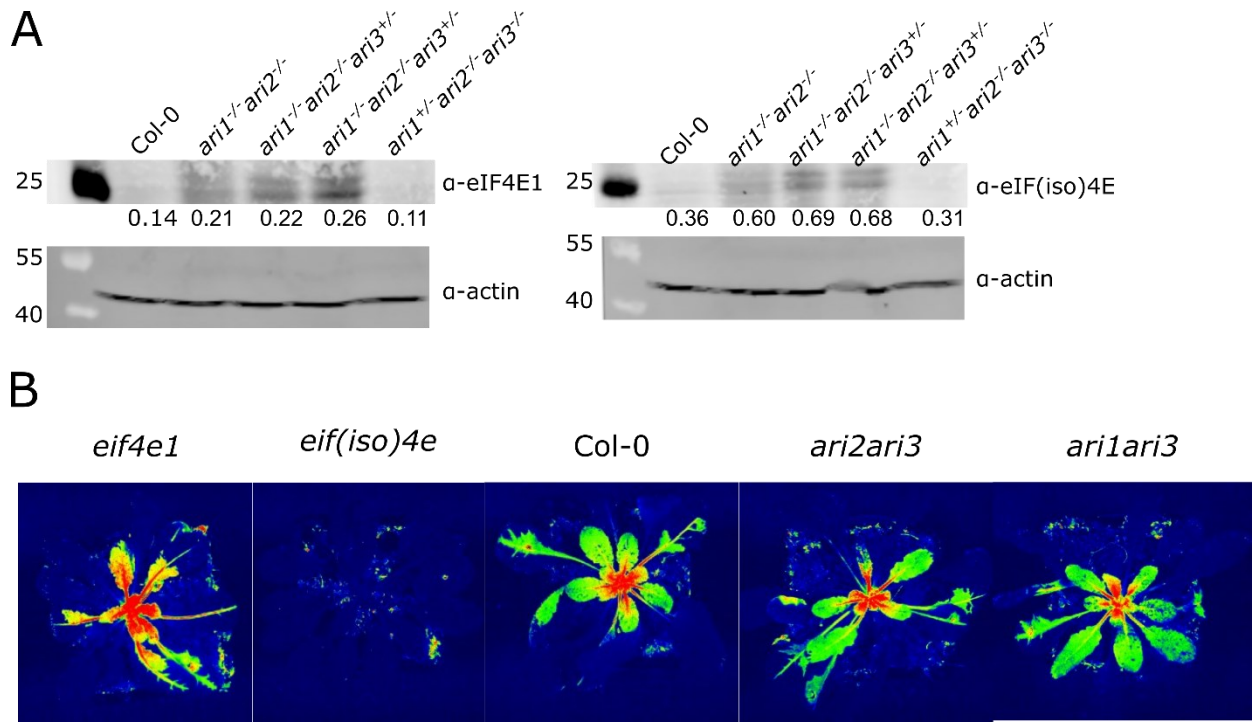


Figure 14. eIF4E1 and eIF(iso)4E accumulate in *ari1ari2* knock-out mutants. A) eIF4E1 and eIF(iso)4E protein levels from ~1 month old Col-0 and mutants' leaves. Quantification was performed using actin as a reference. **B)** Resistance of *ari* mutants to turnip mosaic virus GFP (TuMV GFP). Analysis of GFP accumulation, at 14 days post inoculation of Col-0 (susceptible), *eif(iso)4e* (resistant), *eif4e1* (oversusceptible) and *ari* mutants. The mutants *ari1ari2* and *ari1ari2ari3* were not available. Twelve plants were imaged but no quantification done. Double mutant *ari* plants display regular accumulation as wild-type Columbia.

Additionally, resistance/susceptibility towards TuMV was assayed for different *ari* single and double mutants, except for *ari1ari2*. All these mutants display regular accumulation of the virus as the wild-type Col-0 (Fig. 14B, Supp. Fig. S26). Interestingly, the protein levels of eIF4E1 and eIF(iso)4E in some *ari* mutants were higher than in Col-0 (Fig. 14A). This was especially true for mutants lacking the *AtARI1* and *AtARI2* genes (when both were homozygous). The *AtARI3* gene does not seem to influence much the levels of the translation factors (Fig. 14A). The triple mutant was not available at this moment.

Overall, it seems that eIF4E1 (most likely SUMOylated) might constitute a substrate for AtARIs; however, the link between them at a phenotypic level is yet to be determined.

III. DISCUSSION AND FUTURE PERSPECTIVES

The ubiquitylation cascade comprises the E1—E2—E3 enzymes. ARIs constitute an RBR-type E3 ubiquitin ligases that mediate ubiquitylation through a two-step mechanism⁷⁶. Due to their drastic effects on human development^{104–108}, mammalian ARIs have become increasingly popular in the last 5 years (<https://pubmed.ncbi.nlm.nih.gov> basic search of “Ariadne RBR”). However, their molecular and biological

functions *in planta* are largely unknown. Here, I aimed to uncover the mechanism for which a subset of AtARIs mediate ubiquitylation and assessed their biological role via high order CRISPR/Cas9 mutants. The results of this thesis will set the basis for mechanistically studying AtARIs and will help open the field of RBR E3 ligases in plants.

III.1. Group VI E2s mediate the ubiquitylation of AtARIs.

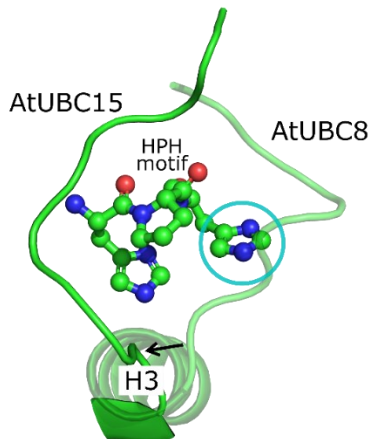
A key step in understanding the function of a specific E3 is to identify its physiological E2, since defined E2—E3 pairs display distinct Ub chain-building properties ⁹⁹. I used several approaches to determine the E2—AtARI specificity. First, I performed *in vitro* and *in vivo* protein—protein interaction assay (Y2H and BiFC, respectively **Fig. 10**) to assess the E2—AtARI pairing selectivity and narrow down the domain where this interaction occurs. Once the physiological E2—E3 pairs were identified, their activity was tested using the UbiGate system and *in vitro* ubiquitylation assays.

Most members of group VI (AtUBC8, AtUBC10, AtUBC11, AtUBC28, AtUBC29, AtUBC30) seem to constitute the physiological E2—AtARI pairs (**Fig. 10-11, Supp. Fig. S3-S15**). All evaluated AtARIs and Group VI E2s have been shown to be expressed in all organs ^{31,76}. Furthermore, this group (except AtUBC9 and AtUBC12) interacted with all the AtARIs through the RING1 domain and mediated their autoubiquitylation (**Fig. 10-11, Supp. Fig. S3-S15**). The group VI are closely related to the human UBED2-4 (**Fig. 5A, Fig. 15A**), of which UB2D3 (also called HsUBCH5C) has already been identified as an E2 that mediates RBR ubiquitylation in humans (**Fig. 15A**) ⁵³. Moreover, this group (e.g., AtUBC8) have been shown to mediate the attachment of the first Ub onto substrates (or priming) ¹⁶. This would also suggest the predicted role of AtARIs in priming the ubiquitylation of substrates ^{49,50,52}. This E2—AtARI pairing constitutes an advantage in ubiquitylating small substrates (such as eIF4E1: 25 kDa), that otherwise could not be reached by other E2—E3 combinations. This advantage is based on the flexible structure of AtARIs (**Supp. Fig. S2**) and the role of these E2s in priming events ³³. However, it is also possible that AtARIs together with Group VI E2s could generate K11-linked polyUb chains, as seen for HsUBCH5A (also named HsUB2D1) ³⁴.

A

		HPN motif	active site	
VII	AtUBC17	HPHIYSNGHICLDVLY-DSWSPAMRLSSIC	117	
	AtUBC16	HPHIYSNGHICLDILY-DSWSPAMTVSSIC	117	
	AtUBC15	HPHIYSNGHICLDILY-DSWSPAMTVNSVC	117	
	AtUBC18	HPHIYSNGHICLDILY-DSWSPAMTVSSVC	117	
	hhUBCH7	HPNIDEKGQVCLPVISAENWKPATKTDQVI	105	
	AtUBC31	HPNINDEGSICMNLK-DKWTPALMVEKVL	109	
VI	hhUBCH5C	HPNINNSNGSICLDILR-SQWSPALTISKVL	103	
	AtUBC29	HPNINNSNGNICLDILK-DQWSPALTISKVL	103	
	AtUBC30	HPNINNSNGSICLDILK-EQWSPALTISKVL	103	
	AtUBC11	HPNINNSNGSICLDILK-EQWSPALTISKVL	103	
	AtUBC8	HPNINNSNGSICLDILK-EQWSPALTISKVL	103	
	AtUBC28	HPNVNSNGSICLDILK-EQWSPALTISKVL	103	
	AtUBC10	HPNINNSNGSICLDILK-EQWSPALTISKVL	103	
**::: . * :*: :: ..*.* : :				

B



C

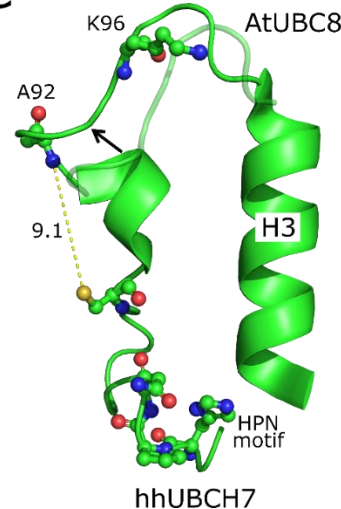


Figure 15. Structural differences between E2s may explain their reactivity profile. **A)** Protein full sequence alignment of AtUBCs, HsUBCH7 and HsUBCH5C using ClustalW (default parameters with manual correction). In cyan is represented the change of N to H in Group VII. In yellow is represented the active site. The distinct residues (near the active site) in HsUBCH7 are represented in magenta. **B)** 3D alignment of AtUBC8 (transparent) and AtUBC15, showing HPH motif (3rd His circled in cyan) and helix 3 (H3 or crossover helix) of AtUBC15. Main difference lies in the loop C-terminal to H3 (also called L7). **C)** 3D alignment of AtUBC8 (transparent) and HsUBCH7, showing HPN motif, active site Cys and distinct residues in ball-stick from the loop N-terminal to H3. Distance between A96 and active site Cys is represented in Angstroms.

One interesting result was the pairing of AtARIs with group VII E2s (AtUBC15-18). It has been shown that the human homologue, HsUBE2W, displays reactivity to the N-terminal α -amino group of substrates³⁶. It is possible that AtARIs could mediate, together with these E2s, this type of ubiquitylation. Interestingly, these E2s do not possess the typical HPN catalytic motif that is found in most E2s, but an HPH, which could explain the difference in reactivity (Fig. 15A-B). As a result of this change (HPN to HPH), the loop located C-terminal to H3 possess a different sequence (residues 124-135) and conformation to accommodate better the changed residue (Fig. 15B). Mutagenesis experiments would be required to test whether HPH

could be responsible for the reactivity towards N-terminal α -amino group, while considering the loop 124-135 in the presence of AtARIs.

The human cysteine-reactive UB2L3 (also called HsUBCH7) has been shown to only transfer ubiquitin specifically to HECT- and RBR- types of E3 ligases⁵³. This HsUBCH7 does not cluster in any clade of *Arabidopsis*, and yeast's, E2s (Fig. 5A). Taking a closer look to the catalytic region, one can notice that there are distinct residues in HsUBCH7 (Fig. 15A) near the active site Cys, when compared to AtUBC31 and Group VI E2s (Fig. 15A). One of these residues corresponds to P88, which was already tested to check for difference between Lys and Cys reactivity in HsUBCH5C⁵³. Here the authors evaluated the effect of the mutation D87P in HsUBCH5C, with the purpose of mimicking HsUBCH7. The D87 residue in HsUBCH5C is conserved in Group VI E2s (Fig. 15A). The HsUBCH5C^{D87P} showed an intermediate reactivity towards Lys compared to WT HsUBCH5C, which discarded the (predominant) role of P87 in Cys reactivity. Another difference between HsUBCH7 and the Group VI E2s lies in the loop (L7) N-terminal to H3 (crossover helix), which is longer in HsUBCH7 by one residue and has been shown to mediate E3 interaction⁹⁹. This "extra" residue was identified by⁵³ as E93. However, upon closer look to the 3D structures and after correcting the alignment it seems that A92 corresponds to the extra residue and not E93. The latter is conserved between group VI and VII as an Asp or Glu. Several residues within loop L7 from HsUBCH7 are not conserved in group VI E2s, such as S91 and K96 (Fig. 15A, C). It would be interesting to check whether this loop could explain the specificity in reactivity towards only cysteine. Overall, there seems to be no cysteine-reactive E2s in *Arabidopsis*, similarly to yeast.

Other E2s, like AtUBC31, AtUBC35, AtUBC36, AtUBC37 showed inconsistent results regarding interaction and activity towards AtARIs (Fig. 10, Supp. Fig. S11-S12). This may be due to the different systems used for assessing the pairing selectivity. There may be some interference in yeast (or *Nicotiana benthamiana*) where both AtUBC35 and AtUBC36 are conserved, in contrast to the UbiGate system in bacteria where the Ubiquitin Proteasome System (UPS) is not found. Nevertheless, they should be further studied to confirm whether they work together with AtARIs.

Of note, this is the first time that UbiGate has been used for an RBR type of E3. This method has been successfully used in U-Box and RING type E3s, with reproducible results¹². In order to use UbiGate as a high throughput screening assay for analyzing the activity of E2—E3 pairs, I would recommend cloning in a single construct all the components of the ubiquitylation cascade, using a small tag for the E3 (such as c-myc) and optimize the expression conditions for each E3 combination.

III.2. E3—E3 binding and AtARI phosphorylation constitute potential activation mechanisms.

In order to fulfill their function, human ARIs need to be activated either via E3—E3 interaction (with Cullins) or through phosphorylation in a conserved serine in the Ariadne domain^{49,50,52}. Both options were initially assessed in this project. Protein—protein interaction assays were performed and AtRBX1A—AtCUL3A and AtPUB26 stood out as potential activators of AtARIs (Fig. 12, Supp. Fig. S17-S19, Supp. Data 3). The interaction between AtRBX1A and AtARIs, through the Ariadne domain, was clear in the Y2H (Fig. 12, Supp. Fig. S17-S19). However, the identification of which Cullin could be the activator of AtARIs was harder to determine. Unlike in humans, AtARIs don't seem to be activated by AtCUL1, since only a faint signal was seen in the assay compared to AtCUL3A and AtRBX1A (Fig. 12, Supp. Fig. S17-S19). This is not surprising, since AtCUL1 is phylogenetically distant from the yeast or metazoans CUL1 members and fall into a separate phylogenetic clade¹⁰⁹. Furthermore, AtCUL1 mediates phytohormone signaling⁵⁶, which is a function that is not related to their human counterpart. Much like our *ari* mutants, *Arabidopsis cul3a/b* single mutants do not display obvious growth defects compared with wild-type plants, but double mutants are embryo lethal, indicating that AtCUL3A and AtCUL3B have overlapping functions and are essential¹¹⁰. Furthermore, HHARI can also be activated by their close homologue HsCUL3¹¹¹. Taken altogether, AtRBX1A-AtCUL3A constitute a good candidate for Cullin-dependent AtARI activation. However, it needs to be further determined whether AtARIs could mediate AtCUL3A-dependent substrate ubiquitylation. This could be achieved by testing known substrates (small and globular) of AtCUL3A and check whether AtARIs could improve the ubiquitylation efficiency as described in⁴⁹.

AtPUB26, but seemingly not AtPUB25, could be another E3 candidate for AtARIs' activation (Supp. Data 3). Both AtPUB25 and AtPUB26 poly-ubiquitylate AtMYB15 and positively regulate freezing tolerance in *Arabidopsis*¹¹². It remains to be determined, whether AtARIs could mediate ubiquitylation of AtPUB26-dependent targets, such as MYB15, and check their role in freezing tolerance. This could be performed by checking the stability and ubiquitylation state of MYB15, whose degradation is enhanced in cold-stress responses, in *ari* mutants.

Another option for releasing the autoinhibition of AtARIs could be phosphorylation in the Ariadne domain. Currently, it has not been identified the kinase responsible for phosphorylating HHARI or TRIAD1, even though both are phosphorylated *in vivo* under genotoxic stress. Even though all AtARIs were ubiquitylated in their native forms, several facts point towards the possibility of this mechanism existing for AtARIs. First, the potential phosphosite serine is conserved in most of the AtARIs (AtARI1/2/3/5/7/8/9/10/11). Second, phosphomimic mutations in this serine increases the binding to AtRBX1A in Y2H (Fig. 12, Supp. Fig. S17-

S19). It has been shown that hyperactivating mutations in HHARI promote their binding to un neddylated HsRBX1—HsCUL1 and stabilizes the TRIAD1—HsRBX1—HsCUL5 complex ^{49,50}. Furthermore, this phosphomimic mutation increased the ubiquitylation and the autoubiquitylation activity of AtARI1, as well its homodimerization (Fig. 11, 13, Supp. Fig. S13-S15). Regrettably, the expression of AtARI2^{S364D} and AtARI3^{S361D} was very low and thus, the hyperactivity could not be truly assessed (Fig. 11, 13, Supp. Fig. S13-S15). Their low expression can be depicted in Supp. Fig. S27, this could be due to their higher exposed surface for protease attack. This limitation could be addressed by co-expressing these AtARIs with known interactors of Ariadne domain or Rcat, maybe AtRBX1A, thus shielding AtARIs from protease attack. Unfortunately, AtARI phosphorylation has not been identified in *in vivo* phosphoproteomics ¹¹³, since the sequence has not been covered by typical trypsin digestion. Other enzymes should be used for further studying this potential mechanism of activation under different environmental conditions (for sequence coverage, one could check each AtARI in <https://www.proteomicsdb.org>).

One striking difference between AtARIs and HHARI/TRIAD1, is the presence of a C-terminal stretch after the Ariadne domain (Fig. 9). This region could constitute an additional layer of regulation in AtARIs and could influence their activation. It remains to be determined the effect of this region in the binding of AtCUL3A, for example, and in the (auto)ubiquitylation activity.

III.3. SUMOylated eIF4E1 constitutes a putative substrate of AtARIs.

After activation, human ARIs transfer Ub to the substrate. This substrate can be presented either by a CRL or the Rcat domain in the ARIs ^{49,50,52}. Since CRL-dependent activation was not further pursued in this project, all the effort was focused on identifying CRL-independent substrates.

In eukaryotes, the initiation of the translation process is assured by at least 16 different translation initiation factors (eIFs), among which the eIF4F complex plays a key role in mediating the loading of mRNA onto ribosomes. This complex is composed of the eIF4E, eIF4G and eIF4A proteins: eIF4E is a cap-binding protein, the eIF4A helicase unwinds mRNA and the eIF4G subunit serves as a scaffold that engages in protein—protein interactions with poly(A) binding proteins (PABP1-PABP5), culminating in the recruitment of the small 40S ribosome to the mRNA ¹¹⁴. There are five members of eIF4E family in *Arabidopsis*, eIF4E1 and eIF(iso)4E constitute the canonical members, while nCBP (homologue of mammalian 4EHP), eIF4E1B (also known as eIF4E3) and eIF4E1C (also known as eIF4E2) constitute the non-canonical ones ^{93,94,115}. Several members of the initiation of translation process were identified as interactors of GST-AtARIs (Table 1, Supp. Data 3); such as PABP2, PABP4, PABP8, eIF4A1, eIF4A3, eIFiso4G1 and eIFiso4G2. Furthermore, preliminary experiments performed in the Hauser group, established that

AtARI1/2/5/7/12 interact with eIF4E1 through GAL4 Y2H assays⁹⁵. Therefore, I aimed to confirm if eIF4Es could constitute physiological substrates of AtARIs.

In vitro assays, Y2H and Pull-downs, were unsuccessful in assessing the interaction between AtARIs and eIF4Es (**Supp. Fig. S20-S21**). In contrast, *in vivo* assays (BiFC) confirmed the interaction between AtARI1/2/3 and eIF4E1/eIF(iso)4E (**Fig. 13A**). This seemingly contradicting experiments could be explained by the following. It has been shown that a mutation of HHARI residues (W386A, Y387A), important for HHARI—4EHP interaction, completely abolished complex formation on size exclusion chromatography⁵². However, the HHARI^{Y387A} mutant maintained its ability to mono-ubiquitylate 4EHP near WT levels⁵². The identification of mutants that weaken binding but are still able to ubiquitylate 4EHP is consistent with transient E3—substrate interactions and suggests that high-affinity substrate interactions are not required for HHARI-mediated ubiquitin transfer⁵². Therefore, it seems that there may be a low affinity (or transient) interaction between AtARIs and the substrate (SUMO-eIF4E1). This would explain why eIF4E1 was not enriched in Pull-down assays but still interacted in BiFC, where transient interactions can be assessed.

The di-aromatic motif W386/Y387, in HHARI, is not conserved in AtARIs; in this position a GH motif is located in the ortho-group. 4EHP residues with a strong effect in HHARI binding were not successfully identified and there are no available 3D structures of this complex⁵².

In many organisms, eIF4E availability is regulated by SUMOylation, although *in planta* data is missing¹¹⁶. Human eIF4E SUMOylation promotes the formation of the active eIF4F translation initiation complex and induces the translation of a subset of proteins that are essential for cell proliferation and preventing apoptosis. Disruption of eIF4E SUMOylation inhibits eIF4E-dependent protein translation and abrogates the oncogenic and antiapoptotic functions associated with eIF4E^{115,116}. As seen in the results, AtARIs ubiquitylated SUMO-eIF4E1 *in vitro*, but not tag-less eIF4E1, in the presence of AtUBC8 (**Fig. 13B-C, Supp. Fig. S22D**). Since the SUMO-eIF4E1~Ub species were not seen by either immunoblot nor MS/MS analysis, it is possible that multi-monoubiquitylation occurred and interfered with trypsin digestion and recognition by antibodies. Therefore, it is possible that SUMOylated eIF4E1, or even eIF(iso)4E, constitute true substrates of AtARIs, which would explain the interaction seen *in vivo*, where the required modifications could occur for either the substrates or the AtARIs. BiFC assays should be repeated in *Arabidopsis* protoplasts to further support this hypothesis. In addition, SUMO could be specifically involved in the activation of AtARIs and consequent ubiquitylation of the substrate. The specific requirements of SUMOylation in this context need to be further investigated. For instance, SUMO-eIF(iso)4E was not ubiquitylated by either AtARIs, even though they interact *in vivo* (**Fig. 13, Supp. Fig. S22**), which could

suggest that either eIF(iso)4E is not really a substrate or SUMO needs to be in a specific position ¹¹⁶ or another biological factor, such as phosphorylation ¹¹⁷, needs to be present for its recognition and efficient ubiquitylation by AtARIs. It has been shown that some human RBRs, and especially HsARIs, require allosteric activation by Ub or UBLs, such as NEDD8 in the case of HHARI ⁴⁹. It is not farfetched that SUMOylated-proteins could act as a substrate and/or allosteric activator of AtARIs.

It is also possible that AtARIs can target other members of the initiation of translation complex, such as eIF4G (and its isoforms) and eIF4EB/C or nCBP. However, further studies are needed to confirm this hypothesis and evaluate the role of AtARIs in translation, either acting as a repressor or activator when certain conditions are reached.

III.4. ARIs may have redundant functions in *Arabidopsis* and/or may be related to coping with stress.

The expression of the *AtARI* genes in *Arabidopsis* is highly variable and some of the members are induced by diverse stresses ^{75,76}. These findings are consistent with the hypothesis that tandemly duplicated genes are more frequently involved in stress responses ^{96,97}. Thus, it is likely that *AtARI* genes either have redundant functions and/or are important for specific environmental conditions ⁷⁷. Therefore, I generated CRISPR/Cas9 lines for assessing the biological role of AtARIs *in planta* (**Supp. Fig. S24**). All the obtained mutants showed no visible phenotype under normal growth conditions (long days 22°C) (**Supp. Fig. S23B**, data not shown). *AtARI7* related mutants showed a phenotype unconnected to the *AtARI7* gene mutation, it is possible that the sgRNA was not specific in this case and affected another gene. Thus, the group of *AtARI5/7/8* mutants were discarded from further analysis. The *ari1ari2* and *ari1ari2ari3* mutants were obtained via crossing much later in the project and therefore, many experiments did not include these mutants. Nevertheless, I assessed the behavior of the available mutants upon osmotic (Mannitol), salt stress (NaCl) and turnip mosaic virus (TuMV) infection (**Fig. 14B**, **Supp. Fig. S23B, S26**). All the mutants showed (including the triple mutant) a wild-type response to both abiotic stresses (**Supp. Fig. S23**).

I previously shown that eIF4E1 and eIF(iso)4E accumulate in *ari1ari2* knock-out mutants (**Fig. 14A**, **Supp. Fig. S23A**). And that it is possible that at least SUMOylated-eIF4E1 constitute a substrate of the AtARIs. All of this hints towards the regulation of eIF4Es by AtARIs, either its levels or complex formation capabilities. Inactivation of *Arabidopsis eIF4E1*, confers resistance to the potyvirus clover yellow vein virus (CIYVV) while also promotes susceptibility to another potyvirus turnip mosaic virus (TuMV) compared to Col-0 ¹¹⁴. In the case of *eIF(iso)4E*, its inactivation confers resistance to TuMV ⁹⁴. Therefore, resistance/susceptibility towards TuMV was assayed for different *ari* single and double mutants, except for *ari1ari2*. All these

mutants display regular accumulation of the virus as the wild-type Col-0. It remains to be seen, whether the mutants, where accumulation of eIF4E1 and eIF(iso)4E was seen, could respond differently towards TuMV infection. The phenotype of plants overexpressing hyperactive versions of AtARIs is yet to be assessed. This should not be restricted to virus infection and other conditions, such as other abiotic stresses, should also be assessed.

Based on the obtained results I envision two possibilities regarding the biological role of AtARIs. One, the redundancy of AtARIs goes beyond AtARI1/2/3, since it was shown that other AtARIs interacted with eIF4E1⁹⁵ and may therefore, target it for ubiquitylation. And two, they are required for a specific environmental response (e.g., drought, freezing, heat stress) that was not tested during the time available for the project. Therefore, higher order mutants must be created, for example *ari1ari2ari3ari5ari7ari12* since they all interact with eIF4E1 (Fig. 13 and⁹⁵), and further experiments should be performed in order to pin-point the biological cues that exert AtARI's function. For instance, analysis of the ubiquitome of the mutants (knockouts and overexpressing hyperactive AtARIs) could help uncover the biological role of these AtARIs. This will give us an idea of the impact of AtARIs in substrate ubiquitylation, either CRL-dependent or independent. Additionally, one should evaluate AtARI's transcripts levels, as well as protein stability, under different environmental conditions. It would be interesting to see if all AtARI1/2/3/5/7/8/9/10/11 possess RBR activity through the catalytic cysteine, and what would be the difference with the other non-cysteine AtARIs (AtARI12/13/14/15/16).

This thesis generated the foundation for the research of AtARIs. Thus, producing many open questions for the field. It would be interesting to identify other targets for AtARIs and check whether they coincide within clades. One could take advantage of the recently developed methods for identifying E3 substrates such as BioE3, which is based on site-specific biotinylation of Ub-modified substrates². This powerful approach identified both known and new targets of two human RING-type E3 ligases: HsRNF4 and HsMIB1, as well as unknown targets of HsMARCH5 and HsRNF214².

It is clear that the ubiquitin code is growing and getting more complex every year. *Arabidopsis* Ariadne RBRs seem to add another layer of complexity to this code, e.g., self-regulation through phosphorylation and autoinhibition, that must be tackled in order to fully understand it. The more we understand this code, the more we can make the most of it for applied science inventions. Many applications have been used in biotechnology, medicine and agriculture by taking advantage of the ubiquitylation cascade. For instance, PROTACs (**p**roteolysis **t**argeting **c**himeras) technology has emerged as a novel therapeutic paradigm in recent years for degrading target proteins by hijacking the UPS¹¹⁸. The PROTAC technology has attracted

significant interest from academia and industry due to its advantages and application in cancer therapy ¹¹⁹. Furthermore, E3 ligases have attracted a lot of attention in cancer therapy due to their substrate specificity, as a result, an increasing number of small molecules targeting E3 ligases have been developed and are currently under clinical trials ¹¹⁹. We could also use the ubiquitylation cascade to improve agricultural productivity, for example, it has been shown that a specific E2—E3 pair contributes to seed size control in grain crops and overexpression of the E3 improved grain yield ¹²⁰. The significant potential inherent in deciphering the ubiquitin code is evident.

The next section covers a project developed in the earlier stages of my PhD, involving the elucidation of the molecular mechanism of Spyro molecules, which were hypothesized to act as Brassinosteroids in plants.

SECTION II

I. INTRODUCTION

I.1. Brassinosteroids, an essential steroidal phytohormone family.

Brassinosteroids (BRs) constitute a phytohormone class derived from 5 α -cholestane phytosterols ¹²¹. Since the identification of the most active BR, brassinolide (BL; **Fig. 16A**), at least 70 chemically different BRs have been found throughout the plant kingdom, including land plants and green algae ¹²². This diversification of BR structure occurs mainly in the cholestane side chain and the A/B rings (**Fig. 16B**), and it's through these structural modifications that the bioactivity of BRs is finely tuned. Natural BRs bear: (I) ring A with one to three oxygen functions (red in **Fig. 16B**); (II) ring B fully saturated or with varying degree of oxidation at carbon 6 (green in **Fig. 16B**); (III) all-trans ring junctions (blue in **Fig. 16B**) and (IV) a cholestane-derived side chain with different substituents (pink in **Fig. 16B**) ^{123,124}.

BRs regulate a wide array of developmental processes such as seed germination, rhizogenesis, flowering, senescence, abscission, and maturation ¹²¹. Mutations in BR biosynthetic genes (such as *DET2* and *DWF4*) lead to distinct growth defects in *Arabidopsis*, such as dwarfism, reduced cell elongation, dark-green and thickened round-shaped leaves, reduced apical dominance, delayed flowering and senescence, male sterility, and de-etiolation in darkness (**Fig. 16C**) ¹²². These phenotypes are rescued by exogenous BL, suggesting that BRs are essential growth-promoting hormones. Endogenous amounts of BRs in plant tissues are extremely low when compared with the other plant hormones, and these levels are tightly controlled by BR signaling ¹²².

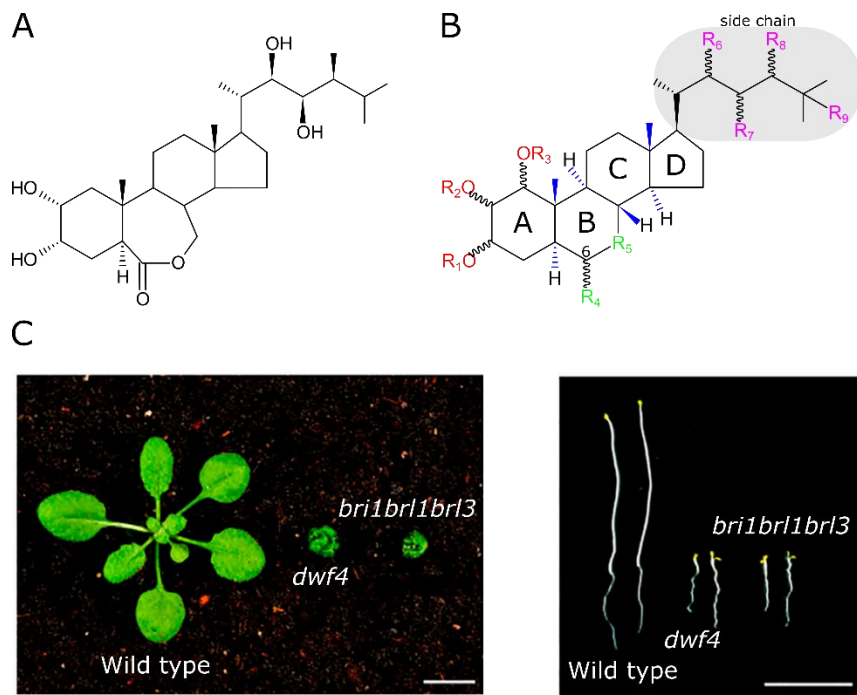


Figure 16. BRs are essential growth-promoting hormones. **A)** Chemical structure of the most active BR, brassinolide (BL). **B)** General chemical structure of the BR family, with the steroid rings labelled as A, B, C and D, with their diverse structural features colored. **C)** Phenotypes of 21-day-old *Arabidopsis* wild-type plant, the BR biosynthetic mutant *dwf4* and the BR receptor mutant *bri1bri1bri3*. The *dwf4* and *bri1bri1bri3* mutants display severe dwarfism, including small, round, and dark-green leaves (left). When grown in complete darkness for 5 days, *dwf4* and *bri1bri1bri3* show de-etiolation phenotypes with open and expanded cotyledons and short hypocotyls (right). Scale bars, 1 cm. Picture extracted from ¹²² (License number: 5704150910731).

I.2. Molecular mechanism of BRs in plants.

I.2.1. BRs Perception.

BRs are recognized outside the cell primarily by the plasma membrane receptor-like-kinase BRI1 (**BRASSINOSTEROID INSENSITIVE 1**). BRI1 consists of an extracellular leucine-rich repeat (LRR) domain (ectodomain), a single-pass transmembrane domain, and a cytoplasmic serine/threonine kinase domain. BRI1 is highly conserved across different plant species, including wheat, barley, corn, rice, and soybean ¹²⁵. In *Arabidopsis*, BRI1 has three homologues, BRL1, BRL2, and BRL3 (**BRI1-like 1, 2 and 3**, respectively). Early binding studies with a biotin-tagged photoaffinity castasterone (a biosynthetic precursor of BL) revealed that BRI1, BRL1, and BRL3, but not BRL2, bind BRs ¹²⁶. Moreover, both BRL1 and BRL3 can rescue the phenotypic defects in the *bri1* type mutant when expressed under the BRI1 promoter, indicating that BRL1 and BRL3 are functional BR receptors. Whereas BRI1 is widely expressed, BRL1 and BRL3 are mainly expressed in vascular tissues and display weak phenotypes when knocked out ^{127,128}. The *bri1bri1bri3*

mutant displays phenotypes that resemble the BR biosynthetic mutants (**Fig. 16C**) but cannot be rescued by exogenous BRs¹²².

The ectodomain of the BR receptors consist of an N-terminal signal peptide, 25 LRRs, and a 70-amino acid island domain inserted between LRR21 and LRR22¹²⁹. Structural studies demonstrated that the BRI1 ectodomain adopts a right-handed superhelix composed of the 25 LRRs^{130,131}. The island domain (cyan in **Fig. 17**) folds back into the interior of the superhelix to create a hydrophobic groove for binding BRs^{130,131}. This nonpolar cleft is lined by nonpolar aromatic and aliphatic residues (I540, I563, W564, Y599, Y642, M657, F681, I682, I706 in BRI1), whereas hydroxyl groups form the cleft ridge (Y597, Y599, Y642, S647 in BRI1). BL fits into the cleft via its nonpolar side (alkyl side chain) and displays its hydroxyl groups from rings A and B towards the solvent and protein partners (**Fig. 17**)¹³². In general, the minimal BR binding unit of BRI1 consists of 94 amino acids that comprise the island domain and the carboxy-terminal flanking LRR22¹²⁶. Residues that are important for BR binding have been revealed by solving the crystal structures of BRI1's ectodomain in complex with BL (**Fig. 17**)^{130,131}. Although most of the residues contributing to the formation of the BL binding pocket are conserved, BRL2 does not bind to BL, and BRL3 showed decreased BL binding compared to BRI1^{126,127}.

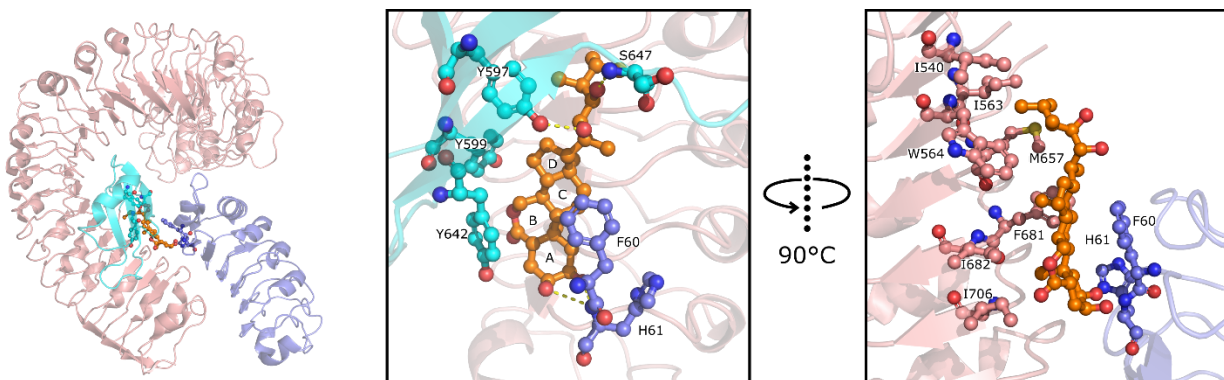


Figure 17. BL perception by BRI1 and SERK3. Alkyl side chain of BL (orange) is inserted in the hydrophobic groove created by the island domain (cyan) and the LRR core (light pink). Oxygenated species from Rings A and B are solvent exposed and interact with residues F60 and H61 from SERK3 (dark blue), while the rest of the ligand engages in an extensive interaction network with several residues of BRI1, e.g., Y642, S647, Y597 and Y599 from the island domain and I540, I563, W564, M657, F681, I682, I706 from the LRR core. Hydrogen bonds between protein residues and BL are denoted as yellow dotted lines. For better depiction, BRI1 island domain and SERK3 were omitted when possible (PDB code: 4M7E).

Upon BL binding, the island domain in the BRI1 ectodomain is stabilized and its position becomes fixed in relation to the LRR core^{130,131}, together they create a docking platform for the binding of a co-receptor protein¹²⁹. Thus, BRs act as a molecular glue by inducing heterodimerization between BRI1/BRLs and the SERK family of co-receptors (SOMATIC EMBRYOGENESIS RECEPTOR KINASES, SERK1 to SERK5)¹³⁰⁻¹³². This

family of small LRR-receptor kinases regulates plant growth, development, and immunity, and plays a critical, redundant role in BR signaling¹²⁹. Both SERK1 and SERK3 (also named BAK1), interact with BRI1—BL and the interacting residues are highly conserved among the SERK proteins, e.g., F61/H62 in SERK1 and F60/H61 (dark blue in **Fig. 17**)^{132,133}. The hydrogen bonds established between SERK1 and the two hydroxyls in ring A of BL seem to be important for BR signaling activation, as BR derivatives in which these two hydroxyls were replaced by methyl ethers¹³⁴ or acetonide¹³⁵ exhibited weakened activity¹²⁹. Muto and Todoroki suggested that the hydroxyl groups in ring A of BL play a more significant role in the interaction with SERKs than with BRI1 itself, in terms of BR bioactivity in the rice lamina joint inclination assay¹³⁵. BR-induced heterodimerization of the BRI1's and SERK3's ectodomains brings together their cytosolic kinase domains and triggers their transphosphorylation (**Fig. 18**)¹²⁹.

1.2.2. BR signaling, a simplified overview.

After BR perception at the plasma membrane by BRI1 and SERK3, a well-described phosphorylation cascade relays BR signals to BES1 (**BRI1-EMS SUPPRESSOR 1**) and BZR1 (**BRASSINAZOLE-RESISTANT 1**) family of transcription factors (TFs), which control BR-regulated gene expression¹²⁹.

When BR levels are low, BR signaling is attenuated through multiple mechanisms. The BIN2 protein (**GLYCOGEN SYNTHASE KINASE3-LIKE KINASE BRASSINOSTEROID INSENSITIVE 2**) functions as a negative regulator of BR signaling. BIN2 phosphorylates numerous substrates including BES1 and BZR1 TFs. BIN2-induced phosphorylation inactivates BES1 and BZR1 by promoting their cytoplasmic retention via 14-3-3 proteins¹³⁶, inhibiting their DNA binding activity¹³⁷, and stimulating their degradation^{129,138}. There are several other mechanisms that control the activity of BIN2 (a central hub) and BES1/BZR1, which were illustrated in a recent review about BR signaling and will not be further discussed in this thesis (**Fig. 18 left**)¹²⁹.

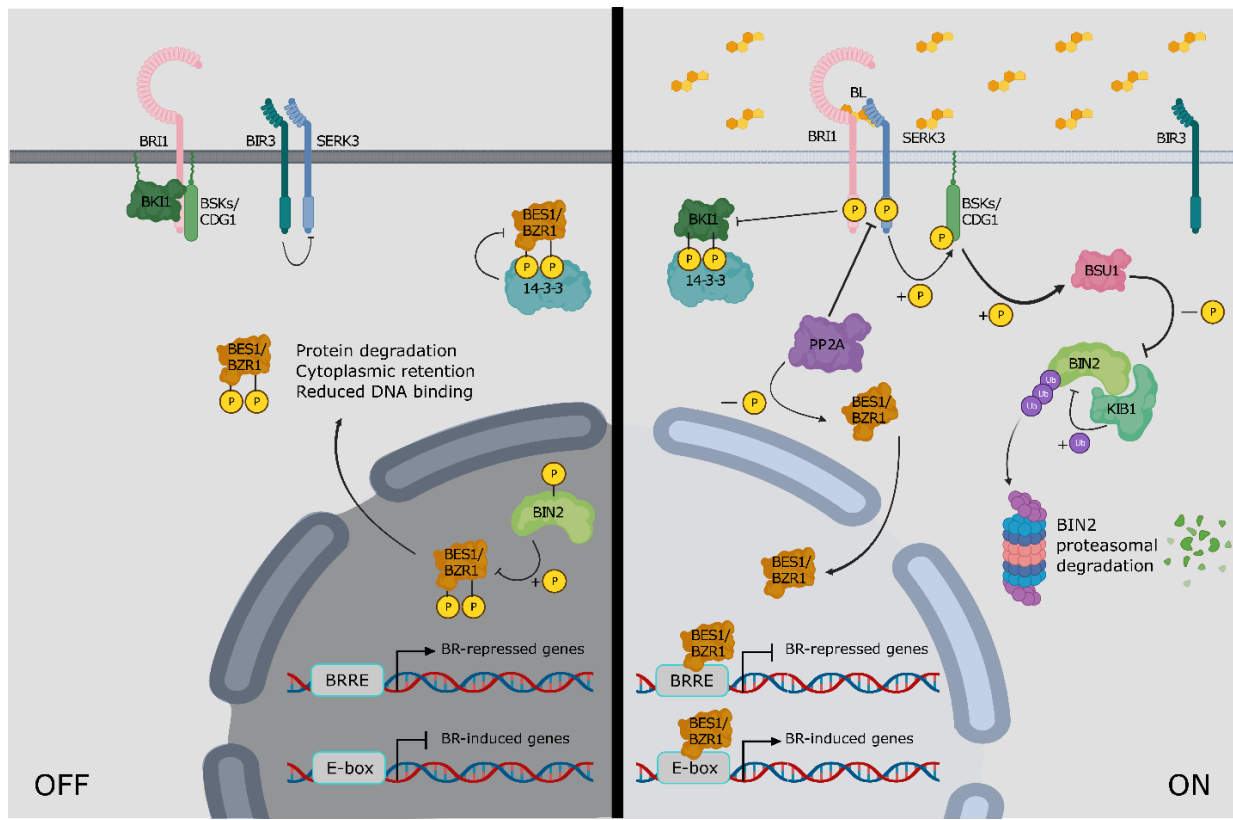


Figure 18. Simplified overview of the BR signaling pathway. When BRs are absent (**left**), plasma membrane-localized receptors BRI1 and SERK3 are inhibited by several factors, including BK11 and BIR3, respectively. Inactivated receptors allow phosphorylated BIN2 to be constitutively active and negatively regulates and phosphorylates BES1/BZR1 TFs. Phosphorylated BES1/BZR1 are inhibited through multiple mechanisms. One of these mechanisms is retention in the cytoplasm by 14-3-3 proteins. This leads to relatively low expression of BR-induced genes and higher expression of BR-repressed genes. When BRs, such as BL are present, they bind to the receptor BRI1 and co-receptor SERK3 to initiate BR signaling (**right**). BK11 and BIR3 dissociate from the receptor complex, allowing BRI1 and SERK3 to become phosphorylated and activated. Consequently, BSKs/CDGs are phosphorylated and activate in turn BSU1 phosphatase. BSU1 de-phosphorylates BIN2 and allows its ubiquitylation, mediated by KIB1, and its consequent degradation by the proteasome. In the absence of BIN2, PP2A dephosphorylates BES1 and BZR1, permitting its shuttling to the nucleus and to function with other TFs and cofactors to promote BR-induced gene expression and inhibit BR-repressed gene expression. BRRE, BR Response Element; BSU1, BRI1 SUPPRESSOR1; P, phosphorylation; Ub, ubiquitylation. Figure was created with the software BioRender (BioRender.com).

When BRs are present, the BRI1 and SERK3 receptor complex activates downstream cytoplasmic kinases BSKs (**BR SIGNALING KINASES**) and CDG1 (**CONSTITUTIVE DIFFERENTIAL GROWTH 1**) by phosphorylation. BSK3, for example, is anchored to the plasma membrane and interacts with BRI1. BSKs/CDG1 in turn phosphorylates the phosphatase BSU1 (**BRI1-SUPPRESSOR1**). This allows BSU1 to dephosphorylate BIN2, thereby inactivating it. One of the mechanisms that controls the activity of BIN2 is through its degradation by the proteasome. For this to happen, dephosphorylated BIN2 is ubiquitylated by the F-box-type E3 ubiquitin ligase KIB1 (**KINK SUPPRESSED IN BZR1-1D**). Once BIN2 is no longer repressing the TFs, the constitutively expressed PP2A (**PROTEIN PHOSPHATASE 2A**) is now free to dephosphorylate BES1 and

BZR1. As a consequence, BES1 and BZR1 become active and translocate to the nucleus to control BR-responsive gene expression (**Fig. 18**)¹²⁹.

I.2.3. *BR-responsive gene expression.*

BES1, BZR1, and the homologues BEH1-BEH4 (**BES1 HOMOLOGUE 1 to 4**) are atypical basic helix-loop-helix (bHLH) TFs that function redundantly as master regulators of BR-responsive gene expression. BRs modulate the expression levels of 5 000 to 8 000 genes, approximately half of which are induced, and the other half repressed by BRs. Both BES1 and BZR1 can either induce or repress gene expression. Comparisons of BES1 and BZR1 targets using BR-responsive transcriptome data showed that BR-induced genes are enriched in E-Box (CANNTG) binding sites, whereas BES1 and BZR1 repress gene expression by binding to BRRE (**BR Response Element**: CGTG(T/C)G) in the promoters of their target genes. BES1 and BZR1 cooperate with other TFs, histone-modifying enzymes, and transcriptional regulators to activate BR-induced gene expression (**Fig. 18**)^{129,139–141}.

I.3. Using of BR in crops.

BRs play pivotal roles in plant growth, development, and responses to adverse conditions, making them major targets for manipulation to improve agronomic traits. BR-deficient and BR-signaling mutants of dicotyledonous plant species, such as pea (*Pisum sativum*) and tomato (*Solanum lycopersicum*), as well as monocotyledonous species, present a dwarf phenotype, similarly to *Arabidopsis*¹⁴². Thus, it seems that BR biosynthetic and signaling pathways are conserved among species and could be used as an advantage in manipulating BR in crops.

Some key examples of how to boost crop yield by modifying BR biosynthesis and signaling will now follow. The erect leaf phenotype of a rice brassinosteroid-deficient mutant, *osdwarf4-1*, is associated with enhanced grain yields under conditions of dense planting, even without extra fertilizer¹⁴³. BRs also regulate inflorescence architecture, which is a key determinant of yield potential in many crops. Specifically, loss-of-function *bs/1* mutants (which encodes for a rate-limiting enzyme in BR biosynthesis) in green foxtail (*Setaria viridis*) fail to initiate a bristle identity program, resulting in homeotic conversion of bristles to spikelets and the emergence of two florets per spikelet. In *Setaria* spp, inflorescence branches terminate in either a spikelet or a sterile bristle, and these structures appear to be paired¹⁴⁴. Overexpression of *Populus trichocarpa* CYP85A3, encoding a P450 monooxygenase that catalyzes the conversion of castasterone to BL, enhanced xylem formation and wood production in poplar while the composition of cellulose and lignin and cell wall thickness was not affected, thus promoting growth and biomass in transgenic trees¹⁴⁵. BR signaling also regulates cotton (*Gossypium hirsutum*) fiber development

by modifying the expression of *GhDET2* and *GhPAG1*, the former a BR-biosynthesis gene and the latter a BR-catabolism gene^{146,147}. In grapevine (*Vitis vinifera*), sugar allocation is regulated by BRs to increase soluble sugar contents in berries, which is achieved by promoting the activities of invertases and sucrose synthase and by upregulating the expression of genes encoding the invertase, as well as the mono- and disaccharide transporters¹⁴⁸. BR treatment increases tolerance to rice blast and bacterial blight diseases in rice¹⁴⁹, to cadmium in tomato^{150,151}, and to cold-induced damage in cucumber (*Cucumis sativus*)¹⁵².

1.3.1. Development of BR-mimics for boosting crop yield.

Manipulating the expression of BR-regulated genes by mutation or overexpression often causes pleiotropic phenotypes, some of which might be undesirable for crop breeding and planting, such as changes of leaf erectness, plant height, inflorescence architecture, or biomass¹²⁹. Alternatively, exogenous application of BRs holds promise for helping crops overcome certain stresses. However, this approach is hindered by the high cost of BR organic synthesis and isolation from plants¹⁴². Therefore, a lot of effort has been focused on developing BR-mimic compounds with a lower production cost and higher activity that can boost crop yield (Fig. 19).

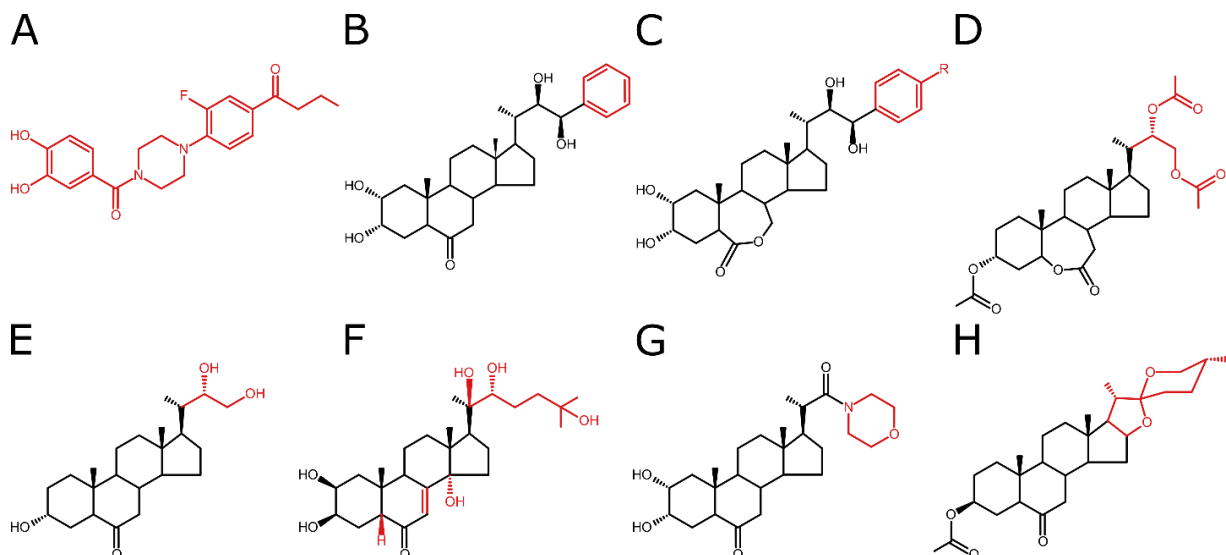


Figure 19. Synthetic compounds developed as BR-mimics. **A)** NSBR1, a non-steroidal BL agonist. Modifications to this structure improved its activity¹⁵³. **B-C)** phenyl analogues of BRs with different substituents in its aryl moiety^{154,155}. **D-E)** Norcholane dihydroxy analogues of BRs¹⁵⁶. **F)** 20-hydroxyecdysone (ECD), an ecdysteroid¹⁵⁷. **G)** BR analogues with a nitrogen-containing side chain¹⁵⁸. **H)** Laxogenin derivative, a spirostan-type of steroid¹⁵⁹. Main structural differences with BRs are highlighted in magenta.

NSBR1 (Fig. 19A) was found to be the first non-steroidal BL agonist¹⁶⁰, which was developed from BL antagonists in *Arabidopsis*. Modified NSBR1 significantly elongated the hypocotyl of *Arabidopsis*, a BR-type

response¹⁵³. However, it was not proven whether these compounds were truly BR-like compounds at the signaling level.

Aryl-brassinosteroids (**Fig. 19B-C**) were found to promote plant growth. Plant growth promoting activity was measured using the pea inhibition biotest and *Arabidopsis* root sensitivity assay; and then was compared with naturally occurring brassinosteroids. Differences in the production of the plant hormone ethylene were also observed in etiolated pea seedlings after treatment with these phenyl analogues. Nevertheless, the only test that the authors performed, in order to prove these were BR-like compounds, was molecular docking simulations. All derivatives were successfully docked into the active site of BRI1 using AutoDock Vina^{154,155}, but experimental binding confirmations were not performed.

A series of norcholane dihydroxy analogues of BRs (**Fig. 19D-E**) were obtained and tested for drought stress tolerance of *Arabidopsis*, as well as their growth-promoting activity in the Rice Lamina Inclination Test (RLIT). The results showed that one of the analogues (**Fig. 19E**) exhibited similar growth activity as BL in the RLIT bioassay. This analogue also showed a higher effect, compared to BL, in drought stress tolerance of *Arabidopsis*. Additionally, the expression of a subset of drought stress marker genes was evaluated in presence and absence of exogenously applied BRs. Results obtained by qRT-PCR analysis, indicated that transcriptional changes of *AtDREBD2A* and *AtNCED3* genes were more significant in *Arabidopsis* treated with the analogue (**Fig. 19E**) than treated with BL¹⁵⁶.

Several plant species produce ecdysteroids, which are known as insect molting steroid hormones. Thussagunpanit and collaborators¹⁵⁷ evaluated the biological activities of three hydroxyecdysteroidal compounds, ECD (**Fig. 19F**), DHECD and α -DHECD, while comparing their activities with that of BL. In rice, DHECD and α -DHECD enhanced the degree of lamina inclination, as do BRs. In *Arabidopsis*, DHECD and α -DHECD increased hypocotyl length in the wild-type, and partially overcame the hypocotyl shortening in the wild-type caused by 0.3 μ M brassinazole, a specific BR biosynthesis inhibitor. DHECD and α -DHECD partially reduced dwarfism in the BR-biosynthesis-deficient mutant *det2*. Treatment with DHECD or α -DHECD downregulated the expression of the BR biosynthesis genes *DWF4* and *CPD*, which are generally suppressed by BR, and upregulated the expression of *TCH4* and *SAUR-AC1*, which are generally promoted by BRs. However, their regulated activities were less effective than BL. In contrast, ECD did not affect rice lamina bending, *Arabidopsis* hypocotyl elongation, the expression levels of BR-related genes and BZR1 phosphorylation status¹⁵⁷.

A total of 25 new BR analogues with a nitrogen-containing side chain were synthesized and their biological activity tested on *Arabidopsis* by Diachkov and collaborators¹⁵⁸. At low concentrations, some of the

compounds (**Fig. 19G**) showed growth promoting activities. They were initially considered as BRs, based on their ability to dock to BRI1 *in silico*. However, the results of the molecular docking, which proved a favorable binding affinity, were not confirmed by *in vitro* or *in vivo* binding experiments ¹⁵⁸.

Another group of molecules, considered as BR-like compounds, are the spirostan-derived steroids (**Fig. 19H**) ^{159,161–164}. These compounds are typically part of steroidal saponins (glycosylated steroids) and are mainly considered as secondary metabolites. However, it has been shown that spirostanic steroids derived from laxogenin (un-glycosylated) possess plant growth-promoting activity in the radish hypocotyl elongation and cotyledon expansion bioassay (**Fig. 19H**) ¹⁵⁹.

I.4. Preliminary data.

In an attempt to reduce the cost of BR synthesis, and increase their stability when applied, spirostanic steroids (*Spyros*) were developed by our collaborator CNPR at Havana University (See *Supplementary Materials and Methods*). These naturally derived non-cholestane steroids, such as DI-31 (or BB16) ¹⁶⁵, have been used as bio-stimulants to increase crop yield. Many of the Spyros exhibited growth stimulation properties in agricultural field experiments of peach, corn, cabbage, beans, coffee, cacao, garlic, potato ¹⁶⁶, onion, rice, pepper ¹⁶⁷, tomato ¹⁶⁸, endive ¹⁶⁹, to name a few (**Fig. 20**). Most recently, DI-31 has been shown to induce a defense response in strawberry plants against avirulent isolate (M11) of *Colletotrichum acutatum*, to exert a protective effect against *Botrytis cinerea* and to enhance the tolerance to abiotic stresses such as salt stress ^{161–163}. Furthermore, this compound promoted growth and plants treated with it yielded fruits with lower acidity, and higher content of soluble solids ¹⁶². This compound also enhanced drought response in *Arabidopsis* ¹⁶⁴.

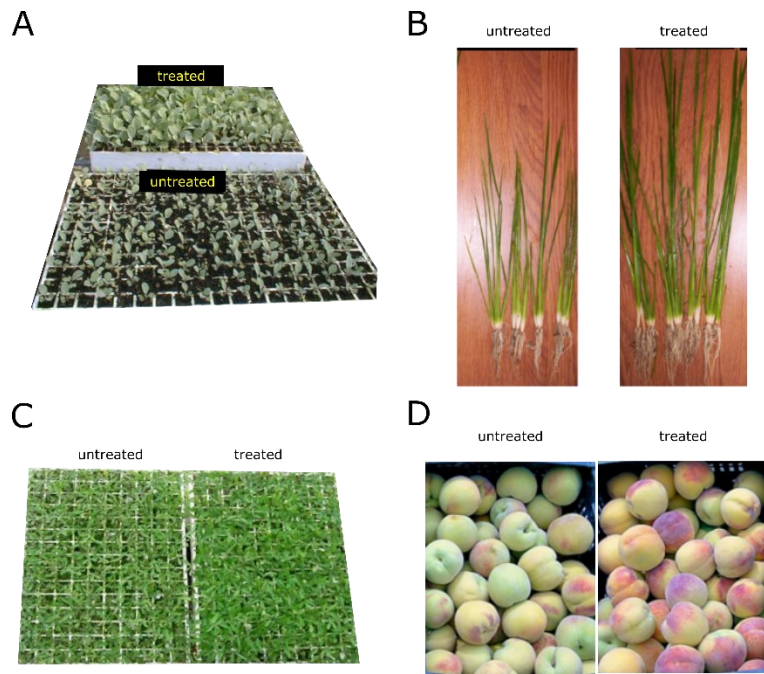


Figure 20. Exogenous application of DI-31 (a Spyro) synthesized at CNPR. A) Cabbage B) Tomato C) Rice D) Peach. Exogenous application was performed by 30 min seed soaking (A, B) and leaf spraying (C, D) from water supplemented with DI-31; 250 nM (A, B) and 30 nM (C, D) (Unpublished agricultural field experiments).

I.5. Aims and objectives.

While the effects of these Spyros have been extensively assessed in agricultural fields (Fig. 20), seldom do we know how they really work. Understanding the mechanisms by which compounds regulate plant responses represents an important direction for boosting crop yield by further derivatization. Previously, I employed molecular docking simulations between 20 synthetic steroids and the ectodomain of BRI1, to identify BR-like active compounds ¹⁷⁰. Three of them were synthesized at CNPR from the plant saponin diosgenin (See *Supplementary Methods*). Thus, my doctoral studies aim at investigating the biological and biochemical effects of the synthesized Spyros: DI-31, MH-5 and DG-15, in the model plant *Arabidopsis*. In frame of my dissertation, the following questions and approaches were designed:

Objective I. What is the phenotypic effect of Spyros?

To fully understand the molecular mechanism of Spyros, *Arabidopsis thaliana* was used as a model plant. First, we must establish the effects that these Spyros have on *Arabidopsis* and other model plants grown in controlled conditions (Greenhouses and Phytochambers). Therefore, I will perform phenotypic assays on *Nicotiana benthamiana*, *Solanum lycopersicum* and *Arabidopsis thaliana*, thus establishing a method of application to be further used.

Objective II. Do Spyros activate BR-dependent signaling?

Once the phenotypic effect is established in *Arabidopsis*, we must link it to a molecular effect. Based on agricultural field experiments and literature search, these compounds were predicted to be BR analogues. Therefore, I will test whether Spyros would activate BR-dependent signaling. There are three general layers of the BR-signaling pathway that can be assessed: I) perception, II) TF activation and translocation to the nucleus and III) expression of BR-marker genes. I will assess whether Spyros can be perceived by BR receptors and consequently promote BZR1/BES1 translocation to the nucleus, which would promote the expression of e.g., *BAS1*. I will use LexA Y2H, SUS and molecular dynamic simulations to evaluate Spyros perception. I will use confocal fluorescence microscopy to analyze the levels of BZR1-YFP, under the BZR1 promoter, in the nucleus/cytoplasm upon Spyro treatment. Finally, I will perform qRT-PCR to check whether Spyros can upregulate *BAS1* and *SAUR-AC1*. Furthermore, I will also evaluate whether Spyros could rescue BR-deficient mutants.

Objective III. What is the molecular mechanism of Spyros?

In order to confirm or disprove our initial hypothesis, I will evaluate the overall molecular effect of Spyros on *Arabidopsis*. Therefore, I will use an omics approach to assess the effect of Spyros on gene expression and whether they bind to proteins to exert their function. For this, I will perform RNAseq of *Arabidopsis* treated plants. Additionally, I will do a photoaffinity crosslinking assay and subsequent LC-MS/MS. One of the Spyros would be coupled to a biotin and a photoreactable moiety (diazirine) via organic synthesis. This compound will be incubated with plant lysate, and upon UV-A photoactivation, the diazirine will react with proximal carboxyl groups ¹⁷¹ from proteins that are bound to the Spyro-biotin. The modified proteins will be enriched using streptavidin-affinity chromatography and identified using LC-MS/MS.

II. RESULTS

II.1. Phenotypic effect of Spyros in Plants.

Three steroid compounds derived from diosgenin were synthesized at the CNPR (Center of Natural Products Research) in Havana University. These compounds were named DI-31, MH-5 and DG-15 and their integrity was confirmed with high resolution mass spectrometry (**Supp. Fig. S28**). Since their lateral chain corresponds to a spirostan structure, these compounds were named *Spyros*. Their effect was evaluated on different plant species, namely *Solanum lycopersicum* (data not shown), *Nicotiana benthamiana* and *Arabidopsis thaliana*, and compared to the effects of a known growth-promoting brassinosteroid phytohormone (eBL) (**Fig. 21**). eBL is a synthetic stereoisomer of BL and it is relatively more effective ¹⁵⁶.

DI-31 promoted growth of *N. benthamiana* adult plants, resulting in increased height (**Fig. 21A**), more branches, greener and bigger leaves and delayed senescence (**Supp. Fig. S29**, data not shown). This effect was more pronounced at higher concentrations (**Fig. 21A-B**). Additionally, this compound increased seed production, since the total seed dry weight was higher (**Fig. 21B**), while maintaining the same seed area (**Supp. Fig. S30A**) compared to mock treated plants. However, neither DI-31 nor MH-5 had any growth effect on *N. benthamiana* seedlings when grown on media supplemented with these compounds (**Supp. Fig. S30B-C**). Both hypocotyl (in dark grown seedlings) and root length (in light grown seedlings) showed no significant difference compared to mock treated seedlings (**Supp. Fig. S30B-C**). As a control, eBL inhibited both root and hypocotyl growth at the evaluated concentration (**Supp. Fig. S30B-C**).

The effect of DI-31 on *Solanum lycopersicum* was also analyzed. This compound increased stem height after the first treatment (data not shown). However, due to space limitations in the greenhouse, these plants were discarded, and the experiment discontinued.

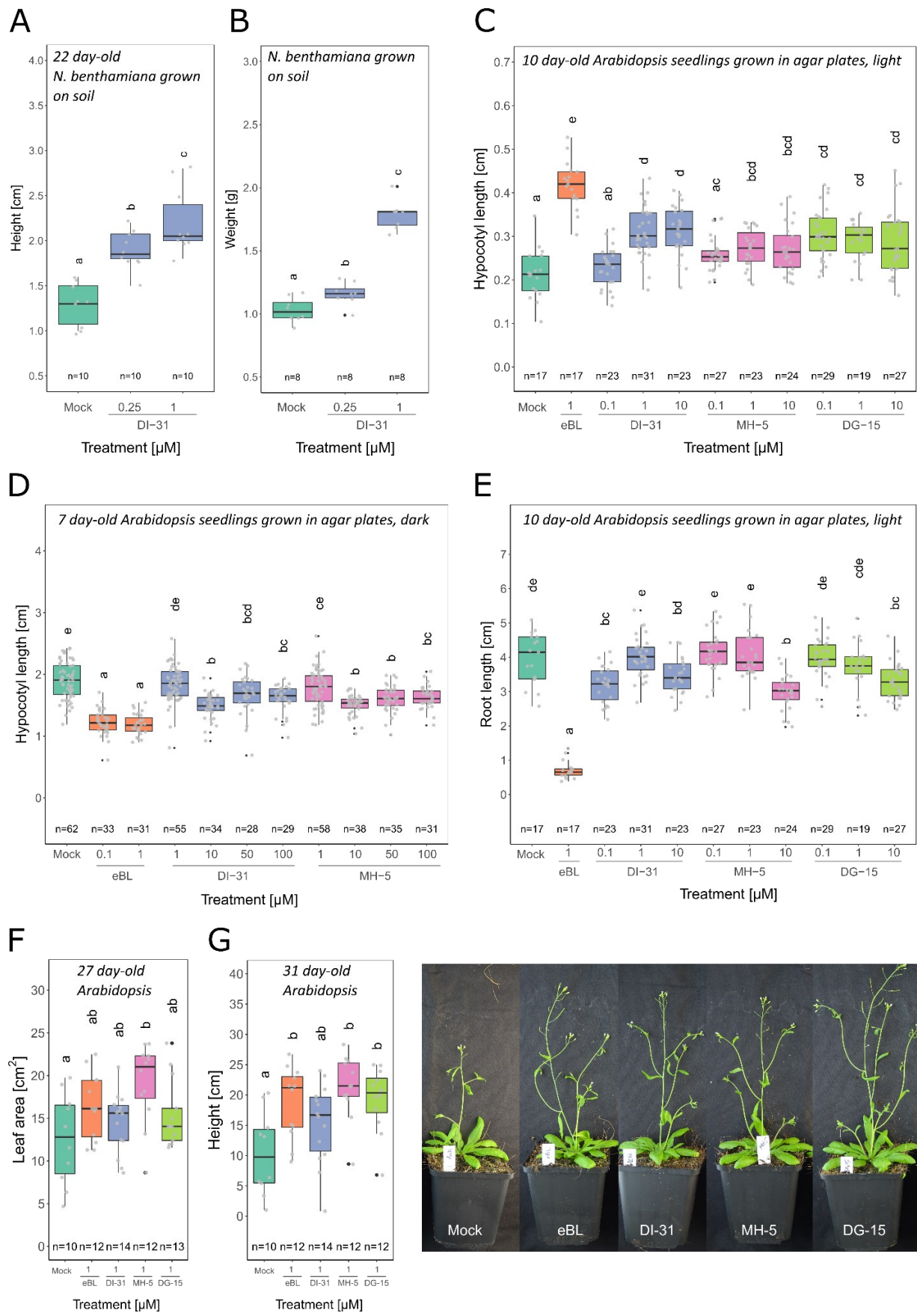


Figure 21. Spyros promote growth in different plant species. **A-B**) DI-31 was exogenously applied (foliar application) to *Nicotiana benthamiana* grown on soil every 21 days. **A)** Stem height of *N. benthamiana*, one day after first treatment. **B)** Total seed weight of eight treated *N. benthamiana* plants. **C-E)** *Arabidopsis* seedlings were grown on media supplemented with Spyros or eBL. **C)** Hypocotyl length of 10-day-old *Arabidopsis* grown in the light. **D)** Hypocotyl length of 7-day-old *Arabidopsis* grown in the dark. **E)** Root length of 10-day-old *Arabidopsis* grown in the light. **F-H)** Spyros or eBL were exogenously applied (foliar application) to *Arabidopsis* plants grown on soil. **F)** Leaf area of 27-day-old *Arabidopsis*, four days after second treatment. **G)** Stem height of 31-day-old *Arabidopsis*, two days after third treatment. One way ANOVA and Tukey Test was performed for all measurements.

The effect of Spyros was further evaluated in *Arabidopsis*. *Arabidopsis* seedlings were grown on media supplemented with either Spyro, eBL or mock and grown for up to 10 days in the light or in the dark. The hypocotyl and root length were measured after 7 and 10 days. After 7 days of growing in the light, the hypocotyl length of *Arabidopsis* seedlings treated with eBL robustly increased, as expected ¹⁷². However, all Spyro-treated seedlings either had a mild increase in hypocotyl length or none at all (Fig. 21C). This effect was slightly more pronounced at higher concentrations, in the case of DI-31. A similar behavior was observed for the hypocotyl length (in dark grown seedlings) and root length (in light grown seedlings). In this case, eBL robustly inhibited hypocotyl and root growth of *Arabidopsis* seedlings, while Spyros had a mild effect at different concentrations, depending on the compound (Fig. 21D-E). In the case of root length after 7 days of growing in the dark, there was no effect for the Spyro-treated seedlings; in contrast to eBL-treated ones, where root length was diminished (Supp. Fig. S30D). Moderate to overaccumulation of BR-hormone concentrations promote curliness of *Arabidopsis* root/hypocotyl growth ^{173,174}, which was observed for eBL- but not for Spyro-treated seedlings. Interestingly, most of the Spyros promoted growth of adult *Arabidopsis* plants (Fig. 21G, Supp. Fig. S30E-F). MH-5 increased the leaf area of 27-day-old *Arabidopsis*, while all increased stem height of ~30-day-old *Arabidopsis* (Fig. 21F-G, Supp. Fig. S30E-F). It seems that Spyros have a growth effect on adult plants, while having little to no effect on seedlings.

II.2. Mode of action of Spyros.

In order to evaluate if Spyros constitute putative BR analogues, BR-deficient mutant (*det2-1*) was treated with Spyros. The *det2-1* plant mutants have a short stature and dark-green leaves at the seedling stage ¹⁷⁵. As expected, eBL alleviated the growth defect of *det2-1*, exemplified by their root length (Fig. 22A). In contrast, Spyros had no effect on the root length of this mutant (Fig. 22A).

Next, it was evaluated whether Spyros upregulated BR-marker genes *BAS1* and *SAUR-AC1* via quantitative real-time PCR (qRT-PCR). *BAS1* is a gene of the BR catabolism, while *SAUR-AC1* is an early auxin-inducible gene, their expression is upregulated by BRs ¹⁷⁶. While eBL induces almost a 2-fold increase for *BAS1* and ~3-fold increase for *SAUR-AC1* expression, MH5 and DI-31 did not trigger changes in *BAS1* expression (Fig.

22B, Supp. Fig. S31). Interestingly, MH-5 promoted *SAUR-AC1* downregulation, although to a minor extent, while DI-31 did not trigger any changes (Fig. 22B).

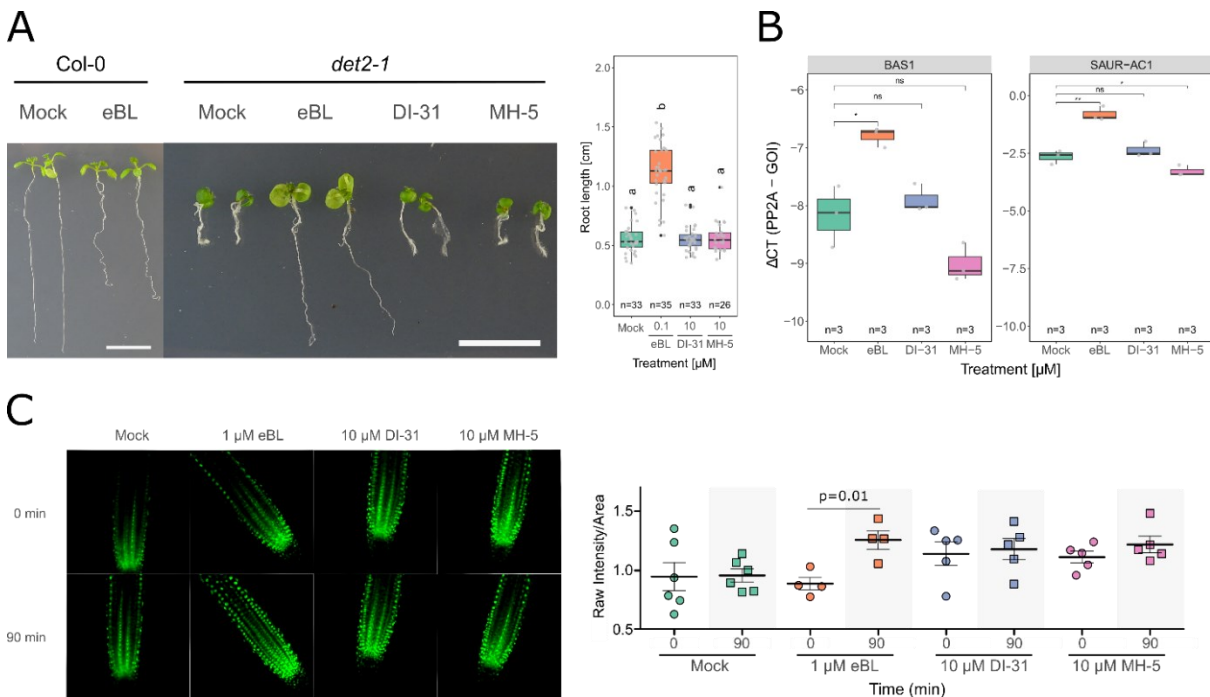


Figure 22. Spyros do not act as typical BR. **A)** Rescue of 7-day-old *det2-1*, three days after treatment with 100 nM of eBL or 10 μ M of DI-31/MH-5. Bar represents 1 cm. The root lengths were measured and statistically compared with one-way ANOVA and Tukey test. **B)** *BAS1* and *SAUR-AC1* expression in 25-day-old *det2-1* plants grown on soil. Plugged-out-whole plants were treated for 4 hours in liquid media containing either DI-31 (1 μ M), MH-5 (1 μ M), eBL (1 μ M) or mock prior sampling (n=3, each biological replicate represents one plant). A t-test was performed against mock-treated plants for each gene (*p = 0.001 and **p ~ 0.04). **C)** Confocal imaging and quantification of *BZR1p::BZR1-YFP* in the middle longitudinal root section of 5-day-old seedlings treated for 90 min in liquid media with either DI-31 (10 μ M), MH-5 (10 μ M), eBL (1 μ M) or mock. Seedlings were imaged using LSM700 (Plan-Neofluar 20x) using 488/518 filters/emission. Paired two-tailed t-test was performed for each treatment at time 0 and 90 minutes.

To address whether Spyros directly impact BR signal transduction, it was evaluated the translocation of the BR-responsive *BZR1* transcription factor to the nucleus of primary root cells. *Arabidopsis* transgenic seedlings expressing a translational fusion of *BZR1* with yellow fluorescence protein (YFP) under the endogenous *BZR1* promoter (*BZR1p::BZR1-YFP*) were treated with eBL and imaged. *BZR1* pools are detected in the cytoplasm as well as in the nucleus, but a rise in intracellular BR levels, triggers *BZR1* rapidly shuttling to the nucleus to activate/repress BR-responsive genes. **Figure 22C** shows *BZR1* re-localization to the nucleus after 90 min of eBL treatment, with also an expansion of *BZR1* signal towards cortex and endodermis root cells (Fig. 22C). Our assays indicate that DI-31 and MH-5 did not affect *BZR1* expression pattern (Fig. 22C), which suggests these compounds do not function as functional analogues of eBL for *BZR1* re-localization under the conditions tested.

To address whether Spyros directly impact BR perception, it was assessed the ligand induced heterodimerization of BR-receptors and co-receptor. I performed LexA Y2H and SUS assays between the ectodomains of BRI1/BRL1/BRL2/BRL3 (receptors) and SERK3 (co-receptor) upon Spyro treatment of mated yeast. Unfortunately, the experimental setup in all cases was not suited to elicit a BR specific response (eBL control). In the Y2H, no interaction was seen (absence of blue color), while in SUS, yeast treated with the BR-specific positive control (eBL) did not grow (**Supp. Fig. S32-S33**).

MD simulations allow us to have a structural detail on the time-dependent behavior of protein—protein complexes and evaluate their binding energies. Here, 20 ns MD simulations were performed five times for BL and Spyros bound to BRI1—SERK3 and BRI1. The initial structure was obtained through docking simulations. There are several mechanistic features that explain the substantial difference in biological activity between BRs. First would be the low binding energy itself, second would be ability to form hydrogen-bond interactions with specific residues in the island domain of BRI1 (e.g., S647), third would be overall stabilization and conformational re-structuring of the island domain, and fourth would be related to nonproductive binding states ¹⁷⁷. Out of the four identified features, I was able to evaluate the first three (**Fig. 23A-B, Table 3**).

In order to fully understand the formation of the BRI1—steroid—SERK3 complexes, it was evaluated the binding of the steroids (Spyros or BL) to BRI1 and then, the binding of SERK3 to the preformed binary complex BRI1—steroid. Here, the LIE (Linear Interaction Energy) method was used to obtain the binding energies of the binary and ternary complexes. The LIE method has been applied mainly to protein-ligand binding complexes to calculate absolute and relative binding affinities ^{178–180}. In the case of protein—protein interfaces, this method can also calculate the binding affinity by considering crucial binding residues as a small ligand ^{178–180}. Considering that only a few amino-acid residues from SERK3 are engaged in binding to BRI1—BL ^{131,132,181,182}, two residues were selected from SERK3 as the ligand, for the calculation of the binding free energy in the ternary complex (BRI1—steroid—SERK3). Both SERK3^{F60} and SERK3^{H61} are in close contact with BL and BRI1 and are possibly the mayor contributors to the formation of the ternary complex. Furthermore, the SERK3^{F60A} mutation completely disrupts binding of SERK3 to BRI1—BL, suggesting its essential role in the complex formation ¹⁸¹. Thus, when calculating the ligand-dependent parameter, β , I used Spyros/BL as the “ligand” in the binary complex (BRI1—steroid) and SERK3^{F60-H61} as the “ligand” in the ternary complex (BRI1—steroid—SERK3). Where $\beta = 0.37$ for all steroids and $\beta = 0.402$ for SERK3^{F60-H61}. The α coefficient was scaled in order to obtain the most similar energy to the reported BRI1—BL—SERK3 and BRI1—BL binding energies ¹⁸¹; where $\alpha = 0.21$ in the case of BRI1—steroid and $\alpha = 0.41$ in the case of BRI1—steroid—SERK3. The γ term was calculated according to the LIE-D

parametrization¹⁸³. Theoretical binding free energy (ΔG_{calc}) values for each complex were obtained by LIE method using the coefficients α , β and γ , electrostatic and van der Waals energies (**Table 3**). The experimental binding energy (ΔG_{exp}) was obtained for BRI1—BL—SERK3 and BRI1—BL using the equation stated in **Table 3**. According to the results, all the Spyros presented higher binding energies in both BRI1—steroid and BRI1—steroid—SERK3 complexes (**Table 3**). This can be translated to a lower affinity of the Spyros towards BRI1, and of SERK3 towards the previously formed BRI1—Spyro complexes; compared to BL containing complexes.

Table 3. Calculation of binding energy and its components for the complexes during 100 ns MD simulation (five times 20 ns simulations). Electrostatic (V^{el}) and van der Waals interactions (V^{vdw}), D parameter, γ coefficient, experimental (ΔG_{exp}), and theoretical free binding energy (ΔG_{calc}) for the complexes are shown.

Complex	$\Delta\langle V_{l-s}^{el} \rangle + \Delta\langle V_{l-l}^{el} \rangle$ (kcal/mol)	$\Delta\langle V_{l-s}^{vdw} \rangle$ (kcal/mol)	D^a (kcal/mol)	γ^b (kcal/mol)	ΔG_{calc} (kcal/mol)	ΔG_{exp} (kcal/mol) ^c
BRI1—BL	4.88	-22.71	6.57	-8.30	-11.27	-11.29
BRI1—MH-5	9.61	-17.44	7.22	-8.92	-9.02	-
BRI1—DI-31	7.06	-15.96	5.96	-7.72	-8.46	-
BRI1—DG-15	9.27	-12.18	5.99	-7.75	-6.87	-
BRI1—BL—SERK3	9.46	-9.12	7.54	-9.23	-9.16	-8.72(GCI) -9.50(ITC)
BRI1—MH-5—SERK3	8.82	-7.87	6.77	-8.50	-8.18	-
BRI1—DI-31—SERK3	6.17	-4.98	4.52	-6.35	-5.91	-
BRI1—DG-15—SERK3	6.48	-4.47	4.43	-6.27	-5.50	-

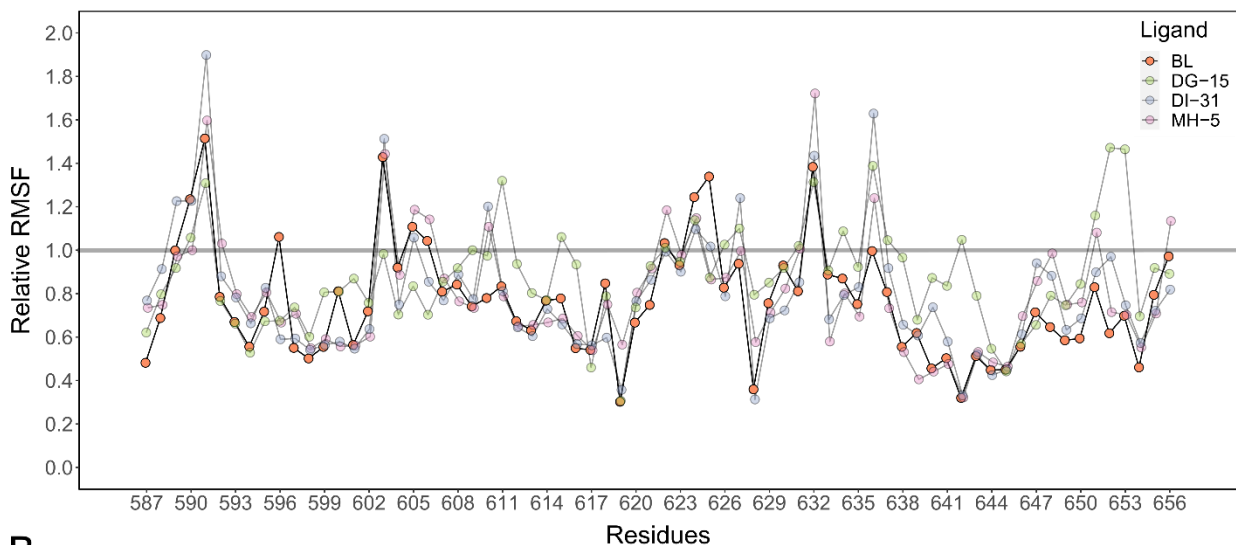
^a Calculated using the LIE-D parametrization model from¹⁸³.

^b Calculated using the equation $\gamma = -0.95D - 2.06$ from the LIE-D parametrization model from¹⁸³.

^c Calculated using the approximation $\Delta G_{exp} = RT * \ln K_D$, where the K_D values were obtained from¹⁸¹ through different methods: Grating-Coupled Interferometry (GCI) and Isothermal Titration Calorimetry (ITC).

Additionally, I evaluated the effect of BL/Spyros upon the conformational re-arrangement of the island domain of BRI1 in the BRI1—steroid simulations. I compared the relative RMSF (root mean square fluctuations) of residues within the island domain upon binding of BL or Spyros. The RMSF of residues are computed after the alignment of atomic coordinates in each trajectory step to a reference structure (initial structure). An RMSF of lower than 1 refers to a stabilized residue, the lower the value the more stabilized (less mobile) it is. In most cases, BL achieved a stabilization of most residues within the island domain. This stabilization was more prominent than all the Spyros, especially for residues 635-656 (**Fig. 23A**).

A



B

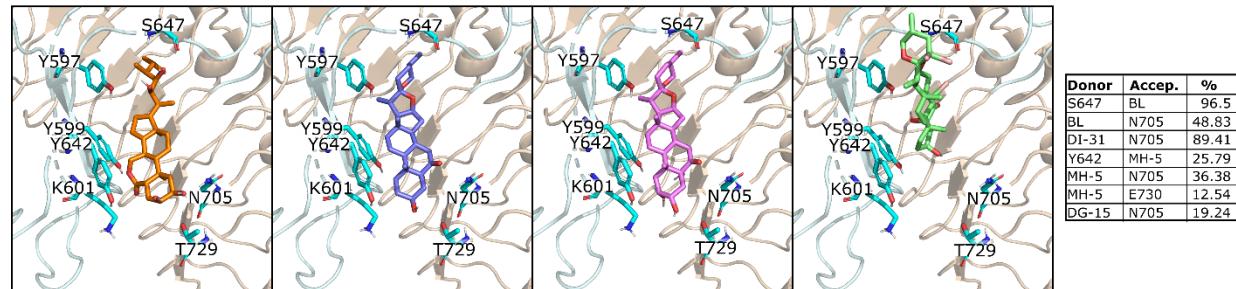


Figure 23. Spyros do not seem to bind BRI1 like a typical BR. A) RMSF of residues from BRI1's island domain in the BRI1—steroid simulation. BRI1 without a steroid (mock) was not included for better depiction. In every case, presence of steroid stabilized the island domain compared to BRI1 alone. RMSF was calculated using the initial structure as reference. B) Interaction interface between the steroids and BRI1. Prevalence of hydrogen bonds in percentage between BRI1 and the steroids, right.

Lastly, I evaluated the hydrogen-bond interaction network when a steroid was bound to BRI1. When BL is present, it sustains a hydrogen bond with S647 for 98 % of the entire simulation, and with N705 for approximately half the simulation (Fig. 23B). In contrast, there was no hydrogen bond between S647 and any of the Spyros. This residue does not seem to be conserved among the BRLs: BRL1^{M632}, BRL2^{L604} and BRL1^{M632}; based on the alignment with PDB and alpha fold structures (PDB 4J0M: BRL1, alpha fold Q9ZPS9: BRL2, alpha fold Q9LJF3: BRL3). The interaction with N705 was maintained with varying degrees (19-89 %) (Fig. 23B). Additional hydrogen bonds were established for MH-5 with other residues of the island domain, Y642 and E730 (Fig. 23B). All Spyros, except DG-15, maintained a stable binding pose within the complex. This is based on the distance fluctuation between the steroids and key residues of the binding site (S647, Y599) (Supp. Fig. S34). Taken altogether, it seems that either Spyros might have a lower activity than BL or none at all.

II.3. Do Spyros constitute a new class of growth regulators?

Based on the afore mentioned results a clear mode of action for Spyros could not be described and therefore, it does not seem that Spyros act like typical BRs. Therefore, I went for a much wider approach, transcriptomics and proteomics. In order to evaluate how Spyros influence gene expression, 25-day-old *Arabidopsis* rosettes were sprayed with 10 µM Spyros (except for DG-15, 2 µM) or mock (DMSO). RNA was extracted after 4 hours, and RNAseq was carried out. All Spyros promoted expression and activation of specific genes (**Fig. 24A-C**), and the effect on gene expression was different for each Spyro with only 63 differentially expressed genes in common (**Fig. 24B**). I further analyzed the most upregulated and downregulated genes after Spyro treatment (based on relative expression values) via Genevestigator™ (**Supp. Fig. S35A**). In line with our previous results, Spyros promoted gene expression differently than natural BRs, and seem to have specific effect on the transcriptome, based on the enriched GO terms (**Fig. 24A**). Genes from circadian rhythm, rhythmic processes and photosynthesis were highly enriched in all Spyro samples (**Fig. 24A**). This might be related to their effect on growth on adult plants. However, the more strikingly results are related to defense genes. It seems that these compounds may have more effect in protecting the plant from fungus, bacteria, and abiotic stresses, based on the enriched GO terms (**Fig. 24A**). Further experiments are required to test their effect on plant immune response.

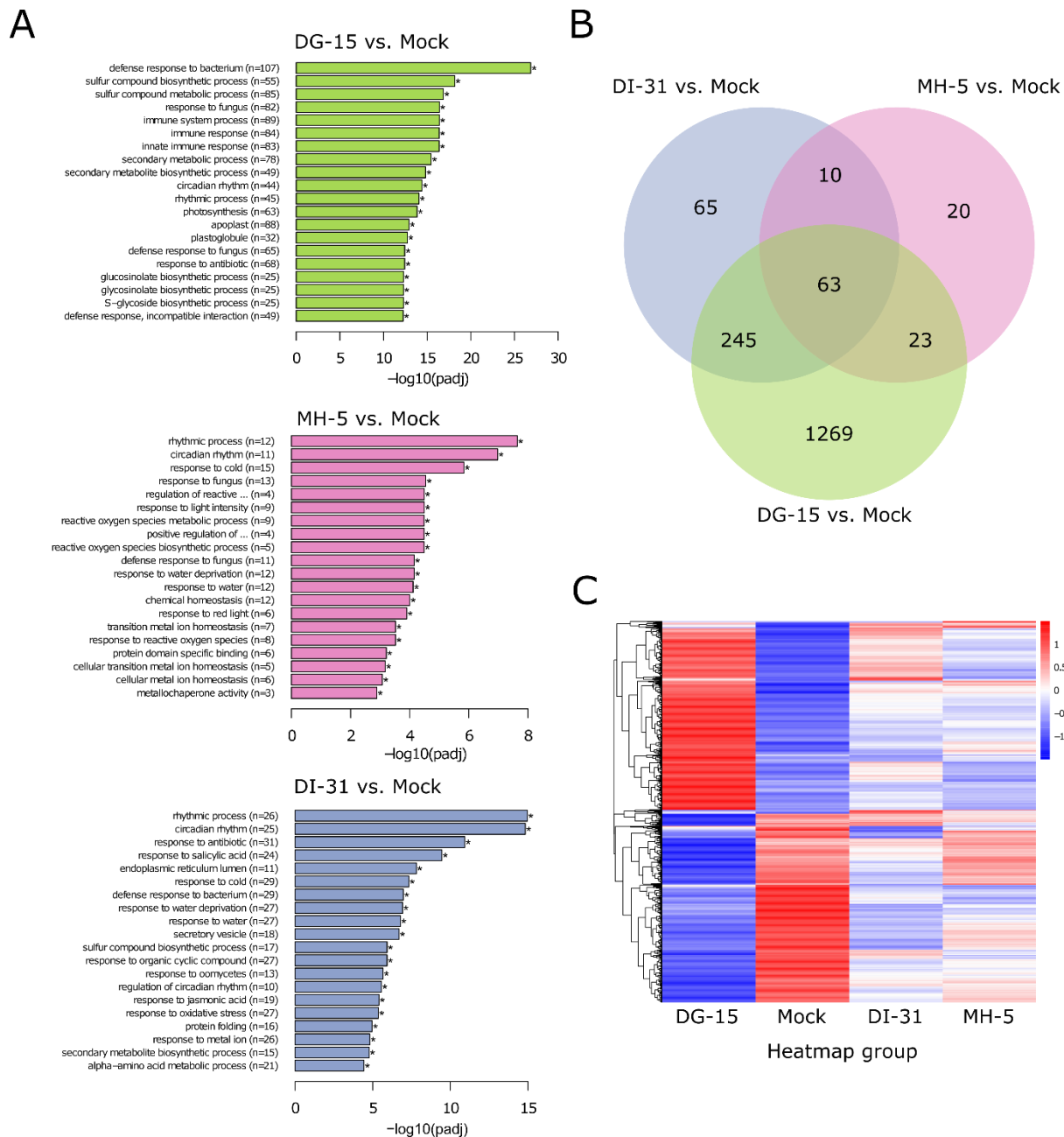


Figure 24. Effect of Spyros on gene expression on *A. thaliana*. A) GO terms enrichment upon Spyro treatment. B) Venn diagram of the differentially expressed genes between mock and Spyro treatment, overlapping area indicates the number of differential genes shared between the groups. C) Hierarchical clustering heatmap of each biological replicate treated with Spyros or mock. Genes within the same cluster show the same trends in expression levels under different conditions.

In order to elucidate the mechanism by which Spyros promote gene expression, I used a proteomics approach to identify which proteins recognize and bind Spyros in *Arabidopsis*. I performed a photoaffinity crosslinking and LC-MS/MS for capturing Spyros-binding proteins. Researchers at the Bioorganic Chemistry department at the IPB chemically synthesized a compound that comprised a photoreactive diazirine, DI-31 and biotin joined by a linker (See *Supplementary Methods*, Supp. Fig. S35B). In collaboration with the

Laboratory of Andrea Sinz at the Martin Luther University (MLU)-Halle (Saale), I performed the photoaffinity assay. The *in-house* produced Spyro-biotin derivative was immobilized in Streptavidin magnetic beads. Afterwards, *Arabidopsis* lysates (2 mg/mL proteins from 7-day-old seedlings) were incubated with the immobilized Spyro, and UV-A light was applied to the final mixture. After washing out the unbound fraction, the putative protein binders were digested with trypsin and further identified using LC-MS/MS. Several putative Spyros-binders that are membrane-localized proteins were identified incl. uclacyanin-2 (O80517), nitrilase 3 (P46010), RPP1C (Q8LEQ0), CML27 (Q9LE22), PDE334 (Q42139) and MSBP2 (Q9M2Z4), a homologue of the latter has been shown to bind several steroids *in vitro*¹⁸⁴. In line with our previous results, none of the BR receptors were identified in this experiment. Further analyses would be required to confirm these findings, and to identify the cognate Spyro receptor(s).

III. DISCUSSION AND FUTURE PERSPECTIVES

III.1. Spyros, a non-classical BR or a new growth-promoting steroid?

Many steroid-derived compounds have been classified as BR-analogues, due to their effect on plant growth/defense and their resemblance to the natural hormones. However, most of the performed research never went deep enough to test whether these compounds were truly BRs^{154–159,164}. The ability to bind *in silico* to BRI1 receptors or the Rice Lamina Inclination Test, were in most cases the only experiments supporting this statement. In this thesis, I aimed to determine if three spirostanic steroids named Spyros where truly BR-analogues, as previously expected^{164,170}.

These compounds had a mild effect on growth on *Arabidopsis* seedlings compared to eBL (an active synthetic BR) (Fig. 21, Supp. Fig. S30). Moreover, Spyros did not induce the typical curliness response in roots that BRs promote^{173,174}. Unlike eBL, these molecules were not able to rescue the BR-deficient *det2-1* and did not promote the translocation to the nucleus of BZR1 nor the upregulation of *BAS1* and *SAUR-AC1* (Fig. 22). When analyzing closely the complexes formed by BRI1—Spyro and BRI1—Spyro—SERK3 via MD simulations, one can notice certain features that are not shared with BL bound complexes. These features include the stabilization of the island domain, the hydrogen bond network within the binding pocket and the binding energy. In all cases, Spyros were not able to mimic the behavior of BL when bound to the receptors (Fig. 23). Even though Spyros promote a BR-like effect on adult plants, they do not seem to constitute classical BRs, which translates to *molecules capable of activating BRI1 and subsequently the BR-signaling pathway*. It is possible though, that these Spyros either constitute a new class of growth-promoting steroids or non-BRI1 binding BRs, here referred to as non-classical BRs. BRL1 and BRL3 encode membrane-localized receptors able to bind BL with high affinity^{127,185}. However, the binding of BL to these

receptors differs among BRLs. Residues within the binding pocket are not conserved between BRI1 and BRLs, such as BRI1^{S647} which is a M632 in BRL1 and BRL3, and L604 in BRL2. When BL is present, it sustains a hydrogen bond with S647 for 98% of the entire simulation, which was absent in the BRI1—Spyro simulations (Fig. 23B). Other island domain residues involved in the binding are BRI1^{Y597}, BRI1^{Y599} and BRI1^{Y642}, all conserved as Phe and Tyr in BRL1, BRL3 and BRL2, except for BRL2^{M557}. BRL2^{M557} is orientated towards the BRL2 core, where the side chain of BL would locate (if binding where possible).

The main structural difference between BL and the Spyros lies in the side chain, where BL possesses a di-hydroxy cholestan (with high rotational freedom) and Spyros, a spirostan (bulkier, with restricted rotational freedom), as seen in the MD simulations of free steroids (Supp. Fig. S36). It is possible that BRL2 would allow to fit Spyros due to these differences with the BR-receptors. The change of BRI1^{S647} (polar) to BRL2^{L604} (non-polar) could change the chemical environment for a better interaction with the side chain, from a hydrogen bond (not present in BRI1—Spyros) to possibly van der Waals interactions. A change of BRI1^{Y597} (bulky) to BRL2^{M557} (small), would allow a better fit for the bulkier Spyros.

In the case of the residues located in the core, most seem to be conserved among BRI1 and the BRLs with two exceptions. Residue BRI1^{M657} (non-polar) changes to BRL2^{E614} (negatively charged), while keeping the same environment in BRL1^{I642} (non-polar) and BRL3^{I642} (non-polar). It was proposed that this substitution to E614 (in BRL2) might interfere with the BL binding by changing the hydrophobicity of this region ¹⁸². It remains to be determined the effect it would have on Spyros. Additionally, BRI1^{F681} (non-polar aromatic) changes to BRL2^{Q638} (polar), BRL1^{Q666} (polar), BRL3^{Q666} (polar). Although this change would not contribute to prevent BR binding since both BRL1 and BRL3 can bind BL.

The expression of the BRL1 and BRL3 genes under the BRI1 promoter reverts the phenotypic defects in the *bri1* mutant, demonstrating that both BRL1 and BRL3 are functional BR receptor genes ^{127,185}. Whereas BRI1 is widely expressed, BRL1 and BRL3 are mainly expressed in vascular tissues and display weak phenotypes when knocked out ¹²². Thus, BRI1 pathway operates in most cells to promote growth, while BRL receptor signaling operates under specific spatiotemporal constraints. Despite a wealth of information on the BRI1 pathway, data on specific BRL pathways and their biological relevance is just starting to emerge ¹⁸⁶. Therefore, we should consider the possibility that Spyros may activate specifically BRLs and not BRI1. Thus, behaving as a non-classical BR, a research venue that has not been consider so far.

Neither BRLs were identified in the XL-MS/MS, however, this experiment was performed on 7-day-old seedlings where the effect of the Spyros was minimal. This experiment was repeated later with older plants. Unfortunately, no proteins were identified due to the chemical instability of the crosslinker. This

type of assay has been previously used for confirming BRI1 binding to castasterone ¹²⁶. Here a biotin-tagged photoaffinity castasterone (BPCS) was incubated with the immunoprecipitate from 500 seedlings (5 days old) of transgenic *Arabidopsis* plants overexpressing BRI1-GFP or 5 µg of purified recombinant GST fusion protein. The authors successfully obtained BRI1-GFP as well as GST-BRL1 and GST-BRL3 upon incubation with BPCS, confirming that this assay is suitable for assessing BR-receptor specific interaction ¹²⁶.

Further experiments are required to test whether Spyros could bind and activate BRLs. Since BRI1 is widely expressed, one could transform plants with the coding sequence of BRLs under the BRI1 promoter, to elicit a wider expression of BRLs, and evaluate plant response towards Spyros. This is considering that Spyros would act as agonists of BL but considering that the pathway of BRLs is understudied it is also possible that Spyros could act as antagonists. Binding assays could be also performed using purified proteins (from insect cells) and ITC/GCI assays, as performed for BRI1^{ectodomain}—BL in the Hothorn Laboratory ¹⁸¹. Further collaboration would be needed to pursue this research avenue. Further optimization of the SUS protocol could also be performed using the ectodomains of the BRI1/BRLs and SERK3. However, besides in this thesis, the ectodomains of these proteins has never been used in this type of assay. Only full-length BRI1 and SERK5 has been successfully used in SUS, due to the BR-independent interaction of their kinase domains ¹⁸⁷. The failing of both Y2H and SUS assays does not seem to be related to the uptake of steroids in yeast. Muddana and collaborators, produce recombinant yeast expressing YFP fused to the ligand binding domains of human steroid-receptors, such as estrogens, androgens and glucocorticoids ¹⁸⁸. Recombinant yeast treated with cognate steroid-receptor ligands exhibited dose-dependent fluorescence enhancements that were correlated with known relative receptor binding affinity values ¹⁸⁸.

Another scenario is that Spyros bind to other proteins. Based on preliminary photoaffinity XL assay, DI-31-derived-crosslinker was bound to MSBP2 (Q9M2Z4). MSBP2 (**m**embrane **s**teroid-**b**inding **p**rotein **2**) is a close homologue of MSBP1, the latter has been shown to bind several steroids *in vitro*, such as eBL ^{184,189}. It was demonstrated that both MSBP1 and MSBP2 serve as a scaffold to physically organize monolignol P450 monooxygenases on the Endoplasmic Reticulum (ER) membrane, thereby regulating the lignin biosynthetic process ¹⁸⁹. Most recently, MSBP2 was identified as a MAMP-responsive plasma membrane-associated protein (**m**icrobe-**a**ssociated **m**olecular **p**atterns) in *Arabidopsis* ¹⁹⁰. MSBP2 constitutes a good candidate for “perceiving” Spyros. However, further studies are required to confirm this hypothesis and to evaluate the implications of a complex formation. The role of MSBP2 in *Arabidopsis* is clearly under discussion.

This thesis generated many questions and opened a new research avenue regarding novel growth promoters. There are many possibilities regarding their molecular mechanism. Given the different effects of Spyros on gene expression it is possible that they bind to different receptors, possibly homologues, like MSBP1/MSBP2 or the BRLs. Thus, eliciting a different signaling pathway and subsequent gene expression.

I would recommend performing and optimizing XL-MS assays with the different Spyros and using lysate from adult plants: WT and transgenic for either overexpression or knock-outs of *BRLs/MSBPs*. If Spyros constitute non-canonical BRs, it could contribute to identify the detailed molecular basis for the differences in BR-binding and BR-signaling among BRI1 and BRLs. If Spyros bind to other proteins, they could constitute a new class of growth promoters. The identified receptor could be used for further studies in crops. For instance, engineering crop varieties with increased crop yield and resistance.

MATERIALS AND METHODS

Table 4. Key resources.

Reagent or resource	Source
<i>Bacterial strains</i>	
<i>Agrobacterium tumefaciens</i> GV3101	in house
<i>Escherichia coli</i> BL21-AI	in house
<i>Escherichia coli</i> TOP10	in house
<i>Chemicals, Peptides, and Recombinant Proteins/Enzymes</i>	
2xYT-Medium	Roth
ATP	Sigma
b-mercaptoethanol	Roth
BP Clonase	Thermo Fisher
cOmplete EDTA free Protease Inhibitor	Roche
CSM, Double Drop-Out -Leu, -Trp	Formedium
CSM, Double Drop-Out -Trp, -Ura	Formedium
CSM, Multiple Drop-Out -Ade, -His, -Leu, -Met, -Trp	Formedium
CSM, Multiple Drop-Out -Ade, -His, -Leu, -Met, -Trp, -Ura	Formedium
CSM, Quadruple Drop-Out -Leu, -Met, -Trp, -Ura	Formedium
CSM, Single Drop-Out -Leu	Formedium
CSM, Triple Drop-Out -Leu, -Trp, -Ura	Formedium
D(+) Glucose	Merck
D(+) Galactose	Roth
Difco Yeast Nitrogen Base w/o Amino Acids	BD (Otto Nordwald)
D-Mannitol	Merck
DMSO	Serva
DpnI FD restriction enzyme	Thermo Fisher
D-Raffinose	Vako
DreamTaq Green PCR Master Mix (2X)	Thermo Fisher
Dropout without His	Clontech
Dropout without His/Trp/Ura	Clontech
Dropout without His/Ura	Clontech
Dropout without Trp	Clontech
Dropout without Ura	Clontech
DTT	Aplichem
EcoRI restriction enzyme	Thermo Fisher
Epibrassinolide	Sigma
Fast SYBR™ Green Master Mix	Thermo Fisher
Fluorescein-labeled Ubiquitin	MoBiTec Molecular Biotechnology
HEPES	Sigma
L-Arabinose	Sigma
Leupeptin	Sigma

L-Methionine	Sigma
LR Clonase	Thermo Fisher
Lysozyme, from Chicken Egg White	Sigma
MES	Roth
Milkpowder	Roth
Murashige and Skoog (MS) Plant Medium	Duchefa
Na ₂ HPO ₄	Merck
NaCl	Roth
NaH ₂ PO ₄	Merck
NotI FD restriction enzyme	Thermo Fisher
Phenylmethylsulfonylfluorid (PMSF)	Roth
Phire Green Hot Start II DNA Polymerase	Thermo Fisher
Phusion High-Fidelity PCR Master Mix with HF Buffer	Thermo Fisher
Plant Agar	Duchefa
Polyethyleneglycol 4000	Merck
SDS	Roth
Sucrose	Merck
T4 DNA ligase	Promega
TRIS	Roth
X-GAL	Roth
Xhol FD restriction enzyme	Thermo Fisher
XmaI restriction enzyme	Thermo Fisher
Yeast Extract	Duchefa
<i>Critical Commercial Assays</i>	
ExoSAP	Thermo Fisher
NucleoSnap Plasmid Midi kit for plasmid DNA	Marcheray & Nagel
NucleoSpin Plasmid, Mini kit for plasmid DNA	Marcheray & Nagel
NucleoSpin RNA Plant, Mini kit for RNA from plant	Marcheray & Nagel
NucleoSpin Gel and PCR CleanUp	Marcheray & Nagel
<i>Experimental Organisms</i>	
<i>Arabidopsis thaliana: BZR1p::BZR1-YFP</i>	Dr. Marcel Quint
<i>Arabidopsis thaliana: det2-1</i>	Dr. Marcel Quint
<i>ari1</i>	This study
<i>ari2</i>	This study
<i>ari3</i>	This study
<i>ari1ari2</i>	This study
<i>ari2ari3</i>	This study
<i>ari3ari1</i>	This study
<i>ari5</i>	This study
<i>ari7</i>	This study
<i>ari8</i>	This study
<i>ari5ari7</i>	This study

<i>ari7ari8</i>	This study
<i>ari8ari5</i>	This study
<i>eif4e1</i>	Dr. Jean-Luc Gallois ⁹⁴
<i>eifiso4e</i>	Dr. Jean-Luc Gallois ⁹⁴
<i>Primers</i>	
Table S1	
<i>Recombinant DNA (plasmids)</i>	
Table S2	

Molecular docking simulation.

Steroid data set.

The steroids examined in the present study included brassinolide (BL) and three synthetic spirostan-derived steroids (Spyros): DG-15, DI-31 and MH-5 (**Supp. Fig. S28**). The structure of BL was obtained from the RCSB protein data bank (<http://www.rcsb.org>) with PDB code 4M7E¹³³. Spyros were constructed in Avogadro 1.1.1¹⁹¹, using as a template the Diosgenin structure available at PubChem (<https://pubchem.ncbi.nlm.nih.gov>), and optimized using Steepest Descent algorithm and MMFF94 force-field¹⁹². All hydrogen atoms were added at this point. All chemical representations were performed using ChemDraw 20.0 (<https://revvitysignals.com/>) or ChemSketch 2023.1.2 (<http://www.acdlabs.com>) packages.

Ligand/Protein preparation.

BRI1—SERK3 3D structure resolved by X-ray diffraction (PDB code: 4M7E resolution, R= 3.6 Å)¹³³ was downloaded from PDB database (<http://www.rcsb.org>). All final PDB files were converted to PDBQT format in order to perform molecular docking simulations. All partial charges were calculated using the Gasteiger model. Non-polar hydrogen atoms were merged to the heavy atoms. In the ligands' case, rotatable bonds were set to default using the TORSDOF utility in AutoDockTools¹⁹³. The residues' side chains of Y597(A), Y599(A), Y642(A), F681(A), F60(C) and H61(C) (de-protonated) from the protein's active site, were considered as flexible, where (A) corresponds to BRI1 and (C) to SERK3. A simulation box of size 25 × 25 × 25 Å³ was constructed so that it could include the ligands and protein's flexible residues. The center of the simulation box was placed at the center of the active site.

BRI1-steroid-SERK3 simulation and analysis.

Semi-flexible docking simulations were performed using AutoDock Vina 1.1.2¹⁹⁴. Docking parameters were set to default, with the exception of *exhaustiveness* = 32. The best docked conformation was analyzed from 10 independent runs. Docked conformations were grouped according to an RMSD (root mean square deviation) threshold of 1.0 Å and the mean binding free energy of each cluster was calculated. This way,

the group with the highest number of conformations and lowest binding free energy was selected as the representative binding mode for each complex ¹⁹⁵. These 3D structures were represented using PyMOL™ 2.5.5 ¹⁹⁶. For each steroid, the BRI1 (with and without SERK3) receptor structure with the best-scoring pose was selected as the initial conformation for the molecular dynamic simulation as described below.

Molecular dynamic (MD) simulation.

Preparation of starting structures for energy minimization and molecular dynamics simulations.

Steroids' parameters were obtained from the Generalized AMBER force-field (GAFF) ¹⁹⁷. The partial atomic charges for the steroid's atoms were calculated using the RESP protocol ¹⁹⁸ implemented in antechamber ^{199,200} from Amber18 package ²⁰¹. Electrostatic potential calculations were performed with B3LYP/6-31G(d) level using Gaussian09 ²⁰².

Before MD simulations several modifications were made to the proteins. First, missing residues were modeled ²⁰³ through the WHAT IF Web (<https://swift.cmbi.umcn.nl/servers/html/index.html>). Second, the protonation state of ionizable residues of the proteins, including the crystal structure (PDB code: 4M7E), were determined at pH = 5 and AMBER forcefield with the server PDB2PQR (<https://server.poissonboltzmann.org/pdb2pqr>), which uses PROPKA for the prediction of pKa values ²⁰⁴.

The parameters corresponding to BRI1 and SERK3 were generated with AMBER99SB force-field ²⁰⁵. We added all hydrogen atoms to the starting structure using the protonation states predicted before. Then, a cubic solvation box was created around the system, with a 10 Å distance from the solute surface and the box walls. Water molecules were added, using TIP3P explicit solvation model, and periodic boundary conditions (PBC) were settled in the limits of the solvation box. Electro-neutrality was guaranteed by adding Na⁺ and Cl⁻ ions into the unit cells at an appropriate ratio to reach final NaCl concentrations of 0.05 mol/L.

Energy minimization and molecular dynamic simulations.

The protocol employed here to perform MD simulations involves prior EM and position-restrained equilibration, as outlined by Lindahl for lysozyme in water ²⁰⁶. The systems were subjected to 50 000 steps of steepest descents minimization with a step size of 0.01 nm ²⁰⁷. The maximum tolerance was set to 1000 kJ*mol⁻¹*nm⁻¹ while cutoff radii of 1.2 nm were established for the calculation of both van der Waals and short-range electrostatic interactions. The Particle Mesh Ewald algorithm was used to handle long-range electrostatic interactions ^{208,209}. The Verlet cutoff-scheme was used, as well as the potential modifier Potential-shift-Verlet for both coulomb and van der Waals interactions. Bond lengths were left unconstrained during EM. Next, the solvent was equilibrated around the system for 300 ps, using position

restraint dynamics, with force constant of 1000 $\text{kJ} \cdot \text{mol}^{-1} \cdot \text{nm}^{-2}$ and 4180 $\text{kJ} \cdot \text{mol}^{-1} \cdot \text{nm}^{-2}$ to all the heavy atoms of BRI1, SERK3 and steroids, respectively. Cutoff radii of 1.2 nm were established for the calculation of van der Waals and electrostatic interactions. Again, the Verlet cutoff-scheme was used, as well as the potential modifier Potential-shift-Verlet for both coulomb and van der Waals interactions. The Newton's equation of motion was solved using the leap-frog integrator ²¹⁰, with a time step of $\Delta t = 2 \text{ fs}$ for a total time of 300 ps (150,000 integration steps). The system was simulated at constant temperature and pressure of 310 K and 1 atm, respectively. In order to accomplish this, we used the Berendsen algorithm ²¹¹ for the pressure and Velocity rescaling ²¹² for the temperature, with time constant (τ) of 3 ps and 0.1 ps, respectively ²⁰⁷. Bond lengths were constrained by the Linear Constraints Solver algorithm ²¹³. Random initial velocities were assigned to each atom prior to the MD simulations, obeying the Maxwell-Boltzmann distribution from 50 K to 310 K ²⁰⁷.

Once the system was equilibrated, we proceeded to the productive dynamic simulation without position restraint ²¹⁴ for 20 ns; in the case of BRI1, SERK3, BRI1—SERK3, BRI1—steroid and BRI1—steroid—SERK3 complexes; and 5 ns, in the case of free steroid. The system simulation was carried out at $T = 310 \text{ K}$ and $p = 1 \text{ atm}$. The Parrinello-Rahman coupling algorithm ^{215,216} was used to keep pressure constant with a time constant (τ) of 1 ps ²⁰⁷. The temperature, non-bonded interaction and time step were controlled or set up similarly as in the equilibration run. The snapshots of all runs were saved each 10 ps. All simulations and the analysis of the resulting trajectories were performed with GROMACS v4.6.5 package ²¹⁷.

Structural analysis of BRI1-steroid-SERK3 complexes.

RMSF (root mean square fluctuation) values for the residues of the island domain of BRI1, were calculated for the entire simulation using the *g_rmsf* program (GROMACS v4.6.5). RMSF corresponds to the standard deviation of atomic positions of a residue in the trajectory compared to a reference frame (time 0 ns). The minimum distance fluctuation was calculated between residues Y599/S647 from BRI1 and steroids during the entire simulation using the *gmx pairdist* program (GROMACS v2018.1). The obtained values were analyzed using the EnvStats R package ^{218–220}.

Hydrogen bonds within the BRI1—steroid—SERK3 complexes were calculated using the *g_hbond* program (GROMACS v4.6.5), based on the following geometrical criteria: i) a distance of 3.5 Å between the donor and the acceptor and ii) an acceptor-donor-hydrogen angle of $\leq 30^\circ$. Time stability of hydrogen bonds was also assessed during MD simulations using *hbmap2grace* ²²¹.

Binding free energy calculation of BRI1-steroid-SERK3 and BRI1-steroid complexes using LIE method.

The Linear Interaction Energy (LIE) equation, for the estimation of binding free energy based on force-field averaged energies, can be written as ^{178,222}:

$$\Delta G_{bind} = \beta(\Delta\langle V_{l-s}^{el} \rangle + \Delta\langle V_{l-l}^{el} \rangle) + \alpha\Delta\langle V_{l-s}^{vdw} \rangle + \gamma \quad (1)$$

With this equation one can calculate the binding free energy by averaging the ligand-surrounding potential energies. Also, β is a scaling factor, which depends on the chemical nature of the ligand, on the basis of free energies of solvation estimated with the FEP method (β_{FEP}) for more than 200 chemical groups ¹⁷⁸. Furthermore, α is a non-polar scaling factor empirically estimated ²²² and γ is an offset parameter that can be estimated using the LIE-D model ¹⁸³.

The interaction energies of BRI1-steroid-SERK3 and BRI1-steroid complexes were calculated with *g_energy* from GROMACS v4.6.5 ²¹⁷. These values were used to calculate the binding free energy using the LIE-D model from ¹⁸³, which uses *Eq 1*. For each ligand, the β coefficient was calculated as β_{FEP} according to the parametrization model E proposed by ¹⁷⁸ from the equation:

$$\beta_{FEP} = \beta_0 + \frac{\sum_i w_i \Delta \beta_i}{\sum_i w_i} \quad (2)$$

where w_i , β_0 , and $\Delta \beta_i$ were calculated using FEP simulations (**Table 5**). In this model $w_i = 1$ was employed as weight for neutral functional groups ¹⁷⁸.

Table 5. Optimized β coefficients according to the parametrization model E from ¹⁷⁸

β_0	0.43
$\Delta \beta_1$ (<i>alcohols</i>)	-0.06
$\Delta \beta_2$ (1,2 – <i>amines</i>)	-0.04
$\Delta \beta_3$ (1 – <i>amides</i>)	-0.02
$\Delta \beta_4$ (<i>COOH</i>)	-0.03
$\Delta \beta_5$ (<i>anions</i>)	0.02
$\Delta \beta_6$ (<i>cations</i>)	0.09
$\Delta \beta_7$ (<i>others</i>)	0

In this study, we have two types of complexes, one where the ligand is a steroid (Spyros and BL) in the BRI1—steroid complexes, and another where the ligand is a small protein (SERK3) in the BRI1—steroid—SERK3 complexes. In the case of BRI1—steroid complexes, the β coefficient was equal to 0.37 for all the ligands (Spyros), while the α coefficient was set to 0.21, similarly to previous works where this coefficient is set to 0.18 ^{223,224}.

Several studies of ligand binding ^{223,224} have determined that a value of 0.18 for α adequately reproduces the free energies of binding for a variety of ligand-protein systems. In those systems the ligands were

primarily of druglike character, particularly their size. The standard LIE model used to study small drug-like ligand binding to proteins is not suitable for protein—protein interactions¹⁷⁸, or in this case protein-ligand-protein interactions. Protein—protein interfaces are usually composed of hot spots where a few residues make up for almost all the binding energy²²⁵. The interface between SERK3 and BRI1—BL is composed of essential residues. In the case of SERK3, residues F60 and H61 are vital for binding¹⁸¹. Mutation of F60 and/or H61 to Ala completely disrupts binding of SERK3 to BRI1—BL, suggesting that interactions between co-receptor and steroid hormone are critical for receptor—co-receptor complex formation¹⁸¹. Another way to calculate binding energies for protein—protein complexes is possible. Instead of absolute binding energies, one can calculate the relative binding energy for some of the hot spot residues. Although this approach cannot give the absolute binding energies, relative energies are useful to examine the difference in affinity of SERK3 to similar BRI1—steroid. In the case of BRI1—steroid—SERK3 complexes, the β coefficient was equal to 0.402 considering F60 and H61 from SERK3 as the ligand, while the α coefficient was optimized to 0.41, in order to accurately reproduced binding experimental results from BRI1-BL-SERK3¹⁸¹.

The D parameter (*Eq 3*) was used for the calculation of the γ coefficient in both types of complexes using the equation $\gamma = -0.95D - 2.06$, from the LIE-D parametrization model from¹⁸³.

$$D = \beta(\Delta\langle V_{l-s}^{el} \rangle + \Delta\langle V_{l-l}^{el} \rangle) - \alpha\Delta\langle V_{l-s}^{vdw} \rangle \text{ [kcal/mol]} \quad (3)$$

The $\Delta\langle V_{l-s}^{el} \rangle$ and $\Delta\langle V_{l-l}^{el} \rangle$ values in *Eq 1* and *Eq 3* were calculated from the trajectories generated for each complex and free steroid, employing the Reaction-Field-zero algorithm²²⁶. The $\Delta\langle V_{l-s}^{vdw} \rangle$ value was calculated using the Shift function combined with the Lennard-Jones potential²²⁶ with a cutoff radius of 10 Å.

Experimental binding free energy calculation of BRI1—BL and BRI1—BL—SERK3 complexes.

The affinity between a molecular target (such as proteins) and its ligand, can be evaluated as the binding free energy (*Eq 4*):

$$\Delta G_{exp} = RT * \ln K_D \quad (4)$$

where R is the universal gas constant, T is the absolute temperature [K] and K_D represents the equilibrium constant for the protein-ligand association process.

Spyro treatment *in planta*.

Wild-type or mutant *Arabidopsis thaliana* (in Col-0 background) seeds were surface sterilized and stratified for 2-4 days at 4 °C in the dark. Seeds were directly sowed in half-strength Murashige and Skoog growth medium (½ MS) with 1% sucrose and 1% plant agar. Seedlings were grown in vertical plates at 22 °C either in the dark or under long day (LD) conditions (16 h light, 8 h dark) and 90 µE/m²/s of light for up to 10 days. Dark treatment was achieved by wrapping the plates with 2 layers of aluminum foil. For seedling treatment, ½ MS was supplemented with either DMSO, eBL or Spyro at different concentrations. Hypocotyl and root length was traced for several days, measured using ImageJ 1.53t (<https://imagej.net/ij/>). The BR deficient mutant *det2-1* and the *BZR1p::BZR1-YFP* transgenic line were donated by the Quint lab (<https://quintlab.landw.uni-halle.de/>).

For adult treatment, *Arabidopsis* seeds were sowed directly on soil (CL clay coir steam-sterilized + Floragard vermiculite) and stratified for 2 days at 4°C in the dark. Seedlings were grown for 18 days under LD conditions as stated before. In the case of *Nicotiana benthamiana* and *Solanum lycopersicum*, they were grown in Special Substrate: SP Topf 11-01800 from Patzer Erden, Day: 23-24°C, 55-75% humidity and Night: 22-24°C, 55-75% humidity. Spyros, eBL or mock were applied to leaves until dripping (foliar application) once a week for Col-0 and every 21 days for *N. benthamiana* and *S. lycopersicum*, always early in the morning. Solutions were prepared by diluting the steroid (2 mM in DMSO) or an equal amount of DMSO (mock) in 500 mL tap water achieving a final concentration of 1 µM or 0.25 µM. Leaf area was calculated from plant photographs using Easy-Leaf-Area (<https://github.com/heaslon/Easy-Leaf-Area>)²²⁷. Stem/plant height was measured using a measuring tape from the base of the stem (at the soil surface) to the highest part of the plant (tip of the apical bud). Seed area was calculated from microscopy pictures of Col-0 or *N. benthamiana* seeds (Leica M165 FC stereomicroscope fitted with a Leica MC170 HD camera) using the Analyze Particles option (size = 0-Infinity and circularity = 0 - 1.00) in ImageJ 1.53t (<https://imagej.net/ij/>). Seed weight was measure using an analytical scale. All graphs and statistical analyses were performed using R package^{218,218,220}.

Growth conditions of *ari* mutants and wild-type.

Wild-type or mutant *Arabidopsis thaliana* (in Col-0 background) seeds were surface sterilized and stratified for 2-4 days at 4 °C in the dark. Seeds were directly sowed in half-strength Murashige and Skoog growth medium (½ MS) with 1% sucrose and 1% plant agar. Seedlings were grown in vertical plates at 22 °C under long day (LD) conditions (16 h light, 8 h dark) and 90 µE/m²/s of light. After 7-10 days, plants were transferred to soil when required.

CRISPR/Cas9 construct design and vectors.

All constructs were generated via Golden-Gate cloning (GG-cloning) with the syntax of the modular cloning system^{228,229}. Primers and constructs used can be found in the supporting information. Cas9 single guide RNAs (sgRNAs) were designed according to²³⁰, whereas the flip extension sgRNA scaffold and the *Arabidopsis* U6-26 t67 terminator were used as template for PCR-based sgRNA amplification²³¹⁻²³³. Purified sgRNA-t67 PCR products were assembled with pU6 Level 0 modules to obtain a transcriptional unit for sgRNA expression. Level 1 position 2 module containing *Arabidopsis* Rps5a promoter, Cas9 (Zcas1), and the nos terminator was obtained from Dr. Sylvestre Marillonet. Level 1 position 1 module containing the *seed-specific* promoter and terminator from OLEOSIN1 (Olep and tOle) and RFP was obtained from Dr. Christin Naumann (IPB). Additional Level 1 modules to ensure proper cloning were obtained from Dr. Sylvestre Marillonet (IPB). Corresponding Level 1 modules were combined to generate transcriptional units, containing RFP, Cas9 and sgRNAs with their corresponding promotores and terminators. Proper Cas9 target sequences were identified with the CRISPOR online tool²³⁴. Further explanation of the modules obtained constructs as well as primers used are located in **Tables S1-S3**.

***Arabidopsis* transformation.**

Agrobacterium tumefaciens strain GV3101, containing CRISPR constructs, were grown in lysogeny broth medium (LB medium) with selective antibiotics at 28°C. *Arabidopsis* plants were grown in the greenhouse and transformed using *Agrobacterium* GV3101 strains by the floral dip method²³⁵.

Screening of CRISPR mutants.

RFP Fluorescent seeds of T1 plants carrying CRISPR cassettes were selected using Leica MZ FLII stereomicroscope with Leica Filter set dsRED (10447079). Seeds were grown and screened for a mutation (see **Genotyping CRISPR lines** section). The mutated plants were propagated, and their next generation (T2) was screened for absence of RFP fluorescence, to obtain non-T-DNA inserted plants (absence of CRISPR cassette). Homozygosity was achieved in T3. Triple mutant *ari1ari2ari3* was obtained from crossing *ari1*^{-/-}*ari3*^{-/-} and *ari2*^{-/-} mutants without the CRISPR cassette and homozygosity was achieved in the next generation.

Genotyping CRISPR lines.

Genomic sequence carrying the mutation (~1 kbp) was amplified directly from *Arabidopsis* leaves using the Phire Polymerase and primers from **Table S1** according to the manufacturer's protocol. Obtained PCR products were treated directly with ExoSAP, for degrading the primers, and purified using PCR cleanup kit, both according to the manufacturer's protocol. Purified PCR products were sequenced with Sanger sequencing (Eurofins). Resulting sequences were compared to corresponding WT gene.

Phenotyping CRISPR lines.

Salt and mannitol stress

Seven-day old seedlings were transferred to ½ MS supplemented with 150 mM NaCl and different concentrations of Mannitol. Root length was traced for several days and measured using ImageJ 1.53t (<https://imagej.net/ij/>).

Assaying resistance of ari mutants to turnip mosaic virus GFP (TuMV GFP).

Performed by Jean-Luc Gallois and Nathalie Giovinazzo, INRAE GAFL

Regular protocol from Dr. Luc- Gallois' Lab was followed ^{94,114}. Seeds were sown *in vitro* and grown for 10 days. Twelve plants per genotype were transferred to soil, including the following controls: Col-0 (susceptible), *eifiso4e* (resistant) and *eif4e1* (oversusceptible to TuMV). Plants were randomized in control chamber before inoculation. Inoculation was performed with a toothpick (2 stabs per plant for 11 plants, plant number 12 is mock). GFP accumulation was analyzed 14 days post inoculation. All plants were imaged but no quantification was done.

Gene expression analysis

RNA extraction was performed using *NucleoSpin RNA Plant, Mini kit for RNA from plant* from Macherey Nagel, as recommended by manufacturer. For RNAseq analysis, RNA was extracted 4 hours after foliar treatment of 25-day-old Col-0 rosettes (10 µM of DI31/MH-5 and 2 µM DG-15) or mock. RNAseq was performed at Novogen using NovaSeq 6000 PE150, directional mRNA library. For qRT-PCR, 1 µg of RNA was extracted from *det2-1* adult plants and cDNA was synthesized using RevertAid First Strand cDNA Synthesis Kit from Thermo Scientific™, as recommended by manufacturer. Three whole plants per treatment were plugged from soil and treated in liquid ½ MS for 4 hours with different concentrations of Spyros. *BAS1* and *SAUR-AC1* transcripts were amplified in triplicates using Fast SYBR™ Green Master Mix and the primers (4 µM) listed in **Table S1**. Signal quantification was performed using Applied Biosystems™ QuantStudio 5 from Fisher scientific.

General Cloning.

All constructs were generated either by Golden Gate, Multisite Gateway Technology (Thermo Fisher), or PCR-directed restriction cloning. Coding DNA sequences of full length ARIs, eIF4E1 and eIFiso4E with a stop codon were amplified from WT cDNA with oligonucleotides containing appropriate sites for the specific cloning strategy. Coding DNA sequences of the ectodomains BRI1¹⁻⁷⁸⁸, BRL1¹⁻⁷⁷⁶, BRL2¹⁻⁷⁵⁵, BRL3¹⁻⁷⁷¹, SERK1¹⁻²³⁸ and SERK3¹⁻²²⁵ with a stop codon were amplified from WT cDNA with oligonucleotides containing appropriate att sites and recombined with pDONR221 using BP clonase enzyme mix. Stop codon

was removed for SUS-derived constructs: pMetYC, pMetOYC, pNX32 and pXN22. Additionally, SERK3¹⁻²²⁵ was amplified with NotI and Xhol restriction sites.

For Gateway cloning, PCR products with appropriate att sites were recombined with pDONR221 using BP clonase enzyme mix. E2s in pDONR201 and pSPYCE were obtained from Trujillo lab^{12,22}. The entry clones were recombined with the corresponding destination vectors using LR clonase. For Golden gate cloning, PCR products containing Bpil sites and pAGM4031 were cut and ligated together. The resulting entry clones were cut and ligated into corresponding destination vectors. For PCR-directed cloning, PCR products with appropriate restriction sites and destination vectors (pENTR1A, pENTR1Amod and pETSUMO) were cut with two restriction enzymes, purified using PCR cleanup kit and ligated using T4 DNA ligase; all according to manufacturer's protocol. All constructs were verified by Sanger sequencing and analysis with the DNASTAR Lasergene software SeqBuilder and SeqMan Ultra. All primers and obtained constructs are available in the supporting information (**Table S1-S2**).

Protoplast isolation and transformation from *Nicotiana benthamiana*.

Protoplasts of *N. benthamiana* were isolated from four- to five-week-old plants, cultivated under long photoperiod conditions (16 h/8 h, 24 °C/22 °C, 70% rH) and transformed as described in²³⁶ using 5-10 µg plasmid-DNA per 20,000 protoplasts. After 18 h, at least 100 protoplasts of each transformation were checked for the occurrence of mCherry-fluorescence using a confocal laser scanning microscope (LSM880 and Apotome, Zeiss, Germany) with an excitation wavelength of 561 nm. The detection wavelength of mCherry was set between 575 nm and 650 nm. Autofluorescence of chlorophyll was detected between 650 nm and 700 nm. YFP fluorescence was checked with excitation at 514 nm and emission at 516–549 nm.

Bimolecular fluorescence complementation (BiFC).

Protoplasts from 4-5 weeks old *N. benthamiana* plants were co-transformed with pSPYCE- and pSPYNE-constructs. NLS-mCherry was also co-transformed as an expression marker. Transformed protoplasts were incubated at room temperature in the dark for 18 h before imaging (Apotome and LSM880; Zeiss, Germany). At least 100 protoplasts were counted for each transformation event and used for quantification. The percentage of transformed protoplast (as indicated by mCherry expression) that showed yellow fluorescent protein (YFP) complementation was scored manually.

Confocal Microscopy of *BZR1p::BZR1-YFP* lines.

Fluorescence of YFP, was visualized under the confocal microscope Carl Zeiss LSM700 (Plan-Neofluar 20x). For this, 5 days-old *BZR1p::BZR1-YFP* seedlings were mounted in ½ MS supplemented with 10 µM DI-31,

10 μ M MH-5, eBL 1 μ M or mock; and YFP was visualized at the moment of treatment ($t = 0$) and 90 min later. Excitation/detection ranges was set to 488/518 nm. All images were taken with identical settings, and by analyzing \sim 5 individuals per treatment. Image processing was performed in ImageJ.

LexA yeast two hybrid assays.

LexA-based yeast two hybrid assays were performed using yeast transformed with the described constructs (DBD-fusions: EGY48+pSH18-34, pGILDA vector; AD-fusions: YM4271, pB42AD vector), freshly mated and grown on selection media (Gal/Raff -Ura -His -Trp). Same amount of yeast cells ($OD_{600} = 0.8$) were spotted on selection plates containing BU salts (final: 7 g/L Na_2HPO_4 , 3 g/L NaH_2PO_4 , pH 7), X-Gal (final 80 mg/L) and the given steroid concentration. Plates were incubated at 30°C for several days and constantly monitored.

SUS assays.

Mating-based split-ubiquitin-system (SUS) was performed following the basic protocol of ²³⁷. Yeast strains were transformed with C-terminal Ubiquitin also known as Cub clones (THY.AP4: pMetYC and pMetOYC vectors) and N-terminal Ubiquitin also known as Nub clones (THY.AP5: pNX32 and pXN22 vectors). Freshly mated yeast were grown for one day and same amount of yeast cells ($OD_{600} = 1$) with dilutions (1:10 and 1:100) were spotted on selection media (SD -Leu -Ura -Trp -Ade -His -Met) with increasing concentration of Met and the given steroid concentration. Plates were incubated at 30°C for several days and constantly monitored.

DI-31-Biotin photoaffinity crosslinking and detection of binding proteins.

Photoaffinity labelling was based on a previously published method with biotin-tagged photoaffinity castasterone with modifications ¹²⁶. *Arabidopsis* seedlings were grown for 7-10 days in liquid $\frac{1}{2}$ MS. Three biological replicates, consisting of 60 seedlings each, were used per treatment (- Spyro, + Spyro and + Spyro&UV-A). Plant material was ground to a fine powder and transferred to a 15 mL Falcon and Grinding buffer (100 μ l of Buffer per 100 mg of plant material) was added (50 mM TRIS pH 7.5, 10 mM NaCl, 2 mM DTT, 2 mM MgCl₂, cComplete EDTA-free protease inhibitor (Roche), 1 μ M Aprotinin, 1 μ M Pepstatin, 1 mM PMSF). Lysates were cleared by centrifugation (21 000 rcf, 10 min), and total protein concentration was measured with Bradford and adjusted to 2 mg/mL of protein.

Photocrosslinker was immobilized in magnetic streptavidin beads (ThermoFisher: 65601) according to manufacturer's manual. Beads (20 μ L) were saturated with the photocrosslinker (2 μ g in 0.5 mL Buffer) by using a two-fold excess of the binding capacity of the biotinylated molecule to saturate streptavidin. Incubation was performed for 30 min at room temperature with gentle rotation of the tube. After washing

(washing Buffer: 50 mM TRIS pH 7.5, 10 mM NaCl, 2 mM DTT, 2 mM MgCl₂), plant lysate (0.5 mL, 2 mg/mL protein) was incubated with the immobilized photocrosslinker (20 μ L) for 60 minutes rotating in the dark at 4°C. The mix was irradiated with UV-A light (365 nm) 2x for 20sec with mixing in-between (thermomixer). After washing 2x, in bead Trypsin (Promega: V5280) digestion was performed using S-trap™ micro columns (Protifi), according to manufacturer recommendations (<https://protifi.com>). TRIS buffer was used instead of TEAB, except in elution step, where Ammonium Bicarbonate Buffer was used. TFA was used instead of formic acid. Iodoacetamide in water was used instead of MMTS. Amount, concentration (and pH when necessary) was always kept the same. Digested proteins were identified with LC-MS/MS (performed by Daniele Ubbiali and Claudio Iacobucci at Sinz Lab).

Assessing eIF4E1 and eIFiso4E protein levels in *ari* mutants.

One month old *ari* mutants were grown and true leaves were harvested and frozen in liquid nitrogen (1 plants per lane). For total protein analysis, extracts were prepared by grinding ~equal amounts of *Arabidopsis* leaves in 100 μ L 2x Lämml buffer per 100 mg of sample and boiling samples for 5 min at 95°C ⁹⁴. Samples were separated via SDS-PAGE (8%) and immunoblotted (anti-actin: Sigma (A0480, 1:1000), anti-eIF4E1/anti-eIFiso4E: (1:1000); anti-mouse Alexa Fluor® Plus 488: invitrogen (A32723, 1:2000); anti-rabbit Alexa Fluor® Plus 647: thermo scientific (A32733, 1:2000)). Detection was performed with a Typhoon FLA 9500 system (473 nm excitation wavelength and LPB filter for actin signal detection and 635 nm excitation wavelength and LPR filter for eIF4Es signal). Antibodies against eIF4E1 and eIFiso4E were kindly donated by Jean-Luc Gallois ⁹⁴.

E1—E2—E3 protein expression and purification.

His-UBA1 and His-UBC8 were expressed and purified according to ²³⁸. ARIs (native and mutated), GFP, eIF4E1 and eIFiso4E were expressed as His-SUMO-tagged proteins in BL21-AI strains. Transformed bacteria were grown in 2YT media (1 L for eIF4Es and 2 L for ARIs) at 37°C until OD₆₀₀ = 1-1.5. After induction with 0.1% L-Arabinose, protein expression was performed for 16-20 hours at 16°C. Bacteria expressing ARI proteins were supplemented with 0.1 mM ZnCl₂ at the moment of induction. Cells were harvested by centrifugation (4 000 rcf, 15 min). Bacteria pellet was resuspended in 5 mL of lysis Buffer (50mM Tris pH 8, 200mM NaCl, aprotinin 1 μ M, pepstatin 1 μ M, 1 mM PMSF, cOmplete EDTA-free protease inhibitor (Roche), lysozyme) per gram of pellet. After lysis by sonication, lysates were cleared by centrifugation (15 000 rcf, 15min), and all the supernatants were purified using IMAC (gravity flow). Tag removal was followed, with SUMO protease, for all ARIs and a second IMAC was performed (gravity flow). Only ARI1 versions were further purified using size-exclusion chromatography (SEC) step (HiLoad Superdex16/600 200pg) in an ÄKTA FPLC system.

Protein pull-down.

His-SUMO-tagged proteins were expressed as stated in the previous section (**Protein expression and purification**). GST-tagged proteins followed the same protocol as before, except for the induction time and temperature (30°C, 4 hours). Cells were harvested by centrifugation (4 000 rcf, 15 min). Bacteria pellet was resuspended in 2 mL of lysis Buffer (50mM Tris pH 8 or pH7.5, 200mM NaCl, aprotinin 1 µM, pepstatin 1 µM, 1 mM PMSF, cOmplete EDTA-free protease inhibitor (Roche), lysozyme) per gram of pellet. After lysis by sonication, lysates were cleared by centrifugation (15 000 rcf, 15min), and all the supernatants were further used for the pull-down assays.

Supernatant containing GST-derivatives were immobilized via GSH agarose (SERVA). Binding was performed in batch mode, 30 min at 4°C with gentle rotation. The unbound fraction was discarded through gravity flow in Biorad columns. After washing one time with 50 mM Tris, 200 mM NaCl, pH 7.5 (washing Buffer), supernatants containing His-SUMO-tagged proteins were added to each column (gravity flow). After washing three times, proteins were eluted with 4X lämmli Buffer and incubated at 80°C 5 min.

Supernatant containing His-SUMO-derivatives were immobilized via IMAC with Talon resin (Takara). Binding was performed in column (gravity flow). After washing one time with 50 mM Tris, 200 mM NaCl, pH 8 (washing Buffer), supernatants containing GST-tagged proteins were added to each column (gravity flow). After washing three times, proteins were eluted with 50 mM Tris, 200 mM NaCl, 200 mM Imidazole, pH 8. An appropriate amount of 4X lämmli Buffer was added to the eluate and incubated at 80°C 5 min.

Samples were separated via SDS-PAGE (10%) and immunoblotted (anti-GST: Sigma Aldrich (G7781, 1:5000); anti-SMT3: abcam (ab14405, 1:1000); anti-rabbit Alexa Fluor® Plus 647: Thermo scientific (A32733, 1:2000)). Detection was performed with a Typhoon FLA 9500 system (635 nm excitation wavelength and LPR filter for both GST and SUMO signal).

UbiGate.

Autoubiquitylation was reconstituted in bacteria by co-expressing GST-ARIs and an operon containing Ub, UBA1, and one E2. This was performed as suggested by^{12,99}. Another approach was used with semi-purified tag-less ARIs, fluorescein-labeled ubiquitin and bacterial lysate containing Ub, UBA1, and one E2. Immunodetection of Ub-conjugated proteins was performed using polyclonal anti-GST in rabbit (1:1000; Sigma, G7781) antibodies combined with secondary anti-rabbit Alexa Fluor® Plus 647 antibody (1:2000; Thermo Fischer Scientific, A32733). Detection was performed with a Typhoon FLA 9500 system (473 nm excitation wavelength and LPB filter for fluorescein-labeled ubiquitin signal detection and 635 nm excitation wavelength and LPR filter for GST signal).

***In vitro* reconstitution of Ub-conjugation (IVU).**

IVU reactions were prepared as follows: 25 μ M ubiquitin (Fl-Ub; fluorescein-labeled Ub^{S20C}), 0.2 μ M 6xHis-UBA1 (E1), 1 μ M 6xHis-UBC8 (E2), ~1 μ M ARIs in reaction buffer (10 mM HEPES pH 7.5, 40 μ M ATP, 100 mM NaCl, 2 mM MgCl₂, +/- 0.5mM DTT). In non-reducing conditions of the reactions, DTT was not added to the Buffer. Concentration of ARIs varied from 0.5-1.5 μ M, where ARI1 had the highest concentration. IVU of eIF4E1 and eIFiso4E followed the same protocol, with the addition of 0.1mM m7GTP in the reaction buffer and saturated amounts of His-SUMO-eIF4E1, -eIFiso4E or -GFP. All reactions were incubated at 37°C for 30 min. Reactions were stopped with either non-denaturing (AtARI autoubiquitylation) or denaturing (AtARI autoubiquitylation and eIF4Es ubiquitylation) Lämmli Buffer. Immunodetection of Ub-conjugated proteins was performed using the polyclonal antibodies anti-SMT3 (1:1000), anti-eIF4E1 (1:1000, ⁹⁴), anti-eIFiso4E (1:1000, ⁹⁴, all in rabbit combined with secondary anti-rabbit Alexa Fluor® Plus 647 antibody (1:2000; Thermo Fischer Scientific, A32733). Detection was performed with a Typhoon FLA 9500 system (473 nm excitation wavelength and LPB filter for fluorescein-labeled ubiquitin signal detection and 635 nm excitation wavelength and LPR filter for SUMO/eIF4Es signals).

LC-MS/MS analyses of IVU reactions.

Performed by Susanne Matschi

Same set of gel-analyzed IVUs were sent for LC-MS/MS analysis. After 30 min, IVUs were stopped by denaturing with lämmli buffer and separated with SDS-PAGE 10%. Proteins were in-gel digested with trypsin and proteins were desalted as described in ²³⁹. Dried peptides were dissolved in 5% acetonitrile, 0.1% trifluoric acid and 2 μ g were injected into an EASY-nLC 1000 liquid chromatography system (Thermo Fisher Scientific). Peptides were separated using liquid chromatography C18 reverse phase chemistry employing a 120 min gradient increasing from 2% to 30% acetonitrile in 0.1% FA, and a flow rate of 250 nL/min. Eluted peptides were electrosprayed on-line into a QExactive Plus mass spectrometer (Thermo Fisher Scientific). The spray voltage was 1.9 kV, the capillary temperature 275°C and the Z-Lens voltage 240 V. A full MS survey scan was carried out with chromatographic peak width set to 15 s, resolution 70 000, automatic gain control (AGC) 3E+06 and a max injection time (IT) of 100 ms. MS/MS peptide sequencing was performed using a Top10 DDA scan strategy with HCD fragmentation. MS scans with mass to charge ratios (m/z) between 400 and 1850 were acquired. MS/MS scans were acquired with resolution 17 500, AGC 5E+04, IT 50 ms, isolation width 1.6 m/z, normalized collision energy 28, under fill ratio 3%, dynamic exclusion duration 20 s, and an intensity threshold of 3E+04.

Peptides were identified and ubiquitinated residues mapped using the Mascot software v2.7.0 (Matrix Science) linked to Proteome Discoverer v 2.4 (Thermo Fisher Scientific). A precursor ion mass error of 10

ppm and a fragment ion mass error of 0.02 Da were tolerated in searches of the *Arabidopsis thaliana* TAIR 10 database (35 935 sequences, 14 487 050 residues) amended with target proteins and common contaminants. Carbamidomethylation of cysteine (C) was set as fixed modification and GG and LRGG on lysine (K) as well as oxidation of methionine (M) were tolerated as variable modifications. A spectrum (PSM), peptide and protein level false discovery rate (FDR) was calculated for all annotated PSMs, peptide groups and proteins based on the target-decoy database model and the percolator module. PSMs, peptide groups and proteins with q-values beneath the significance threshold $\alpha=0.01$ for PSMs and peptide groups and 0.05 for proteins were considered identified.

REFERENCES

1. Squair, D. R. & Virdee, S. A new dawn beyond lysine ubiquitination. *Nat. Chem. Biol.* **18**, 802–811 (2022).
2. Barroso-Gomila, O. *et al.* BioE3 identifies specific substrates of ubiquitin E3 ligases. *Nat. Commun.* **14**, 7656 (2023).
3. Dikic, I. & Schulman, B. A. An expanded lexicon for the ubiquitin code. *Nat. Rev. Mol. Cell Biol.* **24**, 273–287 (2023).
4. Bremm, A., Freund, S. M. & Komander, D. Lys11-linked ubiquitin chains adopt compact conformations and are preferentially hydrolyzed by the deubiquitinase Cezanne. *Nat. Struct. Mol. Biol.* **17**, 939–947 (2010).
5. Eddins, M. J., Varadan, R., Fushman, D., Pickart, C. M. & Wolberger, C. Crystal structure and solution NMR studies of Lys48-linked tetraubiquitin at neutral pH. *J. Mol. Biol.* **367**, 204–211 (2007).
6. Yang, Q., Zhao, J., Chen, D. & Wang, Y. E3 ubiquitin ligases: styles, structures and functions. *Mol. Biomed.* **2**, 1–17 (2021).
7. Dubeaux, G., Neveu, J., Zelazny, E. & Vert, G. Metal sensing by the IRT1 transporter-receptor orchestrates its own degradation and plant metal nutrition. *Mol. Cell* **69**, 953–964. e5 (2018).
8. Leitner, J. *et al.* Lysine63-linked ubiquitylation of PIN2 auxin carrier protein governs hormonally controlled adaptation of *Arabidopsis* root growth. *Proc. Natl. Acad. Sci.* **109**, 8322–8327 (2012).
9. Martinez-Fonts, K. *et al.* The proteasome 19S cap and its ubiquitin receptors provide a versatile recognition platform for substrates. *Nat. Commun.* **11**, 477 (2020).
10. Romero-Barrios, N. *et al.* Advanced cataloging of lysine-63 polyubiquitin networks by genomic, interactome, and sensor-based proteomic analyses. *Plant Cell* **32**, 123–138 (2020).
11. Romero-Barrios, N. & Vert, G. Proteasome-independent functions of lysine-63 polyubiquitination in plants. *New Phytol.* **217**, 995–1011 (2018).
12. Kowarschik, K., Hoehenwarter, W., Marillonnet, S. & Trujillo, M. UbiGate: a synthetic biology toolbox to analyse ubiquitination. *New Phytol.* **217**, 1749–1763 (2018).
13. Nielsen, C. P. & MacGurn, J. A. Coupling conjugation and deconjugation activities to achieve cellular ubiquitin dynamics. *Trends Biochem. Sci.* **45**, 427–439 (2020).
14. Lee, B.-H. *et al.* USP14 deubiquitinates proteasome-bound substrates that are ubiquitinated at multiple sites. *Nature* **532**, 398–401 (2016).
15. Niu, K. *et al.* USP33 deubiquitinates PRKN/parkin and antagonizes its role in mitophagy. *Autophagy* **16**, 724–734 (2020).
16. Brillada, C. & Trujillo, M. E2 ubiquitin-conjugating enzymes (UBCs): drivers of ubiquitin signalling in plants. *Essays Biochem.* **66**, 99–110 (2022).
17. Morreale, F. E. & Walden, H. Types of Ubiquitin Ligases. *Cell* **165**, 248–248.e1 (2016).
18. Yuan, L., Lv, Z., Adams, M. J. & Olsen, S. K. Crystal structures of an E1–E2–ubiquitin thioester mimetic reveal molecular mechanisms of transthiosterification. *Nat. Commun.* **12**, 2370 (2021).
19. Chung, S., Kwon, H.-L., Yun, H. S. & Lee, J.-H. The Function of Deubiquitinating Enzymes in *Arabidopsis*: Recent Progress of Ubiquitin-Specific Proteases (UBPs). *J. Plant Biol.* 1–9 (2023).
20. Bui, Q. T., Hong, J. H., Kwak, M., Lee, J. Y. & Lee, P. C.-W. Ubiquitin-conjugating enzymes in cancer. *Cells* **10**, 1383 (2021).
21. Michelle, C., Vourc'h, P., Mignon, L. & Andres, C. R. What was the set of ubiquitin and ubiquitin-like conjugating enzymes in the eukaryote common ancestor? *J. Mol. Evol.* **68**, 616–628 (2009).
22. Turek, I., Tischer, N., Lassig, R. & Trujillo, M. Multi-tiered pairing selectivity between E2 ubiquitin-conjugating enzymes and E3 ligases. *J. Biol. Chem.* **293**, 16324–16336 (2018).
23. Stewart, M. D., Ritterhoff, T., Klevit, R. E. & Brzovic, P. S. E2 enzymes: more than just middle men. *Cell Res.* **26**, 423–440 (2016).

24. Williams, K. M. *et al.* Structural insights into E1 recognition and the ubiquitin-conjugating activity of the E2 enzyme Cdc34. *Nat. Commun.* **10**, 3296 (2019).

25. Ramadan, A. *et al.* Wheat germ-based protein libraries for the functional characterisation of the Arabidopsis E2 ubiquitin conjugating enzymes and the RING-type E3 ubiquitin ligase enzymes. *BMC Plant Biol.* **15**, 275 (2015).

26. Plechanovová, A., Jaffray, E. G., Tatham, M. H., Naismith, J. H. & Hay, R. T. Structure of a RING E3 ligase and ubiquitin-loaded E2 primed for catalysis. *Nature* **489**, 115–120 (2012).

27. Brzovic, P. S., Lissounov, A., Christensen, D. E., Hoyt, D. W. & Klevit, R. E. A UbcH5/ubiquitin noncovalent complex is required for processive BRCA1-directed ubiquitination. *Mol. Cell* **21**, 873–880 (2006).

28. Dou, H., Buetow, L., Sibbet, G. J., Cameron, K. & Huang, D. T. Essentiality of a non-RING element in priming donor ubiquitin for catalysis by a monomeric E3. *Nat. Struct. Mol. Biol.* **20**, 982–986 (2013).

29. Scott, D. C. *et al.* Structure of a RING E3 trapped in action reveals ligation mechanism for the ubiquitin-like protein NEDD8. *Cell* **157**, 1671–1684 (2014).

30. Eletr, Z. M., Huang, D. T., Duda, D. M., Schulman, B. A. & Kuhlman, B. E2 conjugating enzymes must disengage from their E1 enzymes before E3-dependent ubiquitin and ubiquitin-like transfer. *Nat. Struct. Mol. Biol.* **12**, 933–934 (2005).

31. Kraft, E. *et al.* Genome Analysis and Functional Characterization of the E2 and RING-Type E3 Ligase Ubiquitination Enzymes of Arabidopsis. *Plant Physiol.* **139**, 1597–1611 (2005).

32. Gu, X., Jiang, D., Wang, Y., Bachmair, A. & He, Y. Repression of the floral transition via histone H2B monoubiquitination. *Plant J.* **57**, 522–533 (2009).

33. David, Y., Ziv, T., Admon, A. & Navon, A. The E2 ubiquitin-conjugating enzymes direct polyubiquitination to preferred lysines. *J. Biol. Chem.* **285**, 8595–8604 (2010).

34. Bosanac, I. *et al.* Modulation of K11-linkage formation by variable loop residues within UbcH5A. *J. Mol. Biol.* **408**, 420–431 (2011).

35. Zhou, B. *et al.* A subset of ubiquitin-conjugating enzymes is essential for plant immunity. *Plant Physiol.* **173**, 1371–1390 (2017).

36. Scaglione, K. M. *et al.* The ubiquitin-conjugating enzyme (E2) Ube2w ubiquitinates the N terminus of substrates. *J. Biol. Chem.* **288**, 18784–18788 (2013).

37. Wang, S., Cao, L. & Wang, H. Arabidopsis ubiquitin-conjugating enzyme UBC22 is required for female gametophyte development and likely involved in Lys11-linked ubiquitination. *J. Exp. Bot.* **67**, 3277–3288 (2016).

38. Cao, L. *et al.* The inactivation of Arabidopsis UBC22 results in abnormal chromosome segregation in female meiosis, but not in male meiosis. *Plants* **10**, 2418 (2021).

39. Liu, T.-Y. *et al.* PHO2-dependent degradation of PHO1 modulates phosphate homeostasis in Arabidopsis. *Plant Cell* **24**, 2168–2183 (2012).

40. Fernandez, M. A. *et al.* RBR-type E3 ligases and the ubiquitin-conjugating enzyme UBC26 regulate abscisic acid receptor levels and signaling. *Plant Physiol.* **182**, 1723–1742 (2020).

41. Ahn, M. Y. *et al.* Arabidopsis group XIV ubiquitin-conjugating enzymes AtUBC32, AtUBC33, and AtUBC34 play negative roles in drought stress response. *J. Plant Physiol.* **230**, 73–79 (2018).

42. Chen, Q., Liu, R., Wang, Q. & Xie, Q. ERAD tuning of the HRD1 complex component AtOS9 is modulated by an ER-bound E2, UBC32. *Mol. Plant* **10**, 891–894 (2017).

43. Chen, Q. *et al.* ERAD-related E2 and E3 enzymes modulate the drought response by regulating the stability of PIP2 aquaporins. *Plant Cell* **33**, 2883–2898 (2021).

44. Cui, F. *et al.* Arabidopsis ubiquitin conjugase UBC32 is an ERAD component that functions in brassinosteroid-mediated salt stress tolerance. *Plant Cell* **24**, 233–244 (2012).

45. Li, W. & Schmidt, W. A lysine-63-linked ubiquitin chain-forming conjugase, UBC13, promotes the developmental responses to iron deficiency in Arabidopsis roots. *Plant J.* **62**, 330–343 (2010).

46. Martins, S. *et al.* Internalization and vacuolar targeting of the brassinosteroid hormone receptor BRI1 are regulated by ubiquitination. *Nat. Commun.* **6**, 6151 (2015).
47. Dove, K. K. *et al.* Two functionally distinct E2/E3 pairs coordinate sequential ubiquitination of a common substrate in *Caenorhabditis elegans* development. *Proc. Natl. Acad. Sci.* **114**, E6576–E6584 (2017).
48. Duda, D. M. *et al.* Structure of HHARI, a RING-IBR-RING Ubiquitin Ligase: Autoinhibition of an Ariadne-Family E3 and Insights into Ligation Mechanism. *Structure* **21**, 1030–1041 (2013).
49. Horn-Ghetko, D. *et al.* Ubiquitin ligation to F-box protein targets by SCF–RBR E3–E3 super-assembly. *Nature* **590**, 671–676 (2021).
50. Kostrhon, S. *et al.* CUL5-ARIH2 E3-E3 ubiquitin ligase structure reveals cullin-specific NEDD8 activation. *Nat. Chem. Biol.* **17**, 1075–1083 (2021).
51. Qiu, X. & Fay, D. S. ARI-1, an RBR family ubiquitin-ligase, functions with UBC-18 to regulate pharyngeal development in *C. elegans*. *Dev. Biol.* **291**, 239–252 (2006).
52. Reiter, K. H. *et al.* Cullin-independent recognition of HHARI substrates by a dynamic RBR catalytic domain. *Structure* **30**, 1269–1284. e6 (2022).
53. Wenzel, D. M., Lissounov, A., Brzovic, P. S. & Klevit, R. E. UBCH7 reactivity profile reveals parkin and HHARI to be RING/HECT hybrids. *Nature* **474**, 105–108 (2011).
54. Horn-Ghetko, D. & Schulman, B. A. New classes of E3 ligases illuminated by chemical probes. *Curr. Opin. Struct. Biol.* **73**, 102341 (2022).
55. Vierstra, R. D. The ubiquitin–26S proteasome system at the nexus of plant biology. *Nat. Rev. Mol. Cell Biol.* **10**, 385–397 (2009).
56. Woo, O.-G., Kim, H. & Lee, J.-H. Current Understanding of the CRL1 Complex in *Arabidopsis*. *J. Plant Biol.* **64**, 1–12 (2021).
57. Furniss, J. J. *et al.* Proteasome-associated HECT-type ubiquitin ligase activity is required for plant immunity. *PLOS Pathog.* **14**, e1007447 (2018).
58. Rotin, D. & Kumar, S. Physiological functions of the HECT family of ubiquitin ligases. *Nat. Rev. Mol. Cell Biol.* **10**, 398–409 (2009).
59. Walden, H. & Rittinger, K. RBR ligase–mediated ubiquitin transfer: a tale with many twists and turns. *Nat. Struct. Mol. Biol.* **25**, 440–445 (2018).
60. Spratt, D. E., Walden, H. & Shaw, G. S. RBR E3 ubiquitin ligases: new structures, new insights, new questions. *Biochem. J.* **458**, 421–437 (2014).
61. Wang, X. S. *et al.* The unifying catalytic mechanism of the RING-between-RING E3 ubiquitin ligase family. *Nat. Commun.* **14**, 168 (2023).
62. Marin, I. & Ferrús, A. Comparative genomics of the RBR family, including the Parkinson’s disease–related gene Parkin and the genes of the Ariadne subfamily. *Mol. Biol. Evol.* **19**, 2039–2050 (2002).
63. Eisenhaber, B., Chumak, N., Eisenhaber, F. & Hauser, M.-T. The ring between ring fingers (RBR) protein family. *Genome Biol.* **8**, 209 (2007).
64. Marín, I. RBR Ubiquitin Ligases: Diversification and Streamlining in Animal Lineages. *J. Mol. Evol.* **69**, 54–64 (2009).
65. Aguilera, M., Oliveros, M., Martínez-Padrón, M., Barbas, J. A. & Ferrús, A. Ariadne-1: a vital *Drosophila* gene is required in development and defines a new conserved family of ring-finger proteins. *Genetics* **155**, 1231–1244 (2000).
66. Hart, T. *et al.* High-resolution CRISPR screens reveal fitness genes and genotype-specific cancer liabilities. *Cell* **163**, 1515–1526 (2015).
67. Poush, J. A., Blouin, N. A., Di Bona, K. R., Lažetić, V. & Fay, D. S. Regulation of germ cell development by ARI1 family ubiquitin ligases in *C. elegans*. *Sci. Rep.* **8**, 17737 (2018).
68. von Stechow, L. *et al.* The E3 Ubiquitin Ligase ARIH1 Protects against Genotoxic Stress by Initiating a 4EHP-Mediated mRNA Translation Arrest. *Mol. Cell. Biol.* **35**, 1254–1268 (2015).

69. Wang, T. *et al.* Identification and characterization of essential genes in the human genome. *Science* **350**, 1096–1101 (2015).
70. Kelsall, I. R. *et al.* TRIAD1 and HHARI bind to and are activated by distinct neddylated Cullin-RING ligase complexes. *EMBO J.* **32**, 2848–2860 (2013).
71. Yuan, L., Lv, Z., Atkison, J. H. & Olsen, S. K. Structural insights into the mechanism and E2 specificity of the RBR E3 ubiquitin ligase HHARI. *Nat. Commun.* **8**, 211 (2017).
72. Scott, D. C. *et al.* Two Distinct Types of E3 Ligases Work in Unison to Regulate Substrate Ubiquitylation. *Cell* **166**, 1198–1214.e24 (2016).
73. Mertins, P. *et al.* Ischemia in tumors induces early and sustained phosphorylation changes in stress kinase pathways but does not affect global protein levels. *Mol. Cell. Proteomics* **13**, 1690–1704 (2014).
74. Ramírez, J. *et al.* The ubiquitin ligase Ariadne-1 regulates NSF for neurotransmitter release. *bioRxiv* 2020.01.23.916619 (2020) doi:10.1101/2020.01.23.916619.
75. Marín, I. Diversification and Specialization of Plant RBR Ubiquitin Ligases. *PLOS ONE* **5**, e11579 (2010).
76. Mladek, C., Guger, K. & Hauser, M.-T. Identification and characterization of the ARIADNE gene family in Arabidopsis. A group of putative E3 ligases. *Plant Physiol.* **131**, 27–40 (2003).
77. Lang-Mladek, C. *et al.* UV-B signaling pathways and fluence rate dependent transcriptional regulation of ARIADNE12. *Physiol. Plant.* **145**, 527–539 (2012).
78. Zhang, Y., Wu, Y., Liu, Y. & Han, B. Computational Identification of 69 Retroposons in Arabidopsis. *Plant Physiol.* **138**, 935–948 (2005).
79. Chen, P., Zhang, X., Zhao, T., Li, Y. & Gai, J. Genome-Wide Identification and Characterization of RBR Ubiquitin Ligase Genes in Soybean. *PLOS ONE* **9**, e87282 (2014).
80. Stone, S. L. *et al.* Functional Analysis of the RING-Type Ubiquitin Ligase Family of Arabidopsis. *Plant Physiol.* **137**, 13–30 (2005).
81. Xie, L., Lang-Mladek, C., Richter, J., Nigam, N. & Hauser, M.-T. UV-B induction of the E3 ligase ARIADNE12 depends on CONSTITUTIVELY PHOTOMORPHOGENIC 1. *Plant Physiol. Biochem. PPB* **93**, 18–28 (2015).
82. Zhang, X. *et al.* Overexpression of a Soybean Ariadne-Like Ubiquitin Ligase Gene GmARI1 Enhances Aluminum Tolerance in Arabidopsis. *PLOS ONE* **9**, e111120 (2014).
83. Al-Saharin, R., Hellmann, H. & Mooney, S. Plant E3 Ligases and Their Role in Abiotic Stress Response. *Cells* **11**, (2022).
84. Gipson, A. B., Giloteaux, L., Hanson, M. R. & Bentolila, S. Arabidopsis RanBP2-Type Zinc Finger Proteins Related to Chloroplast RNA Editing Factor OZ1. *Plants* **9**, (2020).
85. Ron, M., Alandete Saez, M., Eshed Williams, L., Fletcher, J. C. & McCormick, S. Proper regulation of a sperm-specific cis-nat-siRNA is essential for double fertilization in Arabidopsis. *Genes Dev.* **24**, 1010–1021 (2010).
86. Ardley, H. C., Tan, N. G. S., Rose, S. A., Markham, A. F. & Robinson, P. A. Features of the Parkin/Ariadne-like Ubiquitin Ligase, HHARI, That Regulate Its Interaction with the Ubiquitin-conjugating Enzyme, UbCH7 *. *J. Biol. Chem.* **276**, 19640–19647 (2001).
87. Elmehdawi, F. *et al.* Human Homolog of Drosophila Ariadne (HHARI) is a marker of cellular proliferation associated with nuclear bodies. *Exp. Cell Res.* **319**, 161–172 (2013).
88. Parelkar, S. S. *et al.* The Parkin-Like Human Homolog of Drosophila Ariadne-1 (HHARI) Can Induce Aggresome Formation in Mammalian Cells and Is Immunologically Detectable in Lewy Bodies. *J. Mol. Neurosci.* **46**, 109–121 (2012).
89. Schallau, A. *et al.* Identification and genetic analysis of the APOSPORY locus in *Hypericum perforatum* L. *Plant J.* **62**, 773–784 (2010).
90. Wahid, S. *et al.* Genome-wide identification and analysis of Ariadne gene family reveal its genetic effects on agronomic traits of *brassica napus*. *Int. J. Mol. Sci.* **23**, 6265 (2022).

91. Komander, D. & Rape, M. The ubiquitin code. *Annu. Rev. Biochem.* **81**, 203–229 (2012).
92. Swatek, K. N. & Komander, D. Ubiquitin modifications. *Cell Res.* **26**, 399–422 (2016).
93. Kropiwnicka, A. *et al.* Five eIF4E isoforms from *Arabidopsis thaliana* are characterized by distinct features of cap analogs binding. *Biochem. Biophys. Res. Commun.* **456**, 47–52 (2015).
94. Zafirov, D., Giovinazzo, N., Bastet, A. & Gallois, J.-L. When a knockout is an Achilles' heel: Resistance to one potyvirus species triggers hypersusceptibility to another one in *Arabidopsis thaliana*. *Mol. Plant Pathol.* **22**, 334–347 (2021).
95. Richter, J. *Characterization of Interactions of ARIADNE Ubiquitin Ligase Family Members with Potential Target Proteins*. (na, 2013).
96. Hanada, K., Zou, C., Lehti-Shiu, M. D., Shinozaki, K. & Shiu, S.-H. Importance of Lineage-Specific Expansion of Plant Tandem Duplicates in the Adaptive Response to Environmental Stimuli. *Plant Physiol.* **148**, 993–1003 (2008).
97. Rizzon, C., Ponger, L. & Gaut, B. S. Striking Similarities in the Genomic Distribution of Tandemly Arrayed Genes in *Arabidopsis* and Rice. *PLOS Comput. Biol.* **2**, e115 (2006).
98. Bernhard, O. K., Diefenbach, R. J. & Cunningham, A. L. New insights into viral structure and virus–cell interactions through proteomics. *Expert Rev. Proteomics* **2**, 577–588 (2005).
99. Brillada, C. & Trujillo, M. Identification and Characterization of Physiological Pairing of E2 Ubiquitin-Conjugating Enzymes and E3 Ubiquitin Ligases. in *Plant Proteostasis: Methods and Protocols* (eds. Lois, L. M. & Trujillo, M.) 13–29 (Springer US, New York, NY, 2023). doi:10.1007/978-1-0716-2784-6_2.
100. Zhang, Y., Chen, M., Liu, T., Qin, K. & Fernie, A. R. Investigating the dynamics of protein–protein interactions in plants. *Plant J.* **114**, 965–983 (2023).
101. Kerppola, T. K. Bimolecular Fluorescence Complementation (BiFC) Analysis as a Probe of Protein Interactions in Living Cells. *Annu. Rev. Biophys.* **37**, 465–487 (2008).
102. Horstman, A., Nougalli Tonaco, I. A., Boutilier, K. & Immink, R. G. A cautionary note on the use of split-YFP/BiFC in plant protein-protein interaction studies. *Int. J. Mol. Sci.* **15**, 9628–9643 (2014).
103. Chu, J., Cargnello, M., Topisirovic, I. & Pelletier, J. Translation initiation factors: reprogramming protein synthesis in cancer. *Trends Cell Biol.* **26**, 918–933 (2016).
104. Geng, S. *et al.* ARIH2 regulates the proliferation, DNA damage and chemosensitivity of gastric cancer cells by reducing the stability of p21 via ubiquitination. *Cell Death Dis.* **13**, 564 (2022).
105. Jiang, X. *et al.* Pyruvate dehydrogenase B regulates myogenic differentiation via the FoxP1–Arih2 axis. *J. Cachexia Sarcopenia Muscle* **14**, 606–621 (2023).
106. Kelsall, I. R. *et al.* Coupled monoubiquitylation of the co-E3 ligase DCNL1 by Ariadne-RBR E3 ubiquitin ligases promotes cullin-RING ligase complex remodeling. *J. Biol. Chem.* **294**, 2651–5314 (2019).
107. Xiong, T.-C. *et al.* The E3 ubiquitin ligase ARIH1 promotes antiviral immunity and autoimmunity by inducing mono-ISGylation and oligomerization of cGAS. *Nat. Commun.* **13**, 5973 (2022).
108. Yao, R.-Q., Ren, C., Xia, Z.-F. & Yao, Y.-M. Organelle-specific autophagy in inflammatory diseases: a potential therapeutic target underlying the quality control of multiple organelles. *Autophagy* **17**, 385–401 (2021).
109. Thomann, A. *et al.* *Arabidopsis* CUL3A and CUL3B genes are essential for normal embryogenesis. *Plant J.* **43**, 437–448 (2005).
110. Ban, Z. & Estelle, M. CUL3 E3 ligases in plant development and environmental response. *Nat. Plants* **7**, 6–16 (2021).
111. Thomann, A., Dieterle, M. & Genschik, P. Plant CULLIN-based E3s: Phytohormones come first. *Bp. Spec. Issue* **579**, 3239–3245 (2005).
112. Wang, X. *et al.* PUB25 and PUB26 Promote Plant Freezing Tolerance by Degrading the Cold Signaling Negative Regulator MYB15. *Dev. Cell* **51**, 222-235.e5 (2019).

113. Mergner, J. *et al.* Proteomic and transcriptomic profiling of aerial organ development in *Arabidopsis*. *Sci. Data* **7**, 334 (2020).

114. Zafirov, D. *et al.* *Arabidopsis* eIF4E1 protects the translational machinery during TuMV infection and restricts virus accumulation. *PLOS Pathog.* **19**, e1011417 (2023).

115. Patrick, R. M. *et al.* Two *Arabidopsis* Loci Encode Novel Eukaryotic Initiation Factor 4E Isoforms That Are Functionally Distinct from the Conserved Plant Eukaryotic Initiation Factor 4E. *Plant Physiol.* **164**, 1820–1830 (2014).

116. Xu, X., Vatsyayan, J., Gao, C., Bakkenist, C. J. & Hu, J. Sumoylation of eIF4E activates mRNA translation. *EMBO Rep.* **11**, 299–304 (2010).

117. Zuberek, J. *et al.* Phosphorylation of eIF4E attenuates its interaction with mRNA 5' cap analogs by electrostatic repulsion: Intein-mediated protein ligation strategy to obtain phosphorylated protein. *Rna* **9**, 52–61 (2003).

118. Liu, Z. *et al.* An overview of PROTACs: a promising drug discovery paradigm. *Mol. Biomed.* **3**, 46 (2022).

119. Sampson, C. *et al.* The roles of E3 ubiquitin ligases in cancer progression and targeted therapy. *Clin. Transl. Med.* **13**, e1204 (2023).

120. Tang, S. *et al.* An E2-E3 pair contributes to seed size control in grain crops. *Nat. Commun.* **14**, 3091 (2023).

121. Swamy, K. N. & Rao, S. S. R. Influence of 28-homobrassinolide on growth, photosynthesis metabolite and essential oil content of geranium [Pelargonium graveolens (L.) Herit]. *Am J Plant Physiol* **3**, 173–174 (2008).

122. Kim, E.-J. & Russinova, E. Brassinosteroid signalling. *Curr. Biol.* **30**, R294–R298 (2020).

123. Zullo, M. A. T. & Adam, G. Brassinosteroid phytohormones - structure, bioactivity and applications. *Braz J Plant Physiol* **14**, 143–181 (2002).

124. Zullo, M. A. T. & Bajguz, A. The brassinosteroids family—structural diversity of natural compounds and their precursors. in *Brassinosteroids: plant growth and development* 1–44 (Springer, 2019).

125. Navarro, C. *et al.* Evolutionary, comparative and functional analyses of the brassinosteroid receptor gene, BRI1, in wheat and its relation to other plant genomes. *PLoS One* **10**, e0127544 (2015).

126. Kinoshita, T. *et al.* Binding of brassinosteroids to the extracellular domain of plant receptor kinase BRI1. *Nature* **433**, 167–171 (2005).

127. Caño-Delgado, A. *et al.* BRL1 and BRL3 are novel brassinosteroid receptors that function in vascular differentiation in *Arabidopsis*. (2004).

128. Kang, Y. H., Breda, A. & Hardtke, C. S. Brassinosteroid signaling directs formative cell divisions and protophloem differentiation in *Arabidopsis* root meristems. *Development* **144**, 272–280 (2017).

129. Nolan, T. M., Vukašinović, N., Liu, D., Russinova, E. & Yin, Y. Brassinosteroids: multidimensional regulators of plant growth, development, and stress responses. *Plant Cell* **32**, 295–318 (2020).

130. Hothorn, M. *et al.* Structural basis of steroid hormone perception by the receptor kinase BRI1. *Nature* **464**, 467–471 (2011).

131. She, J. *et al.* Structural insight into brassinosteroid perception by BRI1. *Nature* **474**, 472–476 (2011).

132. Santiago, J., Henzler, C. & Hothorn, M. Molecular Mechanism for Plant Steroid Receptor Activation by Somatic Embryogenesis Co-Receptor Kinases. *SCIENCE* **341**, 889–892 (2013).

133. Sun, Y. *et al.* Structure reveals that BAK1 as a co-receptor recognizes the BRI1-bound brassinolide. *Cell Res.* **23**, 1326–1329 (2013).

134. Back, T. G., Janzen, L., Pharis, R. P. & Yan, Z. Synthesis and bioactivity of C-2 and C-3 methyl ether derivatives of brassinolide. *Phytochemistry* **59**, 627–634 (2002).

135. Muto, T. & Todoroki, Y. Brassinolide-2, 3-acetonide: A brassinolide-induced rice lamina joint inclination antagonist. *Bioorg. Med. Chem.* **21**, 4413–4419 (2013).

136. Gampala, S. S. *et al.* An essential role for 14-3-3 proteins in brassinosteroid signal transduction in *Arabidopsis*. *Dev Cell* **13**, 177–189 (2007).

137. Vert, G. & Chory, J. Downstream nuclear events in brassinosteroid signalling. *Nature* **441**, 96–100 (2006).

138. Kim, E.-J. *et al.* Plant U-Box40 mediates degradation of the brassinosteroid-responsive transcription factor BZR1 in *Arabidopsis* roots. *Plant Cell* **31**, 791–808 (2019).

139. Otani, Y. *et al.* Expression profiles of four BES1/BZR1 homologous genes encoding bHLH transcription factors in *Arabidopsis*. *J. Pestic. Sci.* **45**, 95–104 (2020).

140. Yin, Y. *et al.* BES1 accumulates in the nucleus in response to brassinosteroids to regulate gene expression and promote stem elongation. *Cell* **109**, 181–191 (2002).

141. Yin, Y. *et al.* A new class of transcription factors mediates brassinosteroid-regulated gene expression in *Arabidopsis*. *Cell* **120**, 249–259 (2005).

142. Vriet, C., Russinova, E. & Reuzeau, C. Boosting crop yields with plant steroids. *Plant Cell* **24**, 842–57 (2012).

143. Sakamoto, T. *et al.* Erect leaves caused by brassinosteroid deficiency increase biomass production and grain yield in rice. *Nat. Biotechnol.* **24**, 105–109 (2006).

144. Yang, J. *et al.* Brassinosteroids modulate meristem fate and differentiation of unique inflorescence morphology in *Setaria viridis*. *Plant Cell* **30**, 48–66 (2018).

145. Jin, Y.-L. *et al.* Overexpression of *Populus trichocarpa* CYP 85A3 promotes growth and biomass production in transgenic trees. *Plant Biotechnol. J.* **15**, 1309–1321 (2017).

146. Luo, M. *et al.* GhDET2, a steroid 5 α -reductase, plays an important role in cotton fiber cell initiation and elongation. *Plant J.* **51**, 419–430 (2007).

147. Yang, Z. *et al.* PAG1, a cotton brassinosteroid catabolism gene, modulates fiber elongation. *New Phytol.* **203**, 437–448 (2014).

148. Xu, F., Xi, Z., Zhang, H., Zhang, C. & Zhang, Z. Brassinosteroids are involved in controlling sugar unloading in *Vitis vinifera* 'Cabernet Sauvignon' berries during véraison. *Plant Physiol. Biochem.* **94**, 197–208 (2015).

149. Nakashita, H. *et al.* Brassinosteroid functions in a broad range of disease resistance in tobacco and rice. *Plant J.* **33**, 887–898 (2003).

150. Hasan, S. A., Hayat, S. & Ahmad, A. Brassinosteroids protect photosynthetic machinery against the cadmium induced oxidative stress in two tomato cultivars. *Chemosphere* **84**, 1446–1451 (2011).

151. Hayat, S., Hasan, S. A. & Ahmad, A. Growth, nitrate reductase activity and antioxidant system in cadmium stressed tomato (*Lycopersicon esculentum* Mill.) cultivars. *BASE* (2011).

152. Jiang, Y.-P. *et al.* Brassinosteroids accelerate recovery of photosynthetic apparatus from cold stress by balancing the electron partitioning, carboxylation and redox homeostasis in cucumber. *Physiol. Plant.* **148**, 133–145 (2013).

153. Takimoto, S. *et al.* Structure modification of nonsteroidal brassinolide-like compound, NSBR1. *Biosci. Biotechnol. Biochem.* **86**, 1004–1012 (2022).

154. Korinkova, P. *et al.* Synthesis of novel aryl brassinosteroids through alkene cross-metathesis and preliminary biological study. *Steroids* **127**, 46–55 (2017).

155. Kvasnica, M. *et al.* Design, synthesis and biological activities of new brassinosteroid analogues with phenyl group in the side chain. *Org Biomol Chem* **14**, 8691–8701 (2016).

156. Díaz, K. *et al.* Exogenous application of brassinosteroid 24-norholane 22 (S)-23-dihydroxy type analogs to enhance water deficit stress tolerance in *Arabidopsis thaliana*. *Int. J. Mol. Sci.* **22**, 1158 (2021).

157. Thussagunpanit, J. *et al.* Characterization of synthetic ecdysteroid analogues as functional mimics of brassinosteroids in plant growth. *J. Steroid Biochem. Mol. Biol.* **172**, 1–8 (2017).

158. Diachkov, M. V. *et al.* Synthesis and biological activity of brassinosteroid analogues with a nitrogen-containing side chain. *Int. J. Mol. Sci.* **22**, 155 (2020).

159. Wang, Q., Xu, J., Liu, X., Gong, W. & Zhang, C. Synthesis of brassinosteroids analogues from laxogenin and their plant growth promotion. *Nat. Prod. Res.* **29**, 149–157 (2015).

160. Sugiura, A. *et al.* Discovery of a nonsteroidal brassinolide-like compound, NSBR1. *J. Pestic. Sci.* **42**, 105–111 (2017).

161. Furio, R. N. *et al.* Effect of natural and synthetic Brassinosteroids on strawberry immune response against *Colletotrichum acutatum*. *Eur. J. Plant Pathol.* **153**, 167–181 (2019).

162. Furio, R. N. *et al.* Brassinosteroid Applications Enhance the Tolerance to Abiotic Stresses, Production and Quality of Strawberry Fruits. *Horticulturae* **8**, 572 (2022).

163. Furio, R. N. *et al.* Brassinosteroids promote growth, fruit quality and protection against *Botrytis* on *Fragaria x ananassa*. *Eur. J. Plant Pathol.* **154**, 801–810 (2019).

164. Pérez-Borroto, L. S. *et al.* Brassinosteroid and brassinosteroid-mimic differentially modulate *Arabidopsis thaliana* fitness under drought. *Plant Growth Regul.* **95**, 33–47 (2021).

165. Jomarrón-Rodiles, I. *et al.* Espirostanonas con funciones oxigenadas en el anillo A. Como reguladores del crecimiento vegetal y su procedimiento de obtención. (1995).

166. Torres, W. & Nuñez, M. The application of biobras-6 and its effect on potato (*Solanum tuberosum* L.) yields. *Cult Trop* **18**, 8–10 (1997).

167. Serna, M., Hernandez, F., Coll, F., Coll, Y. & Amoros, A. Brassinosteroid analogues effects on the yield and quality parameters of greenhouse-grown pepper (*Capsicum annuum* L.). *J Plant Growth Regul* **68**, 333–342 (2012).

168. Núñez, M., Torres, W. & Coll, F. Effectiveness of a synthetic brassinosteroid on potato and tomato yields. *Cultiv. Trop.* **16**, 26–27 (1995).

169. Serna, M., Hernández, F., Coll, F., Coll, Y. & Amorós, A. Effects of brassinosteroid analogues on total phenols, antioxidant activity, sugars, organic acids and yield of field grown endive (*Cichorium endivia* L.). *J Sci Food Agric* **93**, 1765–1771 (2013).

170. Moreno-Castillo, E. *et al.* In silico identification of new potentially active brassinosteroid analogues. *Steroids* **138**, 35–42 (2018).

171. Iacobucci, C. *et al.* Carboxyl-Photo-Reactive MS-Cleavable Cross-Linkers: Unveiling a Hidden Aspect of Diazirine-Based Reagents. *Anal. Chem.* **90**, 2805–2809 (2018).

172. Tanaka, K. *et al.* Physiological roles of brassinosteroids in early growth of *Arabidopsis*: brassinosteroids have a synergistic relationship with gibberellin as well as auxin in light-grown hypocotyl elongation. *J Plant Growth Regul* **22**, 259–271 (2003).

173. Retzer, K. *et al.* Brassinosteroid signaling delimits root gravitropism via sorting of the *Arabidopsis* PIN2 auxin transporter. *Nat. Commun.* **10**, 5516 (2019).

174. Wang, Z. Y. *et al.* Nuclear-localized BZR1 mediates brassinosteroid-induced growth and feedback suppression of brassinosteroid biosynthesis. *Dev Cell* **2**, 505–513 (2002).

175. Chory, J., Nagpal, P. & Peto, C. A. Phenotypic and genetic analysis of *det2*, a new mutant that affects light-regulated seedling development in *Arabidopsis*. *Plant Cell* **3**, 445–459 (1991).

176. Goda, H., Shimada, Y., Asami, T., Fujioka, S. & Yoshida, S. Microarray analysis of brassinosteroid-regulated genes in *Arabidopsis*. *Plant Physiol* **130**, 1319–1334 (2002).

177. Aldukhi, F., Deb, A., Zhao, C., Moffett, A. S. & Shukla, D. Molecular mechanism of brassinosteroid perception by the plant growth receptor BRI1. *J. Phys. Chem. B* **124**, 355–365 (2019).

178. Almlöf, M., Carlsson, J. & Åqvist, J. Improving the Accuracy of the Linear Interaction Energy Method for Solvation Free Energies. *J Chem Theory Comput* **3**, 2162–2175 (2007).

179. Brandsdal, B. O., Åqvist, J. & Smalås, A. O. Computational analysis of binding of P1 variants to trypsin. *Protein Sci.* **10**, 1584–1595 (2001).

180. Wickstrom, L., Gallicchio, E. & Levy, R. M. The linear interaction energy method for the prediction of protein stability changes upon mutation. *Proteins Struct. Funct. Bioinforma.* **80**, 111–125 (2012).

181. Hohmann, U. *et al.* Mechanistic basis for the activation of plant membrane receptor kinases by SERK-family coreceptors. *PNAS* (2018).

182. She, J., Han, Z., Zhou, B. & Chai, J. Structural basis for differential recognition of brassinolide by its receptors. *Protein Cell* **4**, 475–482 (2013).

183. Miranda, W. E., Noskov, S. Y. & Valiente, P. A. Improving the LIE Method for Binding Free Energy Calculations of Protein–Ligand Complexes. *J Chem Inf Model* **55**, 1867–1877 (2015).

184. Yang, X.-H., Xu, Z.-H. & Xue, H.-W. Arabidopsis Membrane Steroid Binding Protein 1 Is Involved in Inhibition of Cell Elongation. *Plant Cell* **17**, 116–131 (2005).

185. Zhou, A., Wang, H., Walker, J. C. & Li, J. BRL1, a leucine-rich repeat receptor-like protein kinase, is functionally redundant with BRI1 in regulating Arabidopsis brassinosteroid signaling. *Plant J.* **40**, 399–409 (2004).

186. Lozano-Elena, F. & Caño-Delgado, A. I. Emerging roles of vascular brassinosteroid receptors of the BRI1-like family. *Curr. Opin. Plant Biol.* **51**, 105–113 (2019).

187. Wu, W. *et al.* Somatic embryogenesis receptor-like kinase 5 in the ecotype Landsberg erecta of Arabidopsis is a functional RD LRR-RLK in regulating brassinosteroid signaling and cell death control. *Front. Plant Sci.* **6**, 852 (2015).

188. Muddana, S. S. & Peterson, B. R. Fluorescent cellular sensors of steroid receptor ligands. *Chembiochem* **4**, 848–855 (2003).

189. Gou, M., Ran, X., Martin, D. W. & Liu, C.-J. The scaffold proteins of lignin biosynthetic cytochrome P450 enzymes. *Nat. Plants* **4**, 299–310 (2018).

190. Hussan, R. H., Dubery, I. A. & Piater, L. A. Identification of MAMP-Responsive Plasma Membrane-Associated Proteins in Arabidopsis thaliana Following Challenge with Different LPS Chemotypes from *Xanthomonas campestris*. *Pathogens* **9**, (2020).

191. Hanwell, M. D. *et al.* Avogadro: an advanced semantic chemical editor, visualization, and analysis platform. *J. Cheminformatics* **4**, 1–17 (2012).

192. Halgren, T. A. Merck molecular force field. Extension of MMFF94 using experimental data, additional computational data, and empirical rules. *J Comput Chem* **17**, 616–641 (1996).

193. Sanner, M. F. Python: A Programming Language for Software Integration and Development. *J Mol Graph. Mod* **17**, 57–61 (1999).

194. Trott, O. & Olson, A. J. Software News and Update AutoDock Vina: improving the speed and accuracy of docking with a new scoring function, efficient optimization, and multithreading. *J Comput Chem* **31**, 455–461 (2010).

195. Rosenfeld, R. J. *et al.* Automated docking of ligands to an artificial active site: augmenting crystallographic analysis with computer modeling. *J. Comput. Aided Mol. Des.* **17**, 525–536 (2003).

196. Schrödinger, LLC. The PyMOL Molecular Graphics System, Version 2.5. (2015).

197. Wang, J. M., Wolf, R. M., Caldwell, J. W. & Kollman, P. A. Development and Testing of a General Amber Force-field. *J Comput Chem* **25**, 1157–1174 (2004).

198. Bayly, C. I., Cieplak, P., Cornell, W. & Kollman, P. A. A well-behaved electrostatic potential based method using charge restraints for deriving atomic charges: the RESP model. *J. Phys. Chem.* **97**, 10269–10280 (1993).

199. Jakalian, A., Bush, B. L., Jack, D. B. & Bayly, C. I. Fast, Efficient Generation of High-Quality Atomic Charges. AM1-BCC Model: I. Method. *J Comput Chem* **21**, 132–146 (2000).

200. Jakalian, A., Jack, D. B. & Bayly, C. I. Fast, Efficient Generation of High-Quality Atomic Charges. AM1-BCC Model: II. Parameterization and Validation. *J Comput Chem* **23**, 1623–1641 (2002).

201. Case, D. A. *et al.* Amber 2018, Univ. Calif. San Fr 1–923 (2018).

202. Frisch, M. J. gaussian09. [Http://www.Gaussian.Com](http://www.Gaussian.Com) (2009).

203. Chinea, G., Padron, G., Hooft, R. W., Sander, C. & Vriend, G. The use of position-specific rotamers in model building by homology. *Proteins Struct. Funct. Bioinforma.* **23**, 415–421 (1995).

204. Olsson, M. H., Søndergaard, C. R., Rostkowski, M. & Jensen, J. H. PROPKA3: consistent treatment of internal and surface residues in empirical p K a predictions. *J. Chem. Theory Comput.* **7**, 525–537 (2011).

205. Hornak, V. *et al.* Comparison of multiple Amber force-fields and development of improved protein backbone parameters. *Proteins* **65**, 712–725 (2006).

206. Lindahl, E. R. Molecular Dynamics Simulations. in *Molecular Modeling of Proteins* (ed. Kukol, A.) vol. 443 (Humana Press, Hertfordshire, 2008).

207. Páll, S., Abraham, M. J., Kutzner, C., Hess, B. & Lindahl, E. Tackling exascale software challenges in molecular dynamics simulations with GROMACS. in *Solving Software Challenges for Exascale* (eds. S Markidis & E Laure) vol. 8759 3–27 (2015).

208. Darden, T., York, D. & Pedersen, L. Particle Mesh Ewald: An $W \log(N)$ Method for Ewald Sums in Large Systems. *J Chem Phys* **98**, 10089–10093 (1993).

209. Essmann, U. *et al.* A Smooth Particle Mesh Ewald Method. *J Chem Phys* **103**, 8577–8592 (1995).

210. Verlet, L. Computer ‘Experiments’ on Classical Fluids. I. Thermodynamical Properties of Lennard-Jones Molecules. *Phys Rev* **159**, 98–103 (1967).

211. Berendsen, H. J. C., Postma, J. P. M., DiNola, A. & Haak, J. R. Molecular Dynamics with Coupling to an External Bath. *J Chem Phys* **81**, (1984).

212. Bussi, G., Donadio, D. & Parrinello, M. Canonical sampling through velocity rescaling. *J Chem Phys* **126**, (2007).

213. Hess, B., Bekker, H., Berendsen, H. J. & Fraaije, J. G. LINCS: A linear constraint solver for molecular simulations. *J. Comput. Chem.* **18**, 1463–1472 (1997).

214. Schneider, T. & Stoll, E. Molecular-Dynamics study of a 3-dimensional one-component model for distortive phase-transitions. *Phys Rev B* **17**, 1302–1322 (1978).

215. Nosé, S. & Klein, M. L. Constant pressure molecular dynamics for molecular systems. *Mol Phys* **50**, 1055–1076 (1983).

216. Parrinello, M. & Rahman, A. Polymorphic Transitions in Single Crystals: A New Molecular Dynamics Method. *J Appl Phys* **52**, 7182–7190 (1981).

217. Pronk, S. *et al.* GROMACS 4.5: a high-throughput and highly parallel open source molecular simulation toolkit. *Bioinformatics* **29**, 845–854 (2013).

218. Millard, S. P. *EnvStats: An R Package for Environmental Statistics*. (Springer Science & Business Media, 2013).

219. Millard, S. P., Kowarik, A. & Kowarik, M. A. Package ‘EnvStats’. *Package Environ. Stat. Version 2*, 31–32 (2018).

220. R Core Team. *R: A Language and Environment for Statistical Computing*. (R Foundation for Statistical Computing, Vienna, Austria, 2021).

221. Gomes, D. E. B., da Silva, A. W. S., Lins, R. D., Pascutti, P. G. & Soares, T. A. HbMap2Grace. Software for mapping the hydrogen bond frequency. LMDM (2009).

222. Gutierrez-de-Teran, H. & Åqvist, J. Linear Interaction Energy: Method and Applications in Drug Design. in *Computational Drug Discovery and Design, Methods in Molecular Biology* (ed. Baron, R.) vol. 819 305–323 (Springer Science+Business, 2012).

223. Hansson, T., Marelius, J. & Åqvist, J. Ligand Binding Affinity Prediction by Linear Interaction Energy Methods. *J Comput-Aided Mol Des* **12**, 27–35 (1998).

224. Marelius, J., Hansson, T. & Åqvist, J. Calculation of Ligand Binding Free Energies from Molecular Dynamics Simulations. *Int J Quantum Chem* **69**, 77–88 (1998).

225. Bogan, A. A. & Thorn, K. S. Anatomy of hot spots in protein interfaces. *J. Mol. Biol.* **280**, 1–9 (1998).

226. van der Spoel, D. *et al.* Gromacs User Manual. Royal Institute of Technology and Uppsala University (2010).

227. Easlon, H. M. & Bloom, A. J. Easy Leaf Area: Automated digital image analysis for rapid and accurate measurement of leaf area. *Appl. Plant Sci.* **2**, 1400033 (2014).

228. Engler, C. *et al.* A Golden Gate Modular Cloning Toolbox for Plants. *ACS Synth. Biol.* **3**, 839–843 (2014).

229. Weber, E., Gruetzner, R., Werner, S., Engler, C. & Marillonnet, S. Assembly of Designer TAL Effectors by Golden Gate Cloning. *PLOS ONE* **6**, e19722 (2011).

230. Grützner, R. *et al.* High-efficiency genome editing in plants mediated by a Cas9 gene containing multiple introns. *Technol. Appl. Plants* **2**, 100135 (2021).

231. Castel, B., Tomlinson, L., Locci, F., Yang, Y. & Jones, J. D. G. Optimization of T-DNA architecture for Cas9-mediated mutagenesis in *Arabidopsis*. *PLOS ONE* **14**, e0204778 (2019).

232. Chen, B. *et al.* Dynamic Imaging of Genomic Loci in Living Human Cells by an Optimized CRISPR/Cas System. *Cell* **155**, 1479–1491 (2013).

233. Dang, Y. *et al.* Optimizing sgRNA structure to improve CRISPR-Cas9 knockout efficiency. *Genome Biol.* **16**, 280 (2015).

234. Concordet, J.-P. & Haeussler, M. CRISPOR: intuitive guide selection for CRISPR/Cas9 genome editing experiments and screens. *Nucleic Acids Res.* **46**, W242–W245 (2018).

235. Clough, S. J. & Bent, A. F. Floral dip: a simplified method for *Agrobacterium* -mediated transformation of *Arabidopsis thaliana*. *Plant J.* **16**, 735–743 (1998).

236. Janik, K., Stellmach, H., Mittelberger, C. & Hause, B. Characterization of Phytoplasma Effector Protein Interaction with Proteinaceous Plant Host Targets Using Bimolecular Fluorescence Complementation (BiFC). in *Phytoplasmas: Methods and Protocols* (eds. Musetti, R. & Pagliari, L.) 321–331 (Springer New York, New York, NY, 2019). doi:10.1007/978-1-4939-8837-2_24.

237. Asseck, L. Y. & Grefen, C. Detecting Interactions of Membrane Proteins: The Split-Ubiquitin System. in *Two-Hybrid Systems: Methods and Protocols* (ed. Oñate-Sánchez, L.) 49–60 (Springer New York, New York, NY, 2018). doi:10.1007/978-1-4939-7871-7_4.

238. Winkler, M. *et al.* Variation in auxin sensing guides AUX/IAA transcriptional repressor ubiquitylation and destruction. *Nat Commun* **8**, (2017).

239. Majovsky, P. *et al.* Targeted proteomics analysis of protein degradation in plant signaling on an LTQ-Orbitrap mass spectrometer. *J. Proteome Res.* **13**, 4246–4258 (2014).

240. Rivera, D. G. *et al.* Synthesis of spirostanic analogues of brassinosteroids via homogeneous permanganate dihydroxylation. *J Chem Res* 53–54 (2004).

241. Hernández-Campoalegre, G. Síntesis de derivados de la diosgenina con potencial actividad promotora del crecimiento vegetal. (Universidad de la Habana, Cuba, 2018).

242. Valdés-Cantero, A. Síntesis de derivados esteroidales de la cafeína con posible actividad biológica. (Universidad de la Habana, Cuba, 2017).

243. Brauch, S. Novel Tools for Protein Analysis and Modification: From Chemical Probes to New Ligation Methods. (Universitäts-und Landesbibliothek Sachsen-Anhalt, 2014).

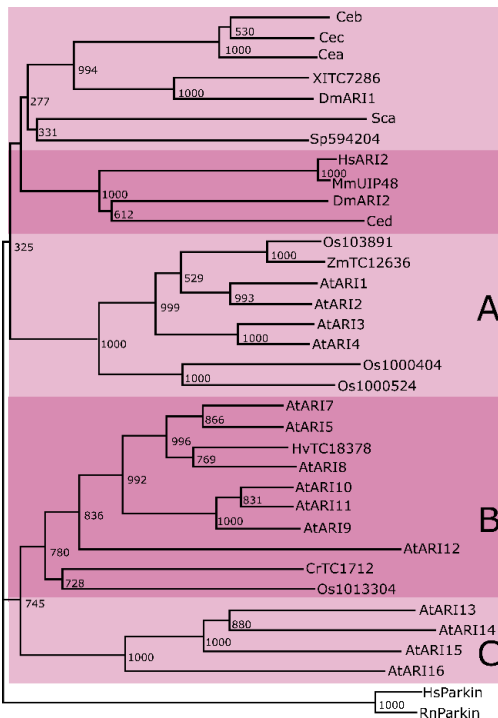
244. Sproß, J. *et al.* Multidimensional nano-HPLC coupled with tandem mass spectrometry for analyzing biotinylated proteins. *Anal. Bioanal. Chem.* **405**, 2163–2173 (2013).

245. Church, R. F. & Weiss, M. J. Diazirines. II. Synthesis and properties of small functionalized diazirine molecules. Observations on the reaction of a diaziridine with the iodine-iodide ion system. *J. Org. Chem.* **35**, 2465–2471 (1970).

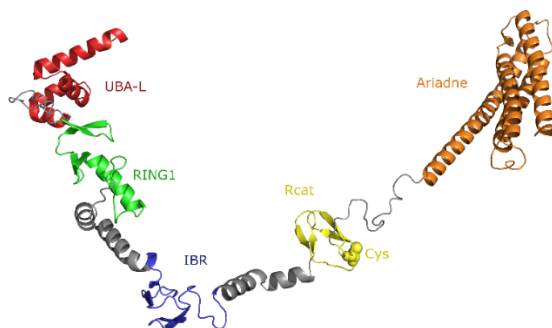
246. Czechowski, T., Stitt, M., Altmann, T., Udvardi, M. K. & Scheible, W.-R. Genome-wide identification and testing of superior reference genes for transcript normalization in *Arabidopsis*. *Plant Physiol.* **139**, 5–17 (2005).

247. Roh, H. *et al.* Genetic evidence for the reduction of brassinosteroid levels by a BAHD acyltransferase-like protein in *Arabidopsis*. *Plant Physiol.* **159**, 696–709 (2012).

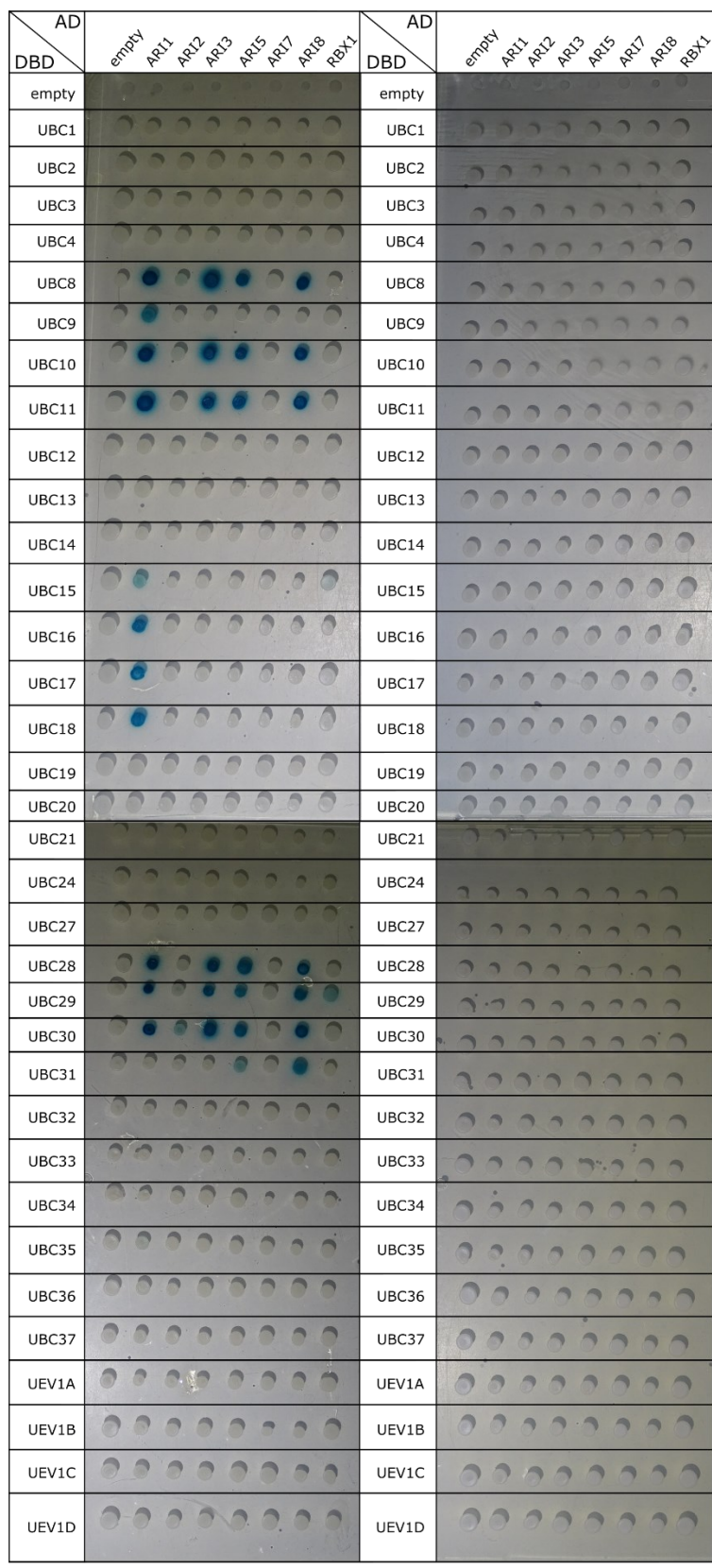
SUPPLEMENTARY INFORMATION



Supplementary Figure S1. Conservation of the RING-IBR-Rcat supradomain and phylogenetic analysis. Phylogenetic tree generated from alignment of the Cys-rich region from the ARI proteins of *Arabidopsis* (AtARI1–AtARI15), fruitfly (DmARI1 and DmARI2), Brewer's yeast (*Saccharomyces cerevisiae*; Sca), fission yeast (*Schizosaccharomyces pombe*; Sp594204), *Caenorhabditis elegans* (Cea, Ceb, Cec, and Ced), mouse (*Mus musculus*; MmUIP48), human (HsARI2), rice (*Oryza sativa*; Os103891, Os1000404, Os1000524, and Os1013304), *Xenopus laevis* (XITC7286), barley (*Hordeum vulgare*; HvTC18378), *Chlamydomonas reinhardtii* (CrTC1712), maize (*Zea mays*; TC12636), and two PARKIN proteins of human (HsParkin) and rat (RnParkin). The two PARKIN proteins (HsParkin and RnParkin) were used as outgroup. The bootstrap values are placed at the nodes. Clades are shaded with different purple levels for better distinction. Adapted from ⁷⁶.



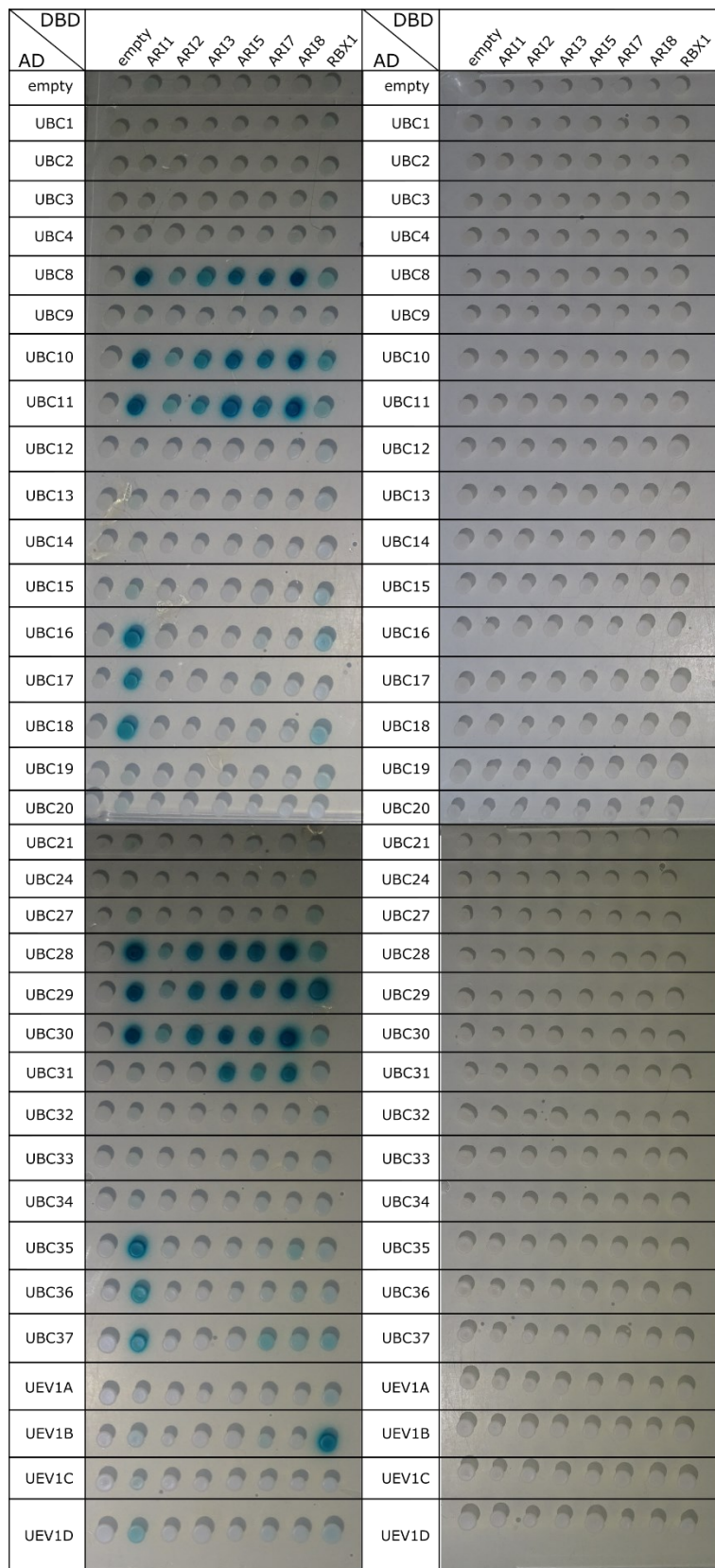
Supplementary Figure S2. Open conformation of AtARI1 alpha-fold structure (Q949V6). N-terminal and C-terminal intrinsic disorder regions were hidden, and domains were re-arranged mimicking an open conformation for better depiction of domains. Ubiquitin associated-like domain (UBA-L, red), RING domain (green), IBR (blue), Rcat (yellow) and Ariadne (orange).



+ X-Gal

- X-Gal

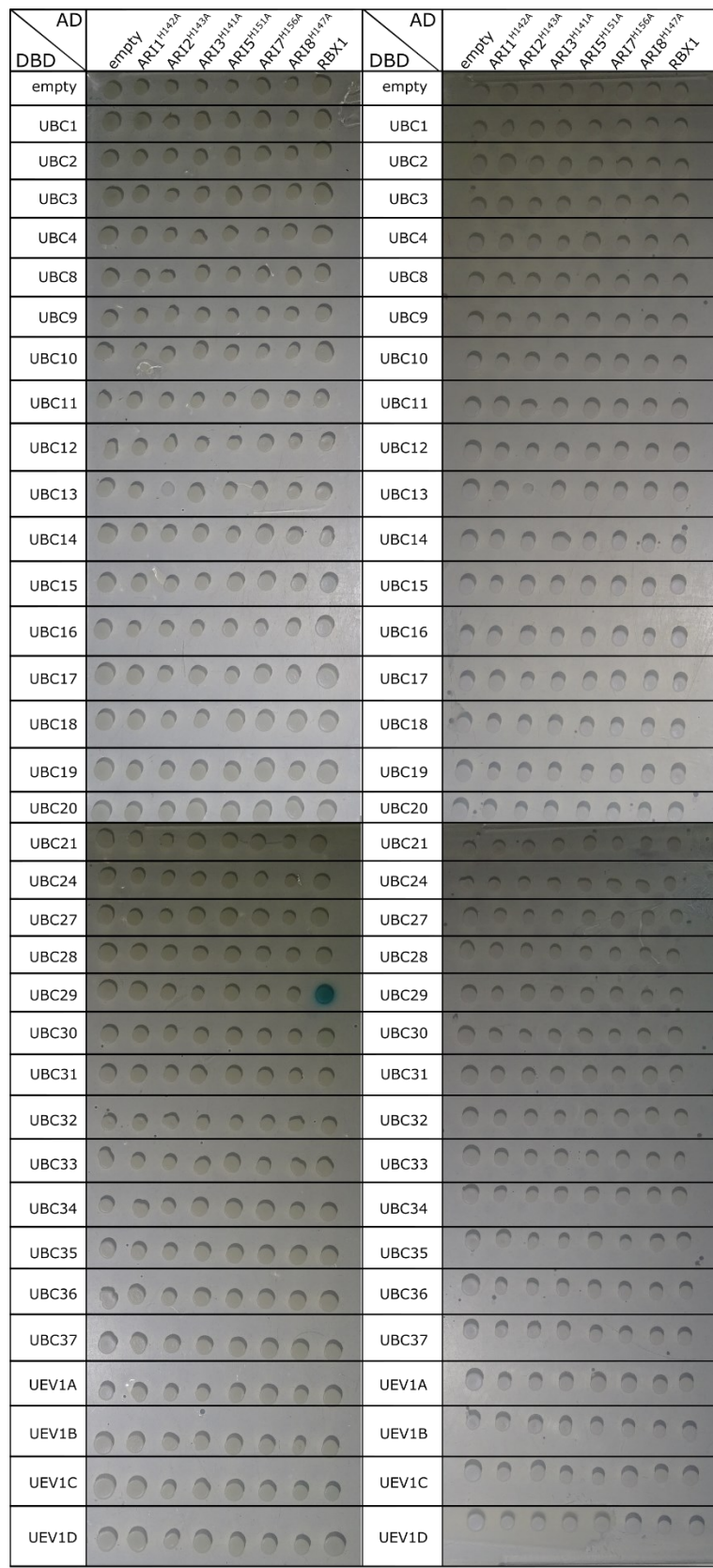
Supplementary Figure S3. Complete LexA Y2H assays between AD-AtARIs (native) and DBD-E2s. Presence of interaction is depicted in blue in the left panel. Growth control corresponds to the right panel.



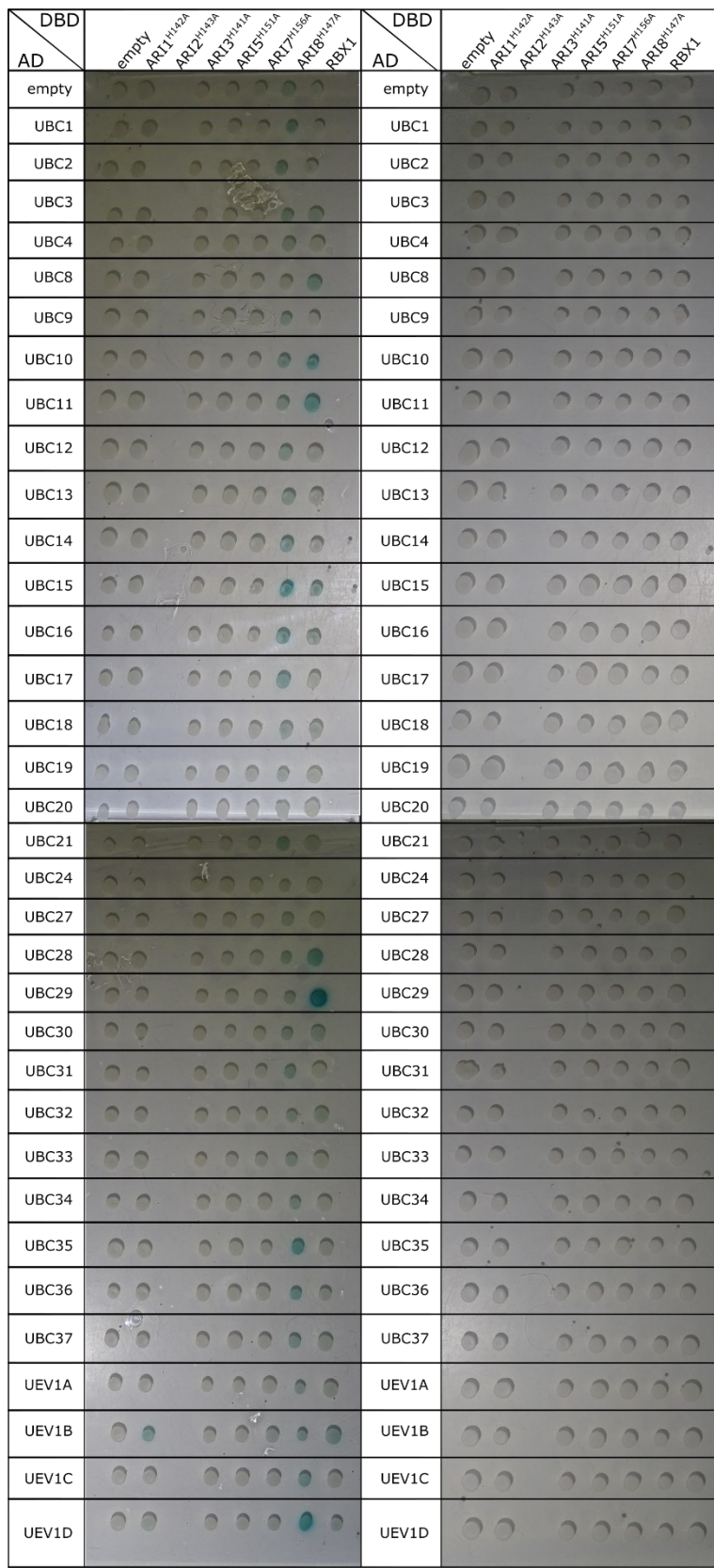
+ X-Gal

- X-Gal

Supplementary Figure S4. Complete LexA Y2H assays between DBD-AtARIs (native) and AD-E2s. Presence of interaction is depicted in blue in the left panel. Growth control corresponds to the right panel.



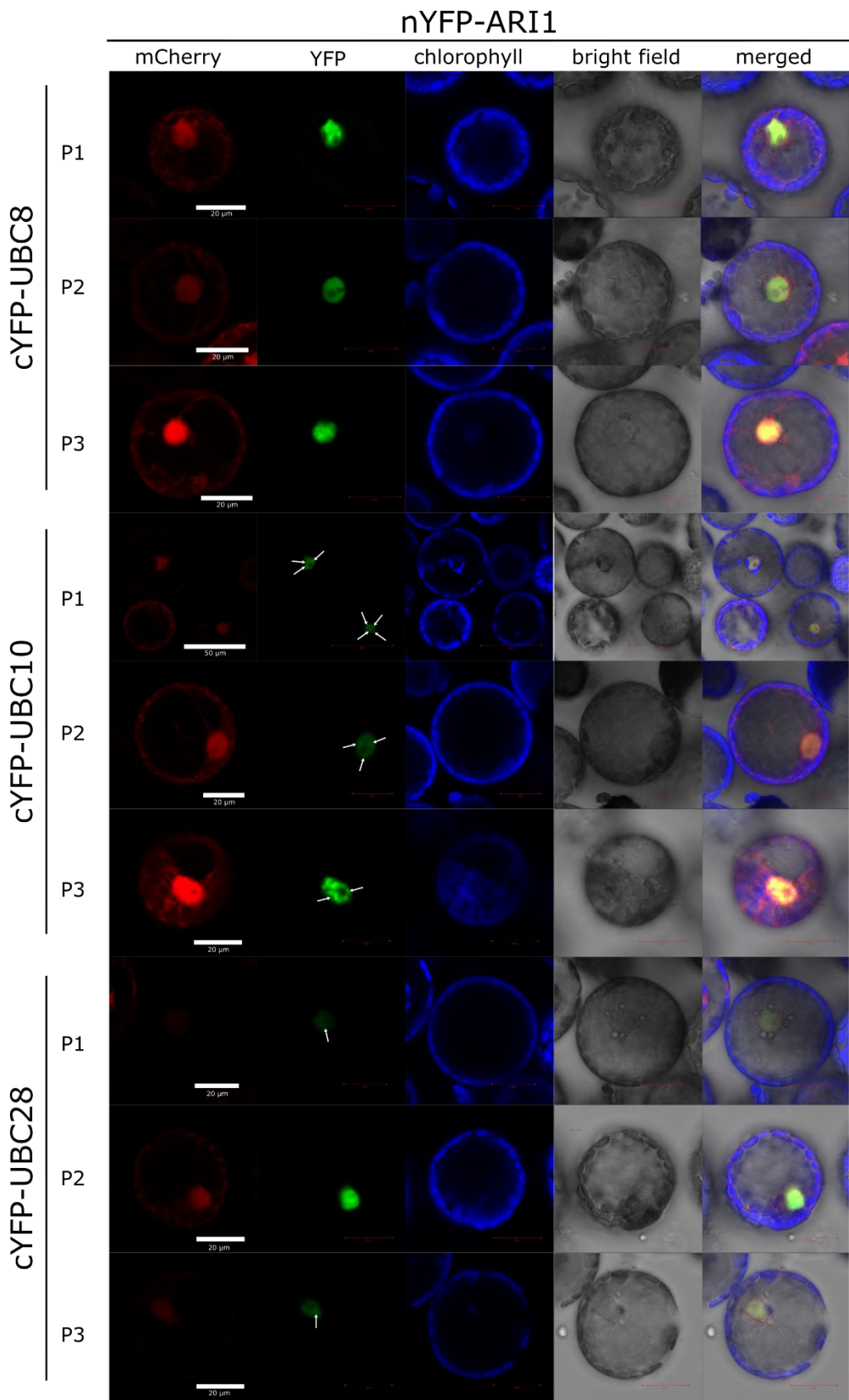
Supplementary Figure S5. Complete LexA Y2H assays between AD-AtARls (mutant) and DBD-E2s. Presence of interaction is depicted in blue in the left panel. Growth control corresponds to the right panel.



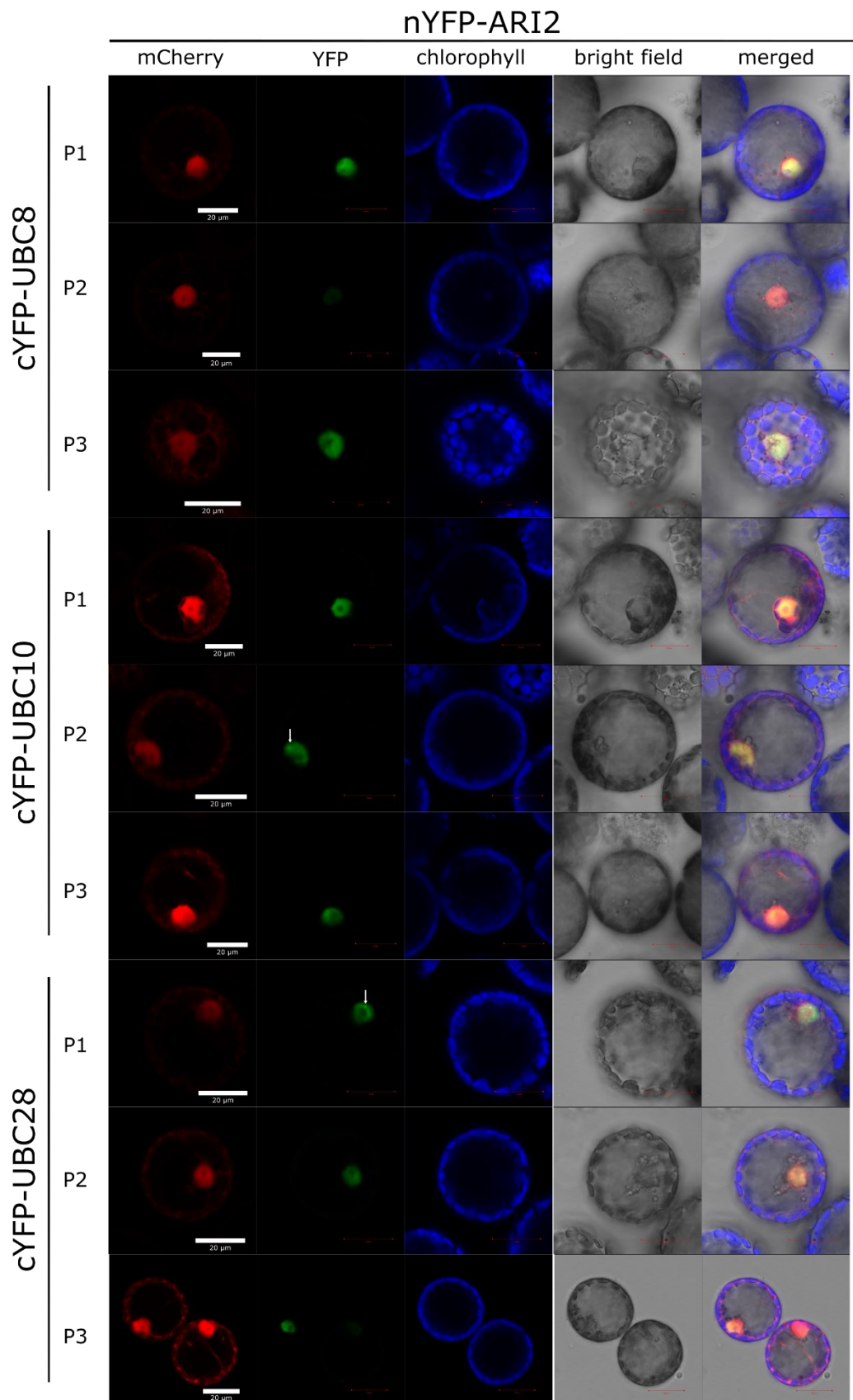
+ X-Gal

- X-Gal

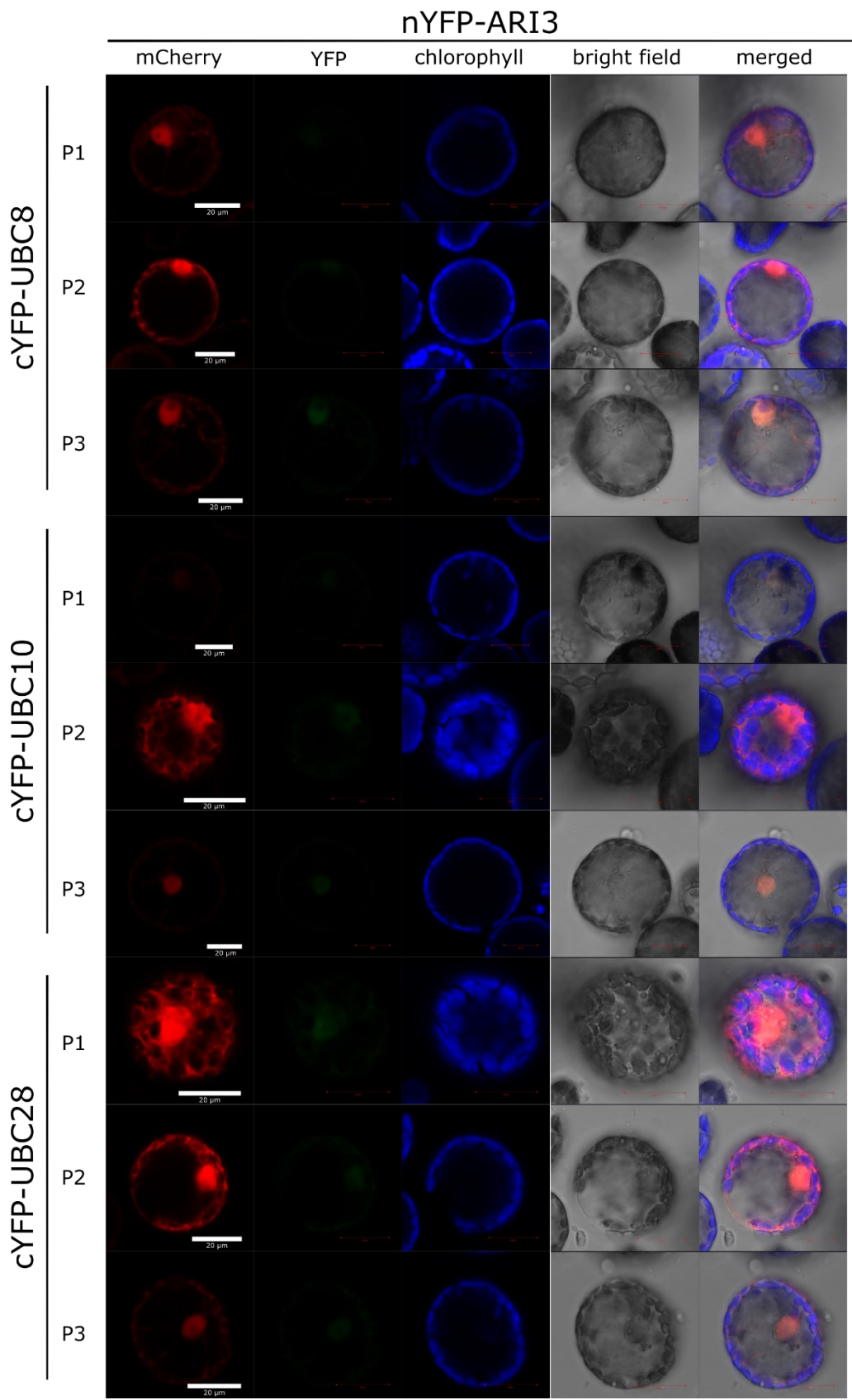
Supplementary Figure S6. Complete LexA Y2H assays between DBD-AtARIs (mutant) and AD-E2s. Presence of interaction is depicted in blue in the left panel. Growth control corresponds to the right panel.



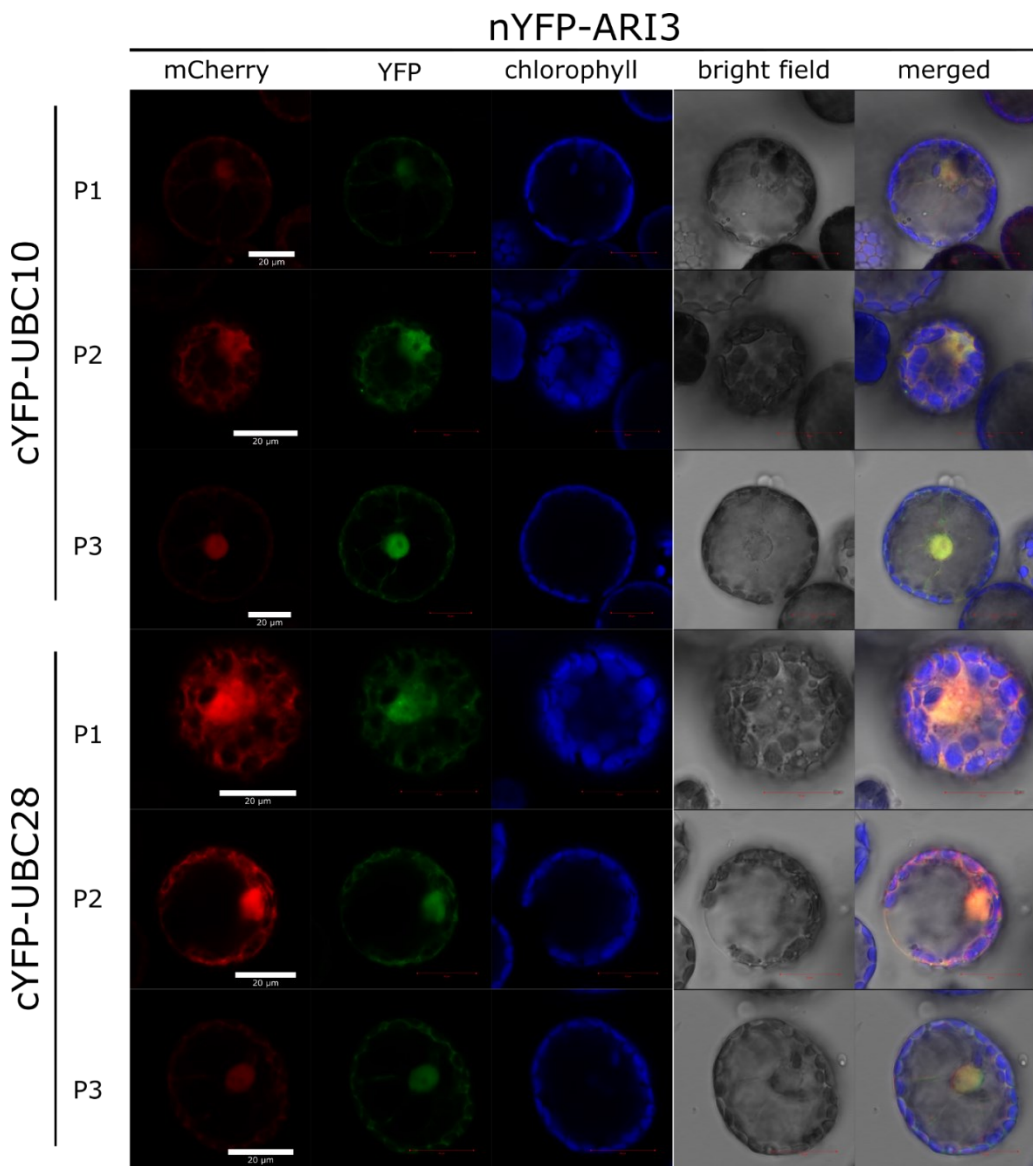
Supplementary Figure S7. Microscopy image of protoplasts expressing nYFP-AtARI1 and cYFP-AtUBC8/AtUBC10/AtUBC28. White arrows indicate specks.



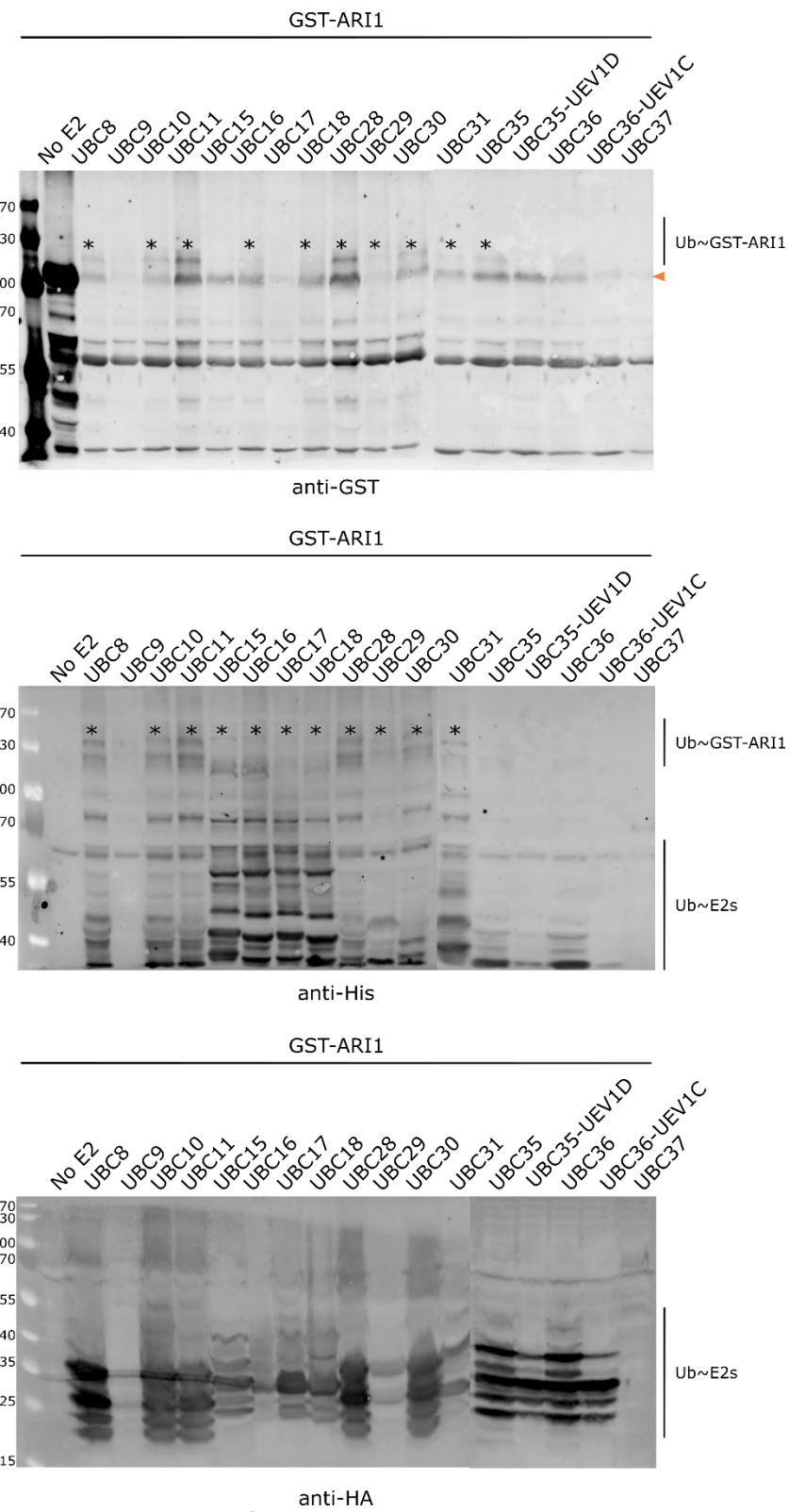
Supplementary Figure S8. Microscopy image of protoplasts expressing nYFP-AtARI2 and cYFP-AtUBC8/AtUBC10/AtUBC28. White arrows indicate specks. Microscopy settings were set as in Supp. Fig. S7.



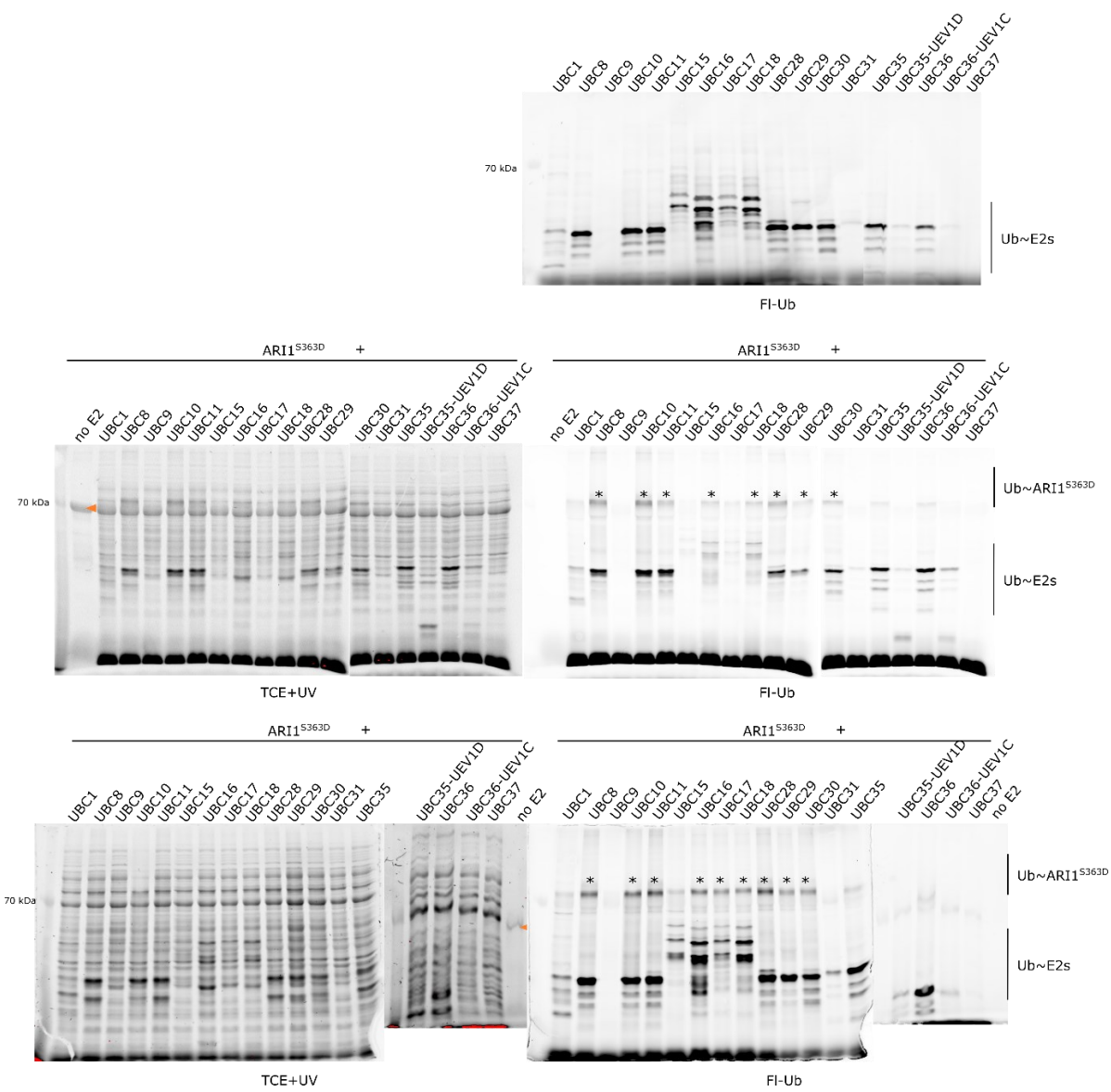
Supplementary Figure S9. Microscopy image of protoplasts expressing nYFP-AtARI3 and cYFP-AtUBC8/AtUBC10/AtUBC28. Microscopy settings were set as in Supp. Fig. S7.

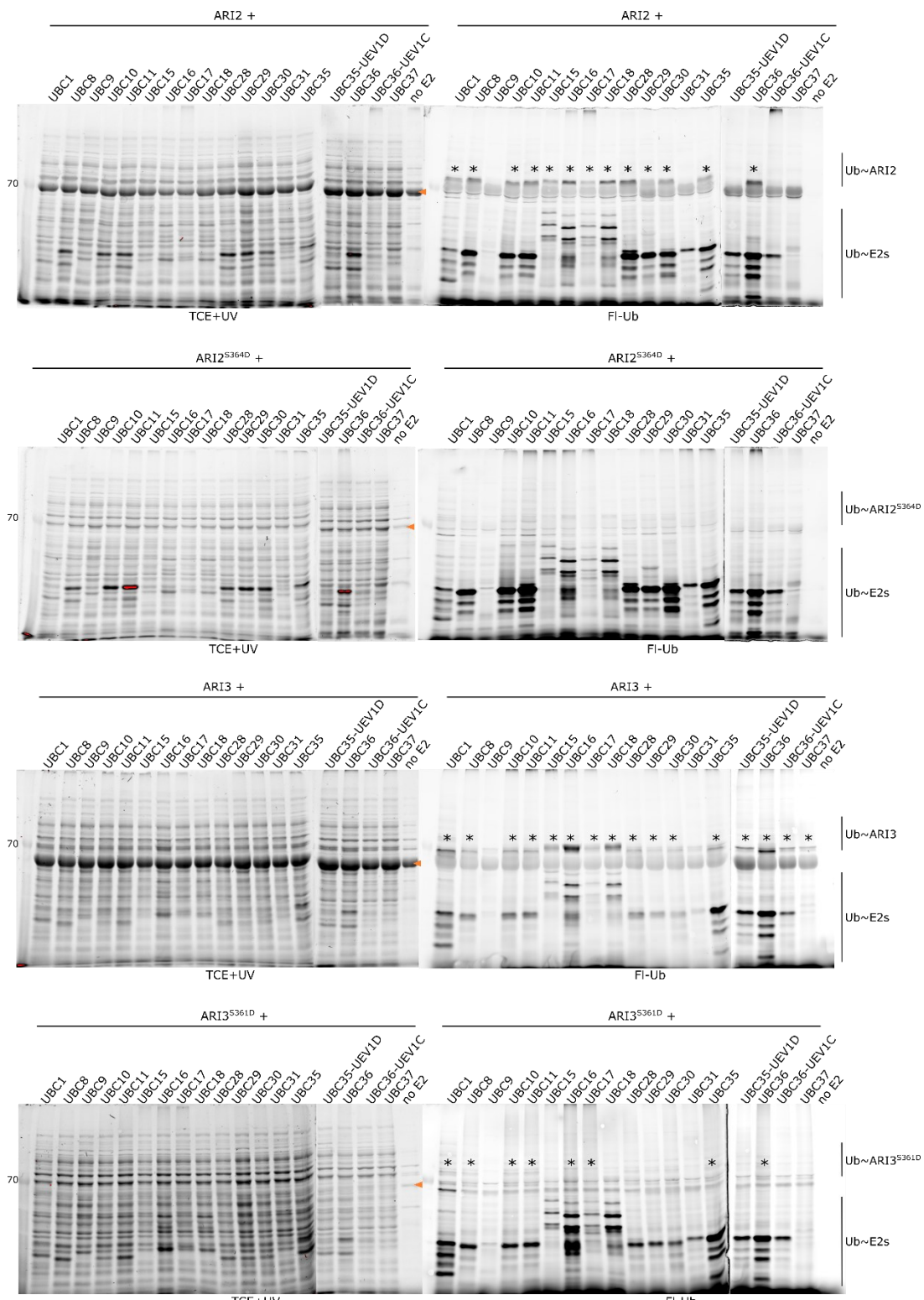


Supplementary Figure S10. Microscopy image of protoplasts expressing nYFP-ARI3 and cYFP-UBC8/UBC10/UBC28.
The contrast was enhanced for better depiction of the interaction.

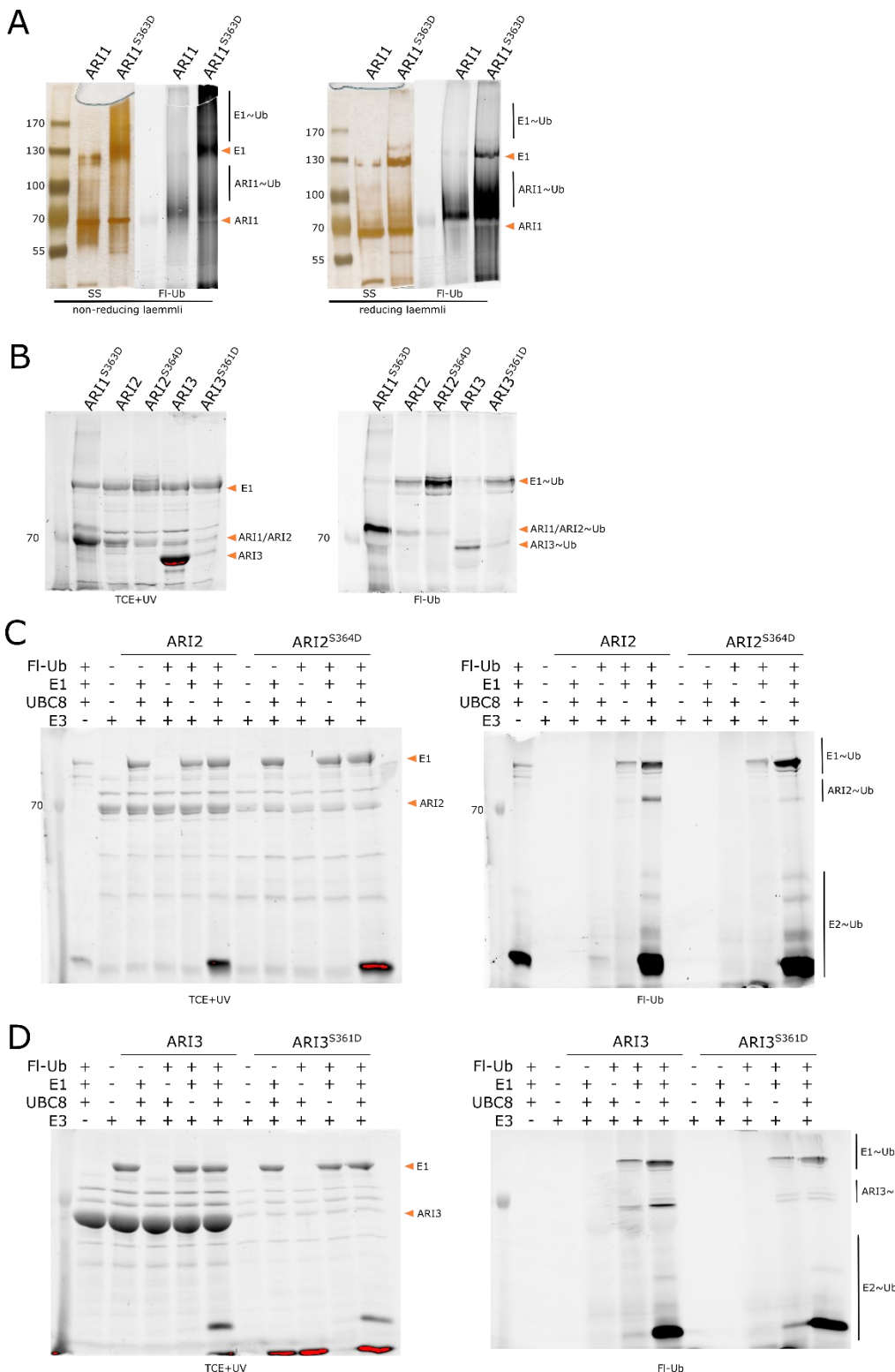


Supplementary Figure S11. UbiGate assay of co-expressed GST-AtARI1 and pUG constructs. pUG constructs contain AtUBA1 (E1), HA-AtUBC# (E2) and His-Ubiquitin. Each pUG construct is depicted by the E2 it contains. Both pUG and GST-AtARI1 constructs were co-expressed in *E. coli* and total protein extracts were analyzed. Immunoblots of autoubiquitylation reactions α -GST, α -His and α -HA. Asterisks represent $\text{Ub}^{\sim}\text{GST-AtARI1}$ and orange triangles depict non-ubiquitylated proteins.

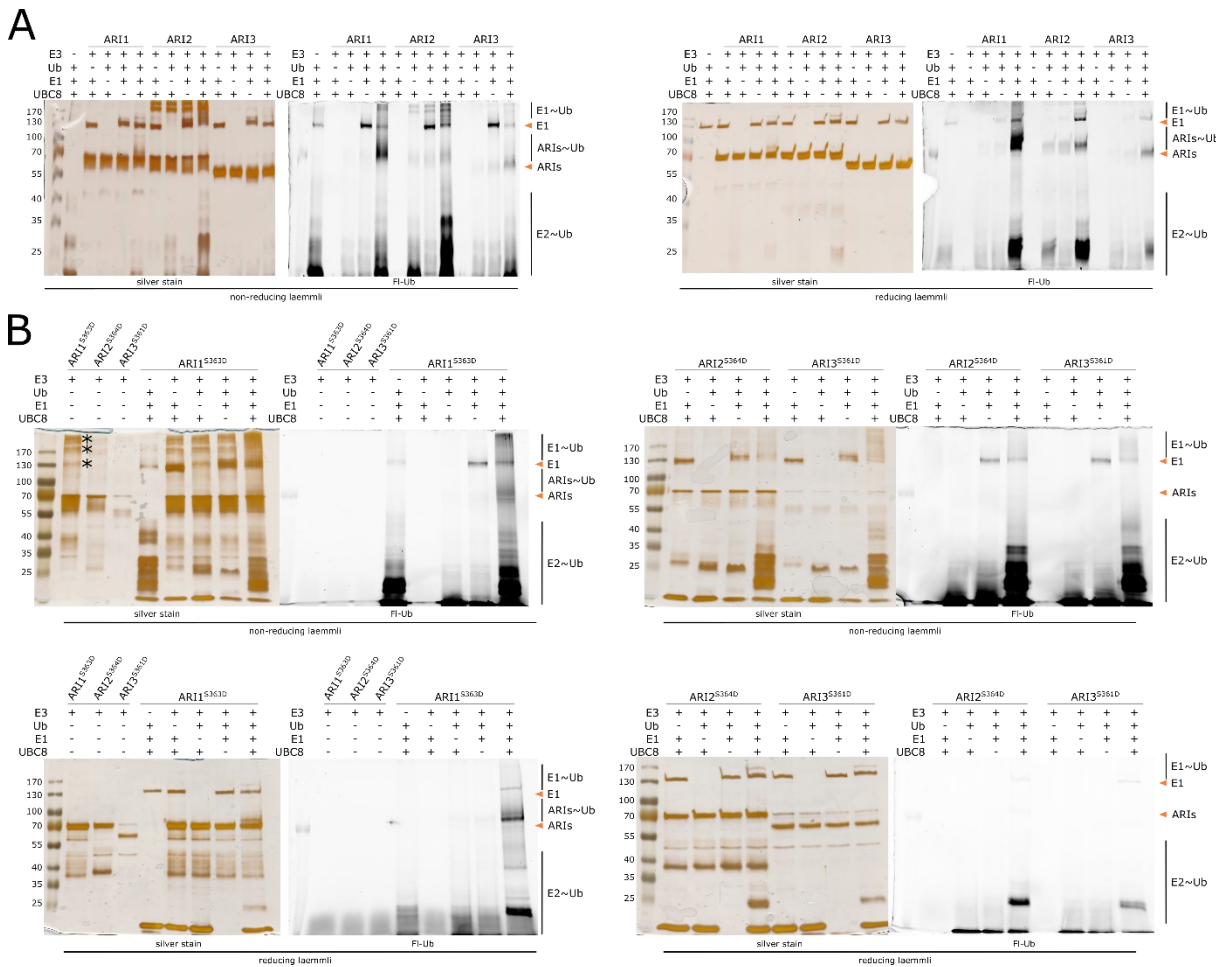




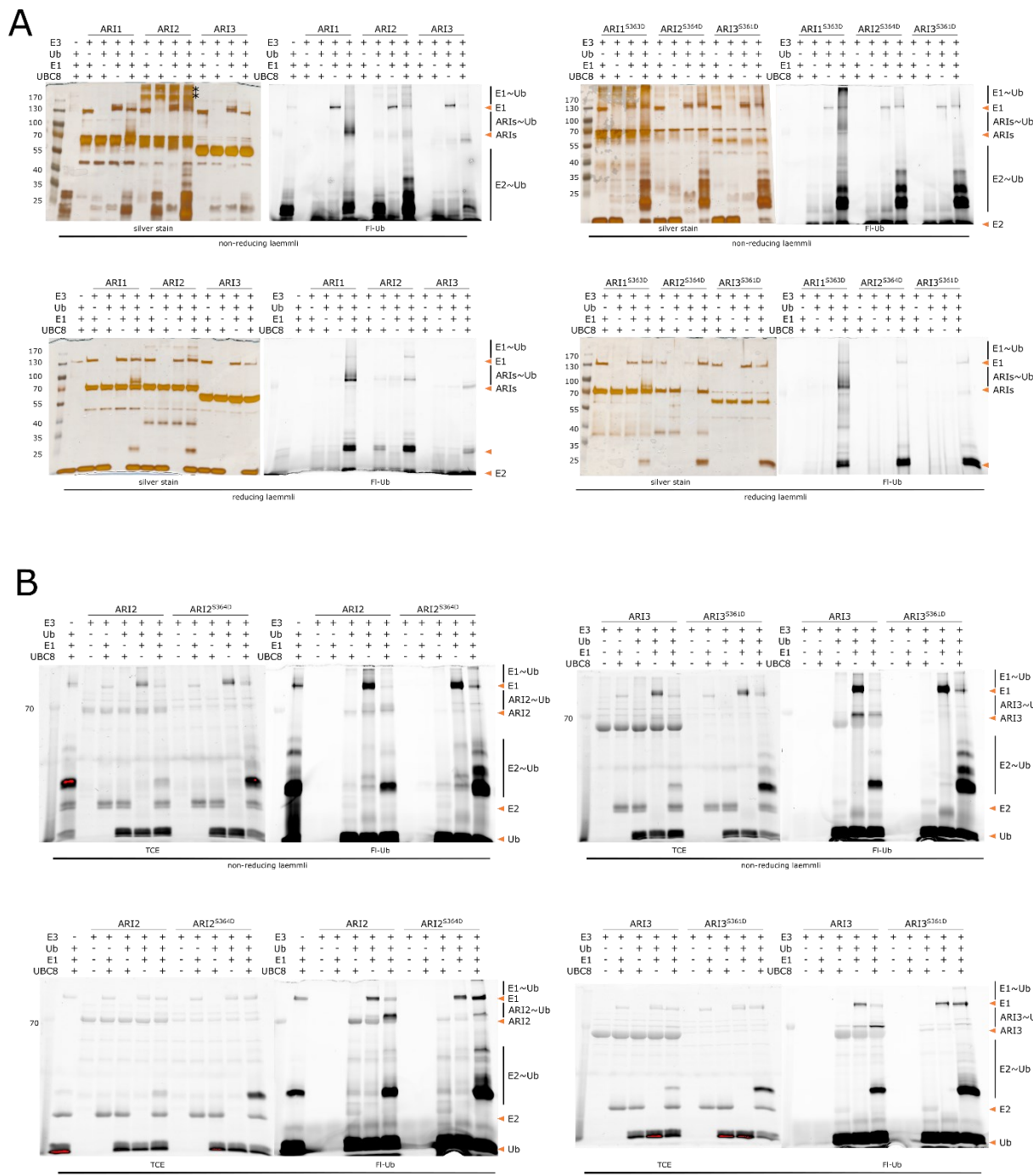
Supplementary Figure S12. UbiGate assay of tag-less AtARIs and pUG constructs. pUG constructs contain AtUBA1 (E1), HA-AtUBC# (E2) and His-Ubiquitin. Each pUG construct is depicted by the E2 it contains. Semi-purified tag-less AtARIs and purified tag-less AtARI1 were incubated with total protein extracts from *E. coli* expressing pUG constructs for 30min. Additionally Fl-Ub was added to the mix. Protein visualization was performed with Trichloroethanol (TCE) in-gel and irradiating with UV for 1-2 min in BioRad transilluminator. Asterisks represent Ub~AtARIs.



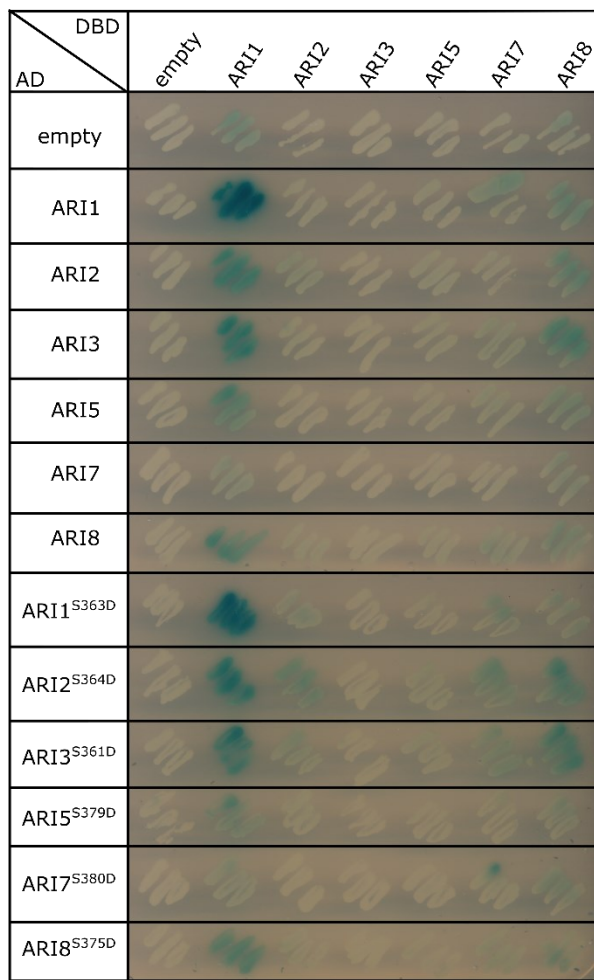
Supplementary Figure S13. In vitro Autoubiquitylation assay of AtARIs. A-B) Autoubiquitylation reaction of AtARI1, AtARI1^{S363D}, AtARI2, AtARI2^{S364D}, AtARI3 and AtARI3^{S361D} mediated by AtUBC8, uncropped gels from **Figure 11B-C**. **C-D)** Autoubiquitylation assay in reducing conditions of AtARI2 and AtARI2^{S364D} mediated by AtUBC8. **D)** Autoubiquitylation assay in reducing conditions of AtARI3 and AtARI3^{S361D} mediated by AtUBC8. **C-D)** Protein visualization was performed with TCE in-gel and irradiating with UV for 1-2 min in BioRad transilluminator (left), while Ub~proteins were visualized with a 488nm fluorescence scan (right).



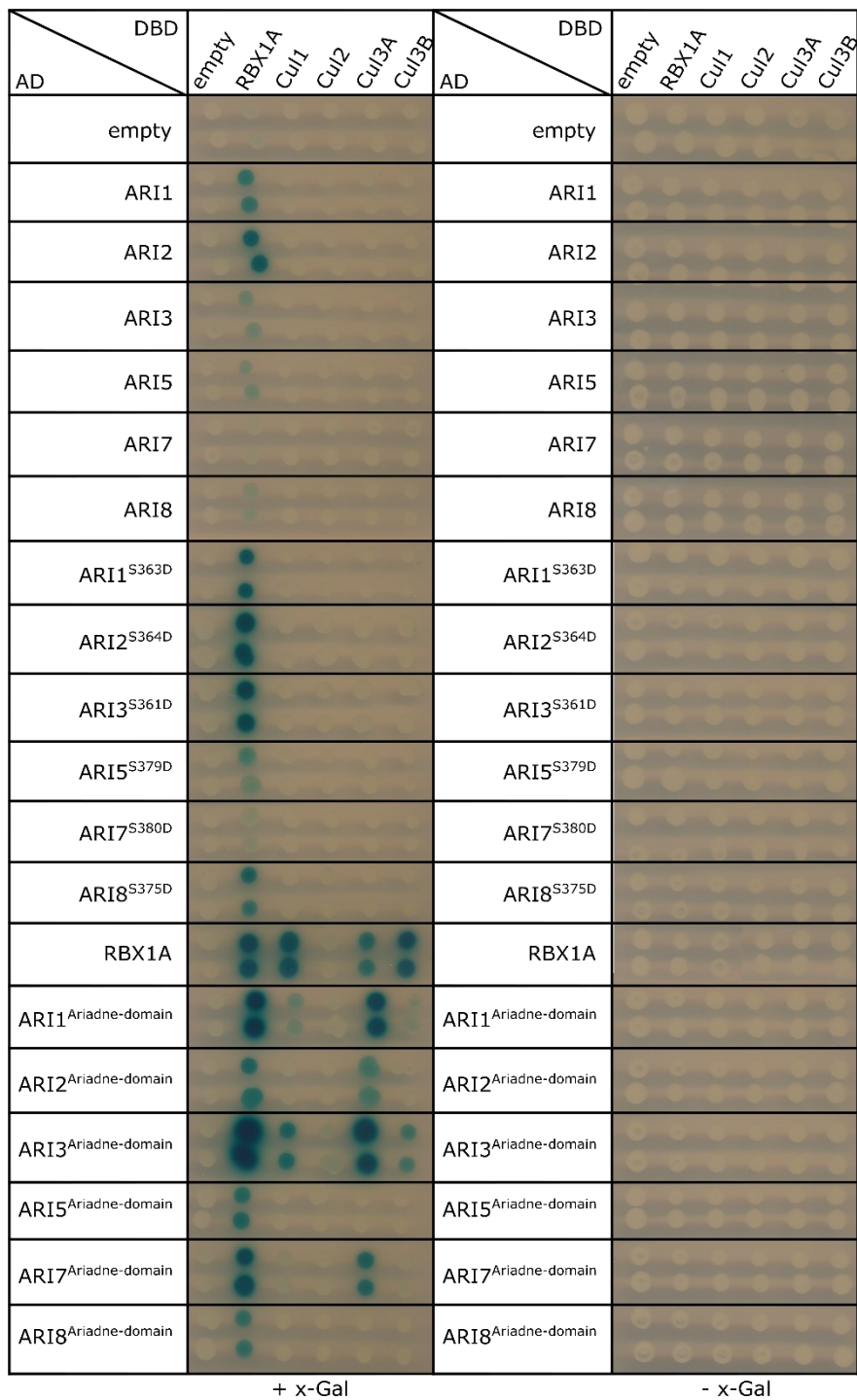
Supplementary Figure S14. *In vitro* Autoubiquitylation assay of AtARIs in non-reducing conditions. **A)** Autoubiquitylation reaction of AtARI1, AtARI2 and AtARI3 mediated by AtUBC8. **B)** Autoubiquitylation assay AtARI1^{S363D}, AtARI2^{S364D} and AtARI3^{S361D} mediated by AtUBC8. **A-B)** Silver stained (SS) and 488nm fluorescence scan (Fl-Ub) of autoubiquitylation reactions in non-reducing (up) and reducing lämmli (down). Asterisks in **B)** indicate possible E3~E3 derivatives.



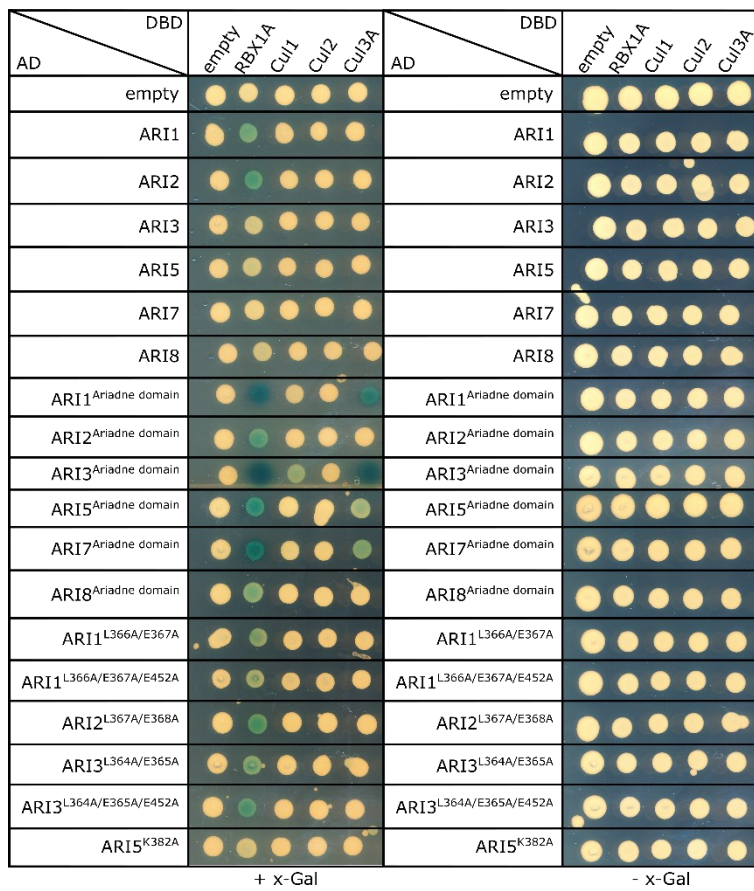
Supplementary Figure S15. *In vitro* Autoubiquitylation assay of AtARIs. A) Autoubiquitylation reaction of AtARI1, AtARI2, AtARI3, AtARI1^{S363D}, AtARI2^{S364D} and AtARI3^{S361D} mediated by AtUBC8. Silver stained (SS) and 488nm fluorescence scan (Fl-Ub) of autoubiquitylation reactions in non-reducing (up) and reducing lämmli (down). **B)** Autoubiquitylation reaction of freshly two-step-purified AtARI2, AtARI3, AtARI2^{S364D} and AtARI3^{S361D} mediated by AtUBC8 under reducing conditions analyzed with non-reducing (up) and reducing lämmli (down). Protein visualization was performed with Trichloroethanol (TCE) in-gel and irradiating with UV for 1-2 min in BioRad transilluminator (left), while Ub~proteins were visualized with a 488nm fluorescence scan (right). Asterisks indicate possible E3~E3 derivatives.



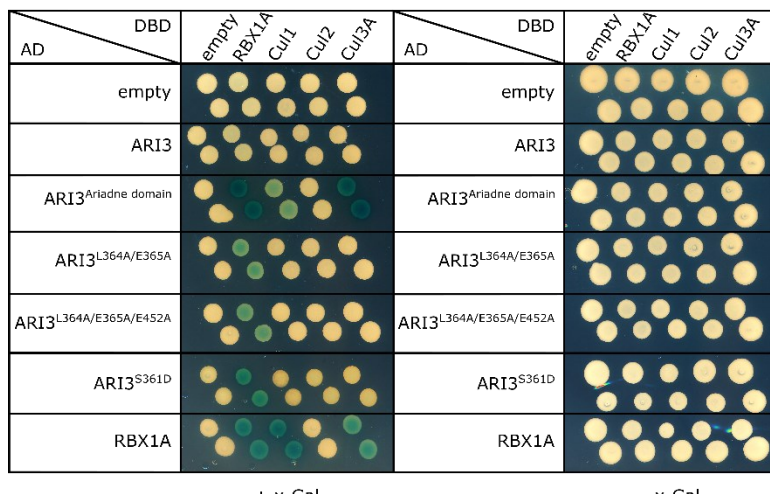
Supplementary Figure S16. LexA Y2H assays between DBD-AtARIs (native) and AD-AtARIs (native and hyperactive).
Presence of interaction is depicted in blue.



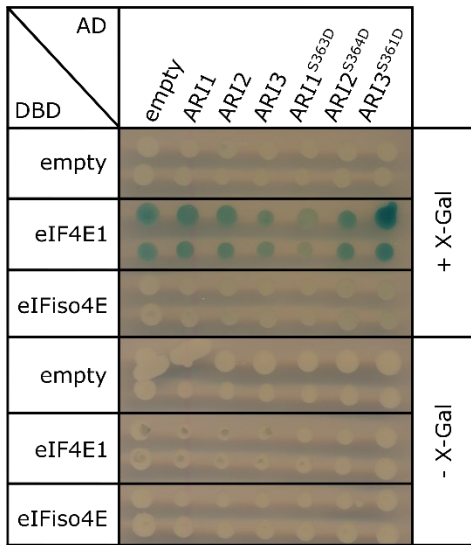
Supplementary Figure S17. LexA Y2H assays between DBD-AtCullins/AtRBX1A and AD-AtARIs (native, hyperactive and Ariadne domains). Presence of interaction is depicted in blue in the left panel. Growth control corresponds to the right panel. AD-AtRBX1A was used as a control for Cullin interaction.



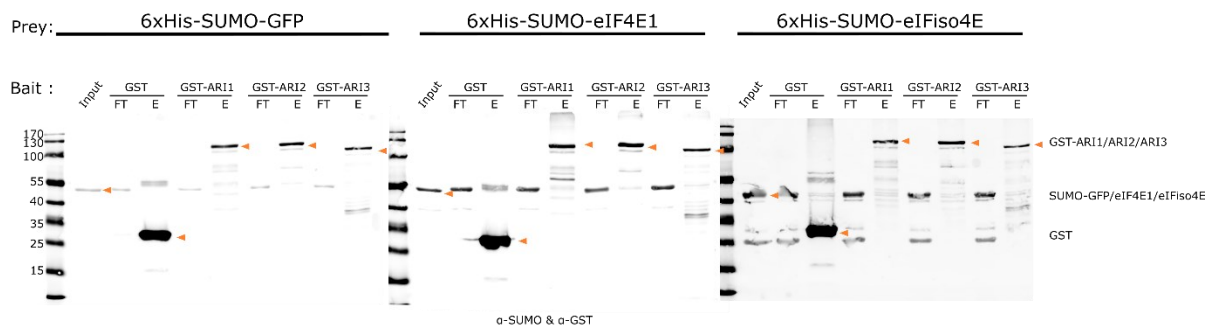
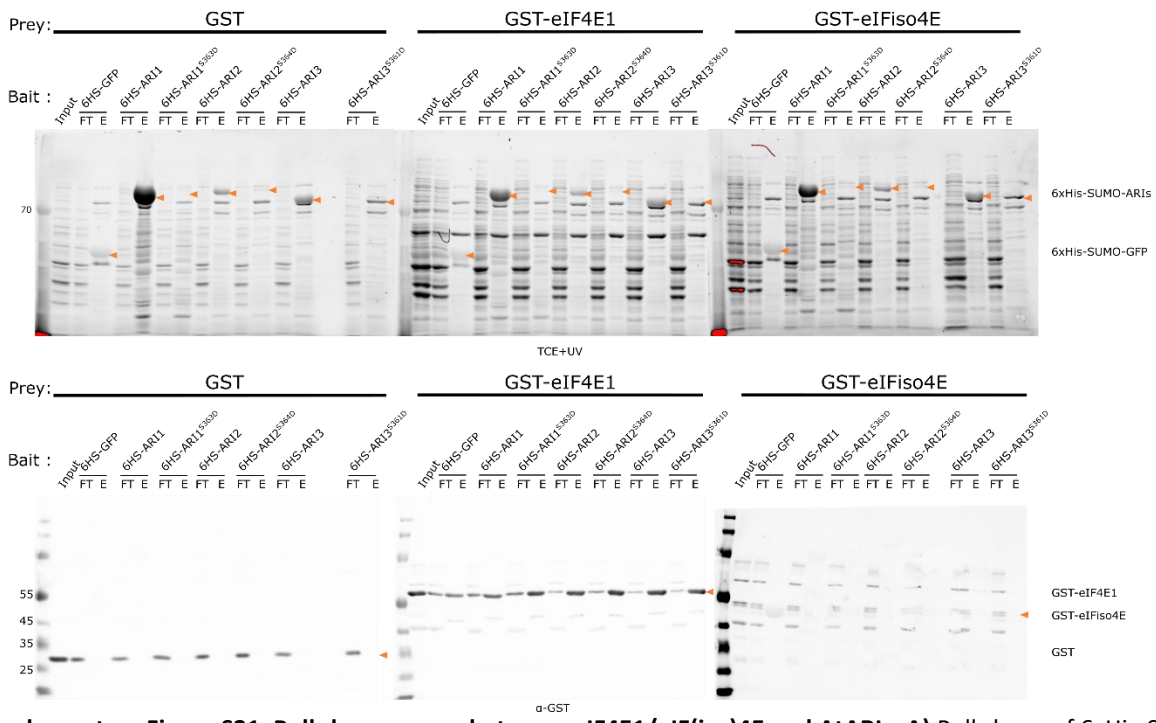
Supplementary Figure S18. LexA Y2H assays between DBD-AtCullins/AtRBX1A and AD-AtARIs (native, mutants and Ariadne domains). Presence of interaction is depicted in blue in the left panel. Growth control corresponds to the right panel.



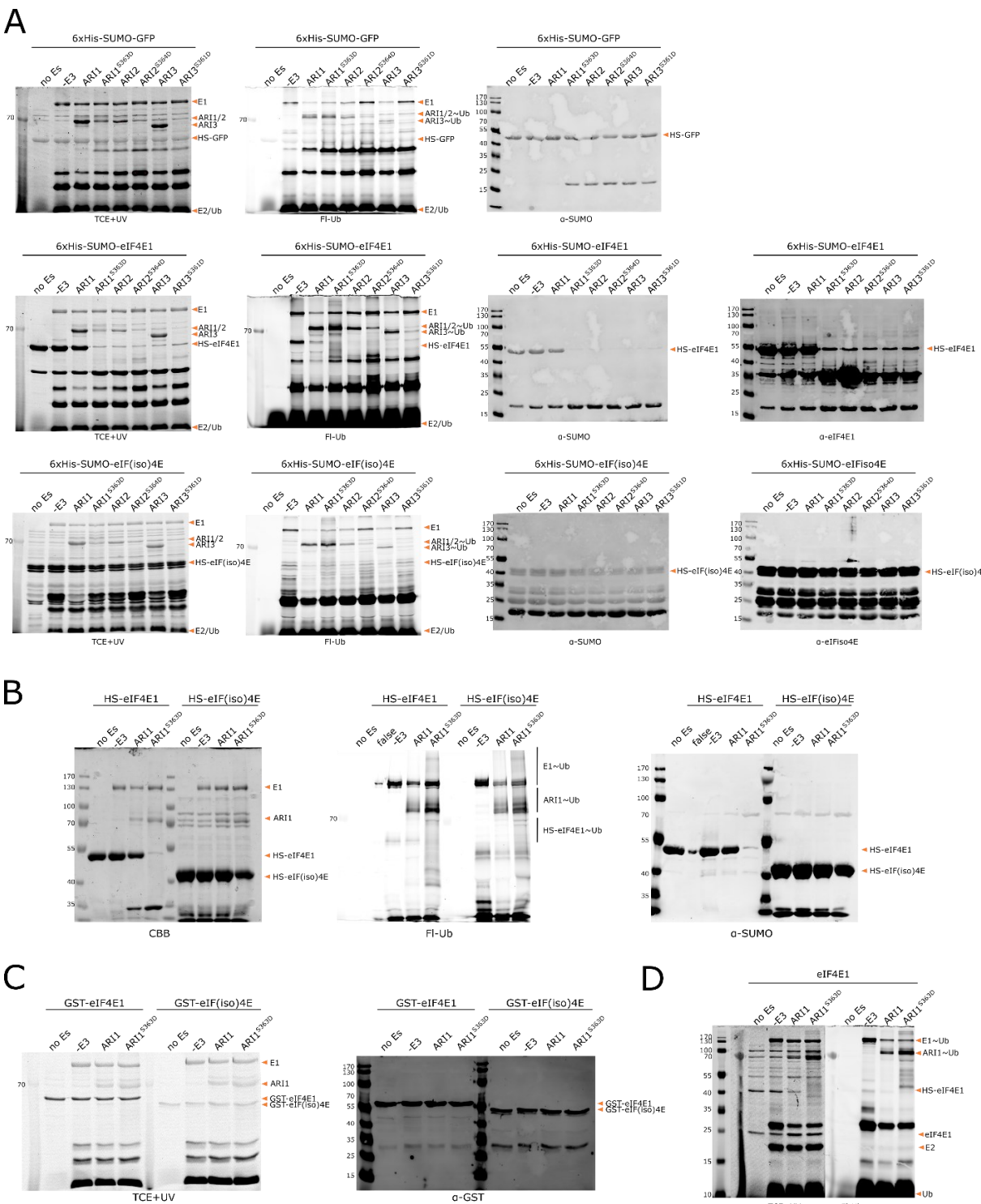
Supplementary Figure S19. LexA Y2H assays between DBD-AtCullins/AtRBX1A and AD-AtARI3 (native, mutants and Ariadne domains). Presence of interaction is depicted in blue in the left panel. Growth control corresponds to the right panel. AD-AtRBX1A was used as a control for Cullin interaction.



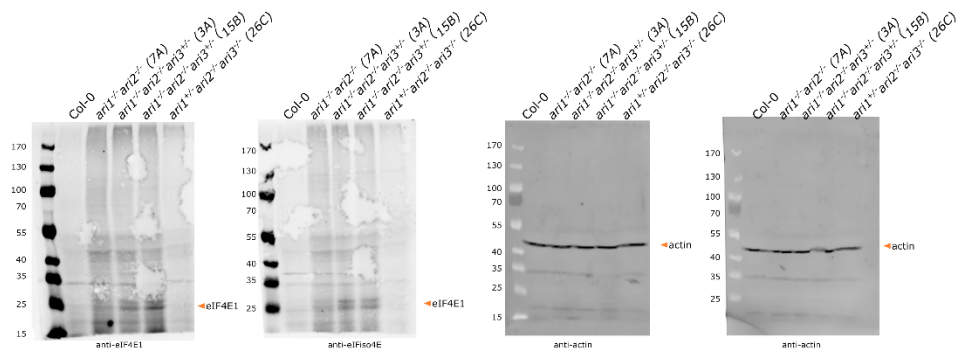
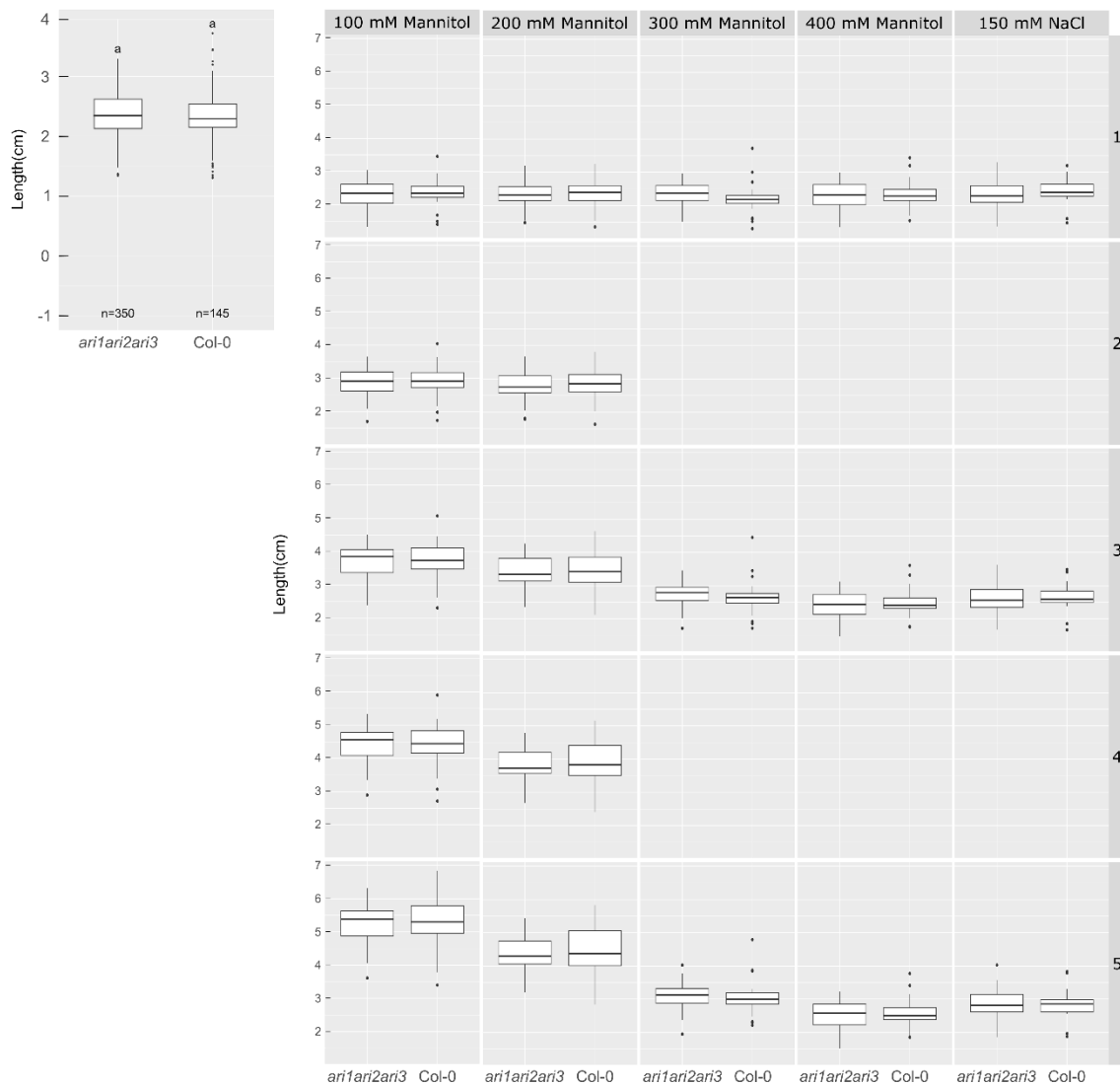
Supplementary Figure S20. LexA Y2H assays between DBD-eIF4E1/eIF(iso)4E and AD-AtARIs (native, mutants and Ariadne domains). Presence of interaction is depicted in blue. Growth control corresponds to the panel without X-Gal. Both assays were performed from the same yeast colonies. Right panel corresponds to plates containing double the amount of X-Gal as the plates from left panel.

A**B**

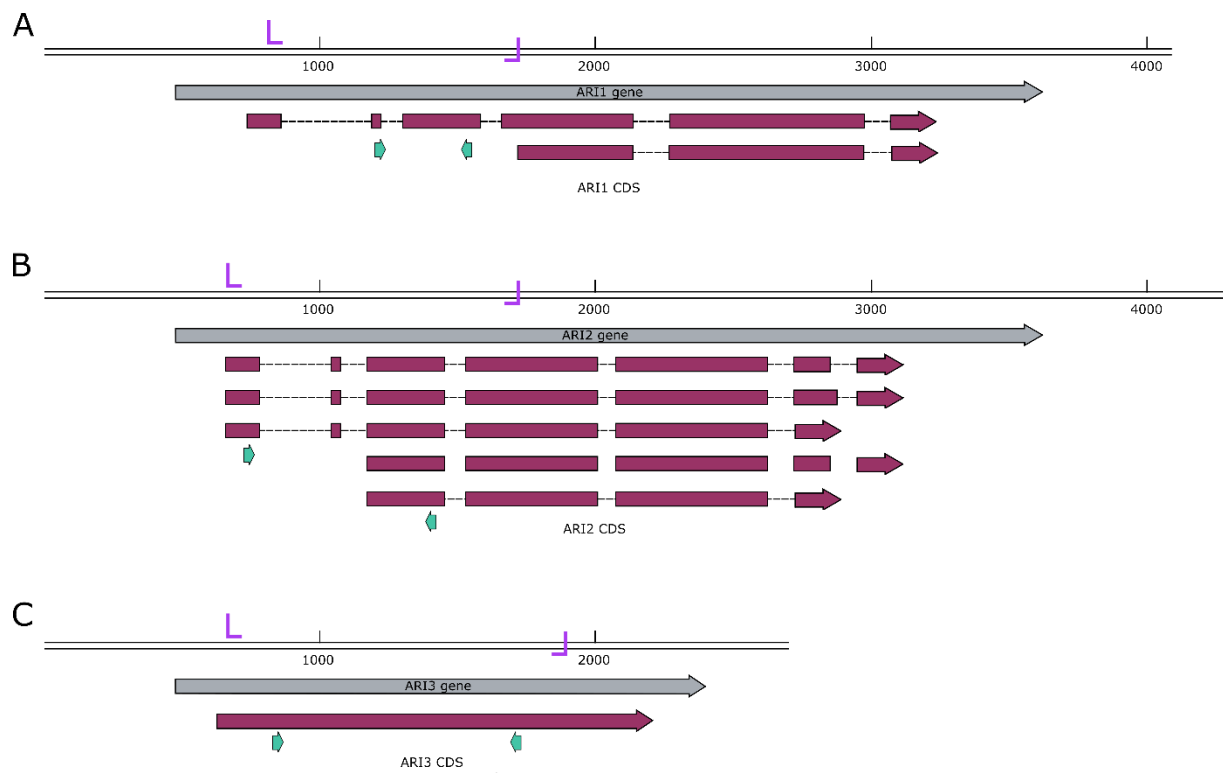
Supplementary Figure S21. Pull-down assays between eIF4E1/eIF(iso)4E and AtARIs. **A)** Pull-down of 6xHis-SUMO-GFP/eIF4E1/eIF(iso)4E using GST-AtARIs as bait. Proteins were visualized in immunoblots with α -SUMO and α -GST. **B)** Pull-down of GST, GST-eIF4E1/eIF(iso)4E using 6xHis-SUMO-AtARIs (6HS-ARIs) as bait. Proteins were visualized with TCE in-gel and in immunoblots with α -GST.



Supplementary Figure S22. *In vitro* ubiquitylation assay of eIF4E1/eIF(iso)4E with different tags. A) *In vitro* ubiquitylation assay of 6xHis-SUMO-GFP, 6xHis-eIF4E1 and 6xHis-SUMO-eIF(iso)4E using all ortho-group AtARIs. Uncropped gels and blots from **Figure 13B**. **B)** *In vitro* ubiquitylation assay of 6xHis-eIF4E1 and 6xHis-SUMO-eIF(iso)4E using AtARI1 and AtARI1^{S363D}. Uncropped gels and blots from **Figure 13C**. **C)** *In vitro* ubiquitylation assay of GST-eIF4E1 and GST-eIF(iso)4E using AtARI1 and AtARI1^{S363D}. Proteins were visualized with TCE in-gel, 488 nm fluorescence scan and in immunoblots with α -SUMO. **D)** *In vitro* ubiquitylation assay of a mixture of tag-less eIF4E1 and 6xHis-eIF4E1 using AtARI1 and AtARI1^{S363D}. Proteins were visualized with TCE in-gel and 488 nm fluorescence scan.

A**B**

Supplementary Figure S23. AtARI CRISPR/Cas9 mutants' analysis. A) elF4E1 and elF(iso)4E protein levels from ~1 month old Col-0 and mutants' leaves. Uncropped gels and immunoblots from **Figure 14A**. **B)** Root length of *ari1ari2ari3* triple mutant before (left) and after (right) treatment with D-Mannitol (100 mM to 400 mM) and NaCl (150 mM).



Supplementary Figure S24. Design of CRISPR/Cas9 mutants. Representation of **A**) *AtARI1*, **B**) *AtARI2* and **C**) *AtARI3* genes. In grey, the genomic DNA is depicted. Exons are represented in dark purple. Both guide RNAs are depicted by cyan arrows, while primers used for sequencing the mutation are depicted in magenta.

A**ARI1**

GTAAAMDDYFSAAEEACYYSSDQSDLGIDNEESELQPLSSKRSNTQVITQESLLAAQREDLLRVMELLSI**KEHHARTLLIHYQWDVEKLFAV**FVE

RING

KGKDSLFGAGVTVF~~DYQYGNSSFPQSSQMS~~CDVCMEDLPGDHMTRMDCGHCFCCNNC~~WTEHFTVQINEGQSKIRCMAHQCNAICDEDIV~~

IBR

RSLVSKKR~~PDLA~~**A**K**FDRYLLESYIEDNRMVW**CPSTPHCGNAIRAE~~DDKLCEVECSCGLQFCFSCLCQAHSPCSCLMWELWRKKR~~DESETINW

Rcat

ITVHT**K**LCPKCYKPVEKNGG**C**NLVRCICGQFCWLCGGATGSDHTYRSIAGHSCGRYQDD**KEKQMERAKRDLNRYTHYHRYKAHIDSSK**LED

Ariadne

KLRDTIHEKVSKSEKREL**K**D~~FSWVTNGLDRLFRSRRVLSY~~AFAYM**FGEMF**K**DEMTP**EEREIK**K**NLFEDQQQLESNVE**K**LSQFLEEPFDE

FSNDKVMAIRIQIINLSAVD**TLCK****K**MYECIEND**LLGSLQLGIHNIS**PYRSKGIEQAQFYASWNS**K**DAD**K**FQPLDSGTSGVTSRPEQASGRSSE

DTICSSSQKRPK**K**EGSFLNN**K**VTLLDLNLPAFDQDQ-

B**ARI2**

GTAAAMDDNLSGEEEDYYSSDQESLNGIDNDESVSIPVSSRSNTVKV**IT**KESLLAAQREDLRRVMELLSV**KEHHARTLLIHYRW**DVEKLFAV/LVE

RING

KGKDSLFGAGVTLLENQSCDSSVGSSSMMSCDICVEDVPGYQLTRMDCGHSCNCWTGHFTVKINEGQSKRIICMAH**K**CNAICDEDVVR

IBR

ALVSKSQPDLA**E**K**FDRYLLESYIEDN**K**MVW**CPSTPHCGNAIRVEDDELCEVECSCGLQFCFS**SSQAHSPCSCVMWELWRKK**CDESETVNWI

Rcat

TVHT**K**PCPKCHPKVE**K**NGG**C**NLVCLCRQSF**WLC**GEATGRDHTWARISGHSCGRF**QED****KEKQMERAKRDLKRYM**HYHNRYKAHIDSSKLEA

Ariadne

KLSNNISKVSI**E**KREL**OLQDFSWATNGLHRLFRSRRVLSY**SYPFAFY**MFGD**E**LFKDEM**SEER**EIK****K**NLFEDQQQLEANVE**K**LSKLEEPFDQF

ADDKVMQIRIQVINLSAVD**TLCE****N**MYECIEND**LLGSLQLGIHNIT**PYRSNGIERASDFYSSQNS**K**EAVGQSSDCGWTSRLDQALESGKSEDTSCS

SGKRARIDESYRNSQTLLDLNLPAEAIER**K**-

C**ARI3**

GTAAAMDDYMM~~MLDDY~~GEEDENYSEEDNYSEA**EV**D**LQPV**T**STK**TSQ**V**IKKESLVA**AQ****K**EILRVMELLSV**K**ENQARTLLIYYQWNVEKLFS

RING

VFADQG**K**DRMFSCAGLTVFVPSLTSK**KT****M****K**CDVCMEDD**LPS**N**VMTR**MECGHRC**NC**W**I**GHFTV**K**INEGESKR**I**LCMA**H****E****C****K**AICDEDVVR

IBR

R**KLV**SP~~E~~LA**D**RY**D**RF**L**IESY**V**EDNN**M**V**W**C**P****S****K**PHCGSAIR**K**I**E****D****G**HD**V**EV**G**C**S****G****L**Q**F**C**S****C****L****E****S****H****P****C****S****C****L****W****K****W****K****K****K**CEDESETVNWI

Rcat

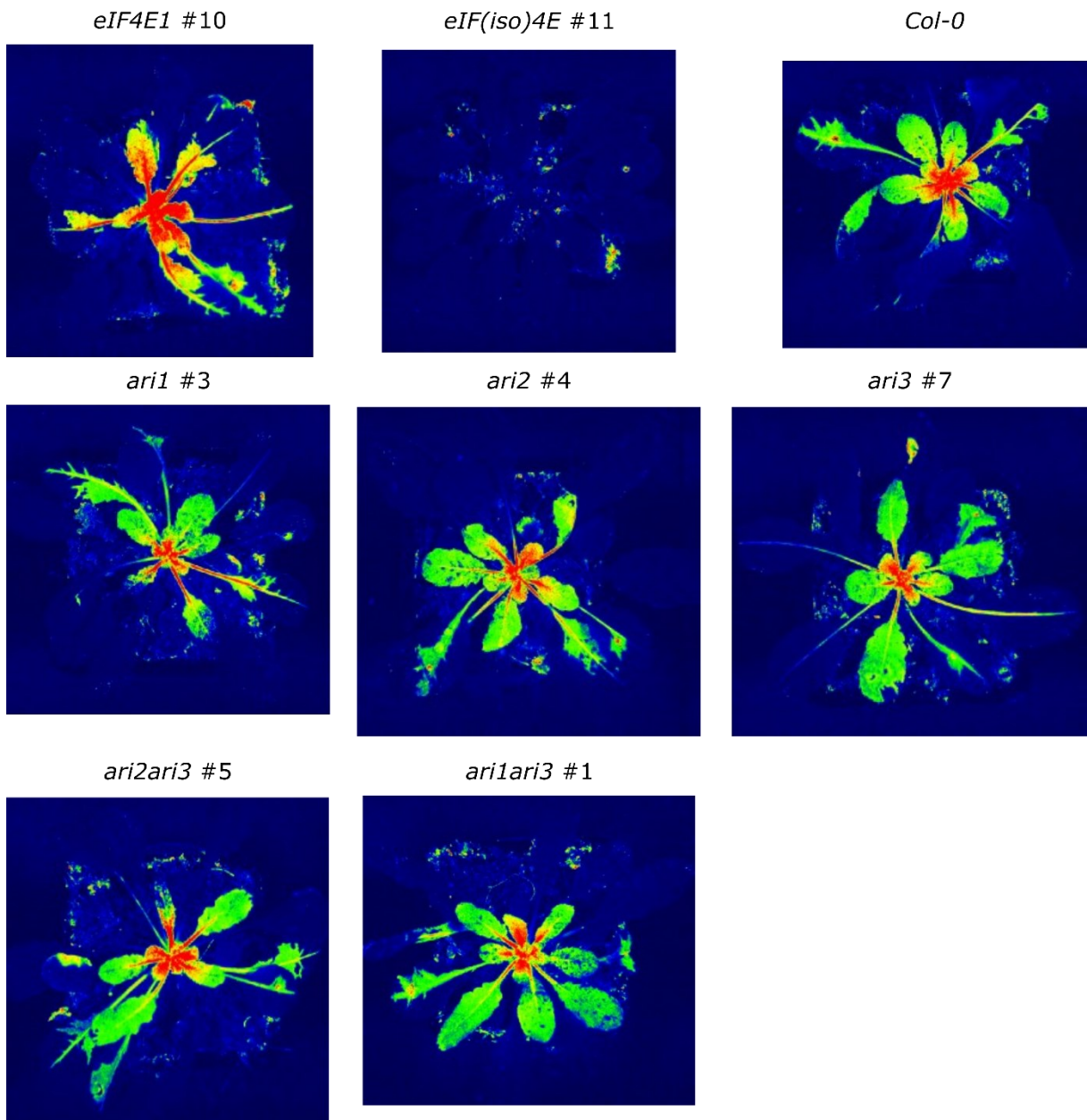
TVNT**K**LCPKCS**K**P**I**Q**K**R**D****G****C****N****L****M****T****C****K**CG**Q**H**F****C****W****L****C****G****Q****A**T**G**R**D****H****T****Y****T****S**IAGHSCGRY**K****D****E****K****V**R**Q**L**E****R**A**Q**R**D****L****D****R****Y****T****H****Y****H****R****Y****K**AH**I**D**S****L****K****L****E****D****K****L**

Ariadne

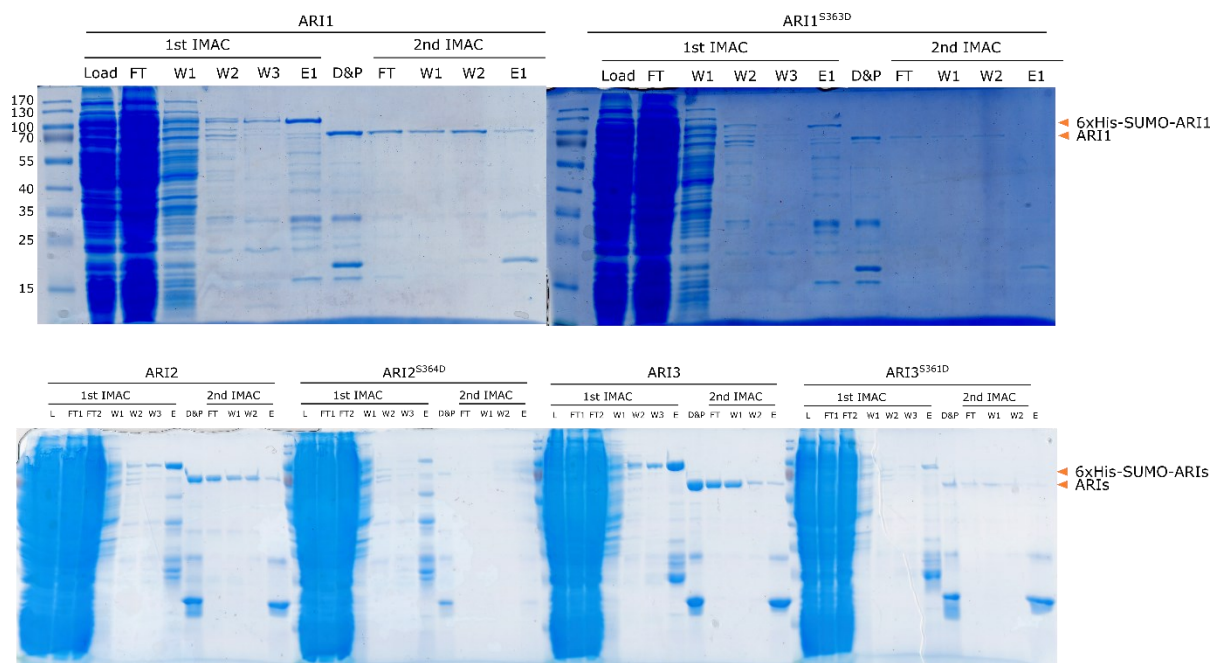
R**K**S**I****L****E****K**A**V****S****N****S****E****T****K**D**Q****K****V****F****K****E****Y****S****W****V****T****D****A****V****N****R****I****F****S****R****R****I****S****Q****S****Y****F****A****F****M****G****E****E****LF****K****D****E****M****I****S****E****K****R****E****I****K****K**NLFEDQQQLEG**N****V****E****K**LSKLEEPFD**EY**

DHE**K**V**V****E****M****M****R****H****L****T****N****L****T****A****V****V****D****N****L****C****E****M****Y****E****C****I****E****N****L****L****G****P****I****Q****F****G****N****H****N****I****A****P****R****S****K****G****I****E****Q****A****T****E****F****C****A****E****S****S****D****C****G****S****G****S****S****S**

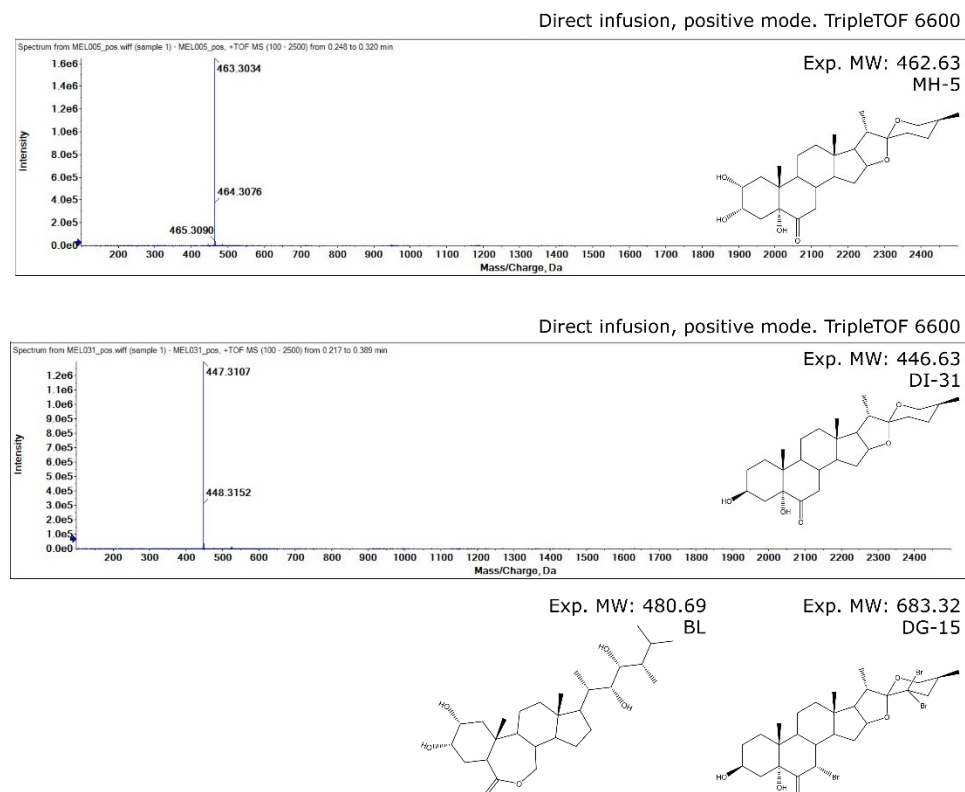
Supplementary Figure S25. Ubiquitylation sites of AtARIs. Sequences of **A**) AtARI1, **B**) AtARI2 and **C**) AtARI3 with ubiquitylated lysine residues in red. RBR domains are depicted with underline, active site cysteine is highlighted in yellow.



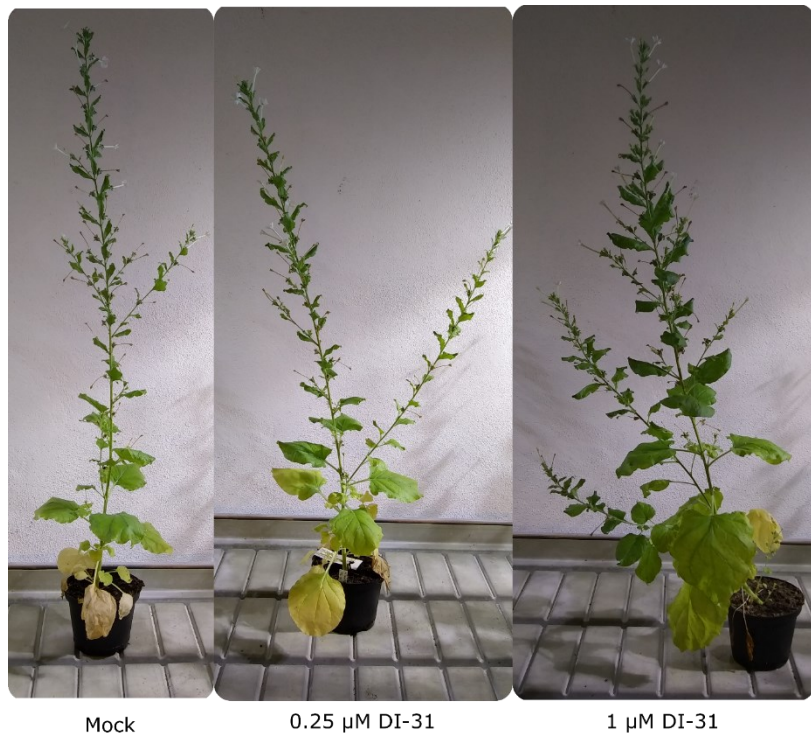
Supplementary Figure S26. Assaying resistance of *ari* mutants to turnip mosaic virus GFP (TuMV GFP). Analysis of GFP accumulation, at 14 days post inoculation of Col-0 (susceptible), *eIFiso4e* (resistant), *eif4e1* (oversusceptible) and *ari* mutants. The mutants *ari1ari2* and *ari1ari2ari3* were not available at that time. Twelve plants were imaged but no quantification done. All *ari* plants display regular accumulation as wild-type Columbia.



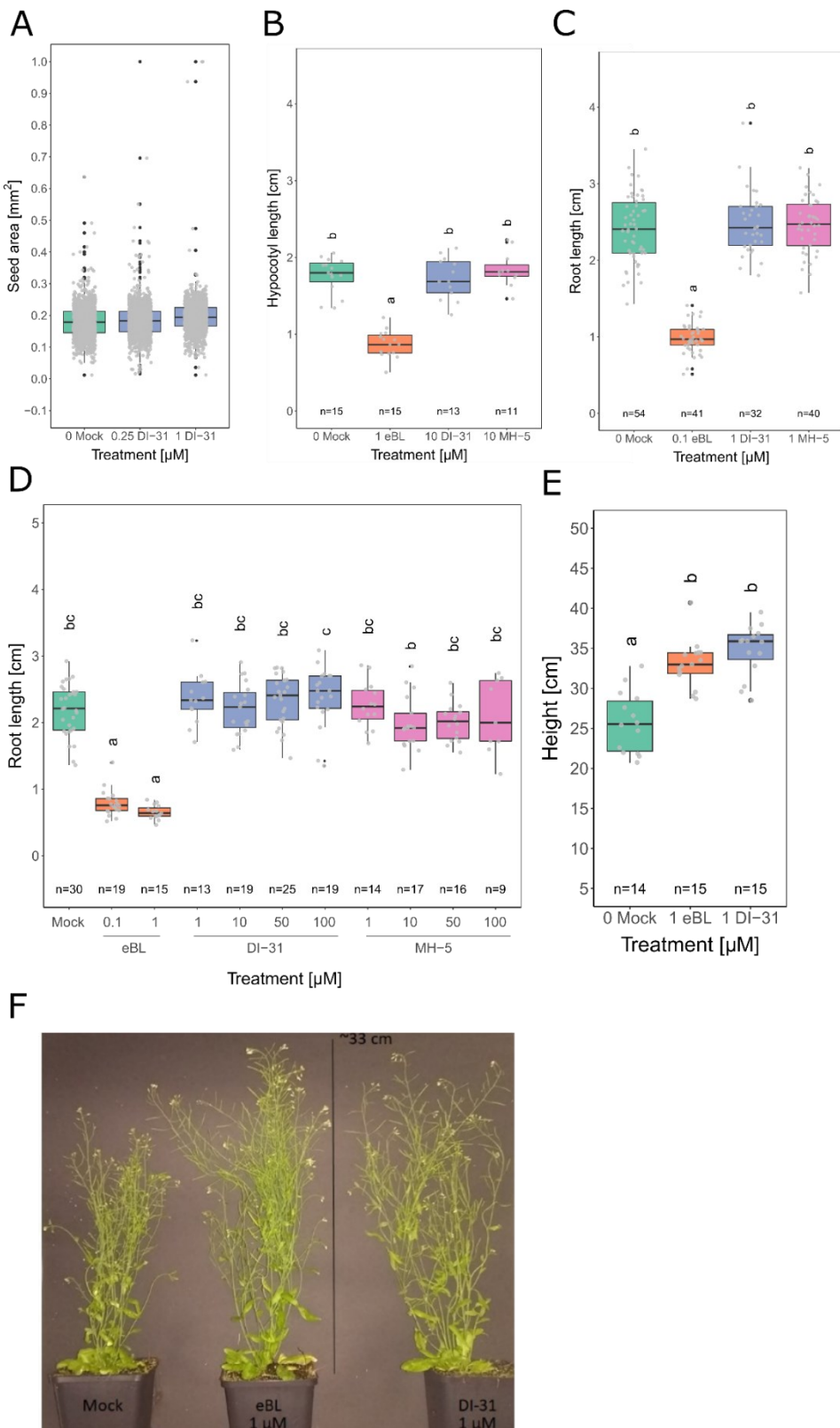
Supplementary Figure S27. First purification steps of AtARIs. First and second IMAC (Immobilized metal affinity chromatography) of 6xHis-SUMO-AtARIs from 1 L of *E. coli* BL21-AI culture. FT: Flow through, W: wash, E: Elution, D&P: Dialysis and protease treatment.



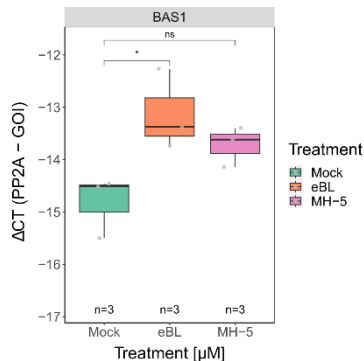
Supplementary Figure S28. Chemical structures of Spyros and BL, analyzed with high resolution mass spectrometry.



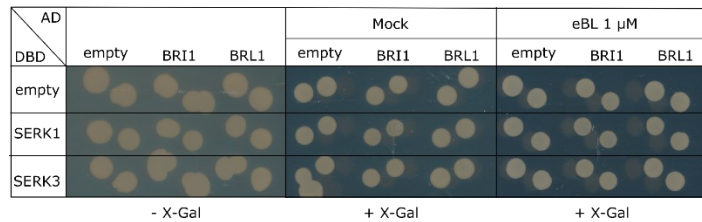
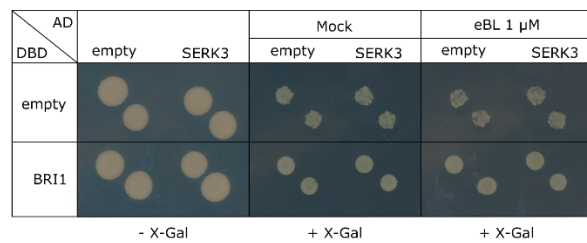
Supplementary Figure S29. Three-month-old *Nicotiana benthamiana* treated plants.



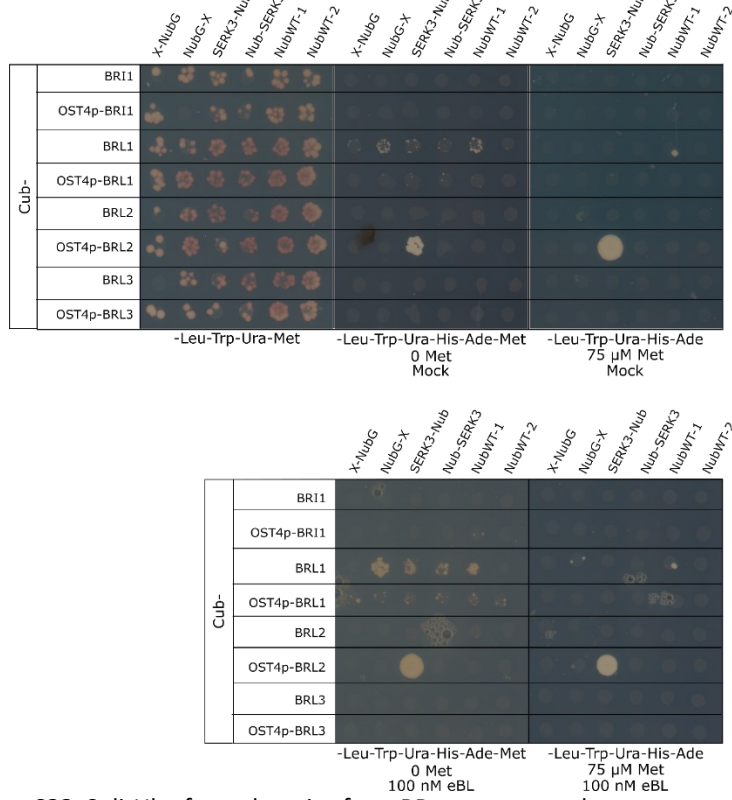
Supplementary Figure S30. Phenotypic effect of Spyros in plants. **A)** Seed area of treated *N. benthamiana*. **B)** Hypocotyl length of treated *N. benthamiana* seedlings grown for 7 days in the dark. **C)** Root length of treated *N. benthamiana* seedlings grown for 13 days in the light. **D)** Root length of treated *A. thaliana* seedlings grown for 7 days in the dark. **E-F)** Stem height of 7-weeks old *A. thaliana* adult plants, fourth treatment.



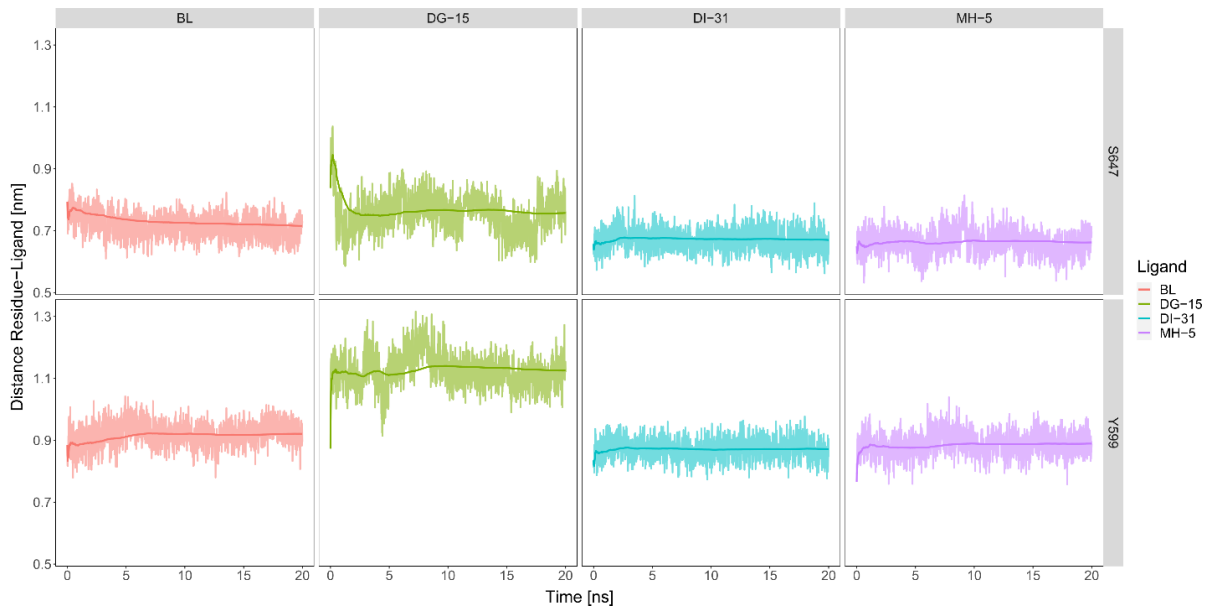
Supplementary Figure S31. *BAS1* expression in 5-week-old *det2-1* plants grown on soil (bolted). Plugged-out-whole plants were treated for 4 hours in liquid media containing either MH-5 (1 μ M), eBL (0.1 μ M) or mock prior sampling (n=3, each biological replicate represents one plant). A t-test was performed against mock-treated plants for each gene (*p = 0.001).



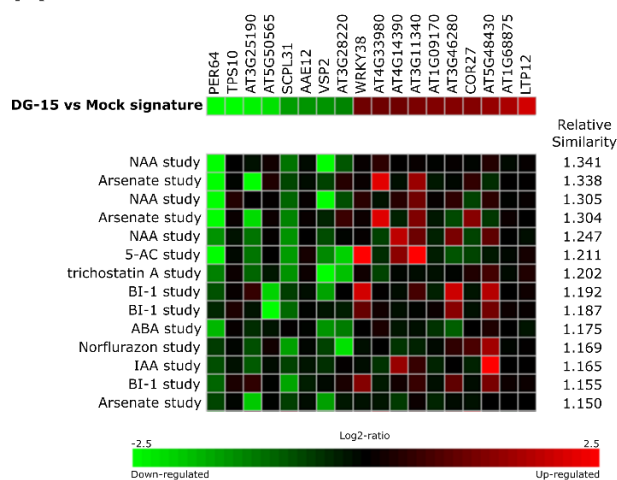
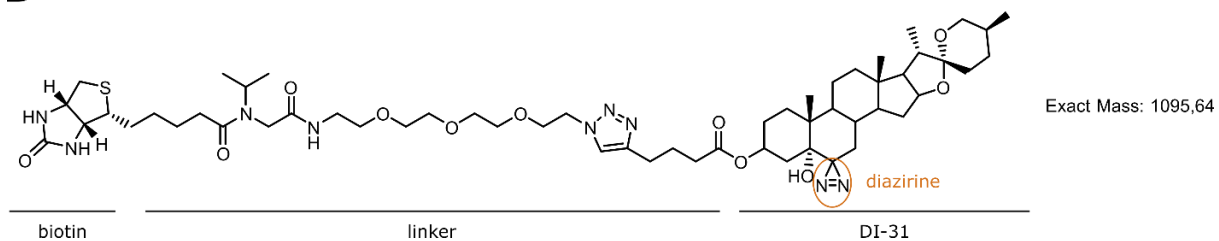
Supplementary Figure S32. LexA Y2H of ectodomains from BR-receptors and co-receptor upon mock or eBL treatment.



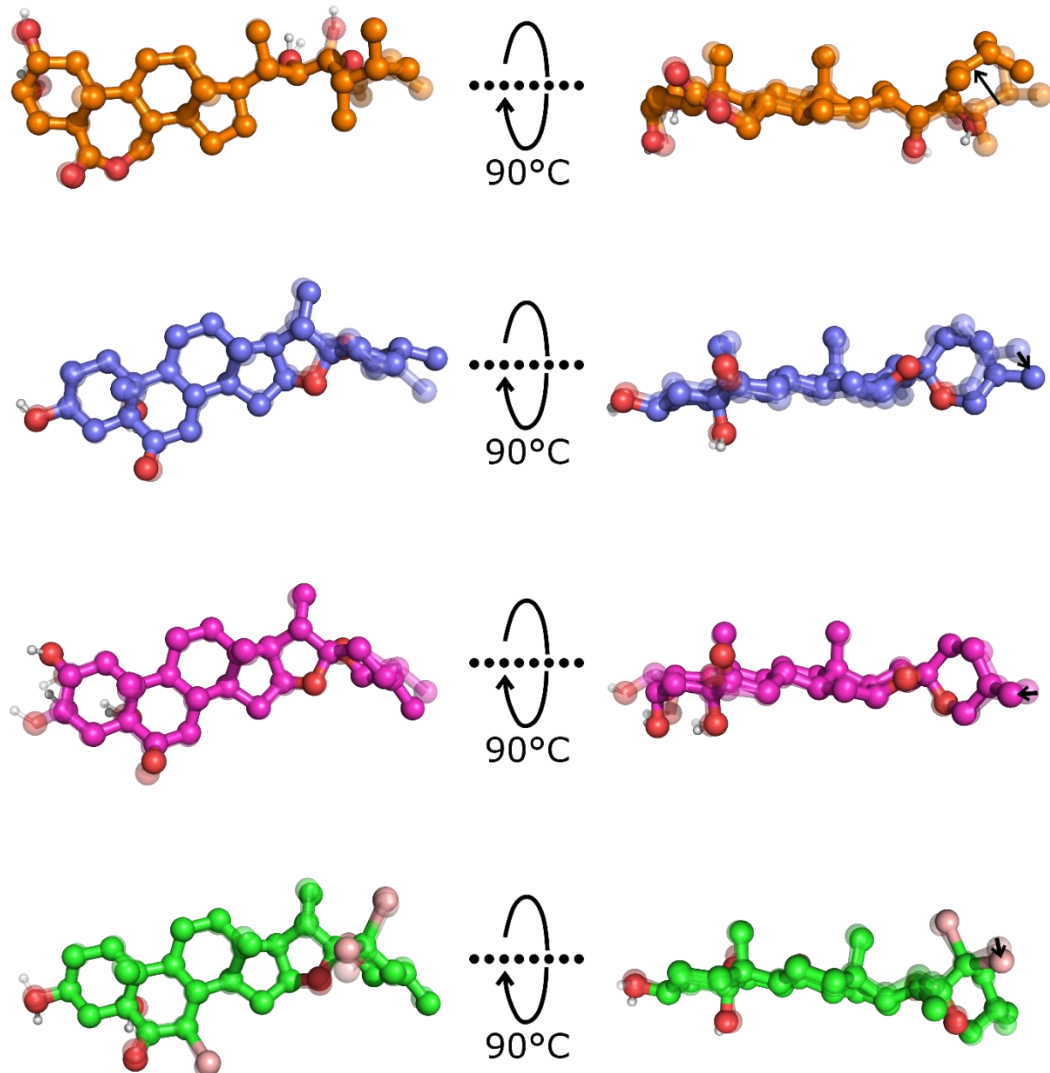
Supplementary Figure S33. SplitUb of ectodomains from BR-receptors and co-receptor upon mock or eBL treatment.



Supplementary Figure S34. Minimum distance (pairdist) between residue S647 or Y599 and the ligand during the entire simulation (20 ns). Thick line corresponds to cumulative mean.

A**B**

Supplementary Figure S35. A) Gene expression signature of the most upregulated/downregulated genes in DG-15 treated plants. The signature was composed as a list of genes and their corresponding relative expression values (DG-15 vs. Mock) using Genevestigator™ signature tool. **B)** Chemical structure of the in-house produced Spyro-biotin derivative.



Supplementary Figure S36. Different views of the first and last (transparent) positions of Steroids during 5 ns MD simulation. Orange (BL), Blue (DI-31), Magenta (MH-5) and Green (DG-15). Arrows denote conformational change within the side chains during the simulation.

Supplementary Data 1. Predicted domains and structural features of AtARIs. Sequences and residue identification was obtained from aligning alpha-fold structures of AtARIs with active/autoinhibited HHARI (PDB codes: 4KC9 and 7B5L) and active TRIAD1 (PDB code: 7ONI). Background color denotes the different subgroups within the AtARI family based on structural similarities. Domain information and alpha-fold structures were extracted from UniprotKB, the code for each protein is depicted in the table. *Features first identified for HHARI and TRIAD1 from ^{49,50,52}.

Supplementary Data 2. Amino acid sequence of the RING1, IBR and Rcat domains of AtARI1/2/3/5/7/8. The domains were predicted based on the sequence alignment with HHARI and alpha fold structure prediction.

Supplementary Data 3. Pull-down of plant proteins using GST-AtARI1/2/3/5/8 as bait. Enriched proteins were identified using MS/MS and quantified via peptide spectral mass (PSM). Interacting proteins were defined as such when: **PSM < 2** from at least two biological replicates (E1, E2, E3) from the GST control **AND PSM ≥ 2** from at least two biological replicates from the GST-AtARI baits.

Supplementary Data 4. Sequences of CRISPR-Cas9 generated mutants. Mutation description and effect of *ari1/2/3* single, double and triple mutants. Only a short sequence where mutation occurred is shown, as well as the native one.

Supplementary Data 5. MS/MS raw data of eIF4E1/eIF(iso)4E IVU. Peptide sequences, coverage and quantification (via peptide spectral mass: PSM) from IVU samples from **Figure 13B**, including modified (GG and LRGG modified residues) and non-modified peptides from SUMO-GFP, SUMO-eIF4E1, SUMO-eIF(iso)4E, AtARI1, AtARI2 and AtARI3.

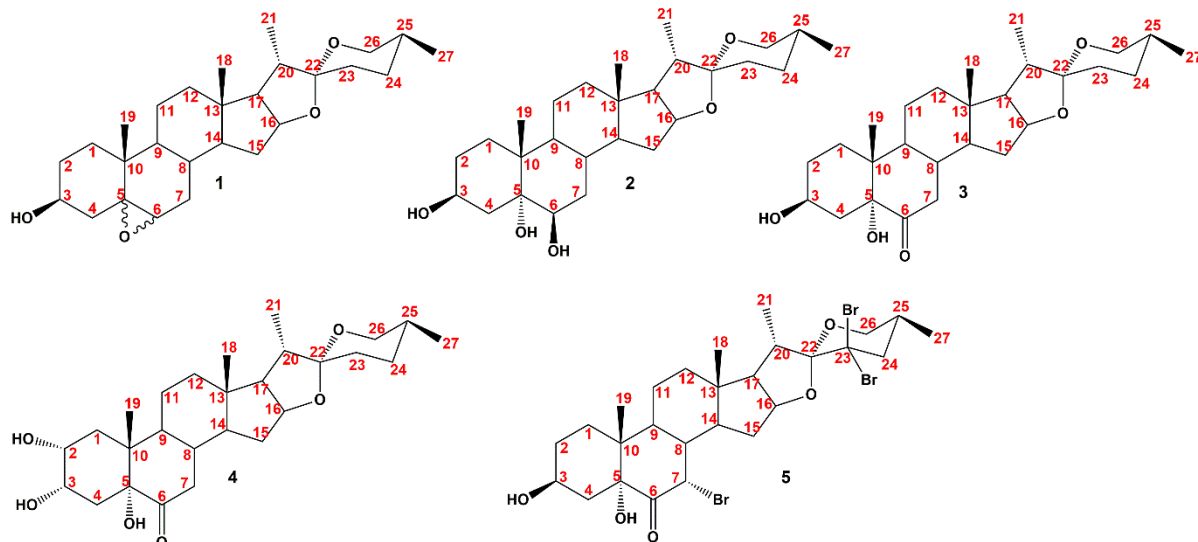
Supplementary Data can be accessed through the following link:

https://drive.google.com/drive/folders/1RoA8e8faGQAmIrpQV4SXKGClfk16_xxA?usp=drive_link

SUPPLEMENTARY MATERIALS AND METHODS

General information for characterization of steroid-derivatives.

Diosgenin derivatives **1-5** were acquired from our collaborator CNPR at Havana University. Their synthesis can be found in previous publications from the group²⁴⁰⁻²⁴². All starting materials were purchased from commercial sources and used without further purification. ¹H-NMR and ¹³C-NMR spectra were recorded in a Varian Mercury 400 NMR spectrometer at 399.94 MHz and 100.57 MHz, respectively or in an Agilent (Varian) VNMRS 600 NMR spectrometer at 599.83 MHz and 150.83 MHz, respectively. Chemical shifts (δ) are reported in ppm relative to the TMS (¹H NMR) and the solvent signal (¹³C NMR). High-resolution mass spectra were obtained in a TripleTOF 6600-1 mass spectrometer (Sciex) equipped with an ESI-DuoSpray-Ion-Source (it operated in positive ion mode) and was controlled by Analyst 1.7.1 TF software (Sciex). The ESI source operation parameters were as follows: ion spray voltage: 5,500 V, nebulizing gas: 60 p.s.i., source temperature: 450 °C, drying gas: 70 p.s.i., curtain gas: 35 p.s.i. Data acquisition was performed in the MS1-TOF mode, scanned from 100 to 1500 Da with an accumulation time of 50 ms. Column chromatography was carried out using Merck silica gel 60 (0.015-0.040 nm) and analytical thin layer chromatography (TLC) was performed on Merck silica gel 60 F254 aluminum sheets.

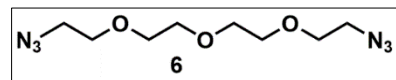


Supplementary Figure S37. Structure of Diosgenin derivatives 1-5. **1:** (25R)-5,6-epoxy-spirostan-3 β -ol; **2:** (25R)-3 β ,5 α ,6 β -trihydroxy-spirostane; **3:** (25R)-3 β ,5 α -dihydroxy-spirostan-6-one (DI-31); **4:** (25R)-2 α ,3 α ,5 α -trihydroxy-spirostan-6-one (MH-5) and **5:** (25R)-7 α ,23 α ,23 β -tribromide-3 β ,5 α -dihydroxy-spirostan-6-one (DG-15).

Synthesis and application of biotin-tagged photoaffinity DI-31 containing chemical photocrosslinking reagents to study protein—protein interactions.

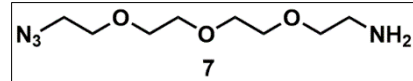
The synthesis of biotin-tagged photoaffinity DI-31 (photocrosslinker) was carried out by Toni Difte, from the department Natural and Active Ingredient Chemistry (NWC) from Leibniz Institute of Plant Biochemistry (IPB). The synthesis was done following the synthetic protocol reported in Sebastian Brauch, PhD thesis Halle 2013 (Novel tools for protein analysis and modification: From chemical probes to new ligation methods)^{243,244}.

Synthesis of 1-Azido-2-{2-[2-(2-azidoethoxy)ethoxy]ethoxy}ethane (6).



Under a nitrogen atmosphere, triethylamine Et_3N (30.6 mL, 220 mmol) in dry tetrahydrofuran THF (20 mL) was added to a solution containing tetraethylene glycol (19.4 g, 100 mmol) and methanesulphonyl chloride (17.0 mL, 220 mmol) in dry THF (80 mL) at 0 °C. The resulting solution was stirred for 1 hour at 0 °C and for another 3 hours at room temperature. Next, distilled water (80 mL), solid sodium hydrogen carbonate NaHCO_3 (4.5 g, 54 mmol) and sodium azide NaN_3 (14.3 g, 220 mmol) were added to the reaction mixture. The organic solvent was removed under reduced pressure and the remaining aqueous solution was heated at 80 °C during 12 hours. Afterwards the aqueous phase was extracted with dichloromethane (4x 200 mL) and the combined extracts were dried over sodium sulphate. The organic solvent was removed under reduced pressure to afford the diazido-PEGylated compound **6** (10.8 g, 88 %), which was stored at -30 °C. ^1H NMR (400 MHz, Chloroform-*d*) δ 3.73 – 3.62 (m, 6H), 3.39 (t, J = 5.1 Hz, 2H). ^{13}C NMR (101 MHz, cdcl_3) δ 72.29, 71.14, 70.51, 70.50, 70.47, 70.43, 70.40, 70.17, 69.85, 69.84, 61.52, 50.49, 50.47, 42.57.

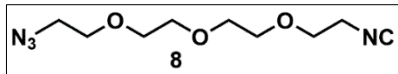
Synthesis of 2-{2-[2-(2-Azidoethoxy)ethoxy]ethoxy}ethanamine (7)



Under a nitrogen atmosphere, a suspension of the diazido-PEGylated compounds **6** (10.8 g, 44 mmol) in 0.65 M aqueous phosphoric acid (100 mL) was cooled to 0 °C. Triphenylphosphine Ph_3P (9.9 g, 37.8 mmol) in dry diethyl ether (100 mL) was subsequently added dropwise. After complete addition, the reaction mixture was allowed to stir at room temperature for an additional 24 hours. The organic phase was separated and the aqueous phase was washed with diethyl ether (3x 100 mL). To the aqueous phase solid potassium hydroxide (3.5 equiv.) was added and traces of organic solvent were removed under reduced pressure. The remaining aqueous solution was placed at 0 °C for 24 hours, after which time a solid had formed which was removed by filtration. The filtrate was transferred in an aqueous 4 M sodium hydroxide solution by addition of solid sodium hydroxide and extracted with dichloromethane (16x 50 mL). The combined organic extracts were dried over sodium sulphate and the solvent was removed under reduced pressure. The residue was purified on silica to afford the mono-amine **7** (6.07 g, 63%) as yellow liquid, which was stored at -30°C. ^1H

NMR (400 MHz, Chloroform-*d*) δ 3.74 – 3.60 (m, 8H), 3.54 (t, *J* = 5.2 Hz, 2H), 3.44 – 3.36 (m, 2H), 3.06 (s, 2H), 2.90 (t, *J* = 5.1 Hz, 2H). ^{13}C NMR (101 MHz, *cdcl*₃) δ 72.43, 72.34, 71.14, 70.47, 70.44, 70.42, 70.40, 70.36, 70.12, 70.05, 69.82, 61.24, 50.48, 50.46, 42.58, 41.19.

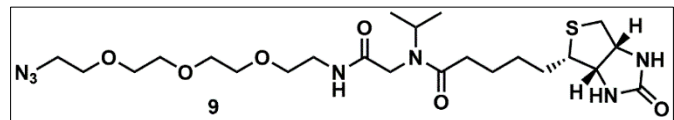
Synthesis of 1-Azido-2-{2-[2-(2-isocyanoethoxy)ethoxy]ethoxy} ethane (8)



A solution of the amine **7** (6.1 g, 27.9 mmol) in ethyl formate (20 mL) was refluxed for 3 hours, whereupon all volatiles were removed by rotary evaporation to yield the corresponding formamides as slightly red liquids. The liquid was dissolved in dry dichloromethane (60 mL) and placed under a nitrogen atmosphere. Diisopropylamine (11.8 mL, 83.7 mmol) was added and the reaction mixture was cooled to 0 °C. After the dropwise addition of phosphorus (3.1 mL, 33.5 mmol), the reaction mixture was warmed to room temperature and allowed to stir for an additional 2 hours. The reaction was quenched with an aqueous sodium carbonate solution (6.5 g in 35 mL distilled water) and the resulting suspension was stirred for further 30 minutes followed by the addition of water. Afterwards the organic layer was separated and the aqueous phase was extracted with dichloromethane (3x 40 mL). The combined organic extracts were dried over sodium sulphate and the organic solvent was evaporated in vacuo. The remaining residue was purified by column chromatography to afford compound **8** (2.31 g, 38%). ^1H NMR (400 MHz, Chloroform-*d*) δ 3.68 (p, *J* = 3.8 Hz, 8H), 3.58 (dq, *J* = 5.7, 3.8, 2.8 Hz, 2H), 3.39 (t, *J* = 5.0 Hz, 2H), 1.28 (dd, *J* = 10.2, 6.8 Hz, 2H). ^{13}C NMR (101 MHz, *cdcl*₃) δ 71.24, 70.72, 70.60, 70.57, 70.55, 70.53, 69.95, 68.56, 50.59, 47.28, 47.23, 42.81, 41.80, 41.73, 41.66, 22.40, 22.38, 21.12, 21.10.

Synthesis of PEG₃-(biotin)-azide(9)

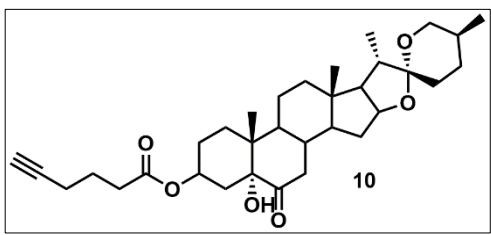
A solution containing paraformaldehyde (0.13 g, 4.45 mmol) and *i*-propylamine (0.36 mL, 4.45 mmol) in



10 mL methanol was stirred at room temperature for 2 hours to pre-form the imine. PEG-Isocyanide **8** (1 g, 4.45 mmol) and Biotin (1.1 g, 4.45 mmol) were subsequently added, and the resulting mixture was heated in a microwave apparatus (1 hour, 100 °C). Finally, the solvent was evaporated and the residue was purified by column chromatography to yield the compound **9** as pale-yellow oil (0.94 g, 39%). *R*_f = 0.26 (EtOAc/MeOH; 7:3); *R*_f = 0.55 (EtOAc/DCM/MeOH; 6:3:1.5). ^1H NMR (400 MHz, DMSO-*d*₆) δ 8.08 (t, *J* = 5.7 Hz, 1H), 7.65 (t, *J* = 5.8 Hz, 1H), 6.47 (d, *J* = 5.1 Hz, 2H), 6.38 (s, 2H), 4.72 – 4.58 (m, 1H), 4.45 – 4.29 (m, 3H), 4.23 – 4.09 (m, 5H), 3.84 (s, 2H), 3.71 (s, 2H), 3.60 (q, *J* = 4.1, 3.4 Hz, 4H), 3.56 – 3.49 (m, 17H), 3.47 – 3.37 (m, 17H), 3.25 (d, *J* = 5.7 Hz, 1H), 3.18 (d, *J* = 3.5 Hz, 7H), 3.17 – 3.11 (m, 1H), 2.88 – 2.77 (m, 2H), 2.60 (dd, *J* = 12.5, 2.2

Hz, 2H), 2.52 (p, J = 1.8 Hz, 2H), 2.38 (t, J = 7.4 Hz, 2H), 2.24 – 2.15 (m, 2H), 1.63 (dtd, J = 9.5, 6.6, 3.2 Hz, 1H), 1.51 (dq, J = 14.0, 7.1, 5.8 Hz, 4H), 1.39 – 1.27 (m, 2H), 1.16 (d, J = 6.7 Hz, 2H), 1.10 (s, 2H), 1.06 (d, J = 7.0 Hz, 2H), 0.97 (d, J = 6.8 Hz, 6H). ^{13}C NMR (101 MHz, dmso) δ 173.39, 172.50, 171.98, 169.49, 169.33, 162.91, 72.41, 70.64, 69.94, 69.89, 69.88, 69.86, 69.80, 69.77, 69.67, 69.62, 69.36, 69.10, 69.01, 64.39, 64.34, 60.31, 56.15, 50.10, 44.64, 43.63, 43.27, 40.13, 39.95, 39.92, 39.71, 39.50, 39.29, 39.08, 38.87, 38.69, 38.56, 37.24, 33.17, 32.73, 32.34, 28.42, 28.35, 28.27, 28.23, 28.10, 28.04, 24.92, 24.79, 24.55, 22.30.

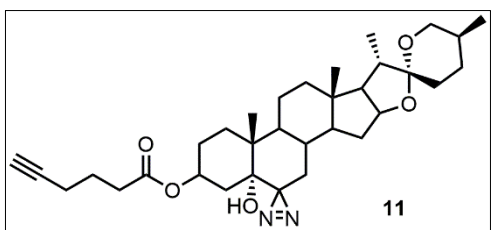
Synthesis of steroid **10**



1-Ethyl-3-(3-dimethylaminopropyl)carbodiimide EDC (0.25 g, 0.12 mmol), 4-Dimethylaminopyridine DMAP in catalytic quantities and hexynoic acid were dissolved in dry THF and stirred for 30 min at room temperature. Afterwards the Steroid **3**: (25R)-3 β ,5 α -dihydroxy-spirostan-6-one was added

and the mixture stirred for 36 h. The solvent was removed under reduced pressure and afterwards redissolved in DCM and washed with brine). The organic layer was dried over NaSO_4 and the solvent removed under reduced pressure. The crude mix was purified by flash column chromatography to yield the product **10** as clear oil (77 mg, 65%). (DCM/MeOH; 40:1). R_f = 0.45. ^1H NMR (400 MHz, Chloroform-*d*) δ 4.41 (td, J = 7.8, 6.3 Hz, 1H), 3.97 (dt, J = 11.2, 5.8 Hz, 1H), 3.47 (ddd, J = 11.0, 4.3, 2.0 Hz, 1H), 3.36 (t, J = 10.9 Hz, 1H), 2.80 – 2.67 (m, 1H), 2.14 (dd, J = 13.2, 3.7 Hz, 1H), 1.97 – 1.72 (m, 11H), 1.69 – 1.54 (m, 3H), 1.45 (tdt, J = 13.7, 8.7, 3.1 Hz, 2H), 1.32 – 1.22 (m, 3H), 0.97 (d, J = 6.8 Hz, 3H), 0.82 (s, 4H), 0.80 – 0.77 (m, 3H), 0.76 (s, 3H). ^{13}C NMR (101 MHz, cdcl_3) δ 212.02, 109.29, 108.90, 107.33, 81.36, 80.64, 80.48, 77.32, 77.00, 76.68, 67.20, 66.87, 66.76, 64.84, 62.00, 61.16, 56.20, 56.11, 55.98, 53.36, 49.57, 44.50, 42.50, 42.40, 42.35, 41.84, 41.75, 41.62, 41.58, 41.06, 40.47, 39.77, 39.59, 38.87, 38.08, 36.90, 36.71, 36.45, 36.35, 33.57, 31.88, 31.52, 31.32, 31.23, 30.33, 30.25, 29.75, 29.41, 28.74, 24.49, 21.25, 21.06, 17.45, 17.10, 16.68, 16.40, 16.27, 16.23, 15.91, 14.44, 14.11, 1.00, -0.02.

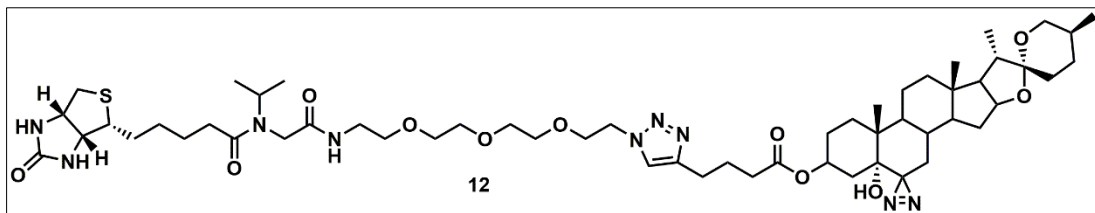
Synthesis of steroid **11**²⁴⁵.



1) A solution of the steroid **10** (0.65g, 0.11 mmol) in 50 mL of liquid ammonia was stirred for 2h at reflux temperature (-33°C). The solution was then cooled in a dry ice bath (acetone, -78°C) and a solution of hydroxylamine-O-sulfonic acid (0.15 g, 0.13 mmol) in 3 mL of MeOH was added over a 30-min period.

The cooling bath was removed, and the ammonia was allowed to evaporate overnight. The resulting slurry was filtered, and the filter cake was washed with several portions of (3x20 mL) methanol. All washings were combined with the original filtrate and the solution was concentrated and the hydrazi-steroid **11** was further used without any purification to yield the product as clear wax-like solid (0,03 g, 46%). ¹H NMR (400 MHz, Chloroform-*d*) δ 5.08 – 4.93 (m, 1H), 4.36 (td, *J* = 7.8, 7.3, 5.8 Hz, 1H), 3.46 (ddd, *J* = 10.9, 4.5, 2.0 Hz, 1H), 3.34 (t, *J* = 10.9 Hz, 1H), 2.41 – 2.31 (m, 1H), 2.22 (td, *J* = 6.9, 2.5 Hz, 2H), 2.09 (s, 1H), 2.01 – 1.92 (m, 2H), 1.88 – 1.75 (m, 6H), 1.70 – 1.55 (m, 3H), 1.52 – 1.42 (m, 1H), 1.28 (s, 3H), 1.20 (ddd, *J* = 15.3, 8.3, 5.1 Hz, 2H), 0.96 (d, *J* = 6.9 Hz, 3H), 0.88 (t, *J* = 7.0 Hz, 1H), 0.83 – 0.77 (m, 7H), 0.65 (dd, *J* = 13.5, 11.1 Hz, 1H), 0.23 (d, *J* = 9.0 Hz, 1H). ¹³C NMR (101 MHz, *cdcl*₃) δ 173.44, 173.16, 172.60, 115.35, 109.24, 83.22, 77.32, 77.00, 76.68, 76.22, 76.21, 69.10, 66.80, 53.40, 40.93, 40.68, 39.72, 36.23, 34.53, 33.79, 33.16, 32.99, 32.33, 31.70, 31.40, 31.30, 31.22, 29.68, 28.75, 26.13, 24.60, 24.04, 23.57, 22.25, 20.94, 17.79.

Synthesis of conjugate **12**.



9 (0.03 g, 0.055 mmol) and **11** (0.03 g, 0.05 mmol) were suspended in a water/MeOH mixture. Sodium ascorbate dissolved in water was added, followed by Cu₂SO₄ (0.01 eq). The mixture was stirred vigorously until completion of the reaction monitored by TLC and ESI-MS. The solution was acidified with aqueous HCl and EtOAc was added. The two phases were separated, and the aqueous phase was washed with EtOAc two times. The combined organic layers were dried over NaSO₄, and the solvent was evaporated under reduced pressure. The crude product was purified by column chromatography, R_f = 0.62 (EtOAc/DCM/MeOH; 6:3:1.5) to afford compound **12** (0.04 g, 38%) as a light yellow solid. ¹H NMR (400 MHz, Chloroform-*d*) δ 7.14 (t, *J* = 6.0 Hz, 0H), 6.29 (d, *J* = 10.6 Hz, 0H), 6.12 (d, *J* = 18.3 Hz, 1H), 5.41 (d, *J* = 15.1 Hz, 1H), 5.07 – 4.92 (m, 0H), 4.89 – 4.76 (m, 0H), 4.51 (dt, *J* = 10.4, 5.0 Hz, 2H), 4.33 (ddd, *J* = 16.5, 8.5, 2.8 Hz, 1H), 4.13 (q, *J* = 6.7 Hz, 1H), 3.89 (d, *J* = 6.6 Hz, 1H), 3.69 (d, *J* = 5.1 Hz, 1H), 3.65 – 3.54 (m, 6H), 3.47 (d, *J* = 1.4 Hz, 6H), 3.15 (dq, *J* = 7.8, 4.0 Hz, 1H), 2.91 (dd, *J* = 12.9, 4.8 Hz, 1H), 2.82 – 2.71 (m, 1H), 2.52 – 2.42 (m, 2H), 2.28 (q, *J* = 6.4, 5.5 Hz, 1H), 1.97 (ddd, *J* = 18.9, 9.3, 6.6 Hz, 2H), 1.89 – 1.55 (m, 5H), 1.47 (t, *J* = 11.2 Hz, 3H), 1.34 – 1.20 (m, 7H), 0.96 (d, *J* = 6.8 Hz, 2H), 0.89 – 0.75 (m, 4H). ¹³C NMR (101 MHz, *cdcl*₃) δ 173.57, 173.53, 172.96, 170.20, 170.08, 163.65, 146.91, 122.27, 109.26, 80.60, 77.35, 77.03, 76.72, 76.25, 75.60, 71.32, 70.74, 70.62, 70.58, 70.54, 70.50, 70.47, 70.43, 70.39, 70.33, 70.13, 70.09, 69.98,

69.69, 69.57, 69.52, 66.82, 61.98, 61.72, 60.12, 55.45, 55.42, 50.66, 50.06, 48.79, 44.33, 44.12, 42.82, 41.56, 40.96, 40.68, 40.54, 39.75, 39.12, 36.03, 33.78, 33.30, 32.90, 32.84, 32.38, 31.85, 31.40, 31.30, 30.23, 29.73, 28.74, 28.24, 28.14, 26.19, 25.02, 24.87, 24.63, 20.97, 19.76, 17.09, 16.45, 14.71, 14.61, 14.44.

Table S1. Primers used in this thesis.

Name	Sequence 5' → 3'	Application	Source
qRT-PCR primers			
SAUR-AC1_FW_qRT	TTGAGGAGTTCTGGTGCTAAG	Amplification of SAUR-AC1 fragment.	This study using QuantPrime
SAUR-AC1_RV_qRT	GCCATGAATCCTCTGGTGTG		
PP2A_FW_qPCR	AGCCAAGTAGGACGGATCTGGT	Amplification of PP2A fragment.	Czechowski <i>et al.</i> , 2005 ²⁴⁶
PP2A_RV_qPCR	GCTATCCGAACCTCTGCCTCATTA		
BAS1_RR55_7_qPCR	CAAATGCTCTTGTGCTGAA	Amplification of BAS1 fragment.	Roh <i>et al.</i> , 2012 ²⁴⁷
BAS1_RR55_8_qPCR	AATTCCCTCTGTCGGAAAAAA		
CRISPR cloning primers			
uni-sgRNA_R-58°	AAGGTCTCAAGCGACCCAGAAATTGAAACGC	Amplification of universal sgRNA reverse primer from pAGT6182	Dr. Tom Schreiber
C9T_Ari1-1_F	TTGGTCTCTATTGGAATCGCTCTAGCAGCACGTTAACAGAGCTATGCTGGAAA	Amplification of ARI1_F sgRNA forward primer from pAGT6182	This study. designed with CRISPOR
C9T_Ari1-2_F	TTGGTCTCTATTGATTCTGTATGTGATCACCGTTAACAGAGCTATGCTGGAAAC	Amplification of ARI1_R sgRNA forward primer from pAGT6182	This study. designed with CRISPOR
C9T_Ari2-1_F	TTGGTCTCTATTGTTCCCGATCAAATAC	Amplification of ARI2_F sgRNA forward primer from pAGT6182	This study. designed with CRISPOR
C9T_Ari2-2_F	TGTCAGTTAACAGAGCTATGCTGGAAAC		
C9T_Ari3-1_F	TTGGTCTCTATTGATCCTGTCAGCTGATAACCGTTAACAGAGCTATGCTGGAAA	Amplification of ARI2_R sgRNA forward primer from pAGT6182	This study. designed with CRISPOR
C9T_Ari3-2_F	TTGGTCTCTATTGTCCGCCGATATGAAATAACCGTTAACAGAGCTATGCTGGAA	Amplification of ARI3_F sgRNA forward primer from pAGT6182	This study. designed with CRISPOR
C9T_Ari3-2_F	ACAGC	Amplification of ARI3_R sgRNA forward primer from pAGT6182	This study. designed with CRISPOR
C9T_Ari5-1_F	TTGGTCTCTATTGTCGAGATATGATCGATAAGTGTAAAGAGCTATGCTGGAA		
	ACAGC	Amplification of ARI5_F sgRNA forward primer from pAGT6182	This study. designed with CRISPOR

C9T_Ari5-2_F	TTGGTCTCTATTGGGTGAGCCTCTCA GTGCACGTTAACAGAGCTATGCTGGAA ACAGC	Amplification of ARI5_R sgRNA forward primer from pAGT6182	This study. designed with CRISPOR
C9T_Ari7-1_F	TTGGTCTCTATTGATCCTTCTGCACTA CATGCGTTAACAGAGCTATGCTGGAAAC AGC	Amplification of ARI7_F sgRNA forward primer from pAGT6182	This study. designed with CRISPOR
C9T_Ari7-2_F	TTGGTCTCTATTGACATCCCGGGCCAT CATTAAGTTAACAGAGCTATGCTGGAAA CAGC	Amplification of ARI7_R sgRNA forward primer from pAGT6182	This study. designed with CRISPOR
C9T_Ari8-1_F	TTGGTCTCTATTGTTCTGCGACTCATGT TGGGAGTTAACAGAGCTATGCTGGAAA CAGC	Amplification of ARI8_F sgRNA forward primer from pAGT6182	This study. designed with CRISPOR
C9T_Ari8-2_F	TTGGTCTCTATTGTGGACCATCTTAAT CGCTGGTTAACAGAGCTATGCTGGAAA CAGC	Amplification of ARI8_R sgRNA forward primer from pAGT6182	This study. designed with CRISPOR
Genotyping primers			
geno_CRIS PR_Ari1-F	CCTCTGCCTCTAAAGATCAAACACT CAGG	ARI1 CRISPR genotyping	This study
geno_CRIS PR_Ari1-R	CATTGATGAGCCATGCATCTAACCT		This study
geno_CRIS PR_Ari2-F	GATCCATGGATGATAATTAAAGCGGC	ARI2 CRISPR genotyping	This study
geno_CRIS PR_Ari2-R	CTCAGCTAAATCTGGTTGGCTTTAC		This study
geno_CRIS PR_Ari3-F	CCAATGGAACGTTGAGAAGTTGTTCT TG	ARI3 CRISPR genotyping	This study
geno_CRIS PR_Ari3-R	GTTGTGGTTCCAAATTGTATTGGACC TA		This study
geno_CRIS PR_Ari5-F	GCTTAGTTCCCTCATGTCGGAAATG CG	ARI5 CRISPR genotyping	This study
geno_CRIS PR_Ari5-R	GGCAAGTATCCTGGGTATGAGGAGG		This study
geno_CRIS PR_Ari7-F	CGGAAGACTGTTGGCATATTGGAGAG	ARI7 CRISPR genotyping	This study
geno_CRIS PR_Ari7-R	CCAGCGACATTAATACCACTGTGTG		This study
geno_CRIS PR_Ari8-F	GTGTAAATGTTTAGGTGTGAGCA GAG	ARI8 CRISPR genotyping	This study
geno_CRIS PR_Ari8-R	GGGACACCACTTGGCTACAAACATAAA AG		This study
Cloning primers			
BRI1_CDS_e cto_top	GGGGACAAGTTGTACAAAAAGCAGGCT TCATGAAGACTTTCAAGCTTCTT	BRI1 ectodomain CDS with stop codon flanked by attB1 and attB2 sites	This study
BRI1_CDS_e cto_bot	GGGGACCACTTGTACAAGAAAGCTGGGT ATCATCTCCTCCATGAGATC		This study

BRL1_CDS_ecto_top	GGGGACAAGTTGTACAAAAAAGCAGGCT TCATGAAGCAGAGATGGCTGTTAGT	BRL1 ectodomain CDS with stop codon flanked by attB1 and attB2 sites	This study
BRL1_CDS_ecto_bot	GGGGACCACTTGTACAAGAAAGCTGGGT ATTAGGTTGCAACAGTTGCTTCT		This study
BRL2-NoStop_GW_top	GGGGACAAGTTGTACAAAAAAGCAGGCT TCATGACTACTTCACCAATCCG	BRL2 ectodomain CDS without stop codon flanked by attB1 and attB2 sites	This study
BRL2-NoStop_GW_bot	GGGGACCACTTGTACAAGAAAGCTGGGT AGCTATTGCCAAGAACAGCTGC		This study
BRL3-NoStop_GW_top	GGGGACAAGTTGTACAAAAAAGCAGGCT TCATGAAACAACAATGGCAGTTCTT	BRL3 ectodomain CDS without stop codon flanked by attB1 and attB2 sites	This study
BRL3-NoStop_GW_bot	GGGGACCACTTGTACAAGAAAGCTGGGT AGCTCTGTTTTAGGGTGAGCAT		This study
SERK1_CDS_ecto_top	GGGGACAAGTTGTACAAAAAAGCAGGCT TCATGGAGTCGAGTTATGTGGTGT	SERK1 ectodomain CDS with stop codon flanked by attB1 and attB2 sites	This study
SERK1_CDS_ecto_bot	GGGGACCACTTGTACAAGAAAGCTGGGT ATTATCCAGTTATACCATACC		This study
SERK3_CDS_ecto_top	GGGGACAAGTTGTACAAAAAAGCAGGCT TCATGGAACGAAGATTAATGATCC	SERK3 ectodomain CDS with stop codon flanked by attB1 and attB2 sites	This study
SERK3_CDS_ecto_bot	GGGGACCACTTGTACAAGAAAGCTGGGT ATTATCCGGTGAGAGGATTGTTG		This study
BRI1_SDM_stop_FW	GGAGATGGTACCCAGCTTCTTGTAC	Remove stop codon from BRI1 entry clone	This study
BRI1_SDM_stop_RV	GAAAGCTGGTACCATCTCCTCCATG		This study
BRI1_SDM_stop_FW	CAACCTACTACCCAGCTTCTTGTG	Remove stop codon from BRL1 entry clone	This study
BRI1_SDM_stop_RV	GGGTAGTAGGTTGCAACAG		This study
SERK3_SDM_stop_FW	CACCGGATACTACCCAGCTTCTTGT	Remove stop codon from SERK3 entry clone	This study
SERK3_SDM_stop_RV	GAAAGCTGGTAGTATCCGGTGAGAGG		This study
SERK3_FW_NotI	AAAAAAGCGGCCGCATGGAACGAAGATT AATG	Add NotI and Xhol sites to SERK3 for cloning into pETSUMO	This study
SERK3_RV_Xhol	TTTTTCTCGAGTTATCCGGTGAGAGGATT G		This study
ari1_CDS_GG_top	TTGAAGACAAATGGATGATTATTTA GCGCGGAGG	amplification from cDNA of ARI1 to remove Bpi1 sites for direct GG cloning resulting in Fragment 1.1	This study
ari1_GG_S DM1.1-RV	TTGAAGACAAACACAGTGACACCAGCT CCAGA		This study

ari1_GG_S DM1.1-FW	TTGAAGACAATGTGTCGATTATCAAT ATGGCAA	amplification from cDNA of ARI1 to remove Bpi1 sites for direct GG cloning resulting in Fragment 1.2	This study
ari1_GG_S DM1.2-RV	TTGAAGACAATGACTGAGGAAAGGAA GAGTTGCC		This study
ari1_GG_S DM1.2-FW	TTGAAGACAAGTCATCACAGATGAGTT GTGA	amplification from cDNA of ARI1 to remove Bpi1 sites for direct GG cloning resulting in Fragment 2	This study
ari1_GG_S DM2-RV	TTGAAGACAATAGACCACAAGAACAT TCAACTTC		This study
ari1_GG_S DM2-FW	TTGAAGACAATCTACAGTTCTGTTCA GTTG	amplification from cDNA of ARI1 to remove Bpi1 sites for direct GG cloning resulting in Fragment 3	This study
ari1_GG_S DM3-RV	TTGAAGACAACCTCCGAGCTCCTTGATC CTGAAG		This study
ari1_GG_S DM3-FW	TTGAAGACAAGGAGGACACCATTGC TCATC	amplification from cDNA of ARI1 to remove Bpi1 sites for direct GG cloning resulting in Fragment 4	This study
ari1_CDS_ GG_bot	TTGAAGACAAAAGCTCAGTTCTGGTCG ACGAAATCAGC		This study
ari2_CDS_ GG_top	TTGAAGACAAAATGGATGATAATTAA GCGGCGAGG	amplification from cDNA of ARI2 to remove Bpi1 sites for direct GG cloning resulting in Fragment 1.1	This study
ari2_GG_F 1_RV	CCATAGTTCCCACATCACACAAGAGCA A		This study
ari2_GG_F 1_FW	GAGGTTGAATGCTCTTGTGGTTGCAG	amplification from cDNA of ARI2 to remove Bpi1 sites for direct GG cloning resulting in Fragment 1.2	This study
ari2_GG_S DM1-RV	TTGAAGACAATGACTGACCAACAGCTT CCTTG		This study
ari2_GG_S DM1-FW	TTGAAGACAAGTCATCGGATTGTGGA TGGACG	amplification from cDNA of ARI2 to remove Bpi1 sites for direct GG cloning resulting in Fragment 2	This study
ari2_GG_S DM2-RV	TTGAAGACAAAATCTCCGACTTCCCTG ACTCC		This study
ari2_GG_S DM2-FW	TTGAAGACAAAGATAACAAGTTGCTCTT CCGGG	amplification from cDNA of ARI2 to remove Bpi1 sites for direct GG cloning resulting in Fragment 3	This study
ari2_CDS_ GG_bot	TTGAAGACAAAAGCTCATTCCGCTCA ATGGCTTCC		This study
ari3_GG_S DM1-FW	TTGAAGACAAGAAAATATGAAATGT GATG	amplification from cDNA of ARI3 to remove Bpi1 sites for direct GG cloning resulting in Fragment 2	This study
ari3_GG_S DM2-RV	TTGAAGACAACTCACACTTCTTTTCCA TAG		This study
ari3_CDS_ GG_top	TTGAAGACAAAATGGATGACGACTAT ATGATGTTAG	amplification from cDNA of ARI3 to remove Bpi1 sites for direct GG cloning resulting in Fragment 1	This study
ari3_GG_S DM1-RV	TTGAAGACAATTCTCGAAGTAACAA AAGAAG		This study
ari3_GG_S DM2-FW	TTGAAGACAATGAGGACGAGTCTGAG ACGG	amplification from cDNA of ARI3 to remove Bpi1 sites for direct GG cloning resulting in Fragment 3	This study
ari3_CDS_ GG_bot	TTGAAGACAAAAGCCTACGAAGATCC GCTTGAACCACA		This study
ari5_GG_S DM1-FW	TTGAAGACAAGGAGGACAAGGAGAA GTATTATAG	amplification from cDNA of ARI5 to remove Bpi1 sites for	This study

ari5_CDS_GG_bot	TTGAAGACAAAAGCTCAATTGCCATCT GGGTTCTGCTG	direct GG cloning resulting in Fragment 2	This study
ari5_CDS_GG_top	TTGAAGACAAAATGGATTCCGATGAT GATATGCACG	amplification from cDNA of ARI5 to remove Bpi1 sites for direct GG cloning resulting in Fragment 1	This study
ari5_GG_S DM1-RV	TTGAAGACAACTCCTAGAAGCCA TATCG	amplification from cDNA of ARI8 to remove Bpi1 sites for direct GG cloning resulting in Fragment 1	This study
ari8_CDS_GG_top	TTGAAGACAAAATGGAAGCTGATGAC GATTCTAC	amplification from cDNA of ARI8 to remove Bpi1 sites for direct GG cloning resulting in Fragment 1	This study
ari8_GG_S DM1-RV	TTGAAGACAACTCAACGTATGATCTGA CAAAATAAC	amplification from cDNA of ARI8 to remove Bpi1 sites for direct GG cloning resulting in Fragment 1	This study
ari8_GG_S DM1-FW	TTGAAGACAATGAGGACAATAGAAAG ACC	amplification from cDNA of ARI8 to remove Bpi1 sites for direct GG cloning resulting in Fragment 2	This study
ari8_GG_S DM2-RV	TTGAAGACAATTCTCACCATGCTCTG TCC	amplification from cDNA of ARI8 to remove Bpi1 sites for direct GG cloning resulting in Fragment 2	This study
ari8_GG_S DM2-FW	TTGAAGACAAGAAAACAGGTGGCTT TATGC	amplification from cDNA of ARI8 to remove Bpi1 sites for direct GG cloning resulting in Fragment 3	This study
ari8_GG_S DM3-RV	TTGAAGACAATTCCCCCTAACGCTCTT TGAAC	amplification from cDNA of ARI8 to remove Bpi1 sites for direct GG cloning resulting in Fragment 3	This study
ari8_GG_S DM3-FW	TTGAAGACAAGAAAACAGGTGGCTT AGTTC	amplification from cDNA of ARI8 to remove Bpi1 sites for direct GG cloning resulting in Fragment 4	This study
ari8_CDS_GG_bot	TTGAAGACAAAAGCTCACCGGCCATG TTCACACATTGG	amplification from cDNA of ARI8 to remove Bpi1 sites for direct GG cloning resulting in Fragment 4	This study
ARI1_cc_F	GAATTCCCGGGATGGATGATTATTT AGCG	amplification of ARI1 with added Xma1/Xhol sites for PCR-directed cloning	This study
ARI1_cc_R	GTCGACTCGAGTCAGTTCTGGTCGACG AAAT	amplification of ARI1 with added Xma1/Xhol sites for PCR-directed cloning	This study
ARI2_cc_F	GAATTCCCGGGATGGATGATAATT AGCGG	amplification of ARI2 with added Xma1/Xhol sites for PCR-directed cloning	This study
ARI2_cc_R	GTCGACTCGAGTCATTCCGCTCAATG GC	amplification of ARI2 with added Xma1/Xhol sites for PCR-directed cloning	This study
ARI3_cc_F	GAATTCCCGGGATGGATGACGACTA TATG	amplification of ARI3 with added Xma1/Xhol sites for PCR-directed cloning	This study
ARI3_cc_R	GTCGACTCGAGCTACGAAGATCCGCT G	amplification of ARI3 with added Xma1/Xhol sites for PCR-directed cloning	This study
ARI5_cc_F	GAATTCCCGGGATGGATTCCGATGA TGATATG	amplification of ARI5 with added Xma1/Xhol sites for PCR-directed cloning	This study
ARI5_cc_R	GTCGACTCGAGTCATTGCCATCTGGG	amplification of ARI5 with added Xma1/Xhol sites for PCR-directed cloning	This study
ARI7_cc_F	GAATTGAATTCTGGATTCTGAAGAG GAC	amplification of ARI7 with added EcoRI/Xhol sites for PCR-directed cloning	This study
ARI7_cc_R	GTCGACTCGAGTTATAAGTTGTCATCT GGG	amplification of ARI7 with added EcoRI/Xhol sites for PCR-directed cloning	This study
ARI8_cc_F	GAATTCCCGGGATGGAAGCTGATGA CG	amplification of ARI8 with added Xma1/Xhol sites for PCR-directed cloning	This study
ARI8_cc_R	GTCGACTCGAGTCACCGGCCATGTTCA C	amplification of ARI8 with added Xma1/Xhol sites for PCR-directed cloning	This study

sdm_Xmal_FW	CCAATCCCCGGGTGGATCCGGTACCG	add Xmal site to pENTR1A to generate pENTR1Amod	This study
sdm_Xmal_RV	GGATCCACCCGGGGAATTGGTTCCCTT		This study
H142A_SD_M_ARI1-F	CTGTGGCGCTTGCTTTGCAATAATTG	SDM PCR of H142A in ARI1	This study
H142A_SD_M_ARI1-R	AAGCAAGGCCACAGTCCATTCTTG		This study
H143A_SD_M_ARI2-F	CTGTGGCGCTAGCTTTGCAATAAC	SDM PCR of H143A in ARI2	This study
H143A_SD_M_ARI2-R	CAAAAGCTAGCGCCACAGTCCATCCTTG		This study
H141A_SD_M_ARI3-F	GTGGTGCTAGGTTTGCAATG	SDM PCR of H141A in ARI3	This study
H141A_SD_M_ARI3-R	CAAAACCTAGCACCACATTCCATTG		This study
H151A_SD_M_ARI5-F	CTTGTGGTGCTCCTTCTGCGCTA	SDM PCR of H151A in ARI5	This study
H151A_SD_M_ARI5-R	GAAAGGAGCACCAAGAAACCG		This study
H156A_SD_M_ARI7-F	GTGGCGCTCCTTCTGCACTACAT	SDM PCR of H156A in ARI7	This study
H156A_SD_M_ARI7-R	GAAAGGAGCGCCACAAGAAACTG		This study
H147A_SD_M_ARI8-F	GTGGTGCTCCATTCTGCGACTCA	SDM PCR of H147A in ARI8	This study
H147A_SD_M_ARI8-R	GAATGGAGCACACAAGCAGCAGC		This study
ari1_CDS_GG_top	TTGAAGACAAAATGGATGATTATTTA GCGCGGAGG	amplify ariadne domain of ARI1 with stop codon in combination for GG cloning with Bpil sites	This study
ARI1_arid-stop-RV	TTGAAGACAAAAGCTTAGAGTAAGTC ATTCTCAATGC		This study
ari2_CDS_GG_top	TTGAAGACAAAATGGATGATAATTAA GCGCGGAGG	amplify ariadne domain of ARI2 with stop codon in combination for GG cloning with Bpil sites	This study
ARI2_arid-stop-RV	TTGAAGACAAAAGCTTACAACAAGTC ATTCTCAATGC		This study
ari3_CDS_GG_top	TTGAAGACAAAATGGATGACGACTAT ATGATGTTAG	amplify ariadne domain of ARI3 with stop codon in combination for GG cloning with Bpil sites	This study
ARI3_arid-stop-RV	TTGAAGACAAAAGCTTATAATAACTCA TTCTCAATGC		This study
ari5_CDS_GG_top	TTGAAGACAAAATGGATTCCGATGAT GATATGCACG	amplify ariadne domain of ARI5 with stop codon in combination for GG cloning with Bpil sites	This study
ARI5_arid-stop-RV	TTGAAGACAAAAGCTTAATTCTCCAGA GCTTTCACC		This study
ARI7_arid_FW	TTGAAGACAAAATGGAGACAGAGAG GAGGAGAG	amplify ariadne domain of ARI7 with stop codon in	This study

ARI7_arid-stop_RV	TTGAAGACAAAGCTTAAGCAAGACC GTTCTCCAGAG	combination for GG cloning with Bpil sites	This study
ari8_CDS_GG_top	TTGAAGACAAATGGAAGCTGATGAC GATTTCTAC	amplify ariadne domain of ARI8 with stop codon in combination for GG cloning with Bpil sites	This study
ARI8_arid-stop-RV	TTGAAGACAAAGCTTACGATAGCCC ATTCTCCAGCGC		This study
ARI1_NotI	ATGCAGCGGCCGCAATGGATGATTAT TTTAGCG	amplification of ARI1 with added NotI/Xhol sites for PCR-directed cloning into pETSUMO	This study
ARI1_cc_R	GTCGACTCGAGTCAGTTCTGGTCGACG AAAT		This study
ARI2_NotI	ATGCAGCGGCCGCAATGGATGATAAT TTAAGCGG	amplification of ARI2 with added NotI/Xhol sites for PCR-directed cloning into pETSUMO	This study
ARI2_cc_R	GTCGACTCGAGTCATTCCGCTCAATG GC		This study
ARI3_NotI	ATGCAGCGGCCGCAATGGATGACGAC TATATG	amplification of ARI3 with added NotI/Xhol sites for PCR-directed cloning into pETSUMO	This study
ARI3_cc_R	GTCGACTCGAGCTACGAAGATCCGCTT G		This study
ARI5_NotI	ATGCAGCGGCCGCAATGGATTCCGAT GATGATATG	amplification of ARI5 with added NotI/Xhol sites for PCR-directed cloning into pETSUMO	This study
ARI5_cc_R	GTCGACTCGAGTCAATTGCCATCTGGG		This study
ARI7_NotI	ATGCAGCGGCCGCAATGGATTCTGAA GAGG	amplification of ARI7 with added NotI/Xhol sites for PCR-directed cloning into pETSUMO	This study
ARI7_cc_R	GTCGACTCGAGTTATAAGTTGTATCT GGG		This study
ARI8_NotI	ATGCAGCGGCCGCAATGGAAGCTGAT GACG	amplification of ARI8 with added NotI/Xhol sites for PCR-directed cloning into pETSUMO	This study
ARI8_cc_R	GTCGACTCGAGTCACCGGCCATGTTCA C		This study
ARI1_L366_A_E367A_FW	CAGATTCATCAAAGGCAGCAGATAAA CTTAGGGATACTATCC	SDM PCR of L366 and E367 to Ala in ARI1	This study
ARI1_L366_A_E367A_RV	CCCTAAGTTATCTGCTGCCCTTGATGA ATCTGTATGAGCTTTG		This study
ARI1_E452_A_FW	GAAAGTAATGTGGCGAAACTTCGCA GTTCCCTTGAGGAGCCC	SDM PCR of E452 to Ala in ARI1	This study
ARI1_E452_A_RV	GCGAAAGTTCGCCACATTACTTCAA GTTGTTGCTGC		This study
ARI2_L367_A_E368A_FW	CGACTCCTCCAAGGCAGCGGCTAAC TTAGTAATAATTAG	SDM PCR of L367 and E368 to Ala in ARI2	This study
ARI2_L367_A_E368A_RV	CTAAGCTTAGCCGCTGCCTGGAGGA GTCGATATGTGCTTTG		This study

ARI2_E453 A_FW	GCTTGAGGCTAATGTTGCGAAACTTCTAAGTTCTGGAGG	SDM PCR of E453 to Ala in ARI2	This study
ARI2_E453 A_RV	GAAAGTTTCGCAACATTAGCCTCAAGCTGCTGCTGATCC		This study
ARI3_L364 A_E365A_FW	CGATTCATTAAGGCAGCGGATAAAC TTAGGAAGAGTATCC	SDM PCR of L364 and E365 to Ala in ARI3	This study
ARI3_L364 A_E365A_RV	CTAAGTTATCCGCTGCCTTAATGAAT CGATATGTGCTTTG		This study
ARI3_E452 A_FW	GAAGGTAATGTTGCGAAACTTCCAA GATTTAGAAGAGGCC	SDM PCR of E452 to Ala in ARI3	This study
ARI3_E452 A_RV	GGAAAGTTTCGCAACATTACCTCAAG TTGCTGCTGC		This study
ARI5_K382 A_FW	GTCGAGGCAAGCAGCTATGGGGATCTGCAG	SDM PCR of K382 to Ala in ARI5	This study
ARI5_K382 A_RV	CCCCCATAGCTGCTTGCCTCGACACTTGATTG		This study
ARI5_E457 A_FW	GTCAGGTTGGCGAGGCTCCACAAAT GCG	SDM PCR of E457 to Ala in ARI5	This study
ARI5_E457 A_RV	GTGGAGCCTCGCCAAACCTGACTCAG CCTCCCC		This study
ARI8_K378 A_FW	CGTCTAGGCAAGCGGCGCTGCTGGAT CTTAAG	SDM PCR of K378 to Ala in ARI8	This study
ARI8_K378 A_RV	CCAGCAGCGCCGCTTGCCTAGACGATT GATTGGTTGCC		This study
ARI8_E455 A_FW	CGGGCCTTGCACGACTTCATCAATGTG CTG	SDM PCR of E455 to Ala in ARI8	This study
ARI8_E455 A_RV	GATGAAGTCGTGCAAGGCCGACTCAGCTTCGCC		This study
ARI7_K387 A_FW	CGTCGAGGCAAGCGGCTATGGCTGAT CTGC	SDM PCR of K387 to Ala in ARI7	This study
ARI7_K387 A_RV	GCCATAGCCGCTTGCCTCGACGTTGA TTGC		This study
ARI7_E464 A_FW	GTCAGGTTAGCGAGGCTCCATCAATG CGTAG	SDM PCR of E464 to Ala in ARI7	This study
ARI7_E464 A_RV	GATGGAGCCTCGCTAACCTGACTCAGCTTCACC		This study
ARI1_S363 D_FW	GCTCATACAGATGATTCAAAGCTAGAA GATAAAC	SDM PCR of S363 to Asp in ARI1	This study
ARI1_S363 D_RV	CTTCTAGTTGAATCATCTGTATGAG CTTTGTATC		This study
ARI2_S364 D_FW	GCACATATCGACGACTCCAAGCTAGA GGCTAACG	SDM PCR of S364 to Asp in ARI2	This study
ARI2_S364 D_RV	CTAGCTTGGAGTCGTCGATATGTGCTT TGTATCGG		This study

ARI3_S361_D_FW	GCACATATCGATGATTAAAGCTAGAG GATAAAC	SDM PCR of S361 to Asp in ARI3	This study
ARI3_S361_D_RV	CTAGCTTAAATCATCGATATGTGCTTT GTAGCGG		This study
ARI5_S379_D_FW	GCAATCAAGTGGATAGGCAAAAGCT ATGGGGG	SDM PCR of S379 to Asp in ARI5	This study
ARI5_S379_D_RV	CTTTTGCCCTATCCACTTGATTGCTTGC CCAG		This study
ARI7_S380_D_FW	GAACGCTGGCAGACAATCAAACGTC GAGGC	SDM PCR of S380 to Asp in ARI7	This study
ARI7_S380_D_RV	CGTTTATTGTCTGCCAGCGTTCATA ATAGTG		This study
ARI8_S375_D_FW	CCAATCAATCGGATAGGCAAAAGGCG CTGCTGG	SDM PCR of S375 to Asp in ARI8	This study
ARI8_S375_D_RV	CTTTGCCTATCCGATTGATTGGTTGCC CATC		This study
AtCUL1_CDS_GW_FW	GGGGACAAGTTGTACAAAAAAAGCAG GCTTCATGGAGCGCAAGACTATT	Amplification of CUL1 from cDNA for GW cloning into pDONR221	Tobias Wagner
AtCUL1_CDS_GW_Rev	GGGGACCACTTGTACAAGAAAGCTG GGTACTAAGCCAAGTACCTAACAT		Tobias Wagner
AtCUL2_CDS_GW_FW	GGGGACAAGTTGTACAAAAAAAGCAG GCTTCATGGCGAAGAAGGATTCTGTGTT	Amplification of CUL2 from cDNA for GW cloning into pDONR221	Tobias Wagner
AtCUL2_CDS_GW_Rev	GGGGACCACTTGTACAAGAAAGCTG GGTACTAAGCCAATACTTGAAAGTGT		Tobias Wagner
AtCUL3A_CDS_GW_Fw	GGGGACAAGTTGTACAAAAAAAGCAG GCTTCATGAGTAATCAGAAGAAAGAGGG	Amplification of CUL3A from cDNA for GW cloning into pDONR221	Tobias Wagner
AtCUL3A_CDS_GW_Rev	GGGGACCACTTGTACAAGAAAGCTG GGTATTAGGCTAGATAGCGGTAAAGTT		Tobias Wagner
Cul3B_XmaI_FW	CAATTCCCCGGGAATGAGTAATCAGAAGAAGAGAAA	Amplification of CUL3B from cDNA and adding XmaI/Xhol sites for PCR-directed cloning into pENTR1Amod	This study
Cul3B_XhoI_RV	GATATCTCGAGTTACGCTAGATAGCGGTAAAGTT		This study
Cul4A_XmaI_FW	CAATTCCCCGGGAATGTCTCTTCTACCAAACG	Amplification of CUL4 from cDNA and adding XmaI/EcoRI sites for PCR-directed cloning into pENTR1Amod	This study
Cul4A_EcoRI_RV	GGCCCGGAATTCTAAGCAAGATAATTGTATATC		This study
RBX1A_NotI_FW	AAAAAAAGCGGCCGCATGGCGACTCTA	Amplification of RBX1A from cDNA and adding NotI/Xhol sites for PCR-directed cloning into pETSUMOmod	This study
RBX1A_Xhol_RV	TTTTTCTCGAGTTAGTGACCATATTT		This study
Cul3A_NotI_FW	AAAAAAAGCGGCCGCATGAGTAATCAGAAGAG	Amplification of CUL3A from cDNA and adding NotI/Xhol	This study

Cul3A_Xho_I_RV	TTTTTTCTCGAGTTAGGCTAGATAGCG GTAAAG	sites for PCR-directed cloning into pETSUMOmod	This study
elf4E1_No_tI_FW	AAAAAAAGCGGCCGCATGGCGGTAGA AGACACTCC	Amplification of elf4E1 from cDNA and adding NotI/Xhol sites for PCR-directed cloning into pETSUMOmod	This study
elf4E1_Xh_oI_RV	TTTTTTCTCGAGTCAGCGGTGAAGC GTTCTTGC	Amplification of elf4E1 from cDNA and adding NotI/Xhol sites for PCR-directed cloning into pETSUMOmod	This study
elfIso4E_N_oI_FW	AAAAAAAGCGGCCGCATGGCGACCGA TGATGTG	Amplification of elfIso4E from cDNA and adding NotI/Xhol sites for PCR-directed cloning into pETSUMOmod	This study
elfIso4E_X_hoI_RV	TTTTTTCTCGAGTCAGACAGTGAACCG GCTTCTTCTG	Amplification of elfIso4E from cDNA and adding NotI/Xhol sites for PCR-directed cloning into pETSUMOmod	This study
elf4E1_G_W_top	GGGGACAAGTTGTACAAAAAAGCAG GCTTCATGGCGGTAGAACGACTCC	Amplification of elf4E1 from cDNA for GW cloning into pDONR221	This study
elf4E1_G_W_bottom	GGGGACCACTTGTACAAGAAAGCTG GGTATCAAGCGGTGAAGCGTTCT	Amplification of elf4E1 from cDNA for GW cloning into pDONR221	This study
elfIso4E_G_W_top	GGGGACAAGTTGTACAAAAAAGCAG GCTTCATGGCGACCGATGATGTGAAC G	Amplification of elfIso4E from cDNA for GW cloning into pDONR221	This study
elfIso4E_G_W_bottom	GGGGACCACTTGTACAAGAAAGCTG GGTATCAGACAGTGAACCGGCTTCTC	Amplification of elfIso4E from cDNA for GW cloning into pDONR221	This study

Table S2. Plasmids used in this thesis.

Vector	Insert	Application	Source	Cloning method
pETSUMO	GFP	bacterial expression. 6xHis-SUMO-fused	Dr. Michael Niemeyer	PCR-directed
pETSUMO	SERK3_ecto*	bacterial expression. 6xHis-SUMO-fused	This study	PCR-directed
pETSUMO	empty	bacterial expression. 6xHis-SUMO-fused	Dr. Michael Niemeyer	PCR-directed
pETSUMO_mod	empty with KpnI, NotI and Xhol RE sites introduced	bacterial expression. 6xHis-SUMO-fused	Dr. Michael Niemeyer	PCR-directed
pETSUMO_mod_NotI/Xhol	ARI1	bacterial expression. 6xHis-SUMO-fused	This study	PCR-directed
pETSUMO_mod_NotI/Xhol	ARI1 ^{S363D}	bacterial expression. 6xHis-SUMO-fused	This study	PCR-directed
pETSUMO_mod_NotI/Xhol	ARI2	bacterial expression. 6xHis-SUMO-fused	This study	PCR-directed
pETSUMO_mod_NotI/Xhol	ARI2 ^{S364D}	bacterial expression. 6xHis-SUMO-fused	This study	PCR-directed

pETSUMO_mod_Not I/Xhol	ARI3	bacterial expression. 6xHis-SUMO-fused	This study	PCR-directed
pETSUMO_mod_Not I/Xhol	ARI3 ^{S361D}	bacterial expression. 6xHis-SUMO-fused	This study	PCR-directed
pETSUMO_mod_Not I/Xhol	ARI5	bacterial expression. 6xHis-SUMO-fused	This study	PCR-directed
pETSUMO_mod_Not I/Xhol	ARI5 ^{S379D}	bacterial expression. 6xHis-SUMO-fused	This study	PCR-directed
pETSUMO_mod_Not I/Xhol	ARI8	bacterial expression. 6xHis-SUMO-fused	This study	PCR-directed
pETSUMO_mod_Not I/Xhol	ARI8 ^{S375D}	bacterial expression. 6xHis-SUMO-fused	This study	PCR-directed
pETSUMO_mod_Not I/Xhol	Cul3A	bacterial expression. 6xHis-SUMO-fused	This study	PCR-directed
pETSUMO_mod_Not I/Xhol	eIF4E1	bacterial expression. 6xHis-SUMO-fused	This study	PCR-directed
pETSUMO_mod_Not I/Xhol	eIFiso4E	bacterial expression. 6xHis-SUMO-fused	This study	PCR-directed
pGEX4T-1	PUB26	bacterial expression. GST-fussed	Dr. Yang Shuhua	N/A
pGEX4T-3_GG	ARI1	bacterial expression. GST-fussed	This study	GG
pGEX4T-3_GG	ARI1 ^{Ariadne-domain}	bacterial expression. GST-fussed	This study	GG
pGEX4T-3_GG	ARI1 ^{L366A-E367A}	bacterial expression. GST-fussed	This study	GG
pGEX4T-3_GG	ARI1 ^{S363D}	bacterial expression. GST-fussed	This study	GG
pGEX4T-3_GG	ARI2	bacterial expression. GST-fussed	This study	GG
pGEX4T-3_GG	ARI2 ^{Ariadne-domain}	bacterial expression. GST-fussed	This study	GG
pGEX4T-3_GG	ARI2 ^{S364D}	bacterial expression. GST-fussed	This study	GG
pGEX4T-3_GG	ARI3	bacterial expression. GST-fussed	This study	GG
pGEX4T-3_GG	ARI3 ^{Ariadne-domain}	bacterial expression. GST-fussed	This study	GG

pGEX4T-3_GG	ARI3 ^{L364A-E365A}	bacterial expression. GST-fussed	This study	GG
pGEX4T-3_GG	ARI3 ^{S361D}	bacterial expression. GST-fussed	This study	GG
pGEX4T-3_GG	ARI5	bacterial expression. GST-fussed	This study	GG
pGEX4T-3_GG	ARI5 ^{Ariadne-domain}	bacterial expression. GST-fussed	This study	GG
pGEX4T-3_GG	ARI5 ^{K382A}	bacterial expression. GST-fussed	This study	GG
pGEX4T-3_GG	ARI8 ^{Ariadne-domain}	bacterial expression. GST-fussed	This study	GG
pGEX4T-3_GG	empty	bacterial expression. GST-fussed	Dr. Michael Niemeyer	GG
pGEX4T-3_GW	Cul3A	bacterial expression. GST-fussed	This study	GW
pGEX4T-3_GW	eIF4E1	bacterial expression. GST-fussed	This study	GW
pGEX4T-3_GW	eIFiso4E	bacterial expression. GST-fussed	This study	GW
pGEX4T-3_GW	empty	bacterial expression. GST-fussed		GW
pGEX4T-3_GW	BRI1_ecto*	bacterial expression. GST-fussed	This study	GW
pGEX4T-3_GW	BRL1_ecto*	bacterial expression. GST-fussed	This study	GW
pGEX4T-3_GW	BRL2_ecto*	bacterial expression. GST-fussed	This study	GW
pGEX4T-3_GW	BRL3_ecto*	bacterial expression. GST-fussed	This study	GW
pGEX4T-3_GW	SERK3_ecto*	bacterial expression. GST-fussed	This study	GW
pUG293	HIS-Ubq_UBA1_HA-UBC1_EL3	bacterial expression. Ubigate	Dr. Marco Trujillo	GG
pUG300	HIS-Ubq_UBA1_HA-UBC9_EL3	bacterial expression. Ubigate	Dr. Marco Trujillo	GG
pUG301	HIS-Ubq_UBA1_HA-UBC10_EL3	bacterial expression. Ubigate	Dr. Marco Trujillo	GG
pUG302	HIS-Ubq_UBA1_HA-UBC11_EL3	bacterial expression. Ubigate	Dr. Marco Trujillo	GG
pUG306	HIS-Ubq_UBA1_HA-UBC15_EL3	bacterial expression. Ubigate	Dr. Marco Trujillo	GG

pUG307	HIS-Ubq_UBA1_HA-UBC16_EL3	bacterial expression. Ubigate	Dr. Marco Trujillo	GG
pUG308	HIS-Ubq_UBA1_HA-UBC17_EL3	bacterial expression. Ubigate	Dr. Marco Trujillo	GG
pUG309	HIS-Ubq_UBA1_HA-UBC18_EL3	bacterial expression. Ubigate	Dr. Marco Trujillo	GG
pUG319	HIS-Ubq_UBA1_HA-UBC28_EL3	bacterial expression. Ubigate	Dr. Marco Trujillo	GG
pUG320	HIS-Ubq_UBA1_HA-UBC29_EL3	bacterial expression. Ubigate	Dr. Marco Trujillo	GG
pUG321	HIS-Ubq_UBA1_HA-UBC30_EL3	bacterial expression. Ubigate	Dr. Marco Trujillo	GG
pUG322	HIS-Ubq_UBA1_HA-UBC31_EL3	bacterial expression. Ubigate	Dr. Marco Trujillo	GG
pUG326	HIS-Ubq_UBA1_HA-UBC37_EL3	bacterial expression. Ubigate	Dr. Marco Trujillo	GG
pUG334	HIS-Ubq_UBA1_HA-UBC35_MMZ4_EL4	bacterial expression. Ubigate	Dr. Marco Trujillo	GG
pUG337	HIS-Ubq_UBA1_HA-UBC36_MMZ3_EL4	bacterial expression. Ubigate	Dr. Marco Trujillo	GG
pUG352	HIS-Ubq_UBA1_HA-UBC8_EL3	bacterial expression. Ubigate	Dr. Marco Trujillo	GG
pUG393	HIS-Ubq_UBA1_HA-UBC35_EL3	bacterial expression. Ubigate	Dr. Marco Trujillo	GG
pUG394	HIS-Ubq_UBA1_HA-UBC36_EL3	bacterial expression. Ubigate	Dr. Marco Trujillo	GG
pSPYCE	elf4E1	BiFC_cYFP	This study	GW
pSPYCE	elfiso4E	BiFC_cYFP	This study	GW
pSPYCE	empty	BiFC_cYFP	Dr. Marco Trujillo	GW

pSPYCE	UBC01	BiFC_cYFP	Dr. Marco Trujillo	GW
pSPYCE	UBC02	BiFC_cYFP	Dr. Marco Trujillo	GW
pSPYCE	UBC03	BiFC_cYFP	Dr. Marco Trujillo	GW
pSPYCE	UBC04	BiFC_cYFP	Dr. Marco Trujillo	GW
pSPYCE	UBC05	BiFC_cYFP	Dr. Marco Trujillo	GW
pSPYCE	UBC06	BiFC_cYFP	Dr. Marco Trujillo	GW
pSPYCE	UBC07	BiFC_cYFP	Dr. Marco Trujillo	GW
pSPYCE	UBC08	BiFC_cYFP	Dr. Marco Trujillo	GW
pSPYCE	UBC09	BiFC_cYFP	Dr. Marco Trujillo	GW
pSPYCE	UBC10	BiFC_cYFP	Dr. Marco Trujillo	GW
pSPYCE	UBC11	BiFC_cYFP	Dr. Marco Trujillo	GW
pSPYCE	UBC12	BiFC_cYFP	Dr. Marco Trujillo	GW
pSPYCE	UBC13	BiFC_cYFP	Dr. Marco Trujillo	GW
pSPYCE	UBC14	BiFC_cYFP	Dr. Marco Trujillo	GW
pSPYCE	UBC15	BiFC_cYFP	Dr. Marco Trujillo	GW
pSPYCE	UBC16	BiFC_cYFP	Dr. Marco Trujillo	GW

pSPYCE	UBC17	BiFC_cYFP	Dr. Marco Trujillo	GW
pSPYCE	UBC18	BiFC_cYFP	Dr. Marco Trujillo	GW
pSPYCE	UBC19	BiFC_cYFP	Dr. Marco Trujillo	GW
pSPYCE	UBC20	BiFC_cYFP	Dr. Marco Trujillo	GW
pSPYCE	UBC21	BiFC_cYFP	Dr. Marco Trujillo	GW
pSPYCE	UBC22	BiFC_cYFP	Dr. Marco Trujillo	GW
pSPYCE	UBC24	BiFC_cYFP	Dr. Marco Trujillo	GW
pSPYCE	UBC25	BiFC_cYFP	Dr. Marco Trujillo	GW
pSPYCE	UBC26	BiFC_cYFP	Dr. Marco Trujillo	GW
pSPYCE	UBC28	BiFC_cYFP	Dr. Marco Trujillo	GW
pSPYCE	UBC29	BiFC_cYFP	Dr. Marco Trujillo	GW
pSPYCE	UBC30	BiFC_cYFP	Dr. Marco Trujillo	GW
pSPYCE	UBC31	BiFC_cYFP	Dr. Marco Trujillo	GW
pSPYCE	UBC32	BiFC_cYFP	Dr. Marco Trujillo	GW
pSPYCE	UBC34	BiFC_cYFP	Dr. Marco Trujillo	GW
pSPYCE	UBC35	BiFC_cYFP	Dr. Marco Trujillo	GW

pSPYCE	UBC36	BiFC_cYFP	Dr. Marco Trujillo	GW
pSPYCE	UBC37	BiFC_cYFP	Dr. Marco Trujillo	GW
pSPYNE	ARI1	BiFC_nYFP	This study	GW
pSPYNE	ARI1 ^{H142A}	BiFC_nYFP	This study	GW
pSPYNE	ARI2	BiFC_nYFP	This study	GW
pSPYNE	ARI2 ^{H143A}	BiFC_nYFP	This study	GW
pSPYNE	ARI3	BiFC_nYFP	This study	GW
pSPYNE	ARI3 ^{H141A}	BiFC_nYFP	This study	GW
pSPYNE	ARI5	BiFC_nYFP	This study	GW
pSPYNE	ARI5 ^{H151A}	BiFC_nYFP	This study	GW
pSPYNE	ARI7	BiFC_nYFP	This study	GW
pSPYNE	ARI7 ^{H156A}	BiFC_nYFP	This study	GW
pSPYNE	ARI8	BiFC_nYFP	This study	GW
pSPYNE	ARI8 ^{H147A}	BiFC_nYFP	This study	GW
pSPYNE	empty	BiFC_nYFP	Dr. Hagen Stellmach	GW
pICH75044	35S:Venus-ARI1	Binary vector	Dr. Sylvestre Marillonet	GG
pICH75044	35S:Venus-ARI1 ^{S363D}	Binary vector	This study	GG
pICH75044	35S:Venus-ARI2	Binary vector	This study	GG
pICH75044	35S:Venus-ARI2 ^{S364D}	Binary vector	This study	GG
pICH75044	35S:Venus-ARI3	Binary vector	This study	GG
pICH75044	35S:Venus-ARI3 ^{S361D}	Binary vector	This study	GG

plCH75044	35S:Venus-ARI5	Binary vector	This study	GG
plCH75044	35S:Venus-ARI5 ^{S379D}	Binary vector	This study	GG
plCH75044	35S:Venus-ARI8 ^{S375D}	Binary vector	This study	GG
plCH75044	35S:Venus-empty	Binary vector	Dr. Sylvestre Marillone t	GG
pLIC6	35S::9xmyc-eIF4E1	Binary vector	ABRC	GW
pLIC6	35S::9xmyc-eIFiso4E	Binary vector	ABRC	GW
pAGM803 1	pCR_ari1	CRISPR final construct containing RFP, Cas9, dgRNA for ARI1 each with their U6promoter	This study	GG
pAGM803 1	pCR_ari2	CRISPR final construct containing RFP, Cas9, dgRNA for ARI2 each with their U6promoter	This study	GG
pAGM803 1	pCR_ari3	CRISPR final construct containing RFP, Cas9, dgRNA for ARI3 each with their U6promoter	This study	GG
pAGM803 1	pCR_ari5ari7	CRISPR final construct containing RFP, Cas9, dgRNA for ARI5 and ARI7 each with their U6promoter	This study	GG
pAGM803 1	pCR_ari5ari8	CRISPR final construct containing RFP, Cas9, dgRNA for ARI5 and ARI8 each with their U6promoter	This study	GG
pAGM803 1	pCR_ari5	CRISPR final construct containing RFP, Cas9, dgRNA for ARI5 each with their U6promoter	This study	GG
pAGM803 1	pCR_ari5ari7ari8	CRISPR final construct containing RFP, Cas9, dgRNA for ARI5, ARI7 and ARI8 each with their U6promoter	This study	GG
pAGM803 1	pCR_ari7ari8	CRISPR final construct containing RFP, Cas9, dgRNA for ARI7 and ARI8 each with their U6promoter	This study	GG
pAGM803 1	pCR_ari7	CRISPR final construct containing RFP, Cas9, dgRNA for ARI7 with their U6promoter	This study	GG
pAGM803 1	pCR_ari8	CRISPR final construct containing RFP, Cas9, dgRNA for ARI8 with their U6promoter	This study	GG
pAGM803 1	pCR_ari1ari2	CRISPR final construct containing RFP, Cas9, sgRNA for ARI1 and ARI2 each with their U6promoter	This study	GG
pAGM803 1	pCR_ari1ari3	CRISPR final construct containing RFP, Cas9, sgRNA for ARI1 and ARI3 each with their U6promoter	This study	GG

pAGM803 1	pCR_ari1ari2ari3	CRISPR final construct containing RFP, Cas9, sgRNA for ARI1, ARI2 and ARI3 each with their U6promoter	This study	GG
pAGM803 1	pCR_ari2ari3	CRISPR final construct containing RFP, Cas9, sgRNA for ARI2 and ARI3 each with their U6promoter	This study	GG
pAGM803 1	TGCC-LacZ-GGGA	CRISPR final destination vector	Dr. Sylvestre Marillonet	GG
pICH50900	CAGA-GGGA	CRISPR vector containing appropriate attachment sites for final construct cloning	Dr. Sylvestre Marillonet	GG
pICH50914	TGTG-GGGA	CRISPR vector containing appropriate attachment sites for final construct cloning	Dr. Sylvestre Marillonet	GG
pICH54033	ACTA-Dummy-TTAC	CRISPR vector containing appropriate attachment sites with a dummy sequence	Dr. Sylvestre Marillonet	GG
pICH54044	TTAC-Dummy-CAGA	CRISPR vector containing appropriate attachment sites with a dummy sequence	Dr. Sylvestre Marillonet	GG
pAGM513 23	RPS5a_Cas9i_tN	CRISPR. Clone containing Cas9	Dr. Sylvestre Marillonet	GG
pAGA2	Olep-RFP-tOle	CRISPR. Clone containing RFP	Dr. Christin Naumann	GG
pAGT6182	ATTG-C9T_sgRNA-CGCT	CRISPR. Clone used for sgRNA PCR amplification	Dr. Sylvestre Marillonet	GG
pICH47751	pCR_sgAri7.2	CRISPR. Entry clone containing U6promoter and sgRNA	This study	GG
pICH47751	pCR_sgAri1.1	CRISPR. Entry clone containing U6promoter and sgRNA	This study	GG
pICH47751	pCR_sgAri2.2	CRISPR. Entry clone containing U6promoter and sgRNA	This study	GG
pICH47751	pCR_sgAri5.1	CRISPR. Entry clone containing U6promoter and sgRNA	This study	GG
pICH47761	pCR_sgAri1.2	CRISPR. Entry clone containing U6promoter and sgRNA	This study	GG

pICH47761	pCR_sgAri2.1	CRISPR. Entry clone containing U6promoter and sgRNA	This study	GG
pICH47761	pCR_sgAri3.2	CRISPR. Entry clone containing U6promoter and sgRNA	This study	GG
pICH47761	pCR_sgAri5.2	CRISPR. Entry clone containing U6promoter and sgRNA	This study	GG
pICH47761	pCR_sgAri7.1	CRISPR. Entry clone containing U6promoter and sgRNA	This study	GG
pICH47761	pCR_sgAri8.2	CRISPR. Entry clone containing U6promoter and sgRNA	This study	GG
pICH47772	pCR_sgAri3.1	CRISPR. Entry clone containing U6promoter and sgRNA	This study	GG
pICH47772	pCR_sgAri8.1	CRISPR. Entry clone containing U6promoter and sgRNA	This study	GG
pICH47751	ACTAGGAG-LacZ-CGCTTAC	CRISPR. Entry vector for both U6promoter and sgRNA	Dr. Sylvestre Marillonet	GG
pICH47761	TTACGGAG-LacZ-CGCTCAGA	CRISPR. Entry vector for both U6promoter and sgRNA	Dr. Sylvestre Marillonet	GG
pICH47772	CAGAGGAG-LacZ-CGCTTGTG	CRISPR. Entry vector for both U6promoter and sgRNA	Dr. Sylvestre Marillonet	GG
pICSL90001	6Up	CRISPR. U6 promoter	Dr. Sylvestre Marillonet	GG
pAGM4031	ARI1	entry clone for GG cloning to destination vector	This study	GG
pAGM4031	ARI1 ^{Ariadne-domain}	entry clone for GG cloning to destination vector	This study	GG
pAGM4031	ARI2	entry clone for GG cloning to destination vector	This study	GG
pAGM4031	ARI2 ^{Ariadne-domain}	entry clone for GG cloning to destination vector	This study	GG
pAGM4031	ARI3	entry clone for GG cloning to destination vector	This study	GG
pAGM4031	ARI3 ^{Ariadne-domain}	entry clone for GG cloning to destination vector	This study	GG
pAGM4031	ARI5	entry clone for GG cloning to destination vector	This study	GG
pAGM4031	ARI5 ^{Ariadne-domain}	entry clone for GG cloning to destination vector	This study	GG

pAGM403 1	ARI7 ^{Ariadne-domain}	entry clone for GG cloning to destination vector	This study	GG
pAGM403 1	ARI8	entry clone for GG cloning to destination vector	This study	GG
pAGM403 1	ARI8 ^{Ariadne-domain}	entry clone for GG cloning to destination vector	This study	GG
pDONR201	UBC01	entry clone for GW cloning to destination vector	Dr. Marco Trujillo	GW
pDONR201	UBC02	entry clone for GW cloning to destination vector	Dr. Marco Trujillo	GW
pDONR201	UBC03	entry clone for GW cloning to destination vector	Dr. Marco Trujillo	GW
pDONR201	UBC04	entry clone for GW cloning to destination vector	Dr. Marco Trujillo	GW
pDONR201	UBC05	entry clone for GW cloning to destination vector	Dr. Marco Trujillo	GW
pDONR201	UBC06	entry clone for GW cloning to destination vector	Dr. Marco Trujillo	GW
pDONR201	UBC08	entry clone for GW cloning to destination vector	Dr. Marco Trujillo	GW
pDONR201	UBC09	entry clone for GW cloning to destination vector	Dr. Marco Trujillo	GW
pDONR201	UBC10	entry clone for GW cloning to destination vector	Dr. Marco Trujillo	GW
pDONR201	UBC11	entry clone for GW cloning to destination vector	Dr. Marco Trujillo	GW
pDONR201	UBC12	entry clone for GW cloning to destination vector	Dr. Marco Trujillo	GW
pDONR201	UBC13	entry clone for GW cloning to destination vector	Dr. Marco Trujillo	GW
pDONR201	UBC14	entry clone for GW cloning to destination vector	Dr. Marco Trujillo	GW
pDONR201	UBC15	entry clone for GW cloning to destination vector	Dr. Marco Trujillo	GW

pDONR201	UBC16	entry clone for GW cloning to destination vector	Dr. Marco Trujillo	GW
pDONR201	UBC17	entry clone for GW cloning to destination vector	Dr. Marco Trujillo	GW
pDONR201	UBC18	entry clone for GW cloning to destination vector	Dr. Marco Trujillo	GW
pDONR201	UBC19	entry clone for GW cloning to destination vector	Dr. Marco Trujillo	GW
pDONR201	UBC20	entry clone for GW cloning to destination vector	Dr. Marco Trujillo	GW
pDONR201	UBC21	entry clone for GW cloning to destination vector	Dr. Marco Trujillo	GW
pDONR201	UBC22	entry clone for GW cloning to destination vector	Dr. Marco Trujillo	GW
pDONR201	UBC24	entry clone for GW cloning to destination vector	Dr. Marco Trujillo	GW
pDONR201	UBC26	entry clone for GW cloning to destination vector	Dr. Marco Trujillo	GW
pDONR201	UBC27	entry clone for GW cloning to destination vector	Dr. Marco Trujillo	GW
pDONR201	UBC28	entry clone for GW cloning to destination vector	Dr. Marco Trujillo	GW
pDONR201	UBC29	entry clone for GW cloning to destination vector	Dr. Marco Trujillo	GW
pDONR201	UBC30	entry clone for GW cloning to destination vector	Dr. Marco Trujillo	GW
pDONR201	UBC31	entry clone for GW cloning to destination vector	Dr. Marco Trujillo	GW
pDONR201	UBC32	entry clone for GW cloning to destination vector	Dr. Marco Trujillo	GW
pDONR201	UBC33	entry clone for GW cloning to destination vector	Dr. Marco Trujillo	GW

pDONR201	UBC34	entry clone for GW cloning to destination vector	Dr. Marco Trujillo	GW
pDONR201	UBC35	entry clone for GW cloning to destination vector	Dr. Marco Trujillo	GW
pDONR201	UBC36	entry clone for GW cloning to destination vector	Dr. Marco Trujillo	GW
pDONR201	UBC37	entry clone for GW cloning to destination vector	Dr. Marco Trujillo	GW
pDONR201	UEV1A	entry clone for GW cloning to destination vector	Dr. Marco Trujillo	GW
pDONR201	UEV1B	entry clone for GW cloning to destination vector	Dr. Marco Trujillo	GW
pDONR201	UEV1C	entry clone for GW cloning to destination vector	Dr. Marco Trujillo	GW
pDONR201	UEV1D	entry clone for GW cloning to destination vector	Dr. Marco Trujillo	GW
pDONR221	eIF4E1	entry clone for GW cloning to destination vector	This study	GW
pDONR221	eIFiso4E	entry clone for GW cloning to destination vector	This study	GW
pDONR221	RBX1A	entry clone for GW cloning to destination vector	Dr. Michael Niemeyer	GW
pDONR221	CUL1	entry clone for GW cloning to destination vector	Tobias Wagner	GW
pDONR221	CUL2	entry clone for GW cloning to destination vector	Tobias Wagner	GW
pDONR221	CUL3A	entry clone for GW cloning to destination vector	Tobias Wagner	GW
pDONR221	BRI1_ecto*	entry clone for GW cloning to destination vector	This study	GW
pDONR221	BRL1_ecto*	entry clone for GW cloning to destination vector	This study	GW
pDONR221	BRL2_ecto*	entry clone for GW cloning to destination vector	This study	GW
pDONR221	BRL3_ecto*	entry clone for GW cloning to destination vector	This study	GW
pDONR221	SERK3_ecto*	entry clone for GW cloning to destination vector	This study	GW

pDONR221	SERK1_ecto*	entry clone for GW cloning to destination vector	This study	GW
pDONR221	empty	entry clone for GW cloning to destination vector	Invitrogen	GW
pENTR1A_EcoRI-Xhol	ARI7	entry clone for GW cloning to destination vector	This study	PCR-directed/GW
pENTR1A_plus_Xmal	empty	entry clone for GW cloning to destination vector	This study	PCR-directed/GW
pENTR1A_Xmal/EcoRI	Cul4	entry clone for GW cloning to destination vector	This study	PCR-directed/GW
pENTR1A_Xmal/Xhol	Cul3B	entry clone for GW cloning to destination vector	This study	PCR-directed/GW
pENTR1A	empty	entry vector for PCR-directed restricted PCR	Dr. Hagen Stellmach	PCR-directed
pMetOYC	empty	SUS	addgene	GW
pMetOYC	BRI1_ecto	SUS	This study	GW
pMetOYC	BRL1_ecto	SUS	This study	GW
pMetOYC	BRL2_ecto	SUS	This study	GW
pMetOYC	BRL3_ecto	SUS	This study	GW
pMetOYC	SERK3_ecto	SUS	This study	GW
pMetYC	empty	SUS	addgene	GW
pMetYC	BRI1_ecto	SUS	This study	GW
pMetYC	BRL1_ecto	SUS	This study	GW
pMetYC	BRL2_ecto	SUS	This study	GW
pMetYC	BRL3_ecto	SUS	This study	GW
pMetYC	SERK3_ecto	SUS	This study	GW
pNubWT	NubWT	SUS	addgene	GW
pNX32	empty	SUS	addgene	GW
pNX32	BRI1_ecto	SUS	This study	GW
pNX32	BRL1_ecto	SUS	This study	GW
pNX32	BRL2_ecto	SUS	This study	GW
pNX32	BRL3_ecto	SUS	This study	GW
pNX32	SERK3_ecto	SUS	This study	GW
pXN22	empty	SUS	addgene	GW
pXN22	BRI1_ecto	SUS	This study	GW
pXN22	BRL1_ecto	SUS	This study	GW
pXN22	BRL2_ecto	SUS	This study	GW
pXN22	BRL3_ecto	SUS	This study	GW
pXN22	SERK3_ecto	SUS	This study	GW

pB42AD_G_G	ARI1	Y2H	This study	GG
pB42AD_G_G	ARI1 ^{Ariadne-domain}	Y2H	This study	GG
pB42AD_G_G	ARI1 ^{H142A}	Y2H	This study	GG
pB42AD_G_G	ARI1 ^{L366A-E367A}	Y2H	This study	GG
pB42AD_G_G	ARI1 ^{L366A-E367A-E452A}	Y2H	This study	GG
pB42AD_G_G	ARI1 ^{S363D}	Y2H	This study	GG
pB42AD_G_G	ARI2	Y2H	This study	GG
pB42AD_G_G	ARI2 ^{Ariadne-domain}	Y2H	This study	GG
pB42AD_G_G	ARI2 ^{H143A}	Y2H	This study	GG
pB42AD_G_G	ARI2 ^{L367A-E368A}	Y2H	This study	GG
pB42AD_G_G	ARI2 ^{S364D}	Y2H	This study	GG
pB42AD_G_G	ARI3	Y2H	This study	GG
pB42AD_G_G	ARI3 ^{Ariadne-domain}	Y2H	This study	GG
pB42AD_G_G	ARI3 ^{H141A}	Y2H	This study	GG
pB42AD_G_G	ARI3 ^{L364A-E365A}	Y2H	This study	GG
pB42AD_G_G	ARI3 ^{L364A-E365A-E452A}	Y2H	This study	GG
pB42AD_G_G	ARI3 ^{S361D}	Y2H	This study	GG
pB42AD_G_G	ARI5	Y2H	This study	GG
pB42AD_G_G	ARI5 ^{Ariadne-domain}	Y2H	This study	GG
pB42AD_G_G	ARI5 ^{H151A}	Y2H	This study	GG
pB42AD_G_G	ARI5 ^{K382A}	Y2H	This study	GG
pB42AD_G_G	ARI5 ^{K382A-K427A}	Y2H	This study	GG
pB42AD_G_G	ARI5 ^{S379D}	Y2H	This study	GG
pB42AD_G_G	ARI7 ^{Ariadne-domain}	Y2H	This study	GG

pB42AD_G_G	ARI8 ^{Ariadne-domain}	Y2H	This study	GG
pB42AD_G_G	ARI8 ^{S375D}	Y2H	This study	GG
pB42AD_G_G	empty	Y2H	Dr. Antje Hellmuth	GG
pB42AD_G_W	empty	Y2H	Dr. Antje Hellmuth	GW
pB42AD_G_W	BRI1_ecto*	Y2H	This study	GW
pB42AD_G_W	BRL1_ecto*	Y2H	This study	GW
pB42AD_G_W	BRL2_ecto*	Y2H	This study	GW
pB42AD_G_W	BRL3_ecto*	Y2H	This study	GW
pB42AD_G_W	SERK3_ecto*	Y2H	This study	GW
pB42AD_G_W	SERK1_ecto*	Y2H	This study	GW
pB42AD_G_W	ARI7	Y2H	This study	GW
pB42AD_G_W	ARI7 ^{H156A}	Y2H	This study	GW
pB42AD_G_W	ARI7 ^{S380D}	Y2H	This study	GW
pB42AD_G_W	Cul1	Y2H	This study	GW
pB42AD_G_W	Cul2	Y2H	This study	GW
pB42AD_G_W	Cul3A	Y2H	This study	GW
pB42AD_G_W	Cul3B	Y2H	This study	GW
pB42AD_G_W	Cul4	Y2H	This study	GW
pB42AD_G_W	RBX1A	Y2H	This study	GW
pB42AD_G_W	UBC01	Y2H	This study	GW
pB42AD_G_W	UBC02	Y2H	This study	GW
pB42AD_G_W	UBC03	Y2H	This study	GW
pB42AD_G_W	UBC04	Y2H	This study	GW
pB42AD_G_W	UBC08	Y2H	This study	GW

pB42AD_G_W	UBC09	Y2H	This study	GW
pB42AD_G_W	UBC10	Y2H	This study	GW
pB42AD_G_W	UBC11	Y2H	This study	GW
pB42AD_G_W	UBC12	Y2H	This study	GW
pB42AD_G_W	UBC13	Y2H	This study	GW
pB42AD_G_W	UBC14	Y2H	This study	GW
pB42AD_G_W	UBC15	Y2H	This study	GW
pB42AD_G_W	UBC16	Y2H	This study	GW
pB42AD_G_W	UBC17	Y2H	This study	GW
pB42AD_G_W	UBC18	Y2H	This study	GW
pB42AD_G_W	UBC19	Y2H	This study	GW
pB42AD_G_W	UBC20	Y2H	This study	GW
pB42AD_G_W	UBC21	Y2H	This study	GW
pB42AD_G_W	UBC24	Y2H	This study	GW
pB42AD_G_W	UBC27	Y2H	This study	GW
pB42AD_G_W	UBC28	Y2H	This study	GW
pB42AD_G_W	UBC29	Y2H	This study	GW
pB42AD_G_W	UBC30	Y2H	This study	GW
pB42AD_G_W	UBC31	Y2H	This study	GW
pB42AD_G_W	UBC32	Y2H	This study	GW
pB42AD_G_W	UBC33	Y2H	This study	GW
pB42AD_G_W	UBC34	Y2H	This study	GW
pB42AD_G_W	UBC35	Y2H	This study	GW
pB42AD_G_W	UBC36	Y2H	This study	GW

pB42AD_G_W	UBC37	Y2H	This study	GW
pB42AD_G_W	UEV1A	Y2H	This study	GW
pB42AD_G_W	UEV1B	Y2H	This study	GW
pB42AD_G_W	UEV1C	Y2H	This study	GW
pB42AD_G_W	UEV1D	Y2H	This study	GW
pGilda	empty	Y2H	Dr. Antje Hellmuth	PCR-direceted
pGilda_EcoRI/Xhol	ARI7	Y2H	This study	PCR-direceted
pGilda_EcoRI/Xhol	ARI7 ^{H156A}	Y2H	This study	PCR-direceted
pGilda_G_W	empty	Y2H	Dr. Antje Hellmuth	GW
pGilda_G_W	BRI1_ecto*	Y2H	This study	GW
pGilda_G_W	BRL1_ecto*	Y2H	This study	GW
pGilda_G_W	BRL2_ecto*	Y2H	This study	GW
pGilda_G_W	BRL3_ecto*	Y2H	This study	GW
pGilda_G_W	SERK3_ecto*	Y2H	This study	GW
pGilda_G_W	SERK1_ecto*	Y2H	This study	GW
pGilda_G_W	Cul1	Y2H	This study	GW
pGilda_G_W	Cul2	Y2H	This study	GW
pGilda_G_W	Cul3A	Y2H	This study	GW
pGilda_G_W	Cul3B	Y2H	This study	GW
pGilda_G_W	Cul4	Y2H	This study	GW
pGilda_G_W	eIF4E1	Y2H	This study	GW
pGilda_G_W	eIFiso4E	Y2H	This study	GW

pGilda_G_W	RBX1A	Y2H	This study	GW
pGilda_G_W	UBC01	Y2H	This study	GW
pGilda_G_W	UBC02	Y2H	This study	GW
pGilda_G_W	UBC03	Y2H	This study	GW
pGilda_G_W	UBC04	Y2H	This study	GW
pGilda_G_W	UBC08	Y2H	This study	GW
pGilda_G_W	UBC09	Y2H	This study	GW
pGilda_G_W	UBC10	Y2H	This study	GW
pGilda_G_W	UBC11	Y2H	This study	GW
pGilda_G_W	UBC12	Y2H	This study	GW
pGilda_G_W	UBC13	Y2H	This study	GW
pGilda_G_W	UBC14	Y2H	This study	GW
pGilda_G_W	UBC15	Y2H	This study	GW
pGilda_G_W	UBC16	Y2H	This study	GW
pGilda_G_W	UBC17	Y2H	This study	GW
pGilda_G_W	UBC18	Y2H	This study	GW
pGilda_G_W	UBC19	Y2H	This study	GW
pGilda_G_W	UBC20	Y2H	This study	GW
pGilda_G_W	UBC21	Y2H	This study	GW
pGilda_G_W	UBC24	Y2H	This study	GW
pGilda_G_W	UBC27	Y2H	This study	GW
pGilda_G_W	UBC28	Y2H	This study	GW
pGilda_G_W	UBC29	Y2H	This study	GW
pGilda_G_W	UBC30	Y2H	This study	GW

pGilda_G_W	UBC31	Y2H	This study	GW
pGilda_G_W	UBC32	Y2H	This study	GW
pGilda_G_W	UBC33	Y2H	This study	GW
pGilda_G_W	UBC34	Y2H	This study	GW
pGilda_G_W	UBC35	Y2H	This study	GW
pGilda_G_W	UBC36	Y2H	This study	GW
pGilda_G_W	UBC37	Y2H	This study	GW
pGilda_G_W	UEV1A	Y2H	This study	GW
pGilda_G_W	UEV1B	Y2H	This study	GW
pGilda_G_W	UEV1C	Y2H	This study	GW
pGilda_G_W	UEV1D	Y2H	This study	GW
pGilda_G_W	empty	Y2H	Dr. Antje Hellmuth	GW
pGilda_Xmal/Xhol	ARI8	Y2H	This study	PCR-directed
pGilda_Xmal/Xhol	ARI8 ^{H147A}	Y2H	This study	PCR-directed
pGilda_Xmal/Xhol	ARI1	Y2H	This study	PCR-directed
pGilda_Xmal/Xhol	ARI1 ^{H142A}	Y2H	This study	PCR-directed
pGilda_Xmal/Xhol	ARI2	Y2H	This study	PCR-directed
pGilda_Xmal/Xhol	ARI2 ^{H143A}	Y2H	This study	PCR-directed
pGilda_Xmal/Xhol	ARI3	Y2H	This study	PCR-directed
pGilda_Xmal/Xhol	ARI3 ^{H141A}	Y2H	This study	PCR-directed

pGilda_Xmal/Xhol	ARI5	Y2H	This study	PCR-directed
pGilda_Xmal/Xhol	ARI5 ^{H151A}	Y2H	This study	PCR-directed

GG: Golden Gate, GW: Gateway, *stop codon

Table S3. CRISPR modules.

attachment sites Mod1-Mod6	TGCC- LacZ	TGCC- GCAA	GCAA- ACTA	ACTA- TTAC	TTAC- CAGA	CAGA- TGTG	TGTG- GGAA	LacZ- GGGA
attachment sites Mod1-Mod5	TGCC- LacZ	TGCC- GCAA	GCAA- ACTA	ACTA- TTAC	TTAC- CAGA	CAGA- GGGA	empty	LacZ- GGGA
Level 1 (Bpil)	Vector	Module 1	Module 2	Module 3	Module 4	Module 5	Module 6	Vector
pCR_ari1ari2ari3	pAGM8 031	pAGA2	pAGM5 1323	pCR_sg Ari1.1	pCR_sg Ari2.1	pCR_sg Ari3.1	pICH50 914	pAGM8 031
pCR_ari1	pAGM8 031	pAGA2	pAGM5 1323	pCR_sg Ari1.1	pCR_sg Ari1.2	pICH50 900	empty	pAGM8 031
pCR_ari2	pAGM8 031	pAGA2	pAGM5 1323	pCR_sg Ari2.2	pCR_sg Ari2.1	pICH50 900	empty	pAGM8 031
pCR_ari3	pAGM8 031	pAGA2	pAGM5 1323	pICH54 033	pCR_sg Ari3.2	pCR_sg Ari3.1	pICH50 914	pAGM8 031
pCR_ari1ari3	pAGM8 031	pAGA2	pAGM5 1323	pCR_sg Ari1.1	pICH54 044	pCR_sg Ari3.1	pICH50 914	pAGM8 031
pCR_ari1ari-2	pAGM8 031	pAGA2	pAGM5 1323	pCR_sg Ari1.1	pCR_sg Ari2.1	pICH50 900	empty	pAGM8 031
pCR_ari2ari-3	pAGM8 031	pAGA2	pAGM5 1323	pICH54 033	pCR_sg Ari2.1	pCR_sg Ari3.1	pICH50 914	pAGM8 031
pCR_ari5	pAGM8 031	pAGA2	pAGM5 1323	pCR_sg Ari5.1	pCR_sg Ari5.2	pICH50 900	empty	pAGM8 031
pCR_ari7	pAGM8 031	pAGA2	pAGM5 1323	pCR_sg Ari7.2	pCR_sg Ari7.1	pICH50 900	empty	pAGM8 031
pCR_ari8	pAGM8 031	pAGA2	pAGM5 1323	pICH54 033	pCR_sg Ari8.2	pCR_sg Ari8.1	pICH50 914	pAGM8 031
pCR_ari5ari7ari8	pAGM8 031	pAGA2	pAGM5 1323	pCR_sg Ari5.1	pCR_sg Ari7.1	pCR_sg Ari8.1	pICH50 914	pAGM8 031
pCR_ari5ari8	pAGM8 031	pAGA2	pAGM5 1323	pCR_sg Ari5.1	pICH54 044	pCR_sg Ari8.1	pICH50 914	pAGM8 031
pCR_ari5ari7	pAGM8 031	pAGA2	pAGM5 1323	pCR_sg Ari5.1	pCR_sg Ari7.1	pICH50 900	empty	pAGM8 031
pCR_ari7ari8	pAGM8 031	pAGA2	pAGM5 1323	pICH54 033	pCR_sg Ari7.1	pCR_sg Ari8.1	pICH50 914	pAGM8 031

Acknowledgements

This work was only possible with the support of many special people, for which I would like to thank you all!!

First of all, I would like to thank Dr. Luz Irina A. Calderón Villalobos, who gave me the opportunity to conduct my thesis in her lab and even though we were apart for most of the time, she was always very supportive. This was especially true when it came to change my main PhD topic. I am especially thankful for all the online discussions we had over the years that allowed me to develop many skills required to managing a lab... confidence, diplomacy, critical thinking... and to establish my own ideas in order to drive both projects forward. I truly benefited from your knowledge and drive and now feel more than ready for whatever task may come during my professional life.

To my previous supervisors Dr. Yamilet Coll and Dr. Daniel García, I fell in love with brassinosteroids because of you. I am grateful that I met you and gave me this opportunity in working in this challenging topic.

There are two people that I would like to especially thank from my heart, without them this thesis would not exist. Micha and Vero, I am very grateful for all your support. You were the epitome of teamwork and support. I really enjoyed working with you and sharing a few *Feierabendbier* (or more than a few). I cannot seem to find the words to express the gratitude that I feel...all I can say is THANK YOU! I owe you everything.

I would like to also thank the people that helped me during many of the experiments: Dr. Hagen Stellmach, I really enjoyed protoplast isolation and transformation in your lab, thanks for teaching me ☺; Prof. Dr. Bettina, I admire your willingness to help anyone that needs it, and your enthusiasm for microscopy was very contagious. Dr. Tom Schreiber, thank you for all your help teaching me CRISPR and helping me design the experiments. Dr. Khabat Vahabi, thank you for helping me understand RNAseq and performing the RNA quality measurement. Dr. Susanne Matschi and the technicians, for performing the MS/MS analysis of my IVUs and Pull-downs. Toni Dippe, for performing the synthesis of the Spyro-biotin photocrosslinker. Dr. Steffen Abel, for your willing ear in checking my progress in this last year. My lab mates, Jhonne and Tobi, for our weekly discussions either in the frame of the JC or our progress reports. Dr. Jean-Luc Gallois for the collaboration with the initiation of translation factors, I am sure we will have a beautiful publication together. Dr. Marco Trujillo, for your advice during the plant proteostasis congresses and sharing the E2s materials. Dr. Marcel Quint and Dr. Carolin Delker, I appreciate your comments and advice for the BR project and for always giving a helping hand. Thanks also to Antje, she was always helping me with paperwork and clear all my doubts regarding the doctoral program. My student Noah Binay, I enjoyed and appreciated working together, you were an excellent student and will become an awesome scientist. I would also like to thank Dr. Elisabeth Chapman for the insightful comments on the thesis and for the encouragement it provided. The gardeners, the cleaning crew, the financial department, the IT department, the handymen, Felix, the people behind the scenes that don't receive much recognition, but the IPB would definitely not function without them...THANK YOU.

I also would like to thank the Gasperinis: Stefan, Yunjing, Debora, Andy and Vero (again); I think I spent half the time in your lab. You were always there for me when I needed it, thanks ☺

I am also grateful for the wonderful people I met during my stay in Germany, thanks to you I fell in love with Halle and Germany, and I am proud to call you, my friends. Micha, Christine and Caro, I loved our time together...eating, having a beer, singing, playing the Uke or just go to the garden for some “hard-worked” beer. Micha I will never forget the beautiful bouquet you gave me for my first birthday in Germany ;)

I am grateful for my Cuban community, especially my friends Dayana and Dayma. Your support means everything to me.

I thank all my colleagues from the MSV department and around the IPB, for all the discussions during my presentations, the support, the pleasant atmosphere and the time outside the lab. I enjoyed being part of our department.

A pesar de estar lejos de mi familia, ellos siempre me apoyaron y los extraño todos los días. Mamá, papá, mis hermanas Eliza y Maureen, y por supuesto mi suegrita Oda, los quiero mucho. Sin su apoyo y amor yo no estaría en Alemania, y ahora en Barcelona, cumpliendo mi sueño y tener una vida cómoda.

Last but not least. Mi esposo, mi belloso, my partner, mein Schatz. Estos años fueron difíciles, requiriendo sacrificios de los dos, pero ambos lo logramos ... y ahora con 4 idiomas en la cabeza. La verdad es que no me imagino esta experiencia sin ti, eres mi roca, mi almohada, mi compañero en todos los sentidos, mi mejor amigo. Soy tan feliz de tenerte en mi vida.

Thank You! Dankeschön! Gracias!

Curriculum vitae

Nachname: Moreno Castillo

Vorname: Elena

Education and research experience

<p><i>05/2019 — Present</i></p>	<p>Doctorate Subject: Biochemistry Faculty of Natural Science – Biological Sciences Martin-Luther University of Halle-Wittenberg Dissertation thesis: “Elucidating molecular mechanisms of Spyros and Ariadne RBR E3 ubiquitin ligases in <i>Arabidopsis</i>” Signal Integration group Research Supervisor: Dr. Luz Irina A. Calderón Villalobos Academic Supervisor: Prof. Steffen Abel Leibniz Institute of Plant Biochemistry, Halle (Saale)</p>
<p><i>11/2015 — 01/2018</i></p>	<p>Master in Chemistry Facultad de Química, Universidad de la Habana, Cuba Supervisor: Dr. Pedro Valiente Flores Dissertation thesis: “In silico analysis of the interactions nature that determine the specificity of PTH inhibitors for Tau hexapeptide $^{306}\text{VQIVYK}^{311}$” Final grade: 5.00/5.00</p>
<p><i>10/2013 — 04/2019</i></p>	<p>Chemistry and Biochemistry Teacher and Researcher Facultad de Química, Universidad de la Habana, Cuba</p>
<p><i>09/2008 — 07/2013</i></p>	<p>Diploma in Biochemistry and Molecular Biology Facultad de Biología, Universidad de la Habana, Cuba Supervisor: MSc. Bessy Cutiño Ávila Dissertation thesis: “FlattenMOL: a new clustering algorithm for the determination of protein-support configuration during immobilization. Refinement of RDID1.0 program” Final grade: 4.89/5.00</p>
<p><i>09/2005 — 07/2008</i></p>	<p>High-School education V.I. Lenin Gymnasium, La Habana, Cuba Abitur, Final grade: 99.69/100</p>

Conference attendances 2019-2023

- Plant Science Student Conference PSSC 2023 (Oral presentation) 03/07/2023 – 04/07/2023
IPK, Gatersleben, Germany
- GRK2243 Symposium "Understanding Ubiquitylation: From Molecular Mechanisms to Disease"
(Poster presentation) 09/05/2022 – 11/05/2022 – Würzburg, Germany
- International Conference on Plant Proteostasis (Poster presentation) 21/09/2022 –
23/09/2022 – Madrid, Spain
- International Conference on Plant Proteostasis (Poster presentation) 10/09/2019 –
13/09/2019 – Freiburg, Germany. Winner of Best Poster Award
- Plant Science Student Conference PSSC 2019 (Poster presentation) 18/06/2019 – 21/06/2019
– Leibniz Institute of Plant Biochemistry, Halle, Germany
- Research Grants – Doctoral Programmes in Germany – DAAD: 2019-2023

Elena Moreno Castillo

List of publications

- Coro-Bermello, J., López-Rodríguez, E. R., Alfonso-Ramos, J. E., Alonso, D., Ojeda-Carralero, G. M., Prado, G. A., & **Moreno-Castillo, E.** (2021). Identification of novel thiadiazin derivatives as potentially selective inhibitors towards trypanothione reductase from *Trypanosoma cruzi* by molecular docking using the numerical index poses ratio Pr and the binding mode analysis. *SN Applied Sciences*, 3, 1–20. <https://doi.org/10.1007/s42452-021-04375-0>
- **Moreno-Castillo, E.**, Álvarez-Ginarte, Y. M., Valdés-Tresanco, M. E., Montero-Cabrera, L. A., Moreno, E., & Valiente, P. A. (2020). Understanding the disrupting mechanism of the Tau aggregation motif “306VQIVYK311” by phenylthiazolyl-hydrazides inhibitors. *Journal of Molecular Recognition*, 33(9), e2848. <https://doi.org/10.1002/jmr.2848>
- Niemeyer, M., **Moreno Castillo, E.**, Ihling, C. H., Iacobucci, C., Wilde, V., Hellmuth, A., Hoehnwarter, W., Samodelov, S. L., Zurbriggen, M. D., Kastritis, P. L., Sinz, A., & Calderón Villalobos, L. I. A. (2020). Flexibility of intrinsically disordered degrons in AUX/IAA proteins reinforces auxin co-receptor assemblies. *Nature Communications*, 11(1), 2277. <https://doi.org/10.1038/s41467-020-16147-2>
- Vicente, F. E. M., González-García, M., Diaz Pico, E., **Moreno-Castillo, E.**, Garay, H. E., Rosi, P. E., Jimenez, A. M., Campos-Delgado, J. A., Rivera, D. G., & Chinea, G. (2019). Design of a helical-stabilized, cyclic, and nontoxic analogue of the peptide Cm-p5 with improved antifungal activity. *ACS Omega*, 4(21), 19081–19095. <https://doi.org/10.1021/acsomega.9b02201>
- **Moreno-Castillo, E.**, Ramírez-Echemendía, D. P., Hernández-Campoalegre, G., Mesa-Tejeda, D., Coll-Manchado, F., & Coll-García, Y. (2018). In silico identification of new potentially active brassinosteroid analogues. *Steroids*, 138, 35–42. <https://doi.org/10.1016/j.steroids.2018.06.009>
- del Monte Martínez, A., Cutiño-Avila, B., **Moreno Castillo, E.**, de Santelices Muñoz, R. M., González, B. Z., & Gasca, F. J. P. (2012). Optimización y racionalización in silico de la síntesis de biocatalizadores inmovilizados para la obtención de prebióticos. *Obtención Enzimática de Compuestos Bioactivos a Partir de Recursos Naturales Iberoamericanos*, 273–292. ISBN: 84-00-09568-5

Eidesstattliche Erklärung (Statutory declaration)

Hiermit erkläre ich an Eides statt, dass ich mich mit der vorliegenden wissenschaftlichen Arbeit erstmals um die Erlangung des Doktorgrades bewerbe, die Arbeit selbstständig und ohne fremde Hilfe verfasst, nur die angegebenen Quellen und Hilfsmittel genutzt und die den benutzten Werken wörtlich oder inhaltlich entnommenen Stellen als solche kenntlich gemacht habe.

Halle (Saale), den _____

Elena Moreno Castillo